Important Notice

THE UNIVERSITY OF CALGARY

Multigrid methods and the surface consistent equations of Geophysics

by

John Millar

A DISSERTATION
SUBMITTED TO THE FACULTY OF GRADUATE STUDIES
IN PARTIAL FULFILLMENT OF THE REQUIREMENTS FOR THE
DEGREE OF Ph.D. IN GEOPHYSICS

DEPARTMENT OF GEOSCIENCE

CALGARY, ALBERTA

June, 2010

UNIVERSITY OF
CALGARY

THE UNIVERSITY OF CALGARY

I would like to thank the following people for their participation in my defence of this thesis.

Supervisor, Dr. John Bancroft, Department of Geoscience

Dr. Gary Margrave, Department of Geoscience

Dr. Larry Lines, Department of Geoscience

Dr. Colin Card, Department of Petroleum Engineering

External Examiner, Dr. Peter Cary

Neutral Chair, Dr. Alan Hildebrand, Department of Geoscience

Abstract

The surface consistent equations are a large linear system that is frequently used in signal enhancement for land seismic surveys. Different signatures may be consistent with a particular dynamite (or other) source. Each receiver and the conditions around the receiver will have different impact on the signal.

Seismic deconvolution operators, amplitude corrections and static shifts of traces are calculated using the surface consistent equations, both in commercial and scientific seismic processing software.

The system of equations is singular, making direct methods such as Gaussian elimination impossible to implement. Iterative methods such as Gauss-Seidel and conjugate gradient are frequently used. A limitation in the nature of the methods leave the long wavelengths of the solution poorly resolved.

To reduce the limitations of traditional iterative methods, we employ a multigrid method. Multigrid methods re-sample the entire system of equations on a more coarse grid. An iterative method is employed on the coarse grid. The long wavelengths of the solutions that traditional iterative methods were unable to resolve are calculated on the reduced system of equations. The coarse estimate can be interpolated back up to the original sample rate, and refined using a standard iterative procedure.

Multigrid methods provide more accurate solutions to the surface consistent equations, with the largest improvement concentrated in the long wavelengths. Synthetic models and tests on field data show that multigrid solutions to the system of equations can significantly increase the resolution of the seismic data, when used to correct both static time shifts and in calculating deconvolution operators.

The first chapter of this thesis is a description of the physical model we are addressing. It reviews some of the literature concerning the surface consistent equations, and provides background on the nature of the problem.

Chapter 2 contains a review of iterative and multigrid methods. A finite difference approximation to Laplaces equation is solved to outline some of the methods used later in the thesis. This includes defining what is meant by long wavelength errors, which is a principal concept in this study.

Chapter 3 begins with a standard definition of the surface consistent equations. The ability of each method to estimate a solution to a synthetic surface consistent system is tested. The error remaining due to limitations in the solving method is shown to reduce the signal quality of a seismic gather. How the errors manifest in the data is demonstrated using static, amplitude and deconvolution corrections. The results from a multigrid method are compared to those of a Gauss-Seidel and bi-conjugate gradient method.

Finally, a surface consistent deconvolution of the CREWES Blackfoot data set is presented. The multigrid solutions to the equations are shown to provide deconvolution operators that improve the resolution of the seismic trace over Gauss-Seidel and conjugate gradient methods.

Table of Contents

List of Figures

Chapter 1

Introduction

The surface consistent equations are a linear set of equations that are used for the processing of seismic data acquired on land. The equations are derived from the assumption that most of the signal degradation that occurs in seismic reflection data can be attributed to conditions surrounding both the source and receiver that contribute to a trace. Surface noise amplitude and velocity traveltime errors are dependent on the source receiver offset.

The solution to the surface consistent equations provide operators that enhance the seismic signal. By calculating a more accurate solution, we should be able to improve the resolution in the data.

1.1 Seismic data

The standard process for collecting seismic data is depicted in Figure 1.1. The green line represents the surface of the earth. Each inverted triangle in the cartoon is a geophone planted into the ground. Dynamite, set in a shallow borehole, is detonated near the geophones (the black asterisk on the surface in the center of the geophones). Seismic waves travel into the earth from the source, and are reflected off changes in the rock layer below the surface. The reflected energy is recorded by the geophones.

The path of the energy is represented by rays that propagate from the source to the reflector, and back to the receiver. These rays are represented in magenta in Figure 1.1. The goal of the reflection seismic survey is to collect and process this reflected data, to gather

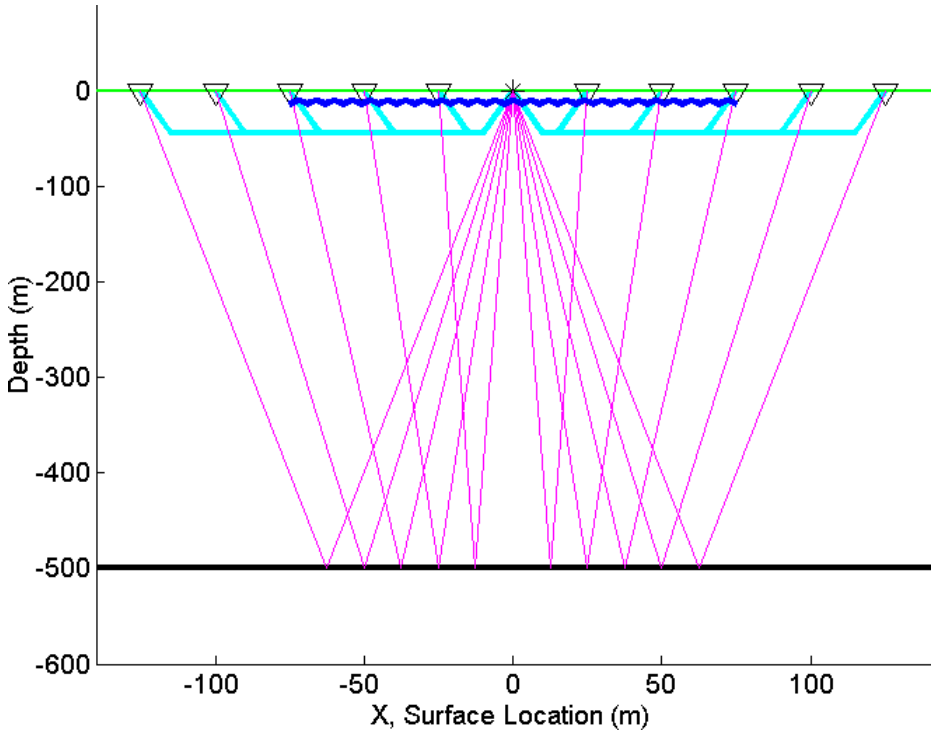

Figure 1.1: Cartoon showing the geometry of a reflection seismic data survey, and the paths various forms of energy take to the surface. Ground roll is depicted in navy blue, the refracted wave in turquoise, and the red lines represent reflections.

images and estimates of physical properties in the subsurface.

The ground roll is a slow moving wave that is confined to the near surface. It is a source of high amplitude and low frequency noise. The ground roll is shown in Figure 1.1 as a navy blue line.

The cyan line that runs along 50 meters below the surface then back up to the receivers represents refracted energy. These waves run into the earth, then run along the boundary where the soft unconsolidated sediment meets the hard subsurface rock. These waves are the first to arrive to the geophones on a seismic record.

Figure 1.2 is a sample seismic record from the CREWES Blackfoot data set. The waves diagrammed in Figure 1.1 are outlined in Figure 1.2 on the gather in the corresponding

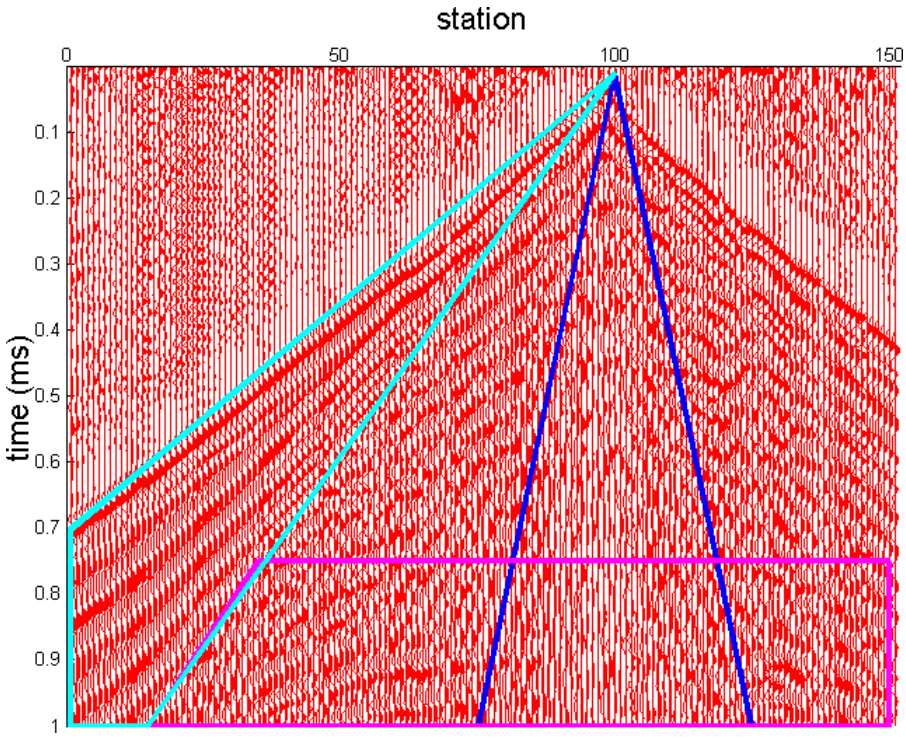

Figure 1.2: A sample seismic record from the CREWES Blackfoot data set. The reflection data that we are interested in is outlined in magenta. The ground roll and refracted waves are outlined in navy blue and cyan respectively.

colors.

The explosive source was buried beneath station 100. Each vertical red line represents a receiver recording the returning seismic data. The refracted waves are the first to arrive, outlined in cyan on the left hand side of the record. The reflections (outlined in magenta) are hyperbolic in shape, due to the geometry of the survey. The slow moving ground roll is the last wave to arrive to each receiver, only the geophones near the source record any ground roll in the first second of data.

The goal of reflection seismic surveying is to use the recorded reflection energy to provide insight into the location and composition of geologic formations. The data may be analysed

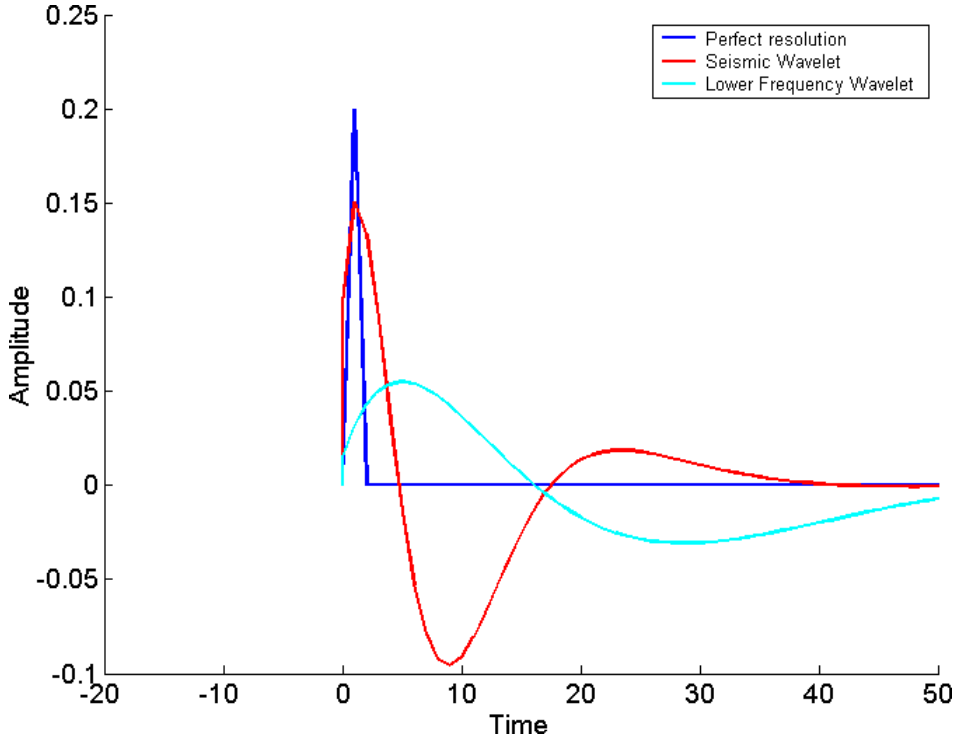

Figure 1.3: The shape of a seismic wavelet from a dynamite source.

in several ways. The reflections can be transformed and summed to form a seismic image of the structure of the subsurface. This imaging procedure is called migration. Other ways to analyse the data include performing tomography, or analysing the amplitude and shape of individual reflectors. An inversion may be performed to calculate rock properties.

Before migrating the data, a number of corrections are applied to the data to account for the geometry of the survey and to enhance the signal relative to the noise.

Figure 1.3 shows the shape of the signal generated using a dynamite source. This wave travels from the source, is reflected of the rock layer below the surface, and is recorded by the geophone at the surface. The shape of the wave we record will be roughly the same shape as the wave produced at the source, but will generally broaden as it propagates. The shape of the wave is modified by energy absorption along the path length, and the properties of

the receiver.

The blue spike represents the perfect seismic signal. When the reflected energy is recorded, a boundary in the subsurface would appear as a clear line in the data. In practice, the seismic wavelet that is reflected is more like the red wave. The shapes of the waves is determined by their frequency content. The cyan wave has the lowest frequency, the blue spike the highest.

Deconvolution aims to transform the shape of the embeded wavelet into a narrow spike, transforming the red line in Figure 1.3 into the blue line.

Figure 1.4(a) shows the recorded signal from a single reflector. Figure 1.4(b) is the same gather with deconvolution applied. The deconvolved data has a higher resolution, and more detail will be visible in the data.

Figure 1.4(a) contains a geometric effect called normal move-out or *NMO*. In Figure 1.1, the path that the seismic wave travels is longer for receivers farther from the source. The traveltime increases with offset, so a perfectly flat reflector in a constant velocity medium would appear as a hyperbola on a seismic section, as is shown in Figure 1.4(a). Normal move-out removal shifts reflections recorded at stations far from the source to line up with the reflections recorded at near offset (Figure 1.4(c)).

Individual seismic traces may have traveltimes modified by variations in the elevation and near surface velocity. These traces need to be bulk shifted up or down in time relative to each other. This process is called static shifting (or statics). Figure 1.5(a) shows a gather requiring statics. The term *statics* implies the entire trace is shifted by the same amount, before NMO corrections. Adding each of the traces from Figure 1.5(a) together results in the stack section of Figure 1.5(c). A stacked trace with the correction applied is compared to the trace without the static correction applied. Applying the correct statics improves the

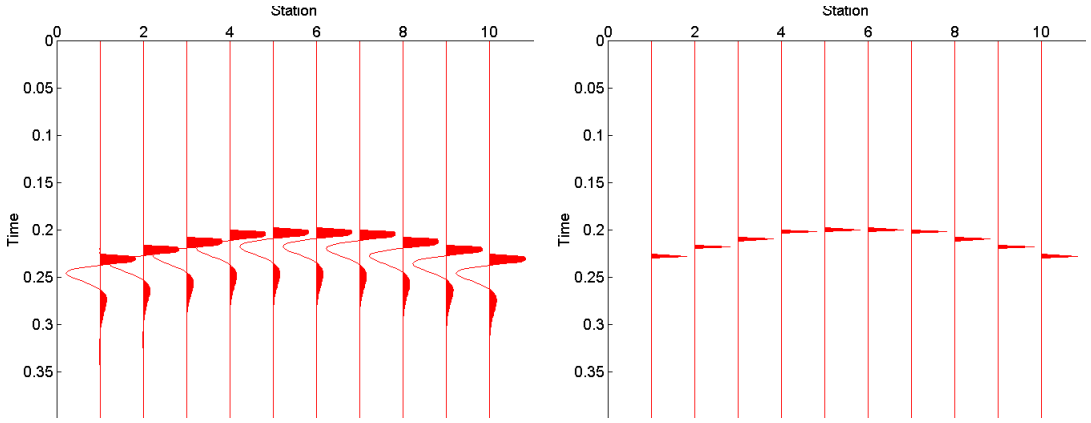

(a) Seismic data as recorded in the field, with normal move-out and an embedded wavelet

(b) After applying a deconvolution algorithm to the raw data, removing the embeded wavelet

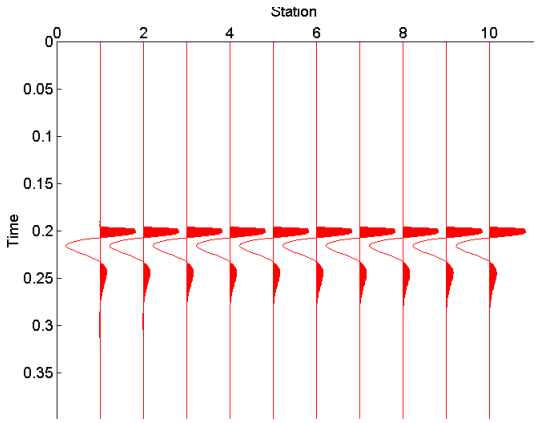

(c) After applying a normal move-out correction to the raw data

Figure 1.4: Cartoon depiction of normal move-out and deconvolution.

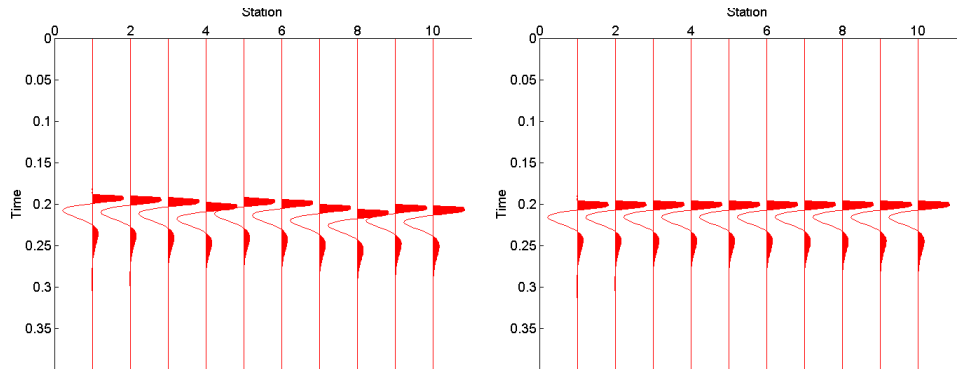

(a) Seismic data requiring static data shifts

(b) After applying static corrections (normal move-out also removed)

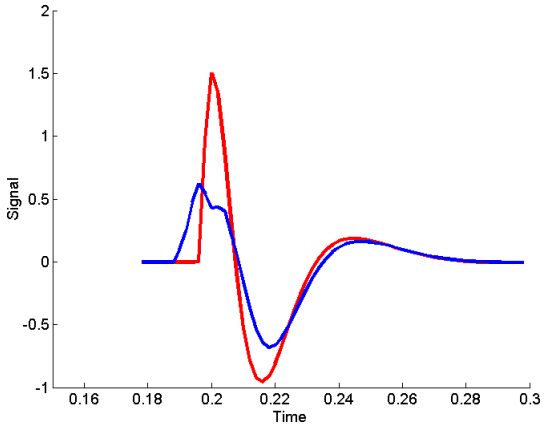

(c) Comparison of stack results with (red) and without (blue) static corrections

Figure 1.5: Each trace is shifted vertically in time to line up the reflections before stacking.

resolution of the data.

Each trace in the gather may record a particular reflection with a different sensitivity. Amplitude corrections are applied to the seismic data to ensure that each trace measures the size of the reflections consistently. This step becomes especially important when using amplitudes directly for interpretation, such as for amplitude versus offset (AVO) studies. We wish to remove the changes in amplitude from trace to trace, without affecting the sensitive amplitude information contained in the data that is used to calculate rock properties.

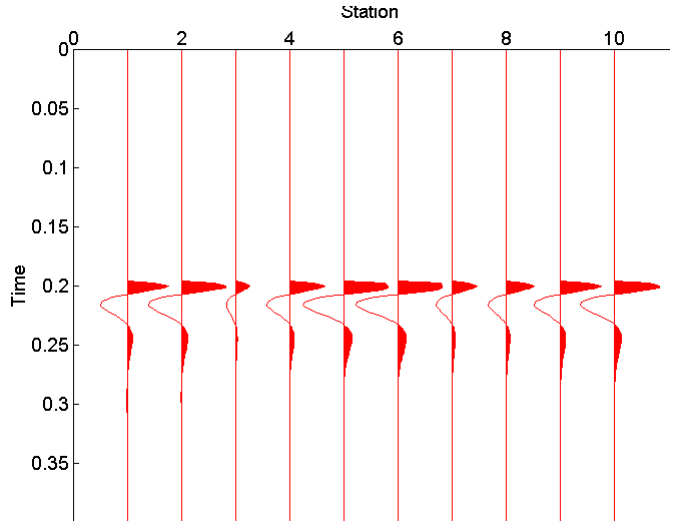

(a) A gather with amplitude errors

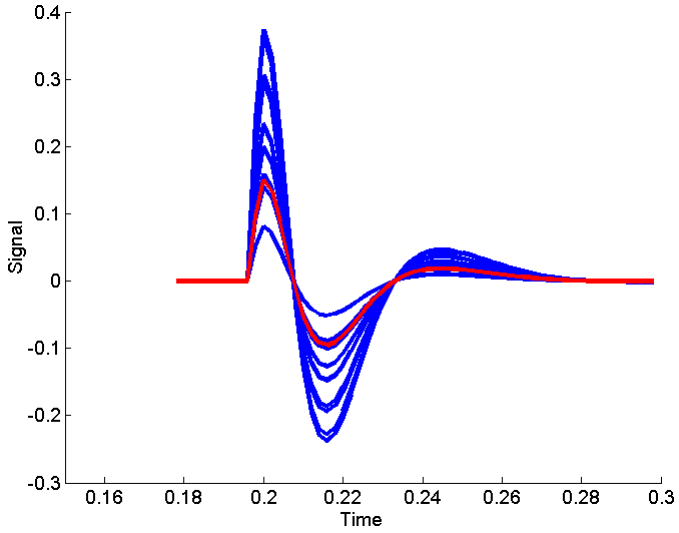

(b) Each trace in the gather plotted over top of each other

Figure 1.6: Each trace has measured a different amplitude for the same reflector.

Figure 1.6(a) is a gather of traces with a varying amplitude. Figure 1.6(b) shows all of the individual traces overlapping each other.

1.2 Surface consistent behaviour

When applying statics, arbitrary shifting of traces is discouraged, as it may unacceptably alter the structure of the subsurface features. Faults and fractures may be obscured or smoothed over in the data (Bancroft et al., 2000). To prevent this from occurring, a constraint on the statics based on the physics of the survey is applied. We therefore need to make an assumption about the nature of the physical problem.

The conditions immediately surrounding a particular receiver do not change from record to record. The delay in the travel-time of a reflection due to the overburden and near surface conditions do not change either. The same can be said for a travel-time delay associated with a particular source.

We assume the total correction needed is the sum of the correction associated with the source and the correction associated with the receiver location that combine to form each trace. This assumption is used to mathematically derive the surface consistent equations (Taner et al., 1974). Furthermore, deriving and using an offset dependent channel allows us to remove velocity moveout errors from the source and receiver estimates.

Amplitude corrections may also be calculated using the surface consistent equations (Taner et al., 1974). The recorded reflection amplitude for a particular reflector will be the multiple of the source amplitude and some absorption factor due to the geophone. An offset term can remove surface noise contamination from the estimate, and the midpoint consistent term will hold the reflectivity.

By solving a system of equations for the amplitude of each frequency, deconvolution operators can be calculated based on the source receiver coordinates (Cary and Lorentz, 1993). The four term surface consistent equations effectively map the ground roll to the offset term. Deconvolution operators are calculated for a trace using only the source and receiver components. By omitting the ground roll in the operator design, deconvolution will focus on whitening the spectrum of the reflectors, improving the resolution.

1.3 Solving the equations

The set of equations we attempt to solve to get a surface consistent solution is singular. This precludes the use of direct methods such as Gaussian elimination. Instead we are forced to estimate the solution, using an iterative method.

Wiggins et al. (1976) reviews the uncertainties that are unavoidable in solving the surface consistent equations. The authors recommend that only a few iterations of a Gauss-Seidel correction be performed, so as to prevent the large long wavelength instabilities from becoming dominant.

Iterative methods start with an initial estimate of the solution and refine it repeatedly until the solution passes some error tolerance.

This thesis addresses the ability of several different methods used to solve the surface consistent equations. Gauss-Seidel and conjugate gradient methods are typically used to provide an approximate solution. With both methods, long wavelengths in the solution are not well represented. A multigrid method is introduced as an alternative, which provides a more accurate solution on all wavelengths.

The quality of the initial estimate is very important for iterative methods. Multigrid

forms a solution to the system on a more coarse grid, allowing the long wavelengths in the solution to be calculated efficiently. Each coarse estimate is interpolated and used as an initial estimate for an iterative method on a more fine grid. The solution is interpolated and refined repeatedly until the desired resolution is acheived.

Multigrid methods are used frequently in many areas of research and computing (eg. computational fluid dynamics (Trottenberg et al., 2001; Wesseling, 1992)), however its exposure in the field of seismic research is limited, although there have been some examples, (eg. (Wang and Zhou, 1992; Bunks et al., 1995)). The methods provide superior error reduction compared to traditional iterative methods, with very efficient computation times.

Multigrid methods project large systems of equations onto a smaller grid, utilizing fewer equations. With a combination of filtering and down-sampling, the high frequencies in both the matrix, and the source term are removed and ignored. An approximate solution on the coarse grid is interpolated up to the original sample rate, and used as an initial estimate for an iterative process at the original resolution. A large part of the calculation effort is spent on the smaller grid, where the smaller number of unknowns and the increased effectiveness of the iterative method help reduce calculation time, and improve the lower frequencies of the solution.

1.4 Scope

This thesis is restricted to examining the solution methods used to invert a system of equations. The variables we are examining are the matrix inversion method used, the quality of the solution it provides, and the effect of the residual error on seismic data.

This paper does not address for instance, how a static shift for a trace is calculated. It

only examines how the static shift for a particular trace is projected into source and receiver consistent components.

For deconvolution, all of the standard assumptions are still present (random and white reflectivity, minimum phase etc.). For a review of the assumptions in deconvolution see Yilmaz and Doherty (1994).

We only examine the process of how the amplitude spectrum for all of the traces can be decomposed into surface consistent channels. The surface consistent equations are constructed in a way that is equivalent to what has been done in the literature (Cary and Lorentz, 1993, eg.). Wavelet estimation, and how to best apply a deconvolution operator to a trace, is not discussed.

1.5 Outline

Chapter 2 is a review and demonstration of using iterative methods to solve a system of equations. Jacobi, Gauss-Seidel, conjugate gradient and multigrid methods are discussed, as well as some of the theoretical tools we can use to evaluate the methods.

The methods are demonstrated on a sample matrix, the finite difference approximation to the Laplacian operator. This example is used to illustrate some of the concepts discussed regarding the iterative methods. The multigrid method is introduced, the discussion is less detailed, but similar to Press et al. (1992). All of the iterative methods are subjected to a spectral analysis prescribed by Shewchuk (2002).

The third chapter concentrates on the surface consistent equations. First, a derivation of the equations is provided. The derivation is consistent with the literature (Taner et al. (1974), Cary and Lorentz (1993)). A synthetic surface consistent model is constructed, and

the various solution methods discussed in the previous chapter are applied and anylysed using the method described in Shewchuk (2002). Contrasting the solution of the surface consistent equations with the results on the Laplaces equation examples help highlight the difficulties we encounter solving ill posed problems.

The results of using different solution methods, and the effects of the associated errors are modeled in a synthetic seismic survey. We use the synthetic seismic surveys to predict the effect that the improved multigrid solutions will provide on field seismic data.

A basic surface consistent deconvolution was tested on the CREWES Blackfoot field data. Different surface consistent operators were calculated using the discussed methods. The relative ability of the various deconvolution operators at whitening the seismic data and suppressing ground roll is tested.

The derivation of the surface consistent equations is equivalent to derivations in the literature, however the analysis based on numerical methods and linear algebra is to my knowledge unique. While multigrid methods have been applied extensively in other areas of computing, this is the first project to apply them to the surface consistent equations. As well, the use of synthetic surface consistent models to test solution algorithms, and modelling the error in seismic data is to the best of my knowledge original.

My original contributions to this dissertation are

1. Taking the error analysis of the Gauss-Seidel method from Shewchuk (2002), and applying it to multigrid methods.

2. Linear algebra analysis of the surface consistent equations.

3. Direct comparison of Jacobi, Gauss-Seidel, conjugate gradient and multigrid, and their ability to solve the surface consistent equations for deconvolution of field seismic data.

4. Amplitude spectrum error analysis of Gauss Seidel, conjugate gradient and multigrid surface consistent solutions.

5. Forward synthetic modeling of long wavelength surface consistent errors, and their effect on seismic sections, in statics, amplitudes and deconvolution.

Chapter 2

Iterative methods

2.1 Introduction

This chapter is a review of iterative methods, and their application to solving a system of linear equations. For more details about Jacobi, Gauss Seidel and multigrid methods see Press et al. (1992). For a detailed analysis of conjugate gradient methods, as well as details on how we predict the theoretical spectral performance, see Shewchuk (2002).

The following discussion describes some of the notation, and defines certain terms that will be used throughout the thesis. There is a derivation of the Jacobi method, both as an iterative scheme, and as a matrix method. By expressing it as a matrix operation, we can subject the method to analysis using linear algebra.

The analysis of the Jacobi method is then re-applied to the Gauss-Seidel method. Lastly, a brief description of the conjugate gradient method is given.

2.2 Definitions

Consider the system of equations,

$$\mathbf{A}\mathbf{x} = \mathbf{b}. \tag{2.1}$$

The matrix $\mathbf{A}$ and the *source term* $\mathbf{b}$ are both known. In general the matrix $\mathbf{A}$ may be rectangular, however for this discussion we will assume it to be square. The vector $\mathbf{x}$ is unknown, and we wish to solve for it.

Iterative methods are useful for solving systems of equations when a direct solution is not available. This may be due to restrictions on calculation time for very large systems, or the presence of one or more singularities in the matrix $\mathbf{A}$ (Press et al., 1992). An iterative method starts with some estimate of the solution, $\tilde{\mathbf{x}}$. The initial estimate is repeatedly refined, using

$$\tilde{\mathbf{x}}_{n+1} = f(\tilde{\mathbf{x}}_n, \mathbf{A}, \mathbf{b}), \tag{2.2}$$

where f is some iterative method, and the subscript n is the iteration number.

After a predetermined number of iterations, or once $\tilde{\mathbf{x}}$ fits within some specified error tolerance, the process is halted and a solution is returned. The method is said to have *converged*. Using the term convergence represents the way that the trial solution gradually improves itself with each iteration, converging on the solution.

To ensure convergence of an iterative method, there are requirements for the form of the matrix. Jacobi and Gauss-Seidel methods both require the matrix to be *diagonally dominant* (Noble and Daniel, 1988). Diagonal dominance implies that the sum of the absolute values of all of the off-diagonal coefficients in each row of the matrix be smaller than the diagonal coefficient.

Conjugate gradient methods require the matrix to be *positive definite*. This is a more restrictive requirement, the matrix must be non-singular, and its Hermitian (symmetric component of the matrix) can have only positive eigenvalues, see Riley et al. (2002) .

If these conditions are not met, then the solution will have errors, which may or may not render the solution useless. In this case, the solution is said not to converge.

The conditions for and rate of convergence of the above solution methods are explored in the following sections.

2.2.1 The residual

The true solution $\mathbf{x}$ can be expressed as our estimate $\tilde{\mathbf{x}}$ plus some (unknown) error, ϵ, or similarly,

$$\tilde{\mathbf{x}} = \mathbf{x} - \epsilon. \tag{2.3}$$

The *residual* δ is a vector the same size as $\mathbf{b}$, calculated by

$$\delta = \mathbf{A}\tilde{\mathbf{x}} - \mathbf{b}. \tag{2.4}$$

The residual is also called the *defect*. In some of the literature the defect is defined as the negative of the residual , (Press et al., 1992), however here we consider the two to be the same thing.

Substitute equation 2.3 into 2.4,

$$\delta = \mathbf{A}\mathbf{x} - \mathbf{A}\epsilon - \mathbf{b}, \tag{2.5}$$

and subtract equation 2.1 to arrive at

$$\mathbf{A}\epsilon = -\delta. \tag{2.6}$$

The residual is directly related to error through equation 2.6. As $\tilde{\mathbf{x}}$ approaches the true solution $\mathbf{x}$, the residual will shrink to zero, as will ϵ.

The sum of the square of the residual is used to quantify the error remaining in the solution,

$$\sum_k (\delta_k^2) = \delta^T \delta. \tag{2.7}$$

This quantity can be used to track the rate of convergence. The true solution is not needed to calculate the residual, we use equation 2.4. This value can be used to halt the calculation, once it falls below some predetermined threshold.

2.2.2 A first estimate of the solution

One way to get an estimate of the solution to a system of equations requires us to separate the matrix $\mathbf{A}$ into components that lie on the main diagonal $\mathbf{D}$ and those that do not, $\mathbf{C}$, such that

$$\mathbf{A} = \mathbf{D} + \mathbf{C}. \tag{2.8}$$

The solution of the system uses the approximation

$$\mathbf{A}^{-1} \approx \mathbf{D}^{-1}. \tag{2.9}$$

Using this approximation generates an estimate of the solution

$$\mathbf{x} \approx \mathbf{D}^{-1}\mathbf{b} \tag{2.10}$$

This estimate of the solution serves as an initial estimate for the other iterative methods used. It requires very little computational effort. The quality of the solution depends solely on the quality of the approximation in equation 2.9. If the matrix $\mathbf{A}$ is very nearly diagonal, the estimate will be very good. As $\mathbf{A}$ becomes less concentrated on the main diagonal the quality of the estimate it provides will decrease.

2.2.3 The Jacobi method

Consider the system of N equations with N unknowns, represented by equation 2.1. Isolating the i^{th} equation (row) and expanding out each term,

$$\mathbf{A}(i,1)\tilde{\mathbf{x}}(1) + \mathbf{A}(i,2)\tilde{\mathbf{x}}(2) + ... + \mathbf{A}(i,i)\tilde{\mathbf{x}}(i) + ...\mathbf{A}(i,N)\tilde{\mathbf{x}}(N) = \mathbf{b}(i). \tag{2.11}$$

We can rearrange equation 2.11, solving for the i^{th} unknown (Riley et al., 2002),

$$\tilde{\mathbf{x}}(i) = \frac{\mathbf{b}(i) - \mathbf{A}(i,1)\tilde{\mathbf{x}}(1) - \mathbf{A}(i,2)\tilde{\mathbf{x}}(2) - ... - \mathbf{A}(i,N)\tilde{\mathbf{x}}(N)}{\mathbf{A}(i,i)}. \tag{2.12}$$

The Jacobi method calculates a new estimate of the solution, $\mathbf{x}_{n+1}$, by applying equation 2.12 to the present estimate, $\mathbf{x}_n$. Adding appropriate subscripts to equation 2.12,

$$\tilde{\mathbf{x}}_{n+1}(i) = \frac{\mathbf{b}(i) - \mathbf{A}(i,1)\tilde{\mathbf{x}}_n(1) - \mathbf{A}(i,2)\tilde{\mathbf{x}}_n(2) - ... - \mathbf{A}(i,N)\tilde{\mathbf{x}}_n(N)}{\mathbf{A}(i,i)}. \tag{2.13}$$

The variable n is the iteration number. An complete iteration consists of calculating a new value for each unknown in the vector $\tilde{\mathbf{x}}$, repeating equation 2.13 using i from $1 \rightarrow N$. An accurate solution usually requires the same order of magnitude number of iterations as unknown values. We use the notation $\mathcal{O}(N)$ to show the number of iterations, that are typically necessary, although this depends largely on the matrix, and the desired accuracy of the solution.

2.2.4 Jacobi as a matrix method

The Jacobi method requires us to split $\mathbf{A}$ from equation 2.1 into two matrices with all of the diagonal coefficients in one matrix $\mathbf{D}$, and all of the off diagonal coefficients in another matrix $\mathbf{C}$, (exactly as was done in equation 2.8)

Substituting equation 2.8 into equation 2.1,

$$\mathbf{D}\mathbf{x} + \mathbf{C}\mathbf{x} = \mathbf{b}. \tag{2.14}$$

Equation 2.14 assumes that we have the exact answer. Instead, we want to use our approximate solution. By substituting 2.8 into equation 2.4,

$$\delta = \mathbf{D}\tilde{\mathbf{x}} + \mathbf{C}\tilde{\mathbf{x}} - \mathbf{b}. \tag{2.15}$$

We replace the δ term in equation 2.15 with $\mathbf{A}\epsilon$, from equation 2.6. Rearranging some terms, we arrive at

$$\mathbf{D}(\tilde{\mathbf{x}} + \epsilon) = \mathbf{b} - \mathbf{C}\tilde{\mathbf{x}} - \mathbf{C}\epsilon. \tag{2.16}$$

We do not know the error ϵ, so we remove the $\mathbf{C}\epsilon$ term on the right hand side. This turns the exact equality into an approximation. We will see later the result of removing this term.

$$(\tilde{\mathbf{x}} + \epsilon) \approx \mathbf{D}^{-1}(\mathbf{b} - \mathbf{C}\tilde{\mathbf{x}}). \tag{2.17}$$

Equation 2.3 tells us that the left hand side of 2.17 is the exact solution. The exact solution to the system of equations is *approximately* equal to the right hand side of equation 2.17.

Evaluating the right hand side of equation 2.17 using $\tilde{\mathbf{x}}$ provides a new estimate of the solution. The revised solution is not exact, it is only assumed to be better,

$$\mathbf{x}_{new} = \mathbf{D}^{-1}(\mathbf{b} - \mathbf{C}\mathbf{x}_{old}). \tag{2.18}$$

The assumption that we are improving the solution with each iteration is the same assertion as saying that a solution process converges. As to whether or not the revised solution is legitimately an improvement is determined by the properties of the matrix of coefficients $\mathbf{A}$.

The solution can be refined repeatedly using equation 2.18. With each iteration an increasingly accurate solution can be found. Reflecting that multiple corrections may be made to our solution, the Jacobi method can be expressed as a manipulation of equation

2.18,

$$\mathbf{x}_{n+1} = \mathbf{D}^{-1}(\mathbf{b} - \mathbf{C}\mathbf{x}_n). \tag{2.19}$$

Equation 2.19 is exactly equivalent to equation 2.13 for all values of i.

Applying a Jacobi operator to an all-zero initial estimate can be shown to be identical to the estimate found using equation 2.10. When the $\mathbf{Cx}$ term in equation 2.19 is set equal to zero, it reduces to equation 2.10.

2.2.5 Spectral performance

An important consideration in evaluating iterative methods is the rate of convergence. Each pass of an iterative method has a regular and predictable effect on the error of the estimate. As will be shown, iterative methods tend to have problems resolving some wavelengths in the solution.

To calculate the spectral performance of an iterative method, first express it as a matrix operation (Shewchuk, 2002). If instead of substituting equation 2.8 into equation 2.1, we instead substituted it into equation 2.6, the analogous result would be

$$\epsilon_{n+1} = \mathbf{D}^{-1}(\delta - \mathbf{C}\epsilon_n). \tag{2.20}$$

In the derivation of the Jacobi method we dropped a $\mathbf{D}^{-1}\mathbf{C}\epsilon$ term in equation 2.16. This term is equal to the term on the right hand side of 2.20. The approximation that we used to derive the Jacobi method reveals itself as the error leftover in the trial solution after a correction.

Each application of the Jacobi method to the solution $\tilde{\mathbf{x}}$ is equivalent to multiplying the error in the solution ϵ, by the matrix $\mathbf{D}^{-1}\mathbf{C}$.

From equation 2.20 the relationship between diagonal dominance and convergence is alluded to. Where a diagonal element in $\mathbf{D}$ to be smaller than the sum of the off diagonal elements in the corresponding row of $\mathbf{C}$, we would be multiplying the error ϵ by a number larger than one with each iteration. The error would grow with each iteration, and we would not get convergence. With a diagonally dominant matrix, $\mathbf{D}$ is defined as being larger than the sum of the corresponding row of $\mathbf{C}$. The net effect will be repeatedly multiplying the error by a number smaller than one, approaching zero as an asymptote, after a large number of iterations. The estimate *converges* to the true solution.

The effect of this reduction in the frequency domain is how we would define the *spectral performance*, ω. Shewchuk (2002) shows ω can be evaluated by finding the eigenvalues of the matrix $\mathbf{D}^{-1}\mathbf{C}$,

$$\omega_{JB} = \lambda, \qquad \lambda\mathbf{v} = \mathbf{D}^{-1}\mathbf{C}\mathbf{v}, \tag{2.21}$$

where $\mathbf{v}$ is an eigenvector of $\mathbf{D}^{-1}\mathbf{C}$.

The value of ω tells us how much each the error of each eigenvector is reduced with each iteration. if ω is 1 or close to 1, the error is not strongly attenuated and the solution will converge slowly at that wavelength. If the value is closer to 0, then strong attenuation of error means we will achieve a more accurate solution faster.

In the case where the matrix varies significantly with each row, the spectral performance can be found locally by examining the Fourier transform of each row of $\mathbf{D}^{-1}\mathbf{C}$.

2.2.6 Gauss-Seidel

The Gauss-Seidel method is similar to the Jacobi method, except it utilizes the updated values as they become available inside of each iteration (Riley et al., 2002). The unknowns already corrected in $\tilde{\mathbf{x}}_{n+1}$ are used, with $\tilde{\mathbf{x}}_n$ to calculate the new estimate. This may improve

the speed of convergence, but may also render the solution unstable.

To adapt equation 2.13 to the Gauss-Seidel method, the right hand side must reflect that the elements in $\mathbf{x}$ which have already been corrected are being used to correct the i^{th} element.

$$\tilde{\mathbf{x}}_{n+1}(i) = \frac{\mathbf{b} - \mathbf{A}(i,1)\tilde{\mathbf{x}}_{n+1}(1) - \mathbf{A}(i,2)\tilde{\mathbf{x}}_{n+1}(2) - ... - \mathbf{A}(i,N)\tilde{\mathbf{x}}_{n}(N)}{\mathbf{A}(i,i)}. \tag{2.22}$$

For the Gauss-Seidel method, split the coefficients of the matrix into a diagonal matrix $\mathbf{D}$, and lower and upper triangular matrices $\mathbf{L}$ and $\mathbf{U}$.

$$\mathbf{A} = \mathbf{L} + \mathbf{D} + \mathbf{U}. \tag{2.23}$$

An important note is that the order in which the Gauss-Seidel method is applied to the elements in the unknown vector matters (Trottenberg et al., 2001). Here we are using the simplest case where each element is corrected in the order they appear from 1 to N. Some different strategies exist to improve convergence by rearranging the order in which the unknowns are addressed. By correcting all of the even indexed elements before correcting all of the odd indexed elements, some improvement in convergence can be achieved with certain matrices. This is called using a *red black* order, using a checkerboard as an analogy. Other schemes rely on the geometry of a problem, correcting alternating lines in a 2-D domain, or radiating out from a specific point in the domain. These changes usually are made to reflect the physics of the problem, or address specific difficulties due to the matrix. In general, the matrix L can be thought of as having the coefficients corresponding to unknown elements already corrected, and U would contain all of the matrix coefficients corresponding to unknowns not yet addressed.

Substituting equation 2.23 into equation 2.1 and rearranging,

$$\mathbf{D}\mathbf{x} + \mathbf{L}\mathbf{x} = \mathbf{b} - \mathbf{U}\mathbf{x} \tag{2.24}$$

Following the same path as we did to derive equation 2.19, but splitting the matrix $\mathbf{A}$ according to equation 2.24, the final result is

$$\mathbf{x}_{n+1} = (\mathbf{D} + \mathbf{L})^{-1}(\mathbf{b} - \mathbf{U}\mathbf{x}_n). \tag{2.25}$$

Similarly, by combining equations 2.24 and 2.6, the effect on the error is given,

$$\epsilon_{n+1} = (\mathbf{D} + \mathbf{L})^{-1}(\delta - \mathbf{U}\epsilon_n). \tag{2.26}$$

To examine the spectral performance of a Gauss-Seidel method, the eigenvalues of $(\mathbf{D} + \mathbf{L})^{-1}\mathbf{U}$ are evaluated,

$$\omega_{GS} = \lambda, \qquad \lambda\mathbf{v} = (\mathbf{D} + \mathbf{L})^{-\mathbf{1}}\mathbf{C}\mathbf{v}. \tag{2.27}$$

2.2.7 Conjugate gradient

Conjugate gradient solvers belong to a class of iterative methods called *quadratic form* methods. The quadratic form of equation 2.1 is given by

$$q(\tilde{\mathbf{x}}) = \frac{1}{2}\tilde{\mathbf{x}}^T\mathbf{A}\tilde{\mathbf{x}} - \tilde{\mathbf{x}}^T\mathbf{b} \tag{2.28}$$

The value of the quadratic form q reaches a minimum at the solution $\mathbf{x} = \tilde{\mathbf{x}}$. This class of iterative methods calculates a correction to $\tilde{\mathbf{x}}$ based on the slope of the quadratic form. The *steepest descent* method for instance, calculates the gradient of the quadratic form around $\tilde{\mathbf{x}}$. The solution is corrected by adding a vector that points in the direction of the steepest decline in q, and leads to a local minimum. The problem with steepest descent methods is

that the direction of steepest decline may not point directly towards the solution (Shewchuk, 2002). This arises when the quadratic form q is more strongly influenced in one direction than another. This makes the shape of the function like a long narrow valley. The method may still converge, but can take a wandering inefficient path to the solution.

The conjugate gradient method ensures that every correction is perpendicular to all previous corrections in N space. By restricting the search for local minimums to mutually orthogonal directions, there is no chance that the solution will be spend time backtracking, and always proceeds towards the solution.

The stability requirements for conjugate gradient methods are related to the shape of its quadratic form. The quadratic form of a positive definite matrix has an absolute minimum at the solution. Indefinite matrices have a saddle point at the solution, where the critical point may be a local maximum in one direction and a minimum in another. The conjugate gradient method cannot detect the local maxima, and proceeds downslope in that direction away from the solution. Conjugate gradient methods will not converge for indefinite matrices.

There is no available method to theoretically evaluate the spectral performance of the conjugate gradient method, as it does not behave in a regular and predictable way in the frequency domain (Shewchuk (2002), Press et al. (1992)).

2.3 The Laplace's equation example

In this section, we solve an example set of equations, using a couple of the common iterative methods available. Some of the convergence properties of the iterative methods are calculated and compared.

We first introduce an example system of equations, in order to demonstrate the described solution methods. The finite difference approximation to the 2-Dimensional Laplace's equation was chosen.

The Laplace's equation is solved frequently in geophysics. Gravity and magnetic methods of exploration both measure potential fields, which are governed by Laplace's equation. Darcy's law fluid flow models, such as the ones used for modelling of oil in a reservoir, are also governed by variations of the Laplace's equation.

The Laplace's equation was chosen as an example for two reasons. First, the solutions are relatively easy to visualize. The shape of the solutions as they develop in an iterative scheme provides useful demonstrations of how the methods work, and their drawbacks.

In addition the resulting matrix problem we need to solve is not singular. It adheres to the requirements of the iterative methods for convergence. The equations are both diagonally dominant and positive definite. Because it is a non singular system, an exact solution is available using a direct method, such as Gaussian elimination. Knowing the solution, and therefore the error, precisely aids in our analysis.

The solution to equation Laplaces equation is zero everywhere, as depicted in Figure 2.1(a). Because our solution is zero everywhere, the error is equal to the solution,

$$\tilde{\mathbf{x}} = \epsilon. \tag{2.29}$$

In order to test our algorithms, we use a very poor initial estimate, and watch the way

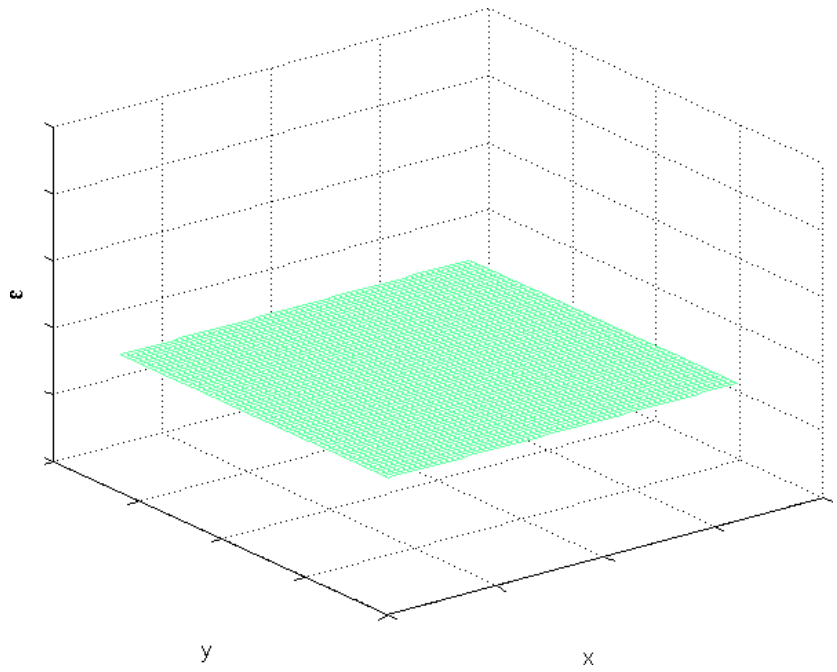

(a) The solution to the Laplace's equation. When the source term **b** is zero, the solution is also zero across the domain

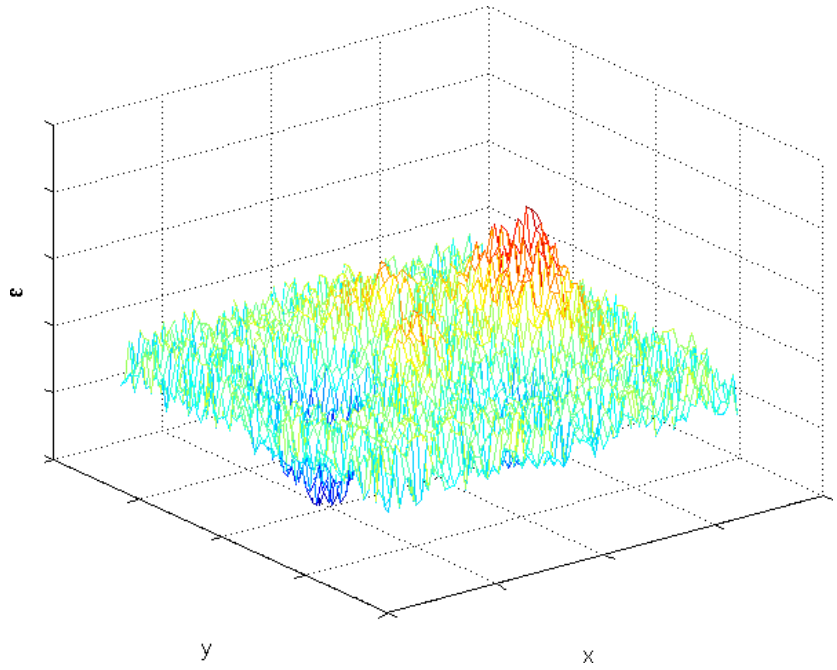

(b) The initial estimate we use in the Laplace's equation example.

Figure 2.1: For the Laplace's equation example, we use a poor initial estimate, and observe how the different iterative methods converge towards the solution.

the solution evolves. The measure of how effective an iterative method is for this problem will be how quickly the solution (and error) is reduced to all zeros.

The initial estimate we use is shown in Figure 2.1(b). The z axis points upwards, and is the error, ϵ. The vertical scale and colour scales are identical for all of the mesh plots in this section. This initial estimate is generated using the Matlab function PEAKS.M, and adding random white noise on top of it. The purpose of this is to provide an error with a fairly white Fourier spectrum, but to assure that there is some long wavelength variation using the PEAKS.M function, as that is a key component in our test.

The faster that the iterative method reduces the error ϵ to the all zeros solution, the better convergence properties of the method.

2.3.1 Partial differential equations as matrix operators

The Laplace's equation in 2 dimensions is

$$\nabla^2 p = 0, \tag{2.30}$$

on the domain $p(x, y) \in (0 < x < 1), (0 < y < 1)$.

Neumann boundary conditions are applied, requiring that the derivative of the solution be zero near the boundaries,

$$\begin{aligned} x = 0, 1 \qquad & \frac{\partial p}{\partial x} = 0, \\ y = 0, 1 \qquad & \frac{\partial p}{\partial y} = 0. \end{aligned} \tag{2.31}$$

The domain is sampled on a square mesh, with equal sampling in the x and y directions, ie. $\Delta x = \Delta y$. The unknowns on the grid are sorted into a vector, starting at $(x = 0, y = 0)$. Each unknown is followed in the vector $\mathbf{p}$ by its neighboring point in the Δx direction. The

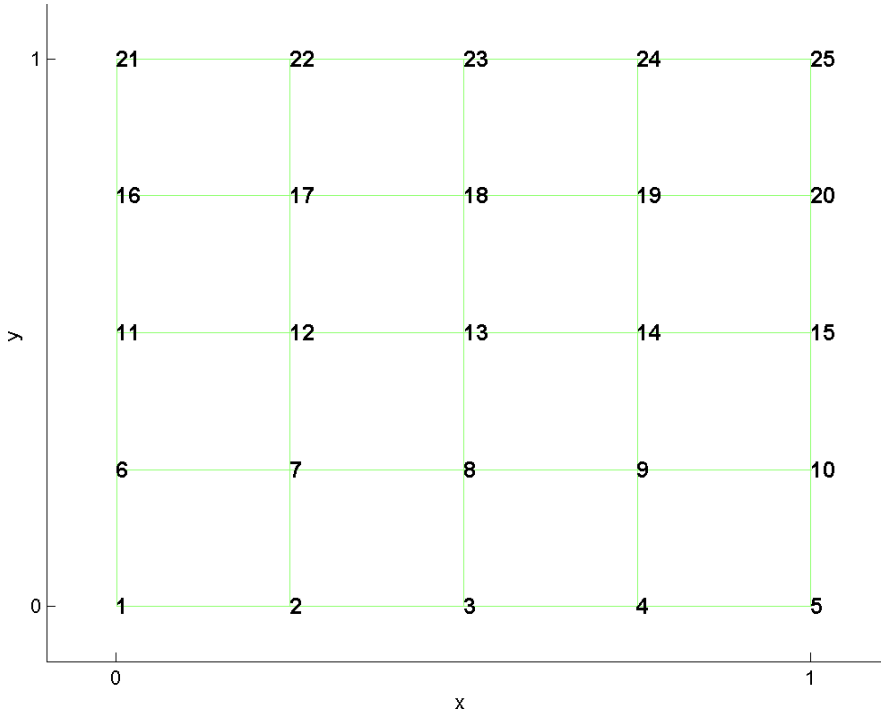

Figure 2.2: The 2-D domain is sampled onto a 5x5 grid. Expressing the variables in a 2-D domain as a single vector requires us to sort the points.

point at the end of the domain, $(x = 1, y = y)$, is followed by the point $(x = 0, y = y + \Delta y)$, the first point on the next line.

The process is shown on a 5x5 grid in Figure 2.2. The numbers represent the index that each unknown will have in the vector. For example, in Figure 2.2 point 18 is the neighbor in the positive y direction from point 13. indexes for adjacent points in the y direction are different by the number of samples in the x direction, N_x.

The reason we resort the 2-D grid into a vector is to express the 2-D finite difference approximation as a matrix operation. The value of the solution $\mathbf{p}$ at each point is an unknown. For each unknown we write an equation. Instead of solving equation 2.30, we solve the discrete system of equations

$$\mathcal{L}\mathbf{p} = 0. \tag{2.32}$$

The vector $\mathbf{p}$ is a vector of all of the unknown points, and $\mathcal{L}$ is a matrix representation of the 2-D Laplacian operator.

The coefficients of the matrix $\mathcal{L}$ are determined using a finite difference approximation. A finite difference approximation to the 2-D Laplacian operator is

$$\begin{aligned} {}^2p \approx \quad & \frac{p(x - \Delta x, y) + p(x + \Delta x, y) - 2p(x, y)}{\Delta x^2} + \\ & \frac{p(x, y - \Delta y) + p(x, y + \Delta y) - 2p(x, y)}{\Delta y^2}. \end{aligned} \tag{2.33}$$

Using $(\Delta x = \Delta y)$ to reflect our square grid, equation 2.33 can be simplified,

$$\frac{p(x - \Delta x, y) + p(x + \Delta x, y) + p(x, y - \Delta y) + p(x, y + \Delta y) - 4p(x, y)}{\Delta x^2} = 0. \tag{2.34}$$

This is the equation for the operator in the middle of the domain.

To access the i^{th} unknown in $\mathbf{p}$, multiply the column vector $\mathbf{p}$ by a row vector, with all zeros, except for a 1 in the i^{th} column,

$$(0 \cdots 0 \quad 1 \quad 0 \cdots 0) \bullet \begin{pmatrix} \mathbf{p}(1) \\ \vdots \\ \mathbf{p}(i-1) \\ \mathbf{p}(i) \\ \mathbf{p}(i+1) \\ \vdots \\ \mathbf{p}(N) \end{pmatrix} = \mathbf{p}(i). \tag{2.35}$$

The i^{th} column of the matrix corresponds to the coefficients of the i^{th} unknown. The indexes of the immediate neighbors of the i^{th} unknown in the positive and negative x directions are $i+1$ and $i-1$ respectively. The indexes of the immediate neighbors of the i^{th} unknown in the positive and negative y directions are $i+N_x$ and $i-N_x$ respectively. The subscript N_x refers to the number of samples in the x direction.

Instead of just selecting the i^{th} unknown, we want a row vector that applies the coefficients of equation 2.34 to the vector $\mathbf{p}$, giving us an expression for $\mathbf{p}(i)$,

$$\frac{1}{\Delta x^2}\,(0\cdots1\cdots1\quad -4\quad 1\cdots1\cdots0)\bullet\begin{pmatrix}\mathbf{p}(1)\\ \vdots\\ \mathbf{p}(i-N_x)\\ \vdots\\ \mathbf{p}(i-1)\\ \mathbf{p}(i)\\ \mathbf{p}(i+1)\\ \vdots\\ \mathbf{p}(i+N_x)\\ \vdots\\ \mathbf{p}(N)\end{pmatrix}\approx\quad {}^2p(x,y)=0. \tag{2.36}$$

Performing the row multiplication, the equation for $\mathbf{p}(i)$ is

$$\frac{\mathbf{p}(i-N_x)+\mathbf{p}(i-1)-4\mathbf{p}(i)+\mathbf{p}(i+1)+\mathbf{p}(i+N_x)}{\Delta x^2}=0. \tag{2.37}$$

The indexes are a result of the way that the 2-D grid was arranged into a vector, and can be seen by looking at the index numbers in Figure 2.2, and comparing it to the kernel.

The *kernel* is a way to visually represent the operators that we will be using on our grids. The kernel for the Laplace's equation is in Figure 2.3.

In Figure 2.3(a) the kernel shown corresponds to the center of the 5x5 domain. This kernel shows the coefficients for the 13^{th} equation in our system.

Each equation for a point that is adjacent to a boundary must be altered to incorporate the boundary conditions set out in equation 2.31. For Neumann boundary conditions, we

require that the derivative of our solution at the boundary (and normal to the boundary) be zero.

On the $x = 0$ boundary, use the backward finite-difference approximation to the derivative,

$$\frac{\partial p}{\partial x} \approx \frac{p(x,y) - p(x - \Delta x, y)}{\Delta x}. \tag{2.38}$$

The right hand side of approximation 2.38 is set equal to zero, according to equation 2.31,

$$\frac{p(x,y) - p(x - \Delta x, y)}{\Delta x} = 0. \tag{2.39}$$

With the right had side equal to zero, we multiply equation 2.39 by $\frac{1}{\Delta x}$.

$$\frac{p(x,y) - p(x - \Delta x, y)}{\Delta x^2} = 0. \tag{2.40}$$

The denominators are the same, so that we may add equations 2.40 and 2.34 to enforce the boundary condition.

$$\frac{p(x + \Delta x, y) + p(x, y - \Delta y) + p(x, y + \Delta y) - 3p(x,y)}{\Delta x^2} = 0. \tag{2.41}$$

The $p(x,y)$ terms coefficient is changed from -4 to -3, and the $p(x - \Delta x, y)$ is cancelled. This makes sense, as the $p(x - \Delta x, y)$ term at $x = 0$ is $p(-\Delta x, y)$, which is outside the domain.

A forward finite-difference is used for the $x = 1$ boundary. At $x = 1$ the $p(x,y)$ term again changes from -4 to -3, and the term outside the boundary, $p(1 + \Delta x, y)$, is cancelled.

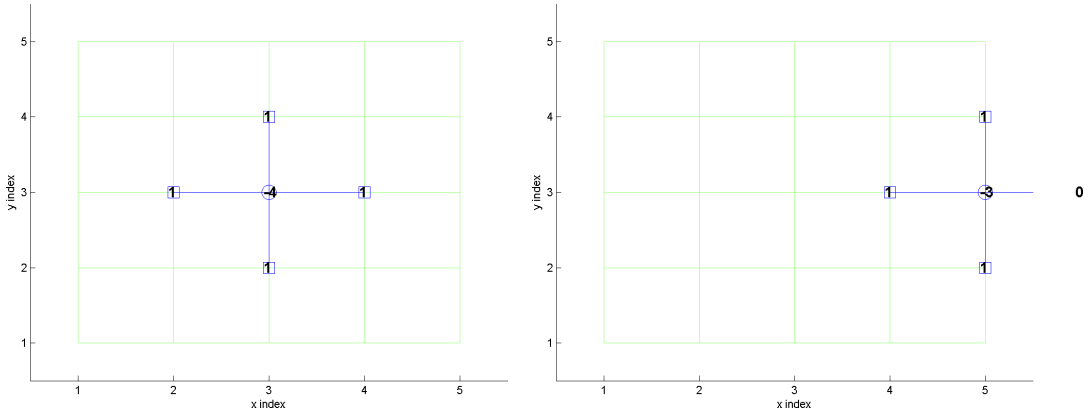

(a) The kernel for the Laplacian operator in the center of the domain. This kernel describes the coefficients for the 13th equation.

(b) The kernel on the $x = 1$ boundary. The coefficients must change when the kernel encounters a boundary to reflect the local boundary conditions.

Figure 2.3: The kernel representation of the 2-D Laplacian operator over top of a 5x5 grid.

To reflect this in our kernel, the outlying (non-existent) point in the kernel is added to the center point of the kernel, yielding the kernel in Figure 2.3(b).

2.3.2 Solutions

In order to get a solution, write an equation for each unknown point in the domain, and assemble all of the resulting equations into a linear system, and express the coefficients in the system as a matrix $\mathcal{L}$. We wish to solve for the unknown vector $\mathbf{p}$ in equation 2.32.

The matrix $\mathcal{L}$ for a 65x65 2-D grid is depicted in Figure 2.4. The blue dots are the non-zero entries. The non-zero coefficients are concentrated in a band 3 elements wide on the main diagonal, with another pair of bands N_x points above and below the main diagonal. The 3 elements in the center are close enough that they appear as a thicker line along the main diagonal. The main diagonal consists of the entries relating to the center of the kernel, and has a value of -4 (ignoring the $\frac{1}{\Delta x^2}$) for points inside the domain, -3 for the points corresponding to the edges, and -2 for the corners. The entries directly to the left and

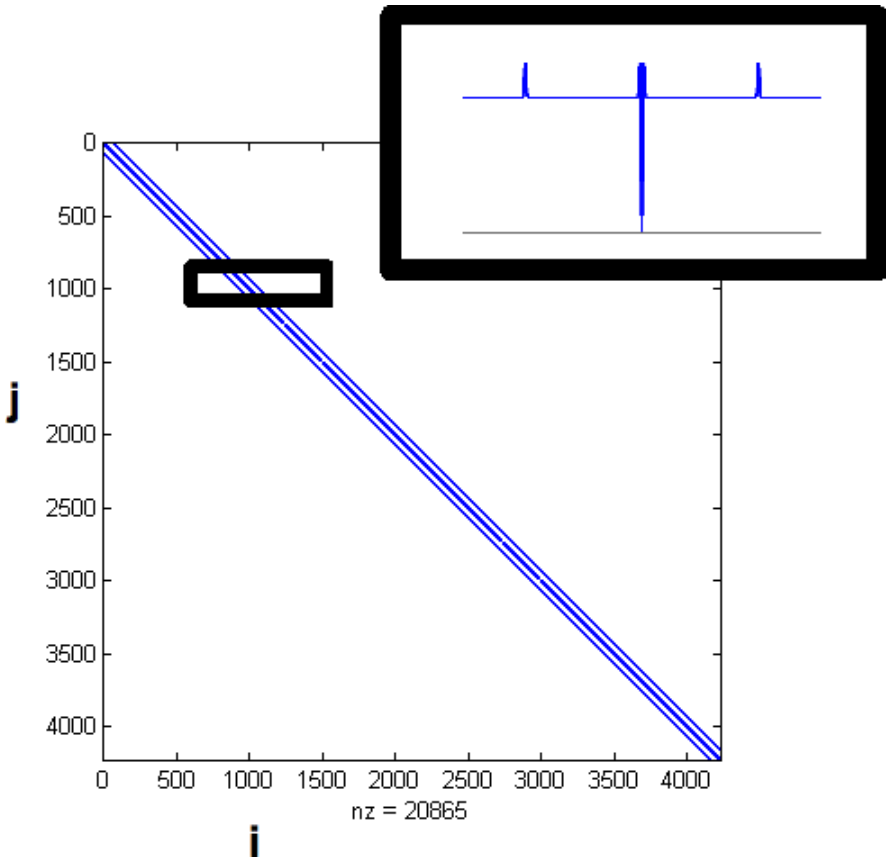

Figure 2.4: The matrix representation of the 2-D Laplacian operator. The non-zero coefficients are concentrated in bands around the main diagonal.

right of the main diagonal are the points in the positive and negative Δx directions, and the outside bands correspond to the neighboring points in the Δy direction. The boundaries are accounted for, points outside the boundary are omitted, and this effect can be seen as notches in the central band of the matrix.

Jacobi

The solution as it evolves using the Jacobi method is depicted in Figure 2.5. The very high and low frequencies are not well handled by the Jacobi method. There is a general smoothing of the error with each iteration.

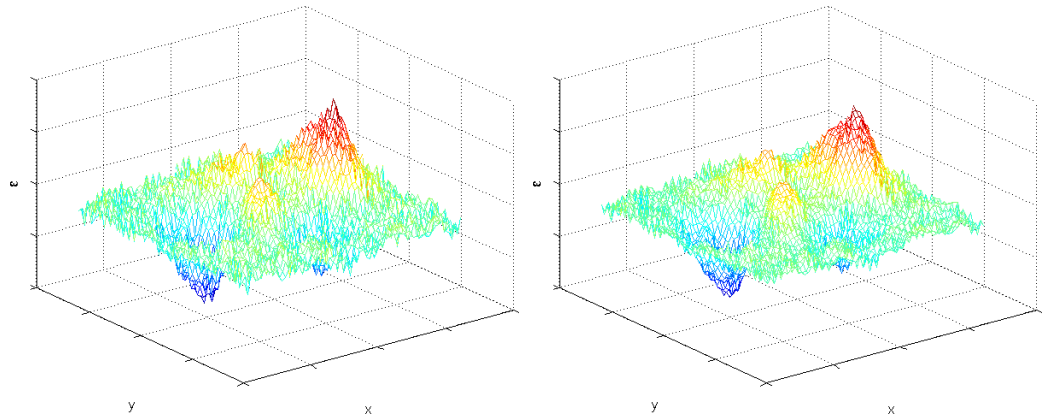

(a) The Jacobi estimate after 1 iteration

(b) After 2 iterations

(c) 5 iterations

(d) 10 iterations

Figure 2.5: The Jacobi solution as it evolves to the Laplace's equation example

The reason for the high frequency error is as follows. The solution for all of the odd indexed unknowns depends only on the values of the unknowns with an even index in the vector, and vice versa. What we get is effectively 2 separate solutions intermingled together, and converging at different rates. This problem is specific to solutions of equations with very compact kernels, and the phenomena is called *checker-boarding*. .

Gauss-Seidel

The Gauss-Seidel method brings some improvement to the solution over the Jacobi method. The results after a number of iterations are provided in Figure 2.6. Because each unknown is dependant on more of the surrounding values, the checker-boarding effect visible in the Jacobi method is not a problem (although can be a problem for other matrices). High frequency errors are attenuated very quickly, however a smooth long wavelength error remains after many iterations.

After 50 iterations, the error is very smooth (Figure 2.7), only errors with wavelengths similar to the size of the entire domain remain.

Conjugate gradient

The conjugate gradient solution is in Figure 2.8. The specific method used for this example is the Bi-conjugate gradient routine packaged with Matlab, BICG.M.

The Gauss Seidel method converges slightly faster than the conjugate gradient method for the first ten iterations. Figure 2.8 appears to have more error than Figure 2.6.

The general shape of the remaining long wavelength error is similar, and the magnitude of the overall error is comparable. The surface of the conjugate gradient solution seems rougher, indicating there is still some error in the high frequencies.

After 50 iterations, the error in the conjugate gradient method is far lower (Figure 2.9)

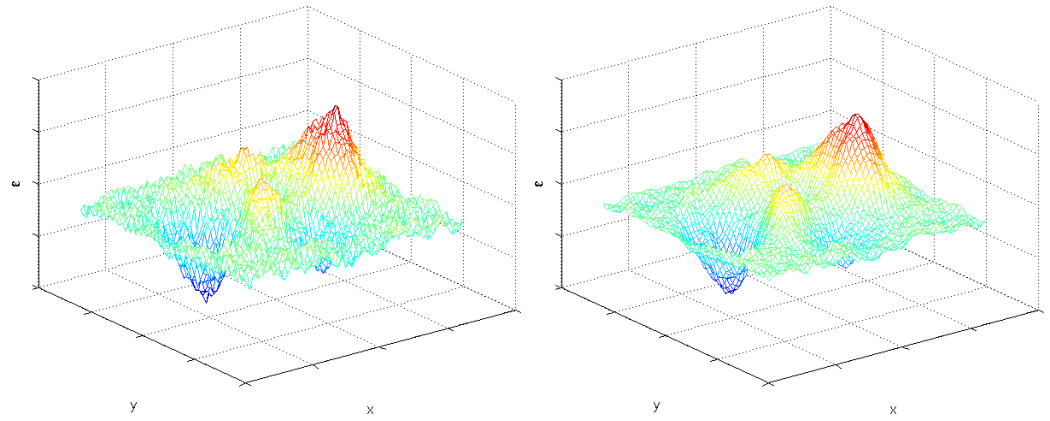

(a) After 1 iteration

(b) After 2 iterations

(c) 5 iterations

(d) 10 iterations

Figure 2.6: The Gauss-Seidel solution as it evolves to the Laplace's equation example

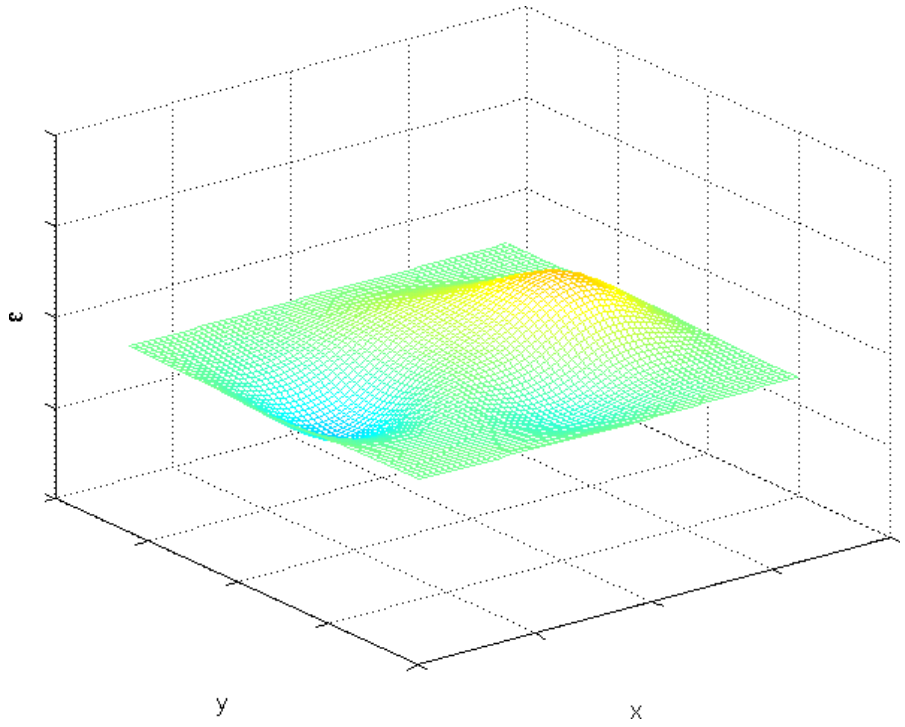

Figure 2.7: The error after 50 iterations of the Gauss-Seidel operator. There is still some long wavelength error in the solution

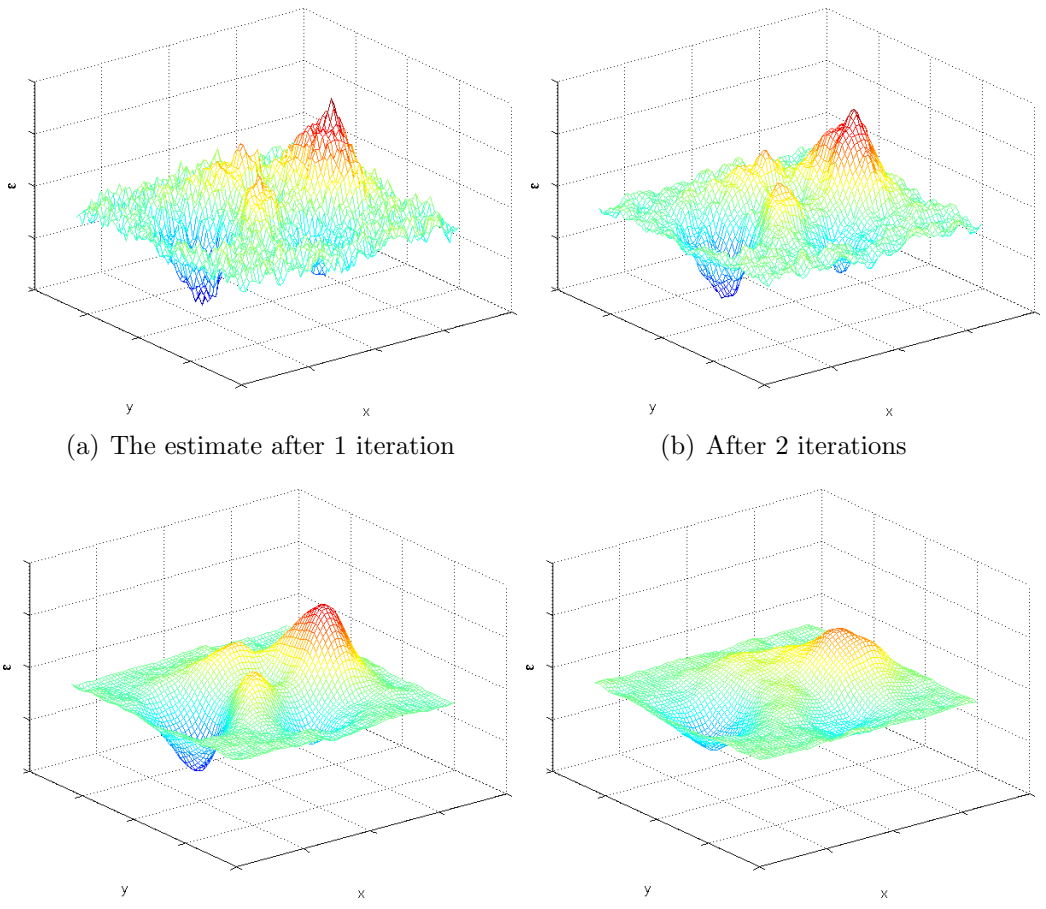

(a) The estimate after 1 iteration

(b) After 2 iterations

(c) 5 iterations

(d) 10 iterations

Figure 2.8: The Conjugate Gradient solution as it evolves to the Laplace's equation example

than the Gauss-Seidel method (Figure 2.7). This result will be discussed later.

For a linear well determined system, the conjugate gradient method will evaluate to the exact solution in as many iterations as there are unknowns (Shewchuk, 2002).

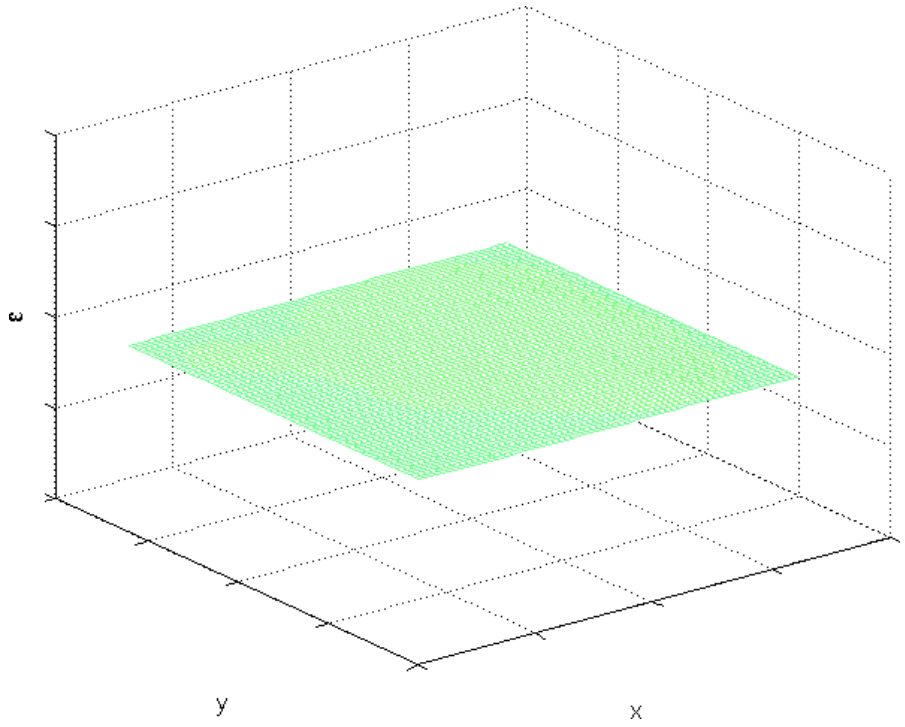

Figure 2.9: The error after 50 iterations of the Conjugate Gradient operator. There is very little long wavelength error in the solution.

2.3.3 Spectral performance

By comparing the Fourier transform of the error after each iteration, we can measure the effect of an iterative method. This gives us a quantifiable means to compare the algorithms. This also allows us to compare their actual convergence properties to the theoretical spectral performance.

In Figure 2.10, the Fourier transform of the error is displayed, initially, and after successive passes of each of the discussed iterative methods. The 2-D Fourier transform is applied to the data, such that

$$\mathcal{F}\left(\mathbf{p}(x,y)\right) = P(k_x, k_y). \tag{2.42}$$

To simplify the display of the 2-D Fourier transform we transform it into radial coordinates. The radially averaged spectrum takes the 2-D transform P, and averages it along the radius, k_r^2, such that

$$P(k_r^2) = P(k_x^2 + k_y^2). \tag{2.43}$$

This turns the 2-D surface into a line, combining the frequency data in the x and y directions. On a discreetly sampled mesh, this is only an approximation, as some form of binning must be done.

The number beside each line in Figure 2.10 (and subsequent figures) corresponds to the iteration number. The plot shows the cumulative effect of the correction on the Fourier spectrum of the error. The error in the first iteration is always the highest, and is subsequently reduced with each correction. This is one of the consequences of a convergent process, the error is always reduced with each iteration.

You can begin to see in Figure 2.10 some of the effects noted when looking at the error

plots in Figures 2.5, 2.6 and 2.8. With the Jacobi method, even after a few iterations, the high frequencies (on the right hand side) are not significantly reduced from iteration to iteration. That corresponds directly to the jitter across the solution seen in Figure 2.5. The Gauss-Seidel method is again seen to be outperforming the conjugate gradient method in the early iterations.

None of the methods have any significant effect on the longest wavelengths, on the left side of Figure 2.10.

The effect of each iteration is calculated by

$$\omega_n = \left| \frac{\mathcal{F}(\epsilon_{n+1})}{\mathcal{F}(\epsilon_n)} \right|. \tag{2.44}$$

The operator $\mathcal{F}$ is the Fourier transform. We are dividing the amplitude spectrum of the error after the correction, by the amplitude before the correction.

A graph of ω_n for each of the discussed iterative methods is provided in Figure 2.11. The horizontal axis is the wavenumber, the vertical axis is the attenuation factor, ω. A value of ω close to 0 shows strong attenuation, while a value close to 1 means that the corresponding wavelength will not be handled well by the iterative method. A value greater than 1 implies the error is growing. Strong attenuation of the error (low ω) leads to faster convergence.

The result is that the Gauss-Seidel method consistently reduces all of the wavelengths of error more than either the Jacobi method or the bi-conjugate gradient method. Importantly, none of the methods have a significant effect on the longer wavelengths. Also, the regular and predictable behavior of the Gauss-Seidel method on the high frequencies is important when discussing multigrid methods later in the thesis.

The theoretical values of ω are calculated for the Jacobi and Gauss-Seidel methods. These calculations are described by equations 2.21 and 2.27. These values are compared to

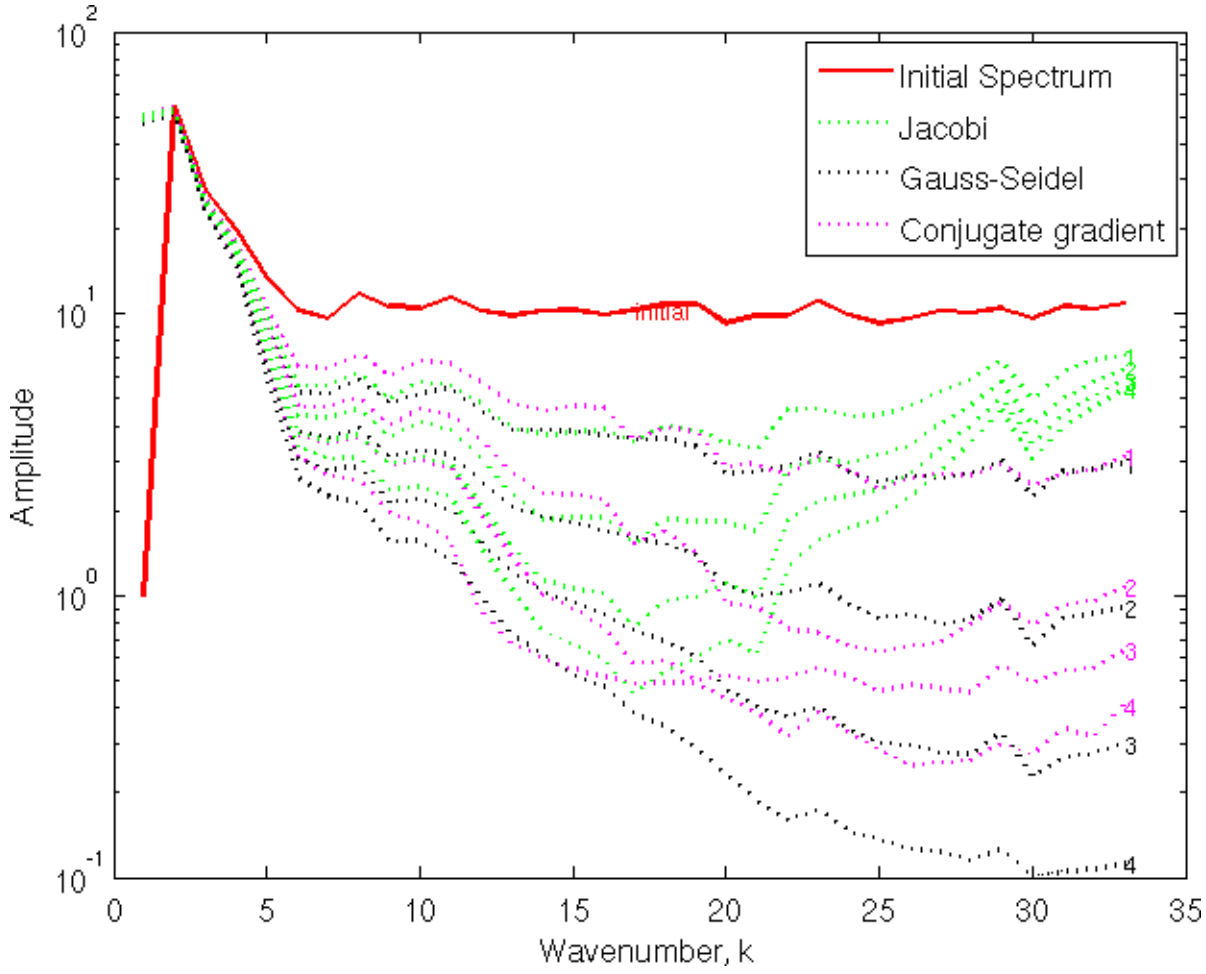

Figure 2.10: The Fourier transform of the error, initially then after successive passes of the respective operator. The number on the right end of each line is the iteration number.

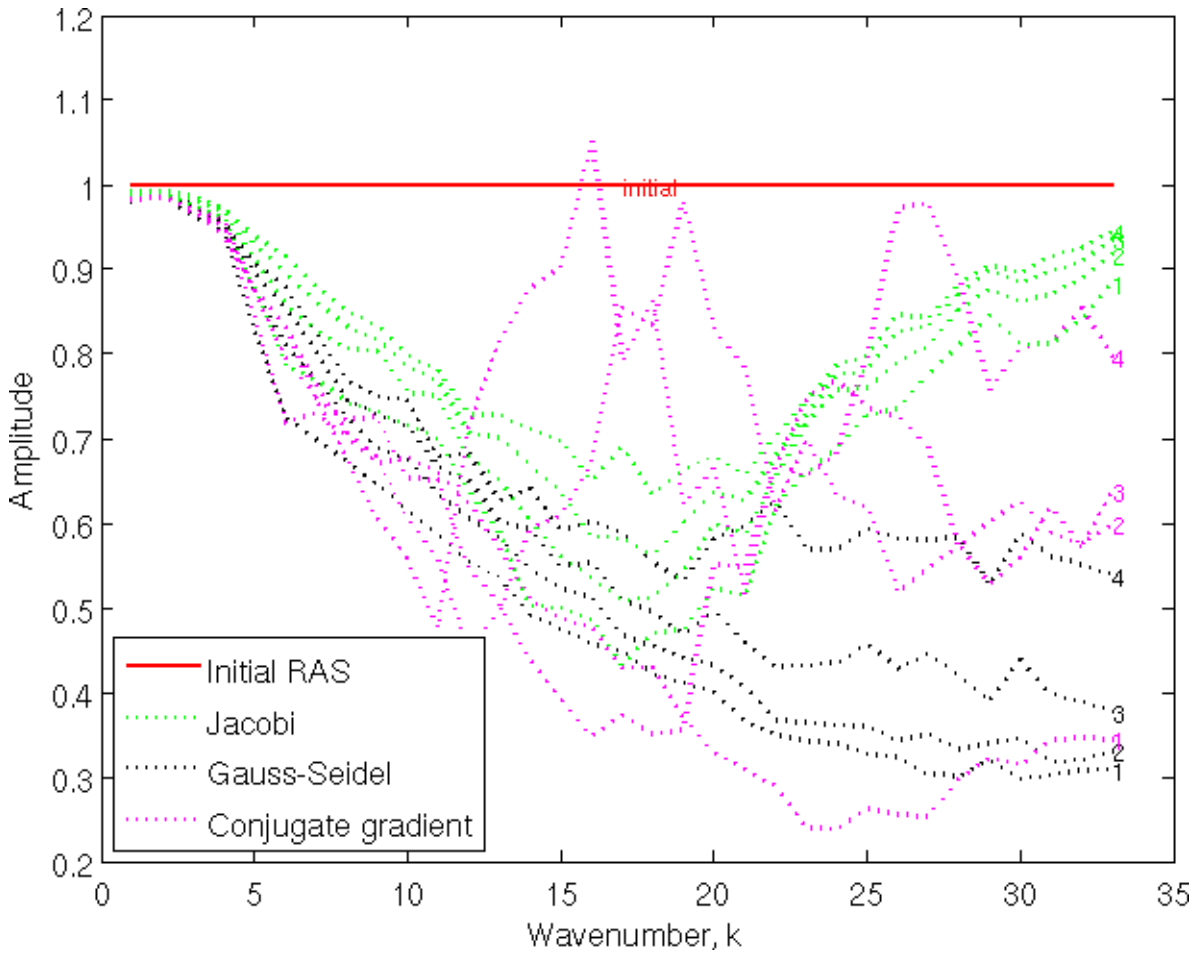

Figure 2.11: The spectral performance of each of the discussed iterative methods. A value close to 0 means that wavenumber of the error is strongly attenuated, and implies faster convergence.

the values calculated and shown in Figures 2.12 and 2.13 and 2.14.

The *Eigenvalue* theoretical value calculates the λ in equations 2.21 and 2.27 by using the single value decomposition.

The *Fourier* theoretical value was obtained by taking the Fourier transform of the matrix $\mathbf{D^{-1}C}$ for the Jacobi, or the matrix $(\mathbf{D}+\mathbf{L})^{-\mathbf{1}}\mathbf{C}$ for the Gauss-Seidel method. This method is in principal like considering the multiplication of the error by the above matrices to be equivalent to applying the above matrices as a filter on the error.

The theoretical calculations relating to the Jacobi method are shown in Figure 2.12. The general shape of the prediction is similar, but the theoretical prediction shows that the middle wavelengths would be attenuated very strongly. In practice, the method only attenuates the middle wavelengths by a factor of 0.5 at first. With each iteration, the effectiveness is reduced.

The conjugate gradient method is shown compared to the Gauss-Seidel method in Figure 2.13. There is no method available to theoretically evaluate the conjugate gradient method. Its first iteration attenuates the middle and high frequencies at a factor about 0.4. After subsequent iterations the effectiveness is lost on the high frequencies, and is reduced on the middle frequencies. Its spectral efficiency is erratic, and at times has an ω greater than 1. Some iterations actually amplify the error at some wavelengths. This is consistent with the literature, eg. Press et al. (1992).

The Gauss-Seidel method outperforms both the Jacobi and conjugate gradient method. It attenuates high frequencies more strongly than either of the other methods. The high frequencies are attenuated by a factor of 0.3 for the first iteration. Its behavior on the middle frequencies are comparable to both the other methods, but seems to suffer less from the reduced efficiency of each iteration.

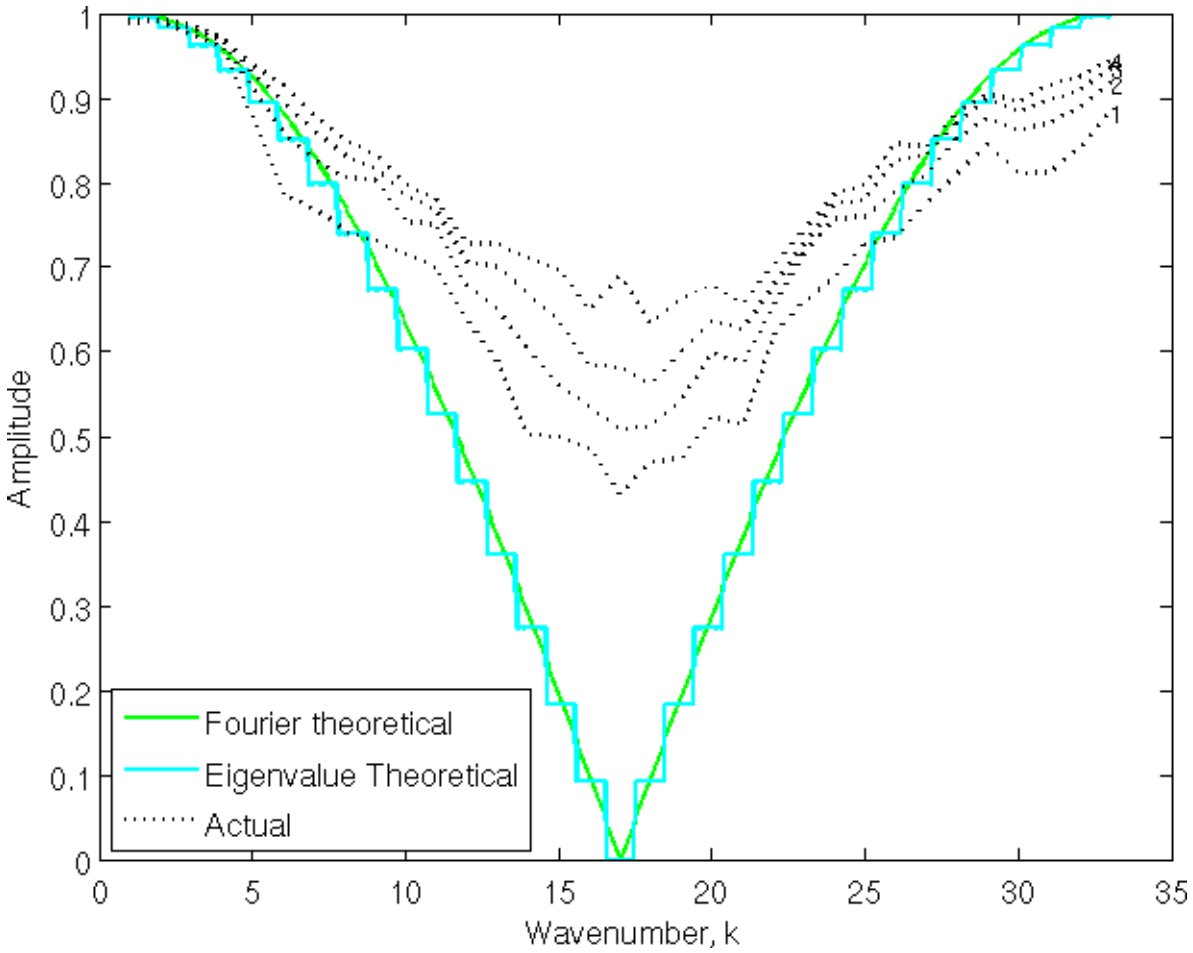

Figure 2.12: The spectral performance of the Jacobi operator on the sample problem

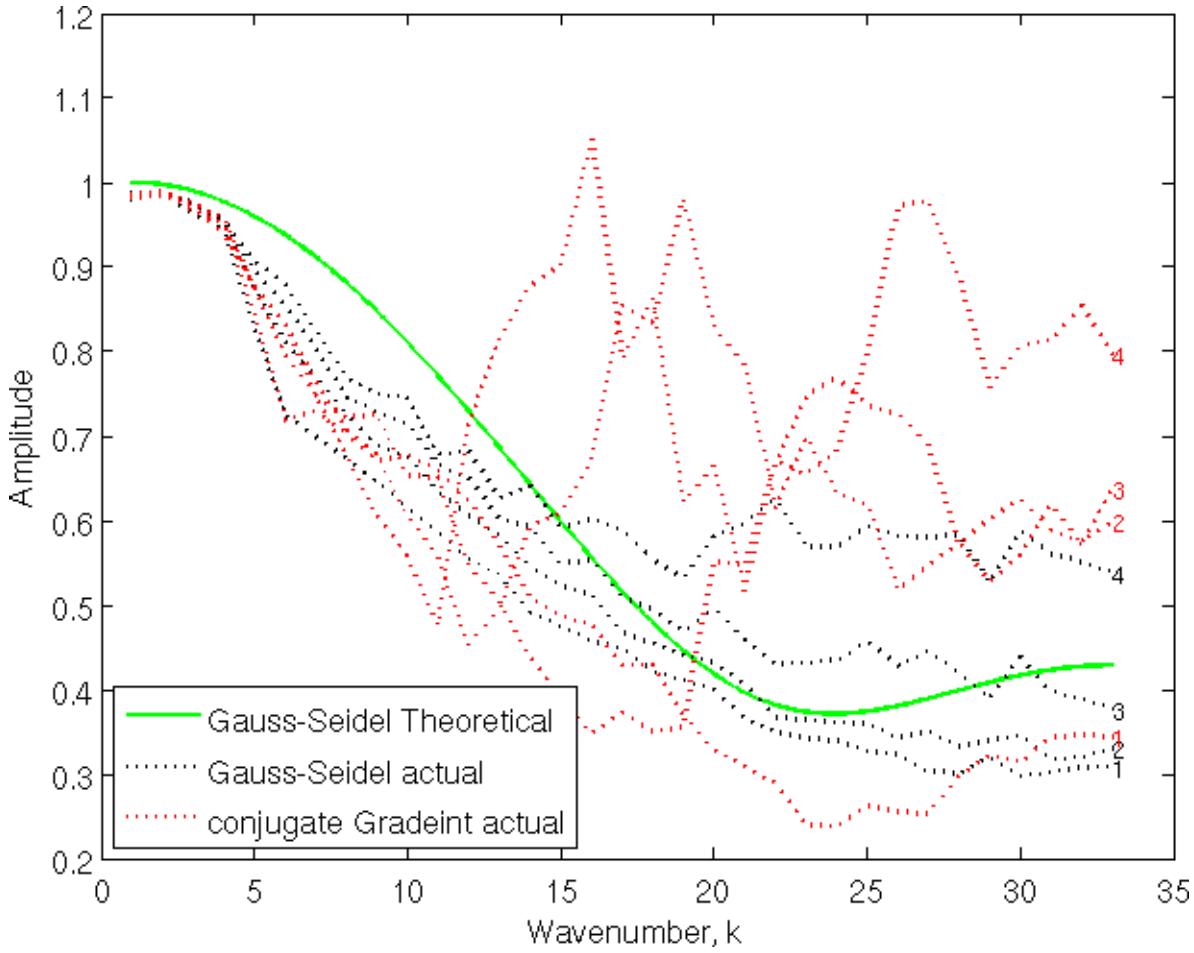

Figure 2.13: The spectral performance of the conjugate gradient operator on the sample problem. It is compared to the Gauss-Seidel method.

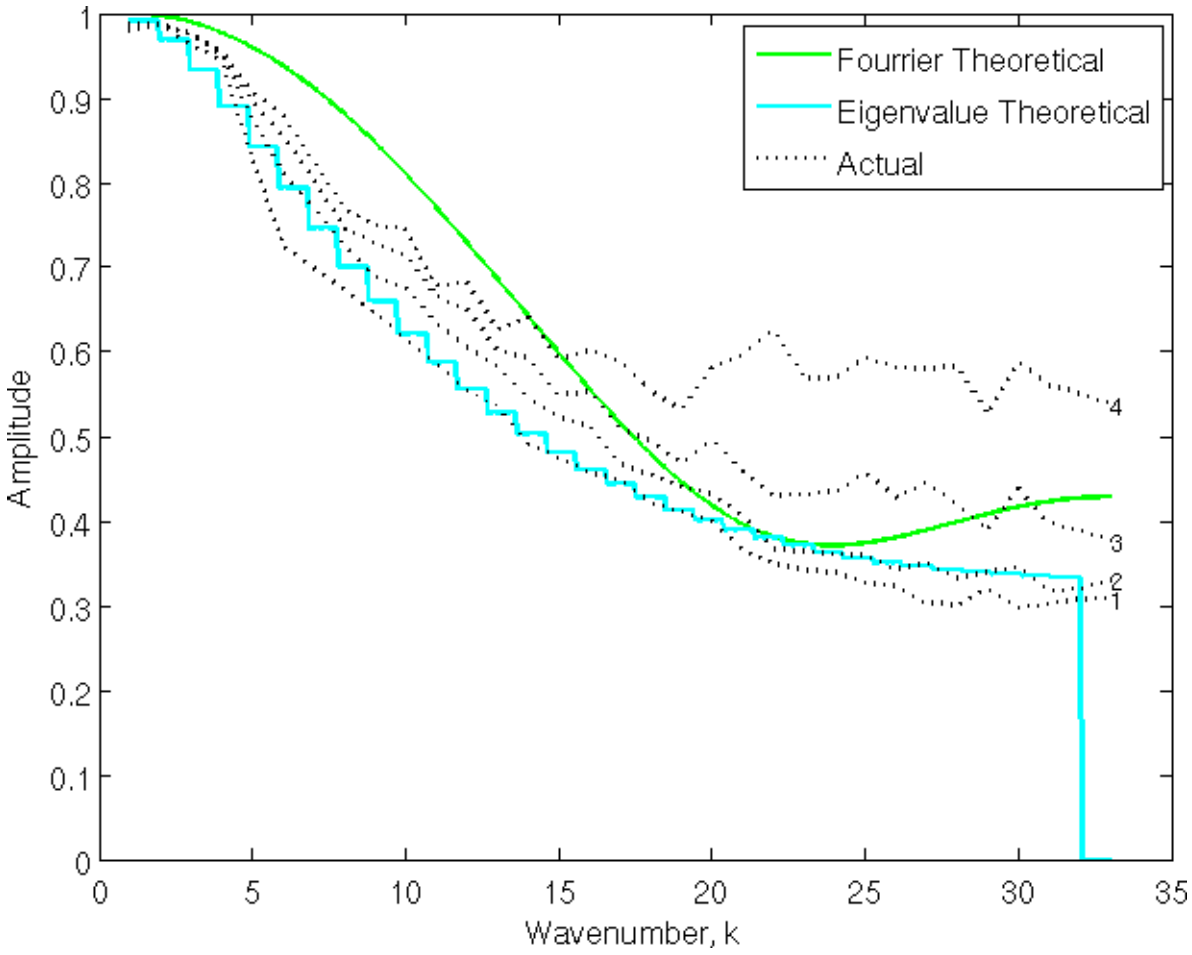

Figure 2.14: The spectral performance of the Gauss-Seidel operator on the sample problem

None of the mentioned methods had a significant effect on the long wavelength errors in the solution. Gauss-Seidel performed the best, attenuating the middle and high frequencies more consistently than the conjugate gradient method. All of the methods suffered from a decreasing effect across all of the wavelengths with each iteration.

Chapter 3

Multigrid Methods

In the previous chapter a variety of iterative methods was introduced. In the example problem, the Gauss-Seidel method performed the best on the medium and short wavelengths, but none of the iterative methods were able to reduce the long wavelength errors.

A multigrid method is one option to overcome these limitations. By a combination of filtering and down-sampling, the system of equations are expressed on a more coarse grid. As will be shown, by re-sampling the problem on a more coarse grid, the long wavelengths in the solution can be more effectively resolved by an iterative method.

After a long wavelength approximation is found on the coarse grid, it can then be interpolated to the original mesh. The iterative method uses this interpolated solution as its initial estimate. While there are some errors associated with interpolation, they are short wavelength errors and can be corrected using the same iterative method.

By focusing some of our calculation effort on a more coarse grid, we both increase the effectiveness of the iterative operator on the long wavelengths, and reduce the number of unknowns that we need to address with each iteration. This provides a way to resolve long wavelengths in the solution with a process far more efficient than relying on iterative methods alone.

There are many books on multigrid available that provide far more depth and detail than this discussion. Press et al. (1992) devote and entire chapter to multigrid, and is the most accessible. Wesseling (1992) and Trottenberg et al. (2001) provide much more detail.

3.1 Coarse grid correction

To demonstrate the increased effectiveness of the Gauss-Seidel method on a coarse grid, we anti-alias filter and re-sample the example problem from the previous chapter. The problem was originally on a 65x65 grid, in Figure 3.1(b), the initial estimate is shown restricted down to a 17x17 grid. Only the long wavelength error is represented on this grid.

As can be seen in Figure 3.2 the error is reduced to near zero very quickly. The error after 10 iterations on the coarse grid is lower than the error after 50 iterations on the fine grid (Figure 2.7).

The spectral convergence for the Gauss-Seidel iteration on the coarse grid is depicted in Figure 3.3. Both the predicted and empirical values of ω show far stronger attenuation of the long wavelength error on the coarse grid.

The first iteration matches the predicted theoretical values, but subsequent iterations again contribute less and less.

This process is called *coarse grid correction*. It serves to show the benefit of using a coarse grid to perform iterative corrections. In practice we can derive far more efficient methods that operate on a variety of grids, and can reduce the problem to a 3x3 matrix to get an initial estimate.

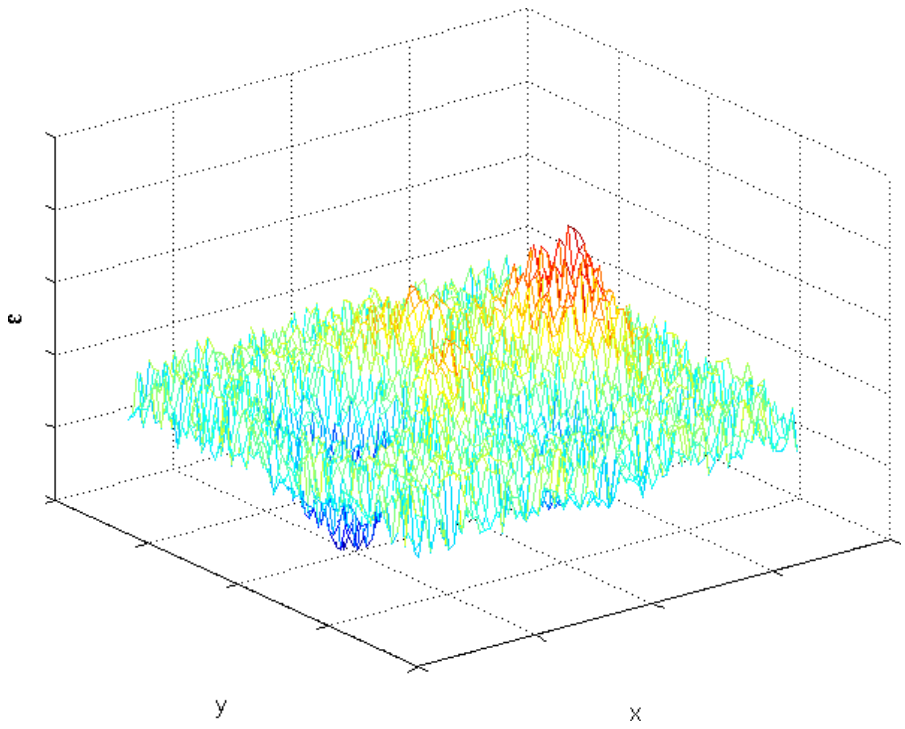

(a) The initial estimate of to the Laplace's equation

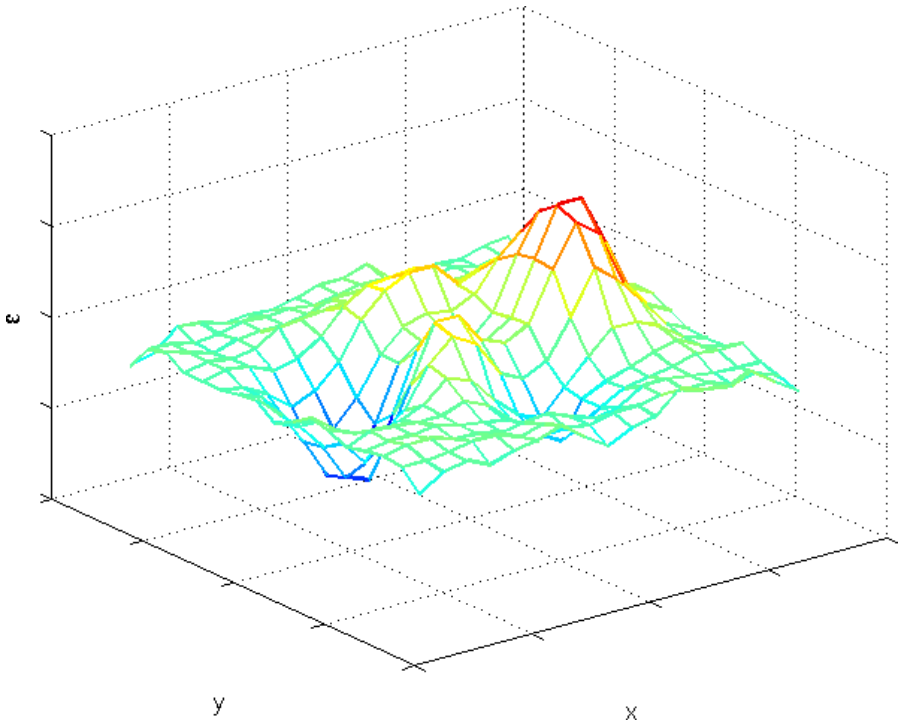

(b) The initial estimate to the Laplace's equations restricted to a more coarse grid

Figure 3.1: The Laplace's equation example initial estimate on different grids.

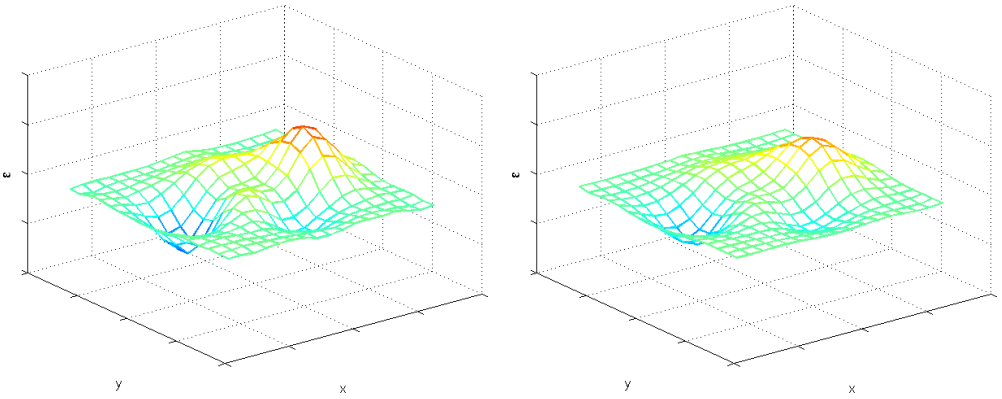

(a) The estimate after 1 iteration

(b) After 2 iterations

(c) 5 iterations

(d) 10 iterations

Figure 3.2: The Gauss-Seidel solution as it evolves to the Laplace's equation example. The estimate was downsampled to a 17x17 grid before being corrected.

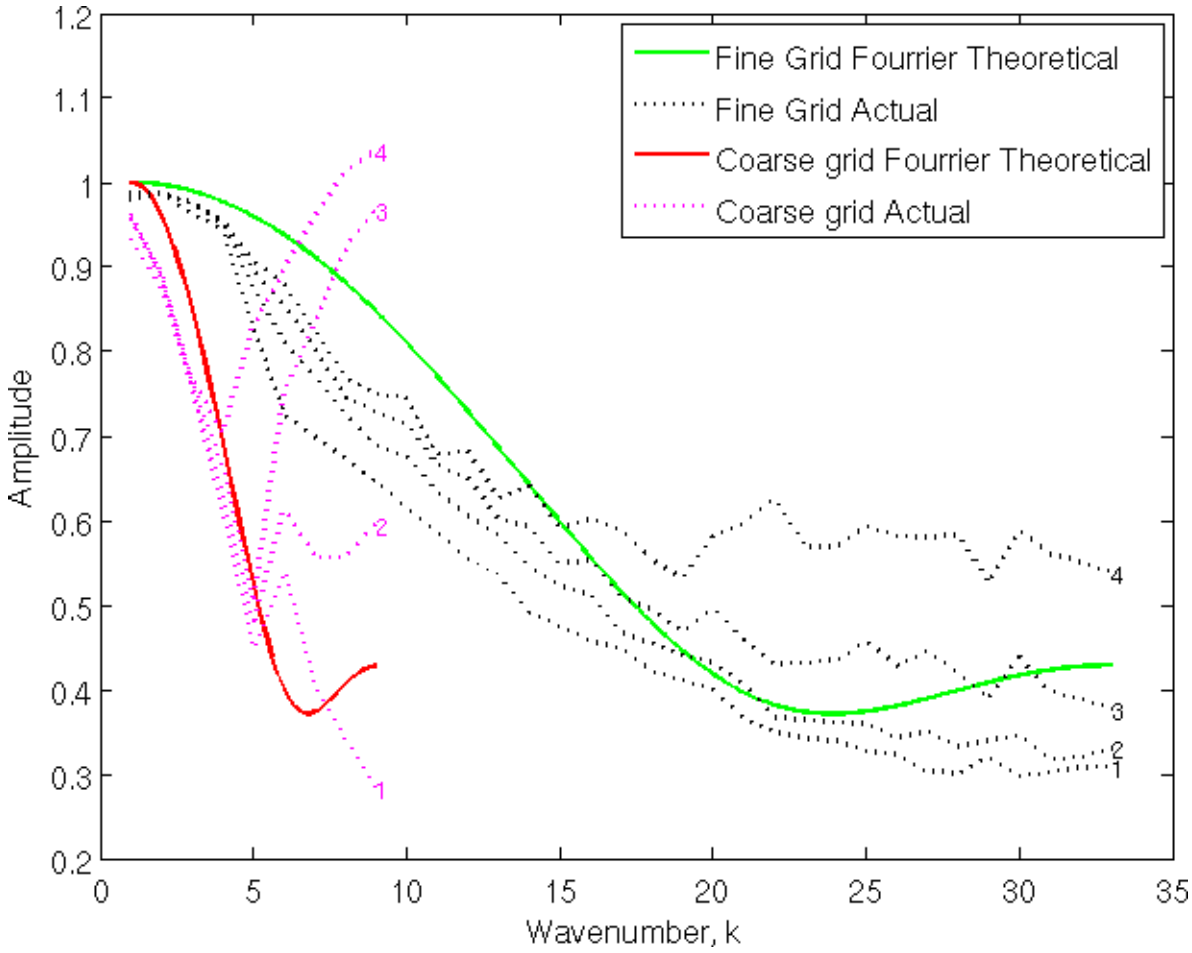

Figure 3.3: The spectrum of a coarse grid Gauss-Seidel operator compared to a fine grid Gauss-Seidel operator.

3.1.1 Multigrid components

As is shown in Figure 3.2, there is value in restating the problem on a more coarse grid, and applying an iterative method on a reduced set of equations. A brief discussion of the tools we will need to accomplish such a goal follows.

Interpolation

Interpolation is the adding of grid points in between existing grid points. The interpolation performed on a 2-D grid is shown in Figure 3.4.

This interpolation has the effect of reducing Δx and Δy in the problem by half. For some problems, it may be advisable to derive interpolators that depend on direction, or to change the distance between the points by a factor other than 2. Complications such as these will not be dealt with, but the logic and methods are similar.

Bi-linear interpolation is the most common form of interpolation in 2 dimensions, and is depicted in Figure 3.5. It calculates the value of each new point based on the average of all existing neighboring points. The following is an example of bilinear interpolation:

$$\mathcal{P}\begin{bmatrix} 0 & 0 & 0 \\ 0 & 1 & 0 \\ 0 & 0 & 0 \end{bmatrix} \Rightarrow \frac{1}{4}\begin{bmatrix} 0 & 0 & 0 & 0 & 0 \\ 0 & \frac{1}{4} & \frac{1}{2} & \frac{1}{4} & 0 \\ 0 & \frac{1}{2} & 1 & \frac{1}{2} & 0 \\ 0 & \frac{1}{4} & \frac{1}{2} & \frac{1}{4} & 0 \\ 0 & 0 & 0 & 0 & 0 \end{bmatrix}. \tag{3.1}$$

The non-zero entries of the right hand side are called the *symbol* of the interpolation.

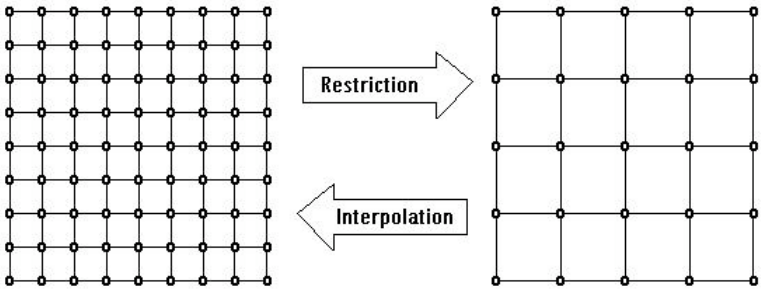

Figure 3.4: Interpolation and restriction depicted on a 2-D grid.

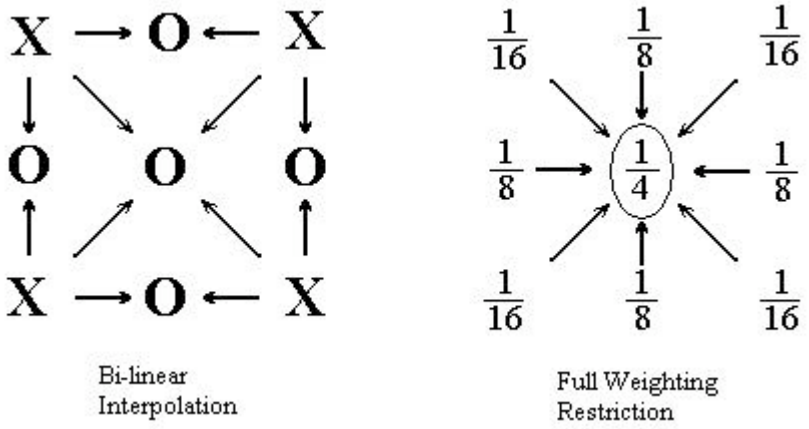

Figure 3.5: Schematic of Bi-linear Interpolation and full weighting restriction. For interpolation, The **x**'s represent previous values and **o**'s interpolated points, and the arrows shows the contribution from neighboring points. For restriction, only the central point remains, and is a weighted average of all 9 points, using the fractions as weights.

Restriction

Restriction (or *downsampling*) is the opposite of interpolation, as pictured in Figure 3.4. The most straight forward restriction is called *straight injection*. All grid points that are not wanted in the coarser grid are simply omitted. While simple, it can cause problems in practice. It leads to the possibility of aliasing.

The best choice for a restriction operator is the *adjoint* of the interpolator. A general method to find the adjoint is given in Press et al. (1992). For bi-linear interpolation, the symbol for the adjoint restriction, called full-weighting, is

$$\mathcal{R} \Rightarrow \begin{bmatrix} \frac{1}{16} & \frac{1}{8} & \frac{1}{16} \\ \frac{1}{8} & \frac{1}{4} & \frac{1}{8} \\ \frac{1}{16} & \frac{1}{8} & \frac{1}{16} \end{bmatrix}. \tag{3.2}$$

To implement, the restriction consists of taking the weighted average of each point and all of its surrounding points, using the corresponding fractions in the symbol. Note that the restriction of the operators symbol (or sum), equals 1, or

$$\mathcal{R} \begin{bmatrix} \frac{1}{16} & \frac{1}{8} & \frac{1}{16} \\ \frac{1}{8} & \frac{1}{4} & \frac{1}{8} \\ \frac{1}{16} & \frac{1}{8} & \frac{1}{16} \end{bmatrix} = [1]. \tag{3.3}$$

Bi-linear interpolation and its adjoint, full weighting restriction, are both fairly simple to implement, and will do for most problems (Press et al., 1992). For partial differential equations involving 3^{rd} or 4^{th} derivatives, cubic and, if necessary, quartic interpolators can be found in many books (eg. Hunter and Pullen (1997-2003)).

Smoothers

A smoother is an iterative method that is appropriate for multigrid use. A good smoother has the properties of not only fast convergence, but also concentrates the error reducing power on the short wavelengths. The focus on short wavelengths is important because interpolation introduces errors into the medium and short wavelengths.

For our purposes, Gauss-Seidel relaxation is best, due to its simplicity and effectiveness. Conjugate gradient methods are not a very good choice for a smoother. Its error reducing capabilities are strong across the whole spectrum, but it does not concentrate on the high frequencies. The error may increase for individual frequencies, as it did in Figure 2.13 for our Laplace's example.

3.1.2 Basic multigrid

The process for a very basic multigrid method is depicted in Figure 3.6. By restricting the problem to a 5x5 grid (3.6(a)), we can solve for the long wavelengths using the Gauss-Seidel method very quickly. Our solution on the 5x5 grid is interpolated to a 9x9 grid (3.6(b)). The problem sampled on the 9x9 grid is again corrected by 2 passes of an iterative method such as the Gauss-Seidel, and interpolated to a 17x17 grid. The process is repeated for a 33x33 grid, and finally our original 65x65 spacing. The final multigrid solution is in Figure 3.7 The surface is reduced to nearly zero on the most coarse grid with only a few iterations.

Figure 3.8 shows the spectrum of the solution as it evolves with each application of the smoother. The interpolation introduces some error on the short wavelengths. For example, the error that sits near a wavenumber of 6 increases from iteration 12 to iteration 13. This reinforces the need for choosing an appropriate smoother.

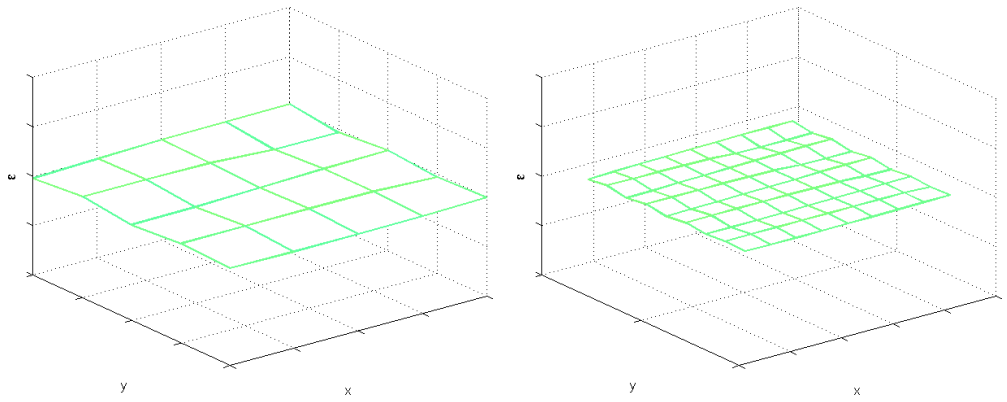

(a) The initial estimate is restricted to a 5x5 grid, then corrected with two Gauss-Seidel iterations.

(b) The solution in a) interpolated to a 9x9 grid and corrected twice.

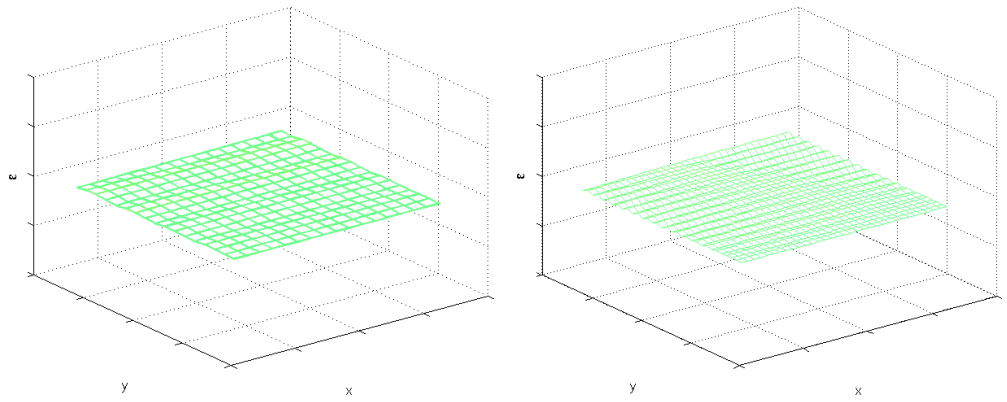

(c) Interpolated to a 17x17 grid and corrected.

(d) Interpolated to a 33x33 grid and corrected.

Figure 3.6: The basic multigrid solution as it evolves to the Laplace's equation example.

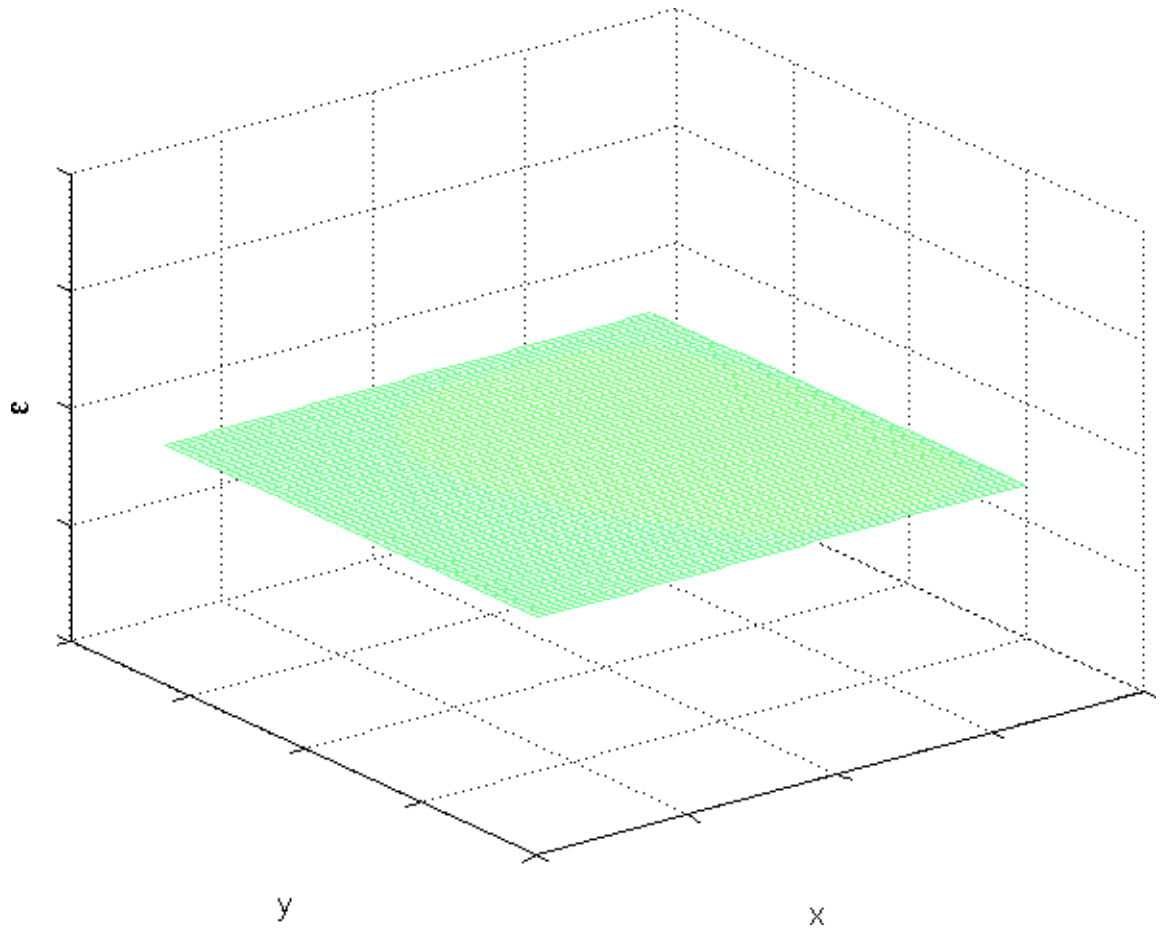

Figure 3.7: The basic multigrid solution interpolated back up to the finest 65x65 grid spacing.

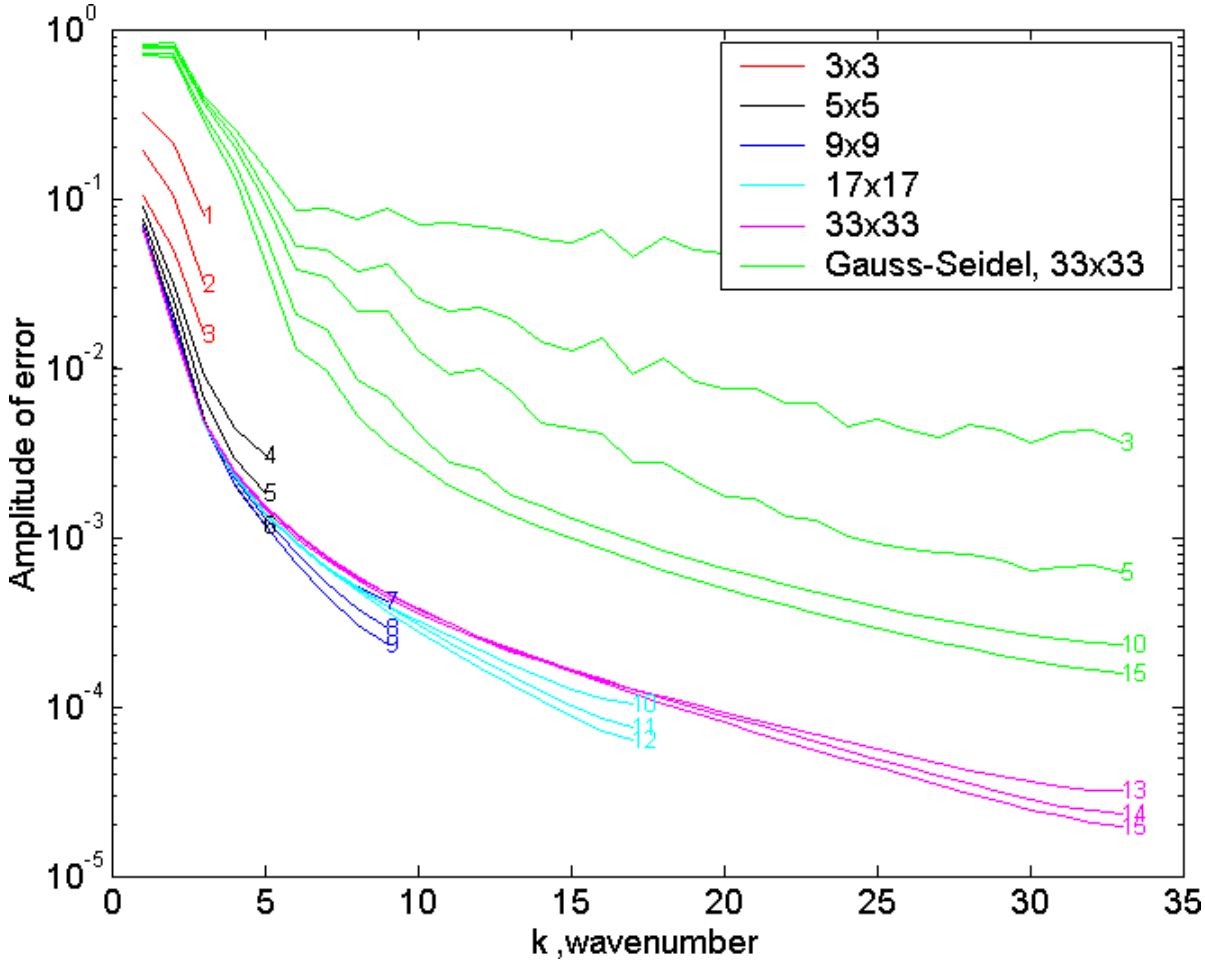

Figure 3.8: The amplitude spectrum of the error in the basic multigrid solution to the Laplace's equation example as it evolves with each coarse grid iteration.

3.1.3 Multigrid corrections

The errors introduced by interpolation in the second example problem are large enough to be of concern. Long wavelengths errors from interpolation may be problematic. Restricting the working solution to return to a more coarse grid destroys the high frequency content. The effort spent making corrections on the finer grids is wasted. The filtering and down-sampling would reverse any gains made.

The strategy to resolve this problem is to employ the residual. At the highest grid spacing we calculate the defect δ, using equation 2.4. Instead of restricting the solution and the source term, we restrict the defect and solve for the correction using equation 2.6. Once the unknown ϵ in equation 2.6 has been solved using a multigrid process, it is added to the estimate $\tilde{\mathbf{x}}$.

The solution found using the single multigrid correction here is identical to the solution we would have found by solving the reduced system directly. The advantage of using corrections as opposed to solving the system directly is that we can return to the coarse grid, after we have resolved some of the solution on the fine grid. This way we can get *corrections* for our estimate on a coarse grid, without restricting our solution and destroying high frequency information that we have already solved for.

A multigrid correction is applied to the initial estimate. The defect δ is calculated (using equation 2.4) and restricted to a 5x5 grid, and the correction ϵ is solved for at that level using 3 iterations of the Gauss-Seidel method. The correction ϵ is interpolated to the 9x9 grid, and again smoothed, using the defect as a source term. This is repeated until we arrive at the original grid spacing. The calculated correction ϵ is added to the estimate $\tilde{\mathbf{x}}$ according to equation Figure 2.3. If the solution is not acceptable, the process may be repeated as

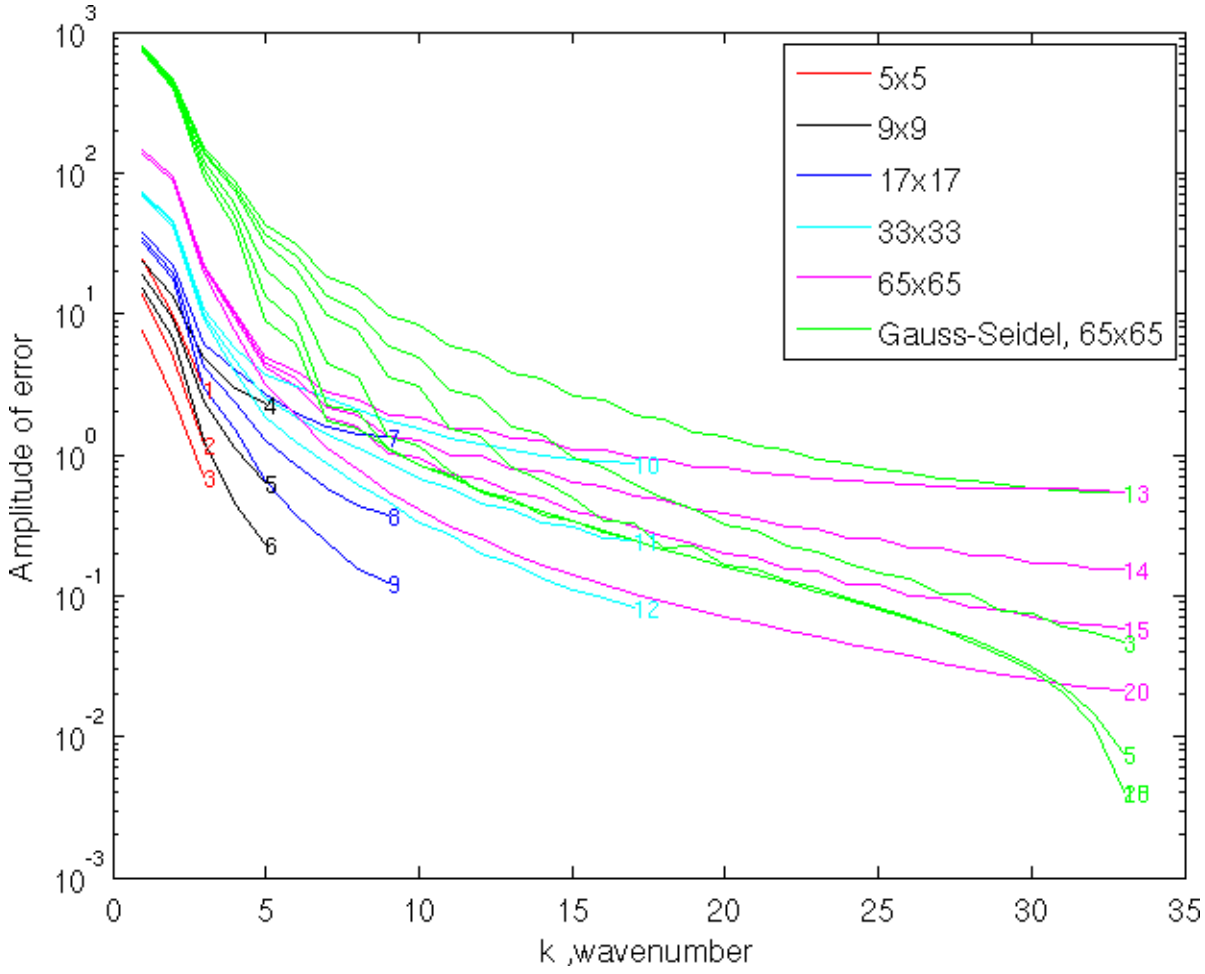

Figure 3.9: The amplitude spectrum of the error in solution found using a multigrid correction.

many times as necessary.

3.1.4 Full multigrid

When the basic multigrid method is combined with multigrid corrections, we arrive at what is known in the literature as *full multigrid*.

Each grid is identified by an integer value, m. There is a direct relationship between m and the number of unknowns, that is intertwined with the restriction, and the geometry of

the problem. For our 2-D Laplace's equation problem, with bilinear interpolation, and its adjoint full-weighting for a restriction, we use the formula

$$N_x = 2^m + 1. \tag{3.4}$$

The value N_x is the number of unknowns in the x direction. The total number of unknowns is equal to N_x^2. For $m = 1$, $N_x = 3$, meaning that the domain is sampled on a 3x3 mesh, for a total of 9 unknowns. Interpolating the grid once to a value of $m = 2$, is equivalent to adding a point in between each existing unknown. We then have a 5x5 system, for a total of 25 unknowns. The Laplace's equation example was expressed on a 65x65 grid, with a value of $m = 6$, for a total of 4225 unknowns.

Multigrid methods are deployed as a loop over this value m, and how this loop is implemented is a multigrid methods defining characteristic. In Figure 3.10 the 3 methods we discussed are graphed. The y axis is the value of m, the x axes is the iteration number. Each circle on the plot corresponds to an application of a smoother. A line with a positive slope shows an application of an interpolation, a downward line corresponds to a restriction. Our basic multigrid method starts at an m value of 1, and proceeds directly up to the finest grid spacing. A multigrid correction is "v" shaped on the plot, starting at the top grid level, restricting the defect down to $m = 1$ and interpolating the correction back up to the finest grid. Full multigrid comprises a series of increasingly taller N's.

Figure 3.10 shows the geometry for a single application of the smoother at each grid level. Our examples employes 3 iterations of a smoother at each grid level.

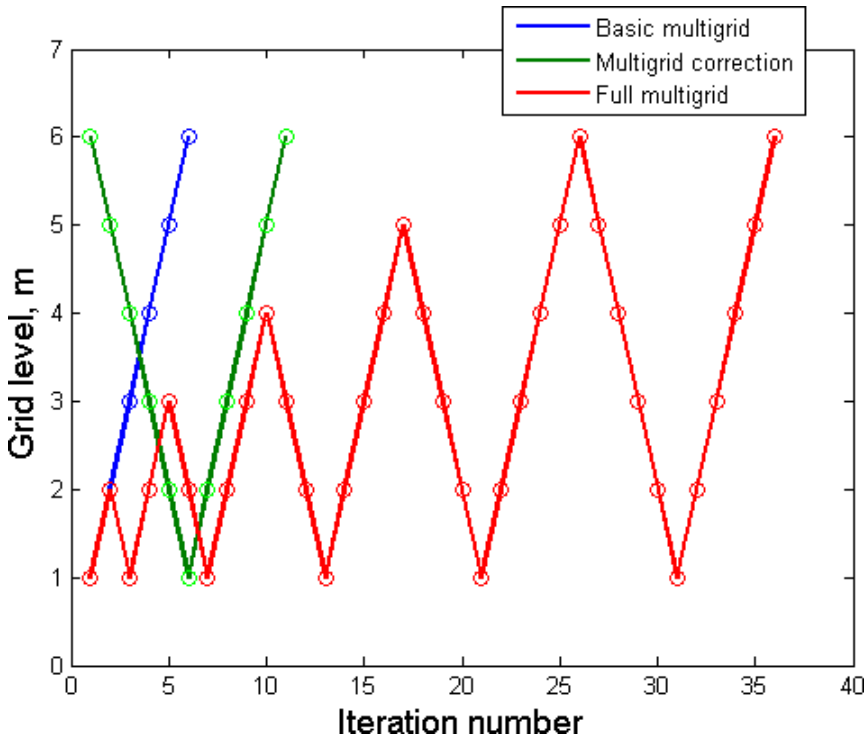

Figure 3.10: A comparison of 3 multigrid strategies, and how they arrive at a solution

3.2 Poisson's equation

In order to better demonstrate how a multigrid process arrives at a solution, we will slightly modify our sample problem. Our previous example with Laplace's equation had a source term $\mathbf{b} = 0$, that was equal to zero across the whole domain. The solution to this problem is all zeros.

Our new problem is an example of Poisson's equation. Poisson's equation is an extension of Laplace's equation. The differential equation is now

$$^2p = b(x, y), \tag{3.5}$$

where the only difference from equation 2.30, is the inclusion of a non zero source term, b.

The operator in the differential equation has not changed, so the discrete operator $\mathcal{L}$ remains the same, the matrix problem we are now solving is

$$\mathcal{L}\mathbf{p} = \mathbf{b}. \tag{3.6}$$

The source term $\mathbf{b}$ is depicted in Figure 3.11(a). It is a dipole source, with a positive delta function at $(x, y) = (2/3, 1/2)$ and a negative delta function at $(x, y) = (1/3, 1/2)$. The exact solution as calculated by Gaussian elimination is depicted in Figure 3.11(b). The positive spike in the source term yields a negative depression in the solution, the negative source term yields a positive depression in the solution. The solution is characterized by a smooth decay away from the spikes in the source term, out to match the boundary conditions.

The solution as it evolves using the Jacobi method is shown in Figure 3.12. The first iteration shown in Figure 3.12(a) is a scaled image of the source term $\mathbf{b}$. This is the approximation provided by equation 2.10 . The subsequent iterations are only able to correct the

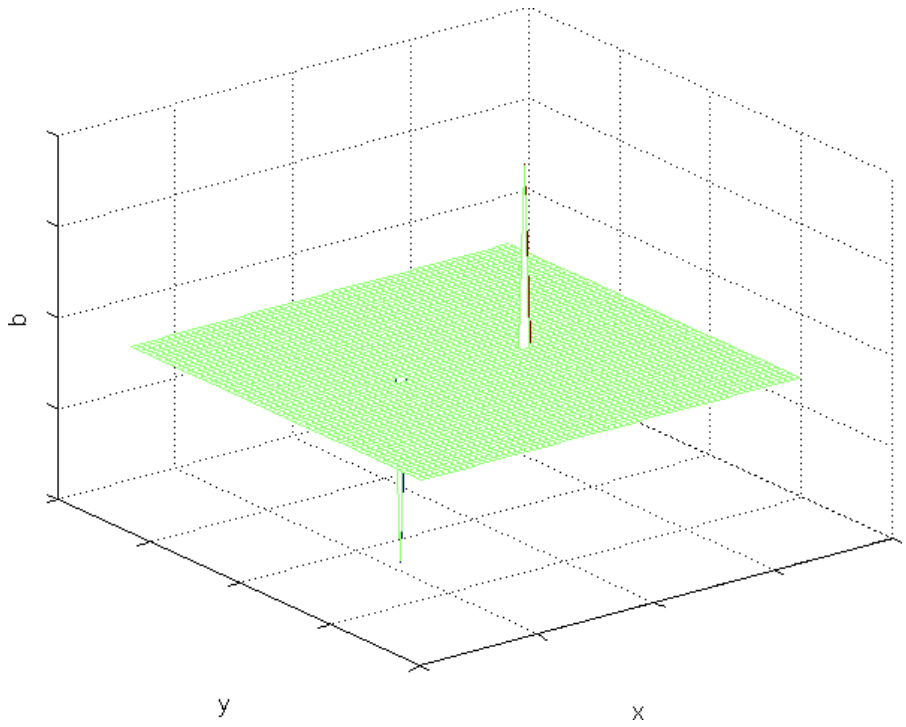

(a) the source term **b** for the second Laplace's example

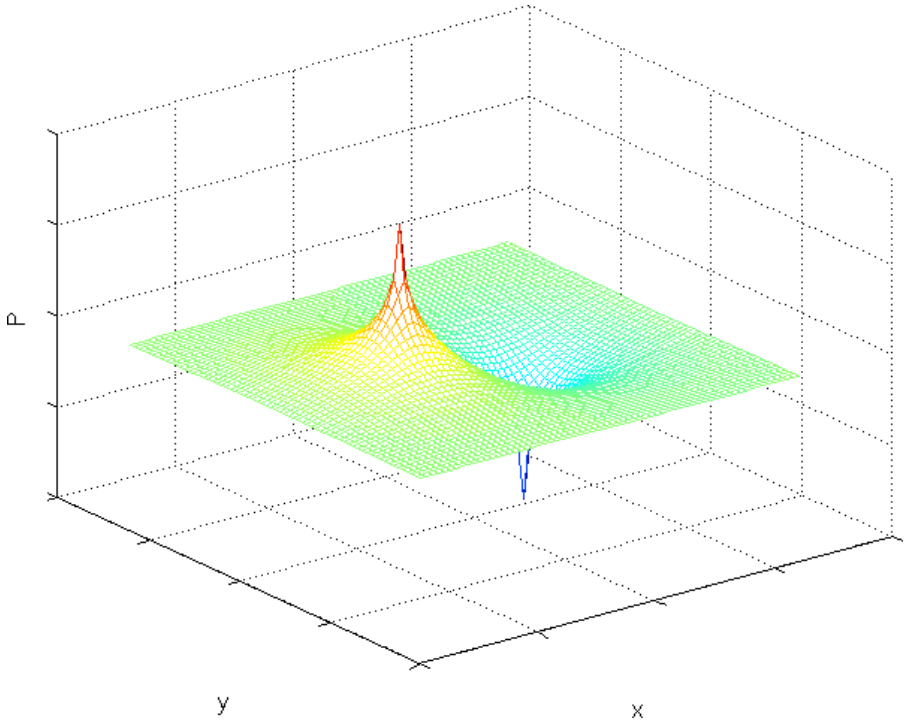

(b) the exact solution **x** for the second Laplace's example, found using Gaussian elimination

Figure 3.11: The second Laplace's equation example.

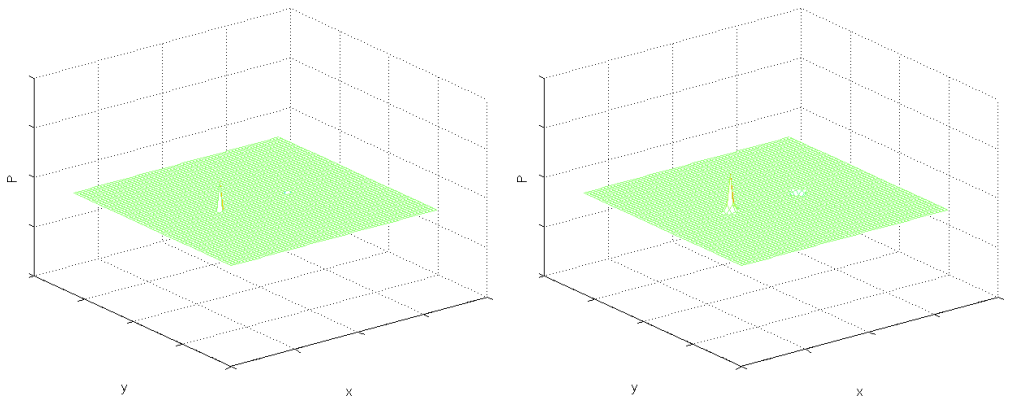

(a) 1 iteration

(b) 3 iterations

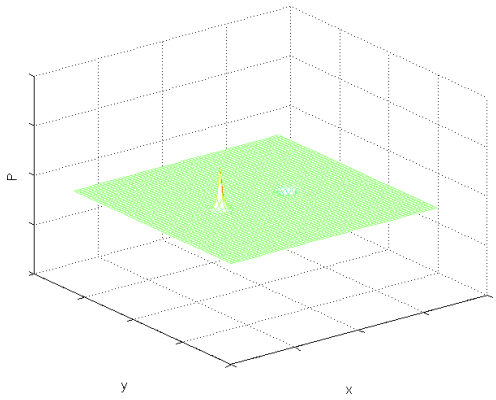

(c) 5 iterations

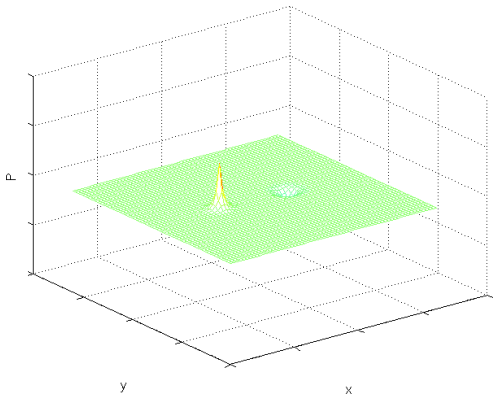

(d) 10 iterations

Figure 3.12: The solution found using the Jacobi method as it converges to the Poisson's solution

points immediately surrounding where the source term is non-zero. It takes many iterations for the influence of the source term to properly spread out throughout the entire domain.

The solution found using the conjugate gradient method is shown in Figure 3.13. The solution after 10 iterations in Figure 3.13(d) reflects the source term having influenced a greater number of points relative to the Jacobi method in Figure 3.12(d).

The solution as it evolves using the Gauss-Seidel method is shown in Figure 3.14. The Gauss-Seidel solution does not appear significantly different from the Jacobi solution.

The solution as it evolves using the basic multigrid method is shown in Figure 3.15. The

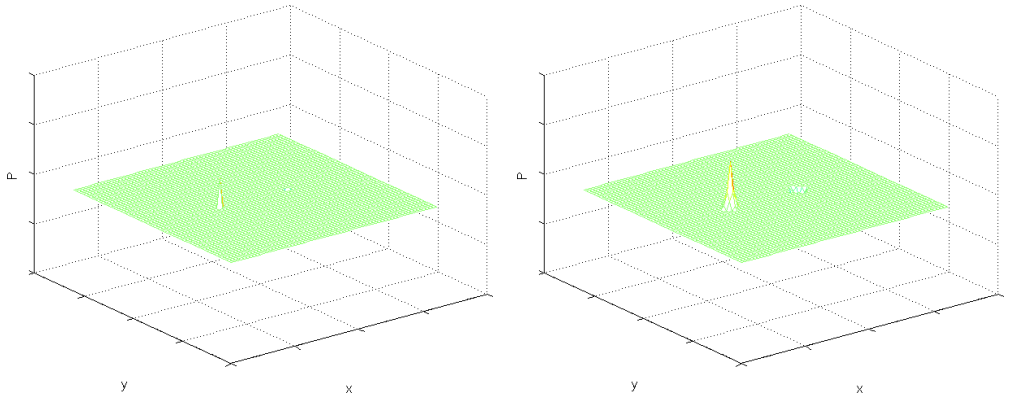

(a) 1 iteration (b) 3 iterations

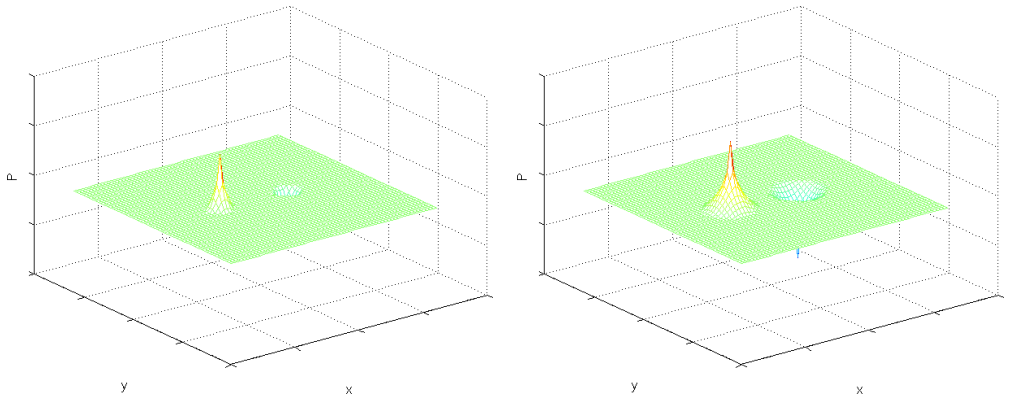

(c) 5 iterations (d) 10 iterations

Figure 3.13: The conjugate gradient method as it converges to the Poisson's solution

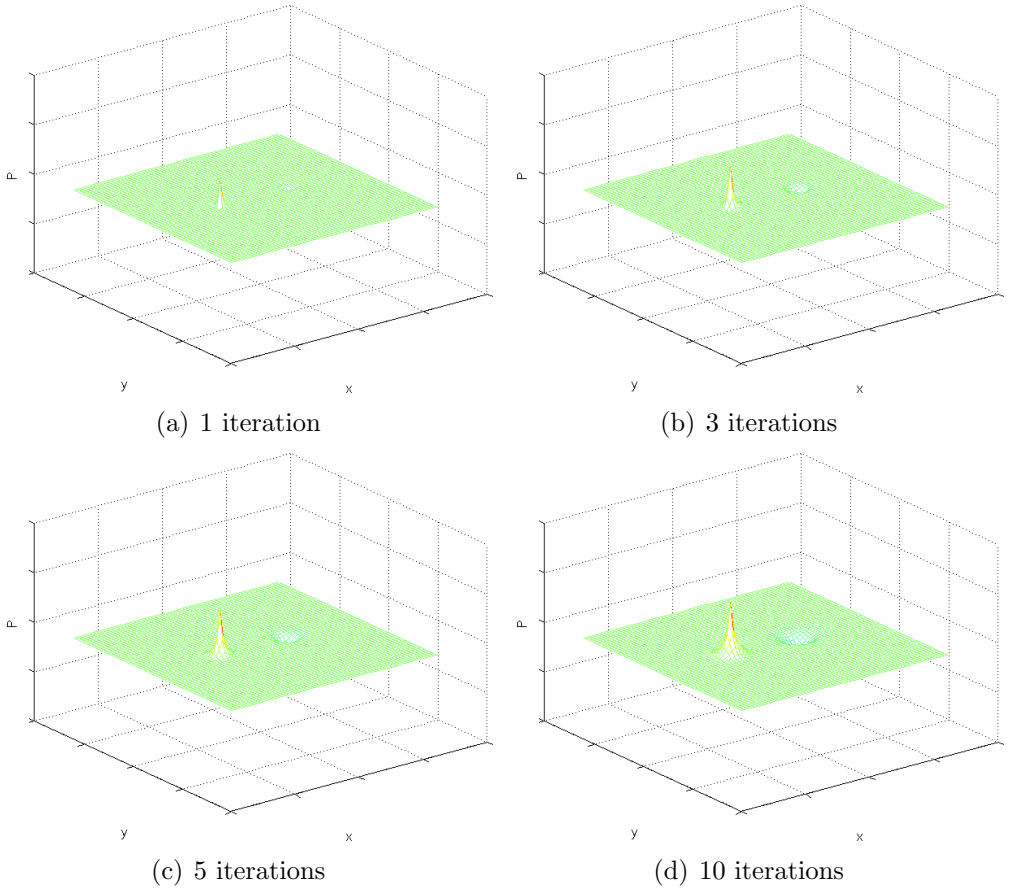

(a) 1 iteration (b) 3 iterations

(c) 5 iterations (d) 10 iterations

Figure 3.14: The Gauss-Seidel method as it converges to the Poisson's solution

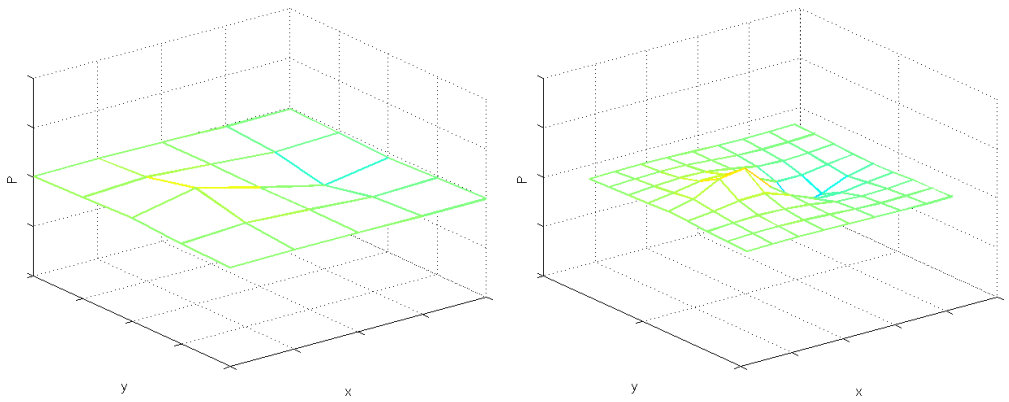

(a) 5x5 grid, iteration 3 (b) 9x9 grid, iteration 6

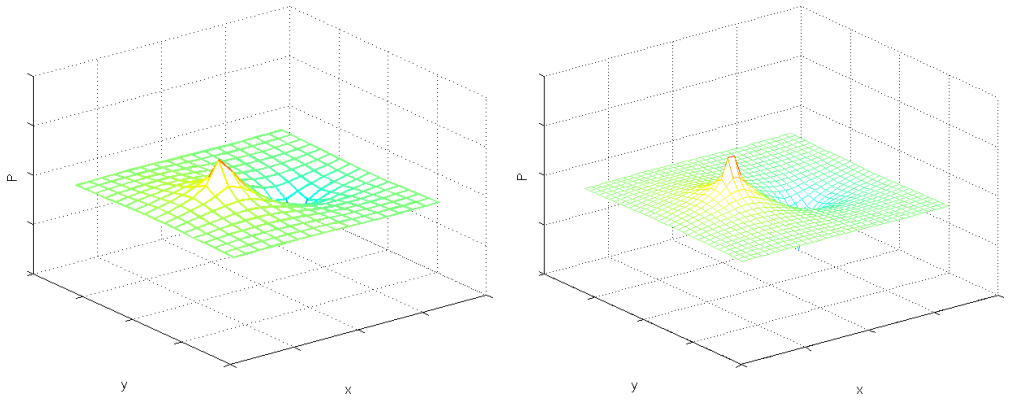

(c) 17x17 grid, iteration 9 (d) 33x33 grid, iteration 12

Figure 3.15: The multigrid solution as it evolves to the second Laplace's equation

matrix $\mathcal{L}$ and source term $\mathbf{b}$ are re-sampled to a $5x5$ grid of unknowns. An estimate to the solution is found on the coarse grid using Gauss-Seidel corrections. The solution after 3 corrections is shown in Figure 3.15(a). This solution is interpolated to a $9x9$ grid, and corrected another 3 times on this grid (Figure 3.15(b)). This process is repeated, until we reach the original $65x65$ grid. The solution may be corrected on the finest grid using a Gauss-Seidel correction any number of times.

Figure 3.16 shows the solution and error remaining after 20 applications of the different iterative corrections. The error remaining in the conjugate gradient solution appears lower

than the error left in the Gauss-Seidel solution. The multigrid solution looks like it has less error than either of the other methods.

The spectra of the error with each iteration of the multigrid, and a few of the Gauss-Seidel iterations is shown in Figure 3.17. For full multigrid, we calculate the residual on the fine grid, then restrict it to a 5x5 system. The correction is calculated on the 5x5 grid using 3 iterations of a Gauss-Seidel correction. The solution is interpolated to the 9x9 grid, where it is corrected using a multigrid correction. This process is repeated until we return to the fine grid.

The addition of the non zero source term introduces interpolation as a source of error to the multigrid method. The multigrid method still outperforms the Gauss-Seidel method across most of the spectra, except for at the high frequencies, where the Gauss-Seidel operator has been concentrating.

The amplitude spectrum of the error for all of the methods after 20 iterations is provided in Figure 3.18. The conjugate gradient method attenuates some of the longer wavelengths in the error more strongly than the Gauss-Seidel method or Jacobi method. It was not able to match the Gauss-Seidel method for most of the middle frequencies. The Jacobi and Gauss-Seidel are very similar throughout most of the frequency domain, except at the high frequencies where the Jacobi becomes more ineffective. The multigrid method provides lower error than the other methods almost everywhere in the spectrum, except at the very highest few frequencies.

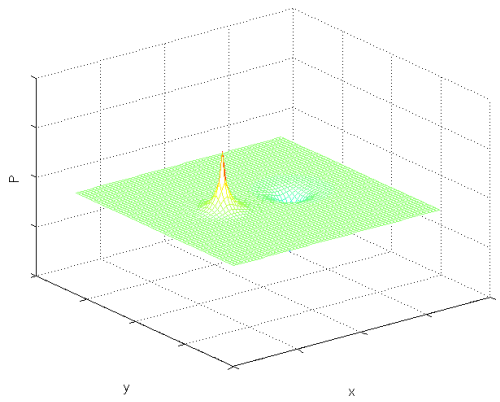

(a) The Gauss-Seidel solution after 20 iterations

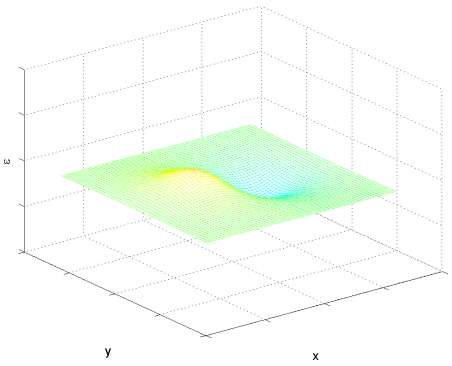

(b) The error in the Gauss-Seidel solution after 20 iterations

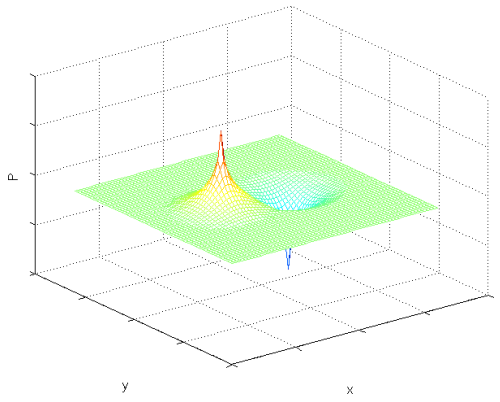

(c) The conjugate gradient solution after 20 iterations

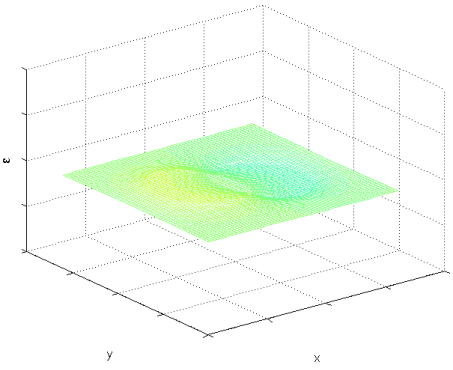

(d) The error in the conjugate gradient solution after 20 iterations

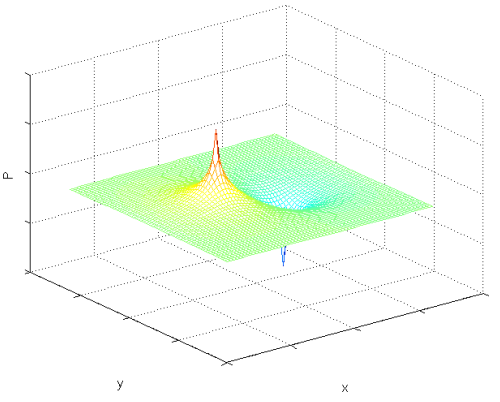

(e) The basic multigrid solution after 20 iterations

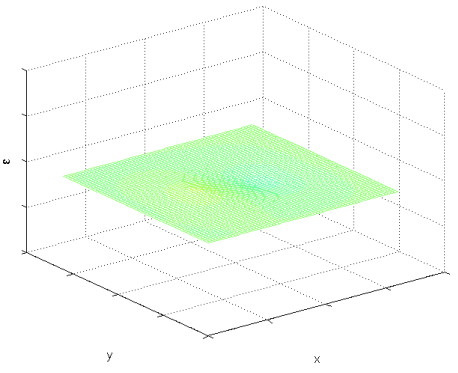

(f) The error in the basic multigrid solution after 20 iterations

Figure 3.16: The solutions to the Poisson's equation and their errors, after 20 iterations of each of the discussed methods

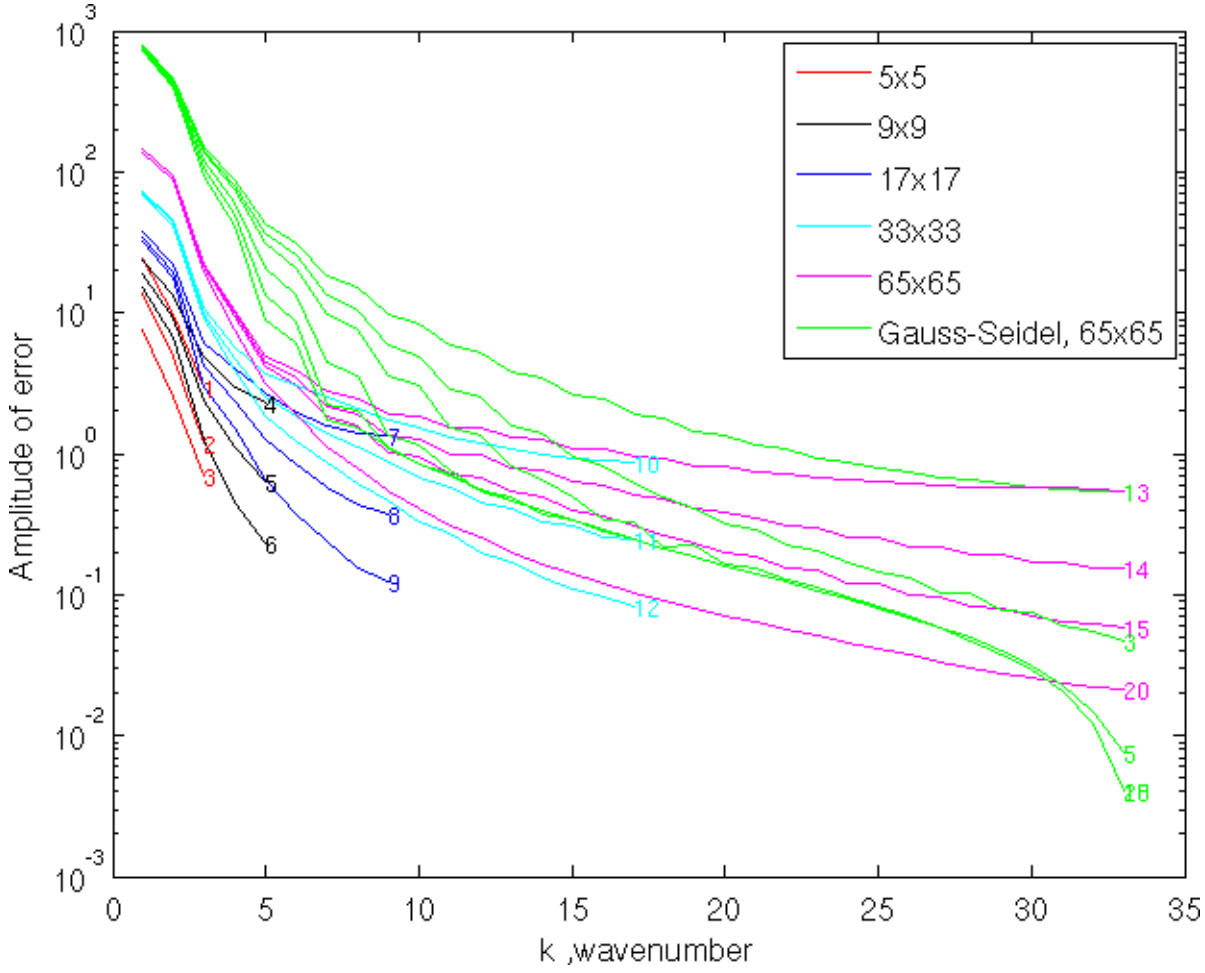

Figure 3.17: The amplitude spectrum of the error. The green line corresponds to a straight forward Gauss-Seidel procedure. The other lines belong to a single multigrid process.

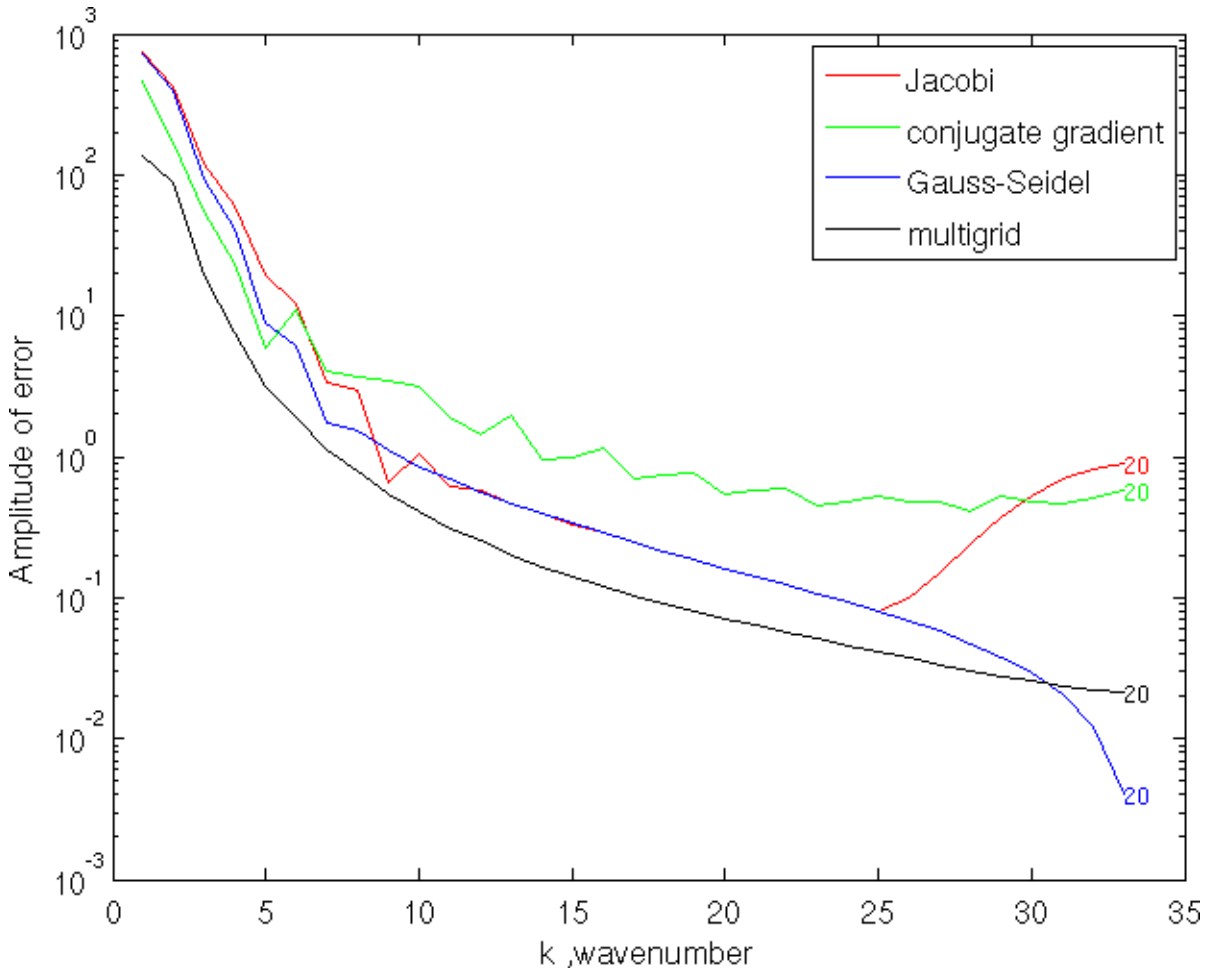

Figure 3.18: The amplitude spectrum of the error after 20 iterations of the different methods.

3.2.1 Calculation time

The most important benefit of multigrid methods is that the great improvements in resolving the long wavelengths do not come at a great sacrifice in computer time. While there may be some overhead time associated with setting up the multigrid procedure, a solution is usually provided in a similar amount of time as it takes to perform a only a few Gauss-Seidel iterations on the full set of equations.

Bancroft and Millar (2003) showed that a single Gauss-Seidel iteration on a system of N unknowns takes $\mathcal{O}(N)$ operations. A Gauss-Seidel iteration on a grid restricted to half the points would require $\mathcal{O}(N/2)$ operations. A multigrid correction that restricts the grid right down to a 3x3 matrix problem, each restriction by a factor of 2, would have a calculation time (only counting the time spent smoothing) proportional to

$$\mathcal{O}(N + N/2 + N/4 + N/8 + \cdots) \approx \mathcal{O}(2N). \tag{3.7}$$

The Laplaces equation example is a 2-D problem, and the restriction we perform must reflect the geometry of the problem. Each restriction reduces the number of points by a factor of approximately four. The calculation time (again only counting the smoothing) is

$$\mathcal{O}(N + N/4 + N/16 + N/32 \cdots) \approx \mathcal{O}(\frac{3N}{2}). \tag{3.8}$$

A 3-D restriction would yield a calculation time of

$$\mathcal{O}(N + N/8 + N/64 + \cdots) \approx \mathcal{O}(\frac{4N}{3}). \tag{3.9}$$

This shows that the efficiency of multigrid only increases relative to other methods when a 3-D problem is tackled, and the geometry of the problem is utilized in the restriction

process.

While these theoretical criteria do provide some insight, the additional computational overhead associated with restricting the operator, and the computational cost of restriction and interpolation are not included.

An interpolation or a restriction takes a similar amount of calculation time as an application of a smoother, and is required. Counting only time spent smoothing, the operation takes $\mathcal{O}(2N)$ operations for a 1-D problem according to equation 3.7. Pairing an interpolation and a restriction with each application of the smoother, the calculation time may be closer to $\mathcal{O}(6N)$, providing there is only one iteration of a smoother at each grid interval. To take away from the added cost of interpolation and restriction, several smoothing runs at each grid are usually performed. In the sample problems, each interpolation/restriction is partnered with 3 applications of a smoother to reduce the computer cost of changing grids.

Multigrid methods are also usually more complex, moving up and down grid levels in more complex patterns, with calculation time somewhere in between the two extremes.

Figure 3.19 is a plot of $\delta^T\delta$, (equal to the sum of δ^2, a measure of error from equation 2.7), versus the iteration number. The conjugate gradient method appears to only slightly outperform the Jacobi method by this measure of error, and only after a number of iterations. The Gauss-Seidel solution outperforms the Jacobi and conjugate gradient methods after 20 iterations. Multigrid provides about an order of magnitude improvement over Gauss-Seidel using this value as a measure.

For the multigrid method, the first 12 corrections are on a reduced grid, meaning that we do not have a proper solution, only a coarse grid estimate. The estimate is interpolated to the fine grid at iteration 13. The final 7 iterations are Gauss-Seidel iterations on the finest grid. Very soon after the solution is interpolated to the finest grid, this measure of error,

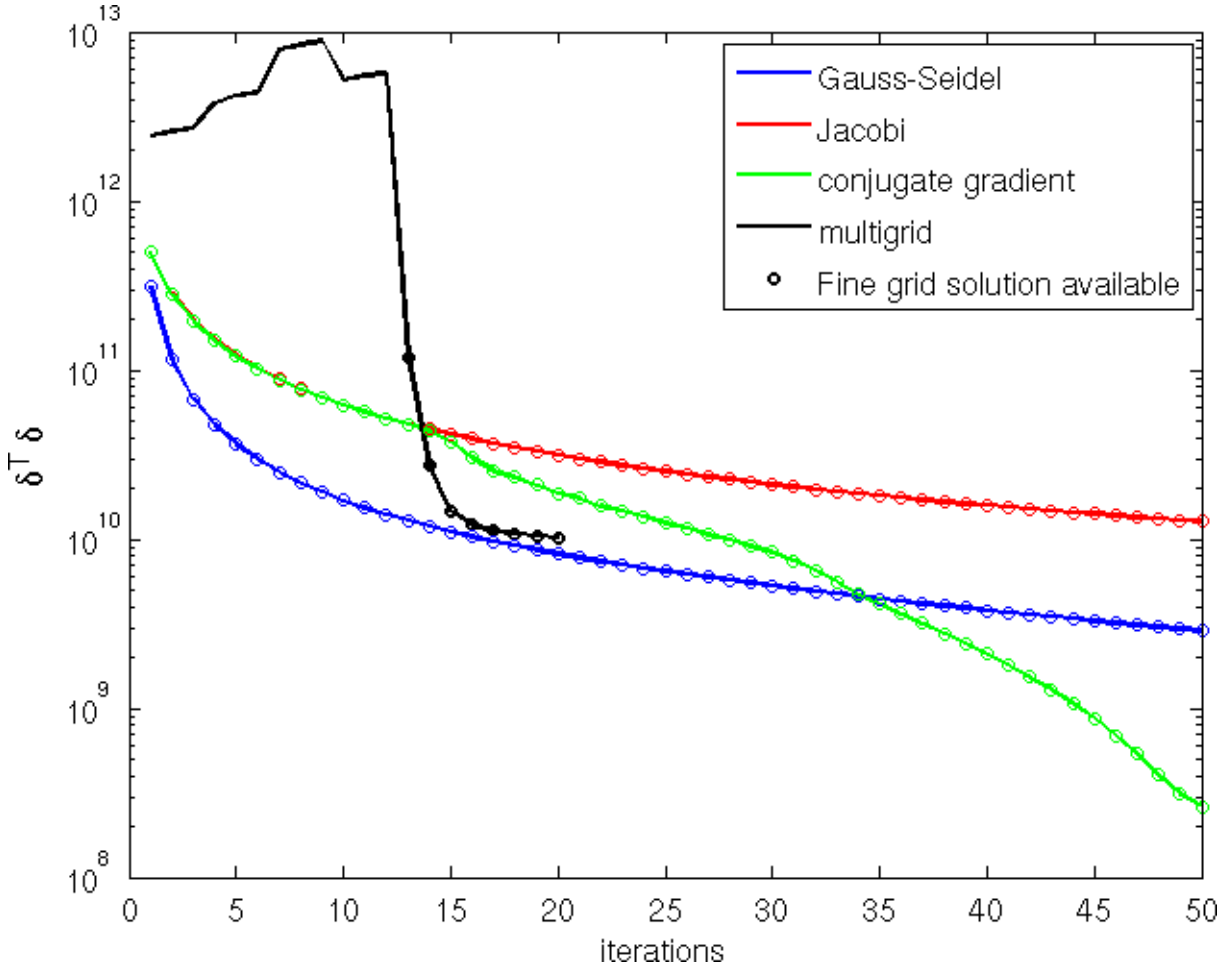

Figure 3.19: The sum of the square of the residual, $\delta^T \delta$ plotted versus iteration number.

$\delta^T \delta$, is far lower in the multigrid solution than for the other solutions .

When we compare the calculation times for the Gauss-Seidel, conjugate gradient and a basic multigrid method in Figure 3.20, the computer time saved by working on the smaller set of equations can be seen. The first 12 Gauss-Seidel iterations on the coarse grids were far more effective at reducing the long wavelengths than any of the Gauss-Seidel iterations on the fine grid. All of the strong attenuation of the long wavelength error was performed in approximately as much time as it took to perform approximately 1.5 iterations of the

Gauss-Seidel method.

The conjugate gradient method does not attenuate the error as strongly as the Gauss-Seidel method for the first few iterations, but subsequent iterations loose their effectiveness more slowly than Gauss-Seidel. The conjugate gradient method is able to continue reducing the error after many iterations. Recalling Figures 2.8 and 2.9, the conjugate gradient method performed poorly compared to Gauss-Seidel, but is able to continue reducing the error long after Gauss-Seidel has slowed converging.

The error in the multigrid solution is far lower than the error in the Gauss-Seidel method, even after many iterations. The conjugate gradient method continues converging and does reduce the error more than the basic multigrid, but it takes over 30 iterations, and nearly four times as much calculation time.

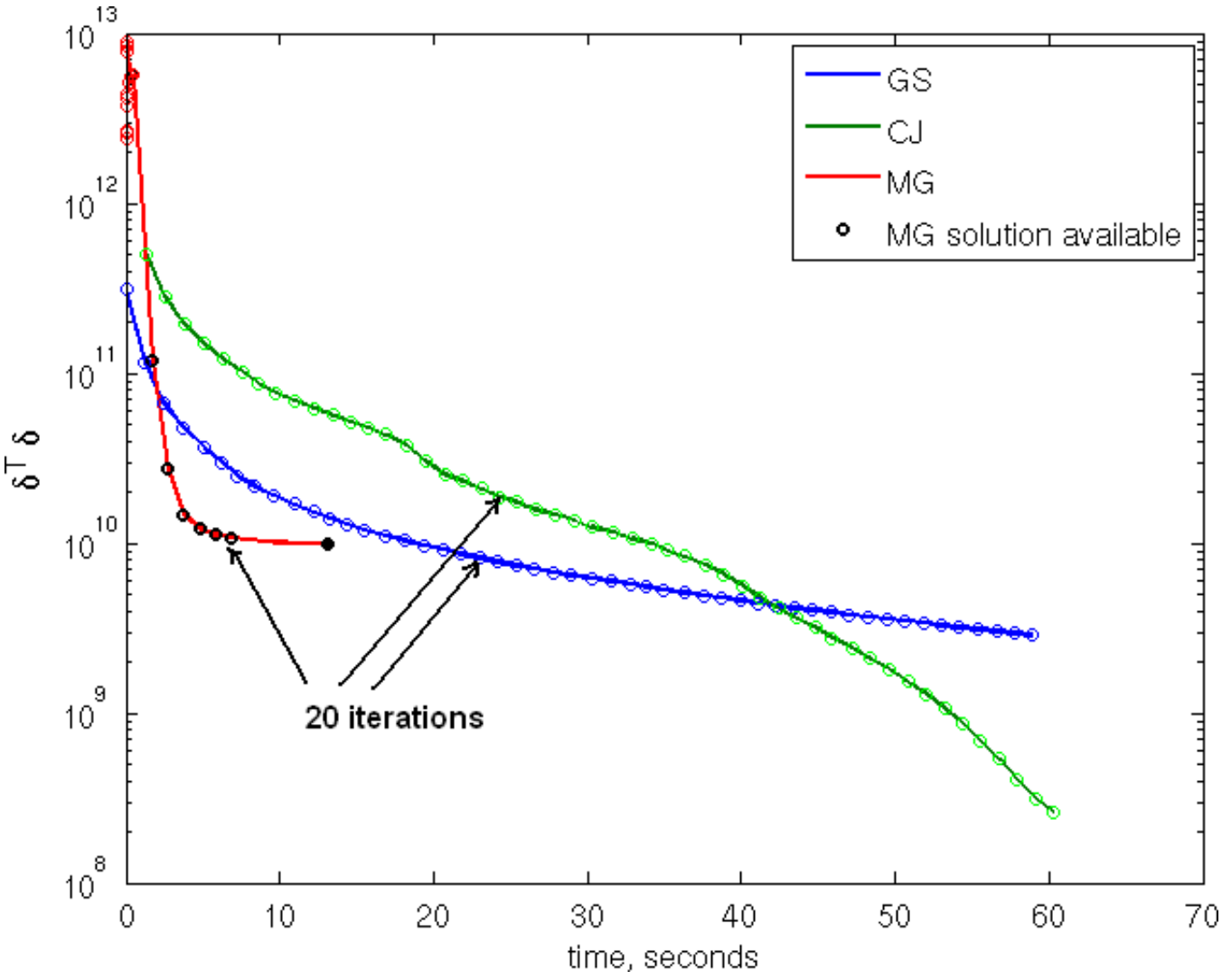

Figure 3.20: Error plotted versus calculation time

Chapter 4

The surface consistent equations

The surface consistent equations are commonly used to calculate static shifts, amplitude corrections, and deconvolution operators. The underlying principle behind applying the surface consistent equations to seismic data stems from the approximation that a large part of the signal degradation for each trace is due to the near surface conditions of both the source and the receiver.

Figure 4.1 depicts how elevation changes may lead to surface consistent time anomalies. The near surface most often has a seismic velocity far below that of the rock beneath. If the near surface propagates waves suitably slow, the raypaths of the reflected data are near vertical (red arrows in Figure 4.1). The surface consistent time delay for a particular trace is the sum of the delay of the downward propagating wave from the source and the time delay for the upwards moving wave at the receiver.

All of the traces associated with the same source location should have the same amplitude and source signature related to the conditions near the source. Varying depths of the dynamite charges, the strength of the coupling between the source and the surrounding rock, and other conditions can lead to source specific effects. Likewise the environment immediately around each receiver and the quality of the coupling between the receiver and the ground will be consistent and specific to particular receiver stations.

This section discusses the development of the system of equations for a 2 channel (source, receiver) surface consistent decomposition. The 2 channels used are the shot and receiver consistent terms. Following this the inclusion of an additional two channels, an offset and a

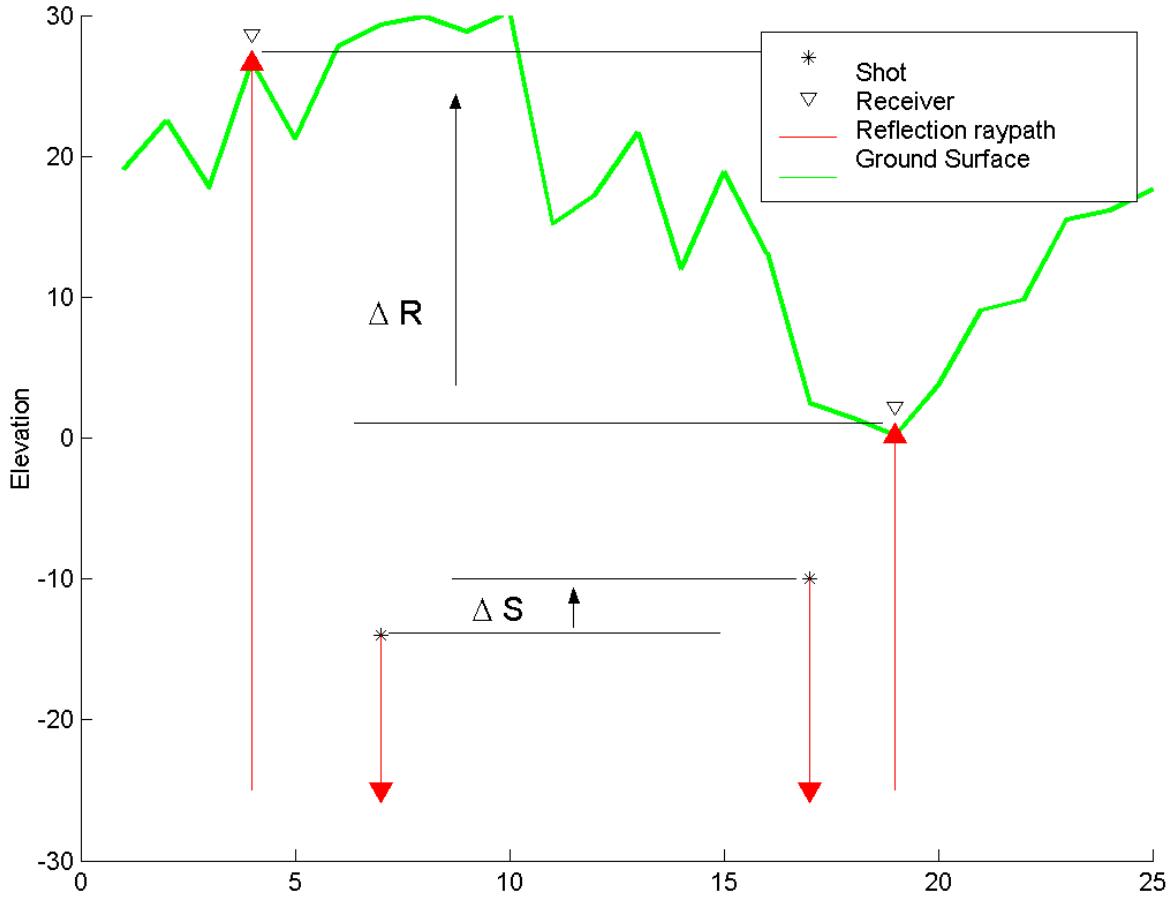

Figure 4.1: Changes in elevation lead to a traveltime delay that is dependent on the source and receiver location. All of the traces recorded with these 2 receivers will have a travel time anomaly of ΔR, and likewise any reflections from these sources will have a traveltime difference of ΔS.

midpoint consistent channel, is discussed.

4.0.2 Two term derivation

Consider the problem of de-coupling separate source and receiver consistent statics from a seismic survey. We assume the total static correction for each trace t_{ij} can be expressed as a contribution from the (both unknown) i^{th} source, S_i, and the j^{th} receiver,

$$t_{ij} = S_i + R_j. \tag{4.1}$$

Each trace contributes an equation to the linear system, which we express as a matrix operation of the form

$$\mathbf{As} = \mathbf{t}. \tag{4.2}$$

Here, $\mathbf{A}$ is a matrix of coefficients, whose form is dependent on the geometry of the seismic survey. The vector $\mathbf{t}$ is the calculated total static shifts for each trace (as calculated using a stack power optimization, auto correlations, etc.), and $\mathbf{s}$ is an unknown vector of each separated source and receiver consistent component of $\mathbf{t}$.

We assign a column of $\mathbf{A}$ to each unique shot and each unique receiver. It has as many rows as traces, which is usually much greater than the number of columns. For each trace, the corresponding row in the matrix $\mathbf{A}$ has a 1 in the column that is associated with the shot number, and a 1 in the column associated with the receiver station.

For an example of how $\mathbf{A}$ is constructed, consider a simple seismic survey, with 3 shots and 8 possible receivers. The live spread of 4 active receivers moves forward 2 receivers with each shot.

The following diagram is called a stack chart, and shows how the 8 receivers are activated 4 at a time:

rec stn.	1	2	3	4	5	6	7	8	
shot 1	⋆	⋆	⋆	⋆					
shot 2			⋆	⋆	⋆	⋆			
shot 3					⋆	⋆	⋆	⋆	

Writing down an equation for each of the traces, and organizing the sources and receivers into columns,

$$
\begin{array}{cccccccccccc}
S_1 & & + & R_1 & & & & & & & = & T_1 \\
S_1 & & + & & R_2 & & & & & & & T_2 \\
S_1 & & + & & & R_3 & & & & & & T_3 \\
S_1 & & + & & & & R_4 & & & & & T_4 \\
& S_2 & + & & & R_3 & & & & & & T_5 \\
& S_2 & + & & & & R_4 & & & & & T_6 \\
& S_2 & + & & & & & R_5 & & & & T_7 \\
& S_2 & + & & & & & & R_6 & & & T_8 \\
& & S_3 & + & & & & R_5 & & & & T_9 \\
& & S_3 & + & & & & & R_6 & & & T_{10} \\
& & S_3 & + & & & & & & R_7 & & T_{11} \\
& & S_3 & + & & & & & & & R_8 & T_{12}
\end{array}
\tag{4.3}
$$

The twelve values T on the right side of the equation are the traveltime anomalies, one measurement per seismic trace.

We can factor the left hand side of equation 4.3 into a matrix multiplication

$$\begin{bmatrix}
1 & & 1 & & & & & & & & & \\
1 & & & 1 & & & & & & & & \\
1 & & & & 1 & & & & & & & \\
1 & & & & & 1 & & & & & & \\
 & 1 & & & 1 & & & & & & & \\
 & 1 & & & & 1 & & & & & & \\
 & 1 & & & & & 1 & & & & & \\
 & 1 & & & & & & 1 & & & & \\
 & & 1 & & & & 1 & & & & & \\
 & & 1 & & & & & 1 & & & & \\
 & & 1 & & & & & & 1 & & & \\
 & & 1 & & & & & & & 1 & &
\end{bmatrix}
\begin{bmatrix} S_1 \\ S_2 \\ S_3 \\ R_1 \\ R_2 \\ R_3 \\ R_4 \\ R_5 \\ R_6 \\ R_7 \\ R_8 \end{bmatrix}
=
\begin{bmatrix} T_1 \\ T_2 \\ T_3 \\ T_4 \\ T_5 \\ T_6 \\ T_7 \\ T_8 \\ T_9 \\ T_{10} \\ T_{11} \\ T_{12} \end{bmatrix} \tag{4.4}$$

The vector **s** has 11 unknowns. The first three unknowns correspond the shot consistent values. The other 7 unknowns are the receiver consistent values.

The system of equations that results from this problem is over-determined (more equations than unknowns), requiring a least squares solution,

$$\mathbf{A}^T\mathbf{A}\mathbf{s} = \mathbf{A}^T\mathbf{t}. \tag{4.5}$$

The matrix $\mathbf{A}^T\mathbf{A}$ is closely related to the geometry. The row corresponding to a particular shot will have the number of live receiver stations for that shot on the main diagonal, and a 1 in each column that represents a receiver that is live during that shot. For the receiver rows, each main diagonal is the number of shots that receiver is live for, and also has a 1

in all of the columns corresponding to shot records that have a trace associated with that receiver.

The matrix $\mathbf{A}^T\mathbf{A}$ from the 3 shot - 8 receiver example in equation 4.4 would be

$$\mathbf{A}^T\mathbf{A} = \begin{bmatrix} 4 & & & 1 & 1 & 1 & 1 & & & & \\ & 4 & & & & 1 & 1 & 1 & 1 & & \\ & & 4 & & & & & 1 & 1 & 1 & 1 \\ 1 & & & 1 & & & & & & & \\ 1 & & & & 1 & & & & & & \\ 1 & 1 & & & & 2 & & & & & \\ 1 & 1 & & & & & 2 & & & & \\ & 1 & 1 & & & & & 2 & & & \\ & 1 & 1 & & & & & & 2 & & \\ & & 1 & & & & & & & 1 & \\ & & 1 & & & & & & & & 1 \end{bmatrix} \tag{4.6}$$

Each non zero column in a particular row of $\mathbf{A}^T\mathbf{A}$ indicates the unknowns that contribute to the trace. For example, the third row has coefficients of one in the columns for receivers 5 through 8, indicating which receivers are a member of that (the third) shot gather. The main diagonal is equal to the fold of the gather for the unknown. Its value is the number of traces that contribute to the sum $\mathbf{A}^T\mathbf{t}$.

The location of the band of ones on the upper right side of the main diagonal in equation 4.6 correspond to the indexes of the receiver unknowns. The ones in the i^{th} row of matrix $\mathbf{A}^T\mathbf{A}$ are in the columns corresponding to the receivers that are live during the i^{th} shot.

The symmetric band of ones to the lower left of the main diagonal represents the shot indexes that contribute to the receiver gathers. The column that each non zero coefficient

sits in indicates that one of the traces summed into $\mathbf{A}^T\mathbf{t}$ was recorded using that source.

An element in vector $\mathbf{A}^T\mathbf{t}$ associated to a shot is the sum of all of the values of $\mathbf{t}$ corresponding to that shot. For example, the i^{th} value in vector $\mathbf{A}^T\mathbf{t}$, across from the i^{th} unknown, is the sum of all of the statics for the traces in the i^{th} shot gather.

The $\mathbf{A}^T\mathbf{t}$ across from the i^{th} receiver gather is the sum of all of the trace statics in the common receiver gather.

$$\mathbf{A}^T\mathbf{t} = \begin{bmatrix} T_1 + T_2 + T_3 + T_4 \\ T_5 + T_6 + T_7 + T_8 \\ T_9 + T_{10} + T_{11} + T_{12} \\ T_3 + T_5 \\ T_4 + T_6 \\ T_7 + T_9 \\ T_8 + T_{10} \\ T_{11} \\ T_{12} \end{bmatrix} \tag{4.7}$$

There are two fundamental limitations we encounter when solving the surface consistent equations. The first problem is that the matrix $\mathbf{A}^T\mathbf{A}$ is singular. It is rank deficient by one. This means that we have one equation that is dependent on the other equations, giving us a parametric solution. Direct methods such as Gaussian elimination will fail (Wiggins et al., 1976). The singular element in the system leads to an uncertainty in our iterative solutions. There is a single degree of freedom in all of the solutions that will not be resolved.

The solution is unconstrained in this case by a constant. If we add a constant to all of the shot unknowns, the equations can still be solved by adding the negative of the constant

to all of the receiver term.

Secondly, it is also not strictly diagonally dominant. The main diagonal in each row is equal to the sum of all of the off diagonal components. This means that the Gauss-Seidel and Jacobi methods in theory do not necessarily converge. The matrix is also indefinite, which means that conjugate gradient methods will not necessarily converge either. The fact that the surface consistent equations do not strictly adhere to the requirements for convergence of our iterative methods means that we may at times be amplifying some wavelengths of error, ie. the solution is unstable.

These two numerical limitations contribute to the errors that we know exist in our solutions, and we have very little control over. The two instabilities exist only on the very longest wavelengths, over the scale of the whole survey.

In all of the surface consistent solutions we add a constant to the main diagonal of the matrix, to try and mute the instabilities. This method was mentioned in Wiggins et al. (1976). The equation we are trying to solve, equation 4.5 becomes

$$(\mathbf{A}^T\mathbf{A} + \mu\mathbf{D})\mathbf{s} = \mathbf{A}^T\mathbf{t}. \tag{4.8}$$

The matrix $\mathbf{D}$ is the main diagonal of $\mathbf{A}^T\mathbf{A}$, and the stability factor μ is a small number, 10^{-3} in our examples. This stability factor pads the denominator in our inversion, and prevents the small singular values from overpowering our solution (Sacchi, 2006). This has a strong effect on the long wavelengths of the solution. It stabilizes the singularities in the system by influencing the free parameters in the solution towards the origin at 0.

A synthetic seismic survey was generated using 100 source points, with 51 live receivers centered on each shot. The shot, along with the spread of the active geophones, is moved by 4 stations with each shot. This results in 100 shot stations, and 447 receiver stations. There

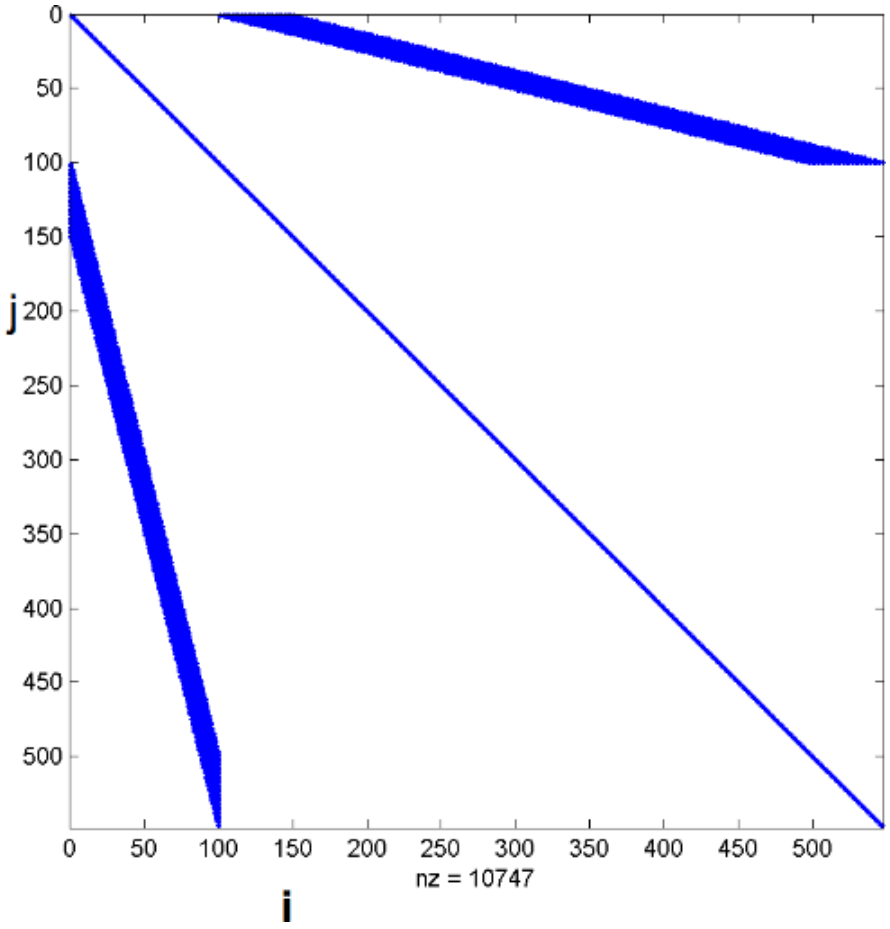

Figure 4.2: The non-zero coefficients in the 2 term surface consistent equations. This example has 100 shots and 447 receivers.

are 5100 traces, and 843 midpoints.

The two term surface consistent matrix $\mathbf{A}$ is a 5100x547 matrix. The least squares system in equation 4.5 has 547 equations in 547 unknowns. The non zero coefficients in $\mathbf{A}^T\mathbf{A}$ are displayed in Figure 4.2.

The main diagonal has a value equal to the fold for its corresponding unknown. For example, the main diagonal corresponding to a shot will have a value equal to the number of traces in that shot record. The value of the main diagonal for a particular receiver will be

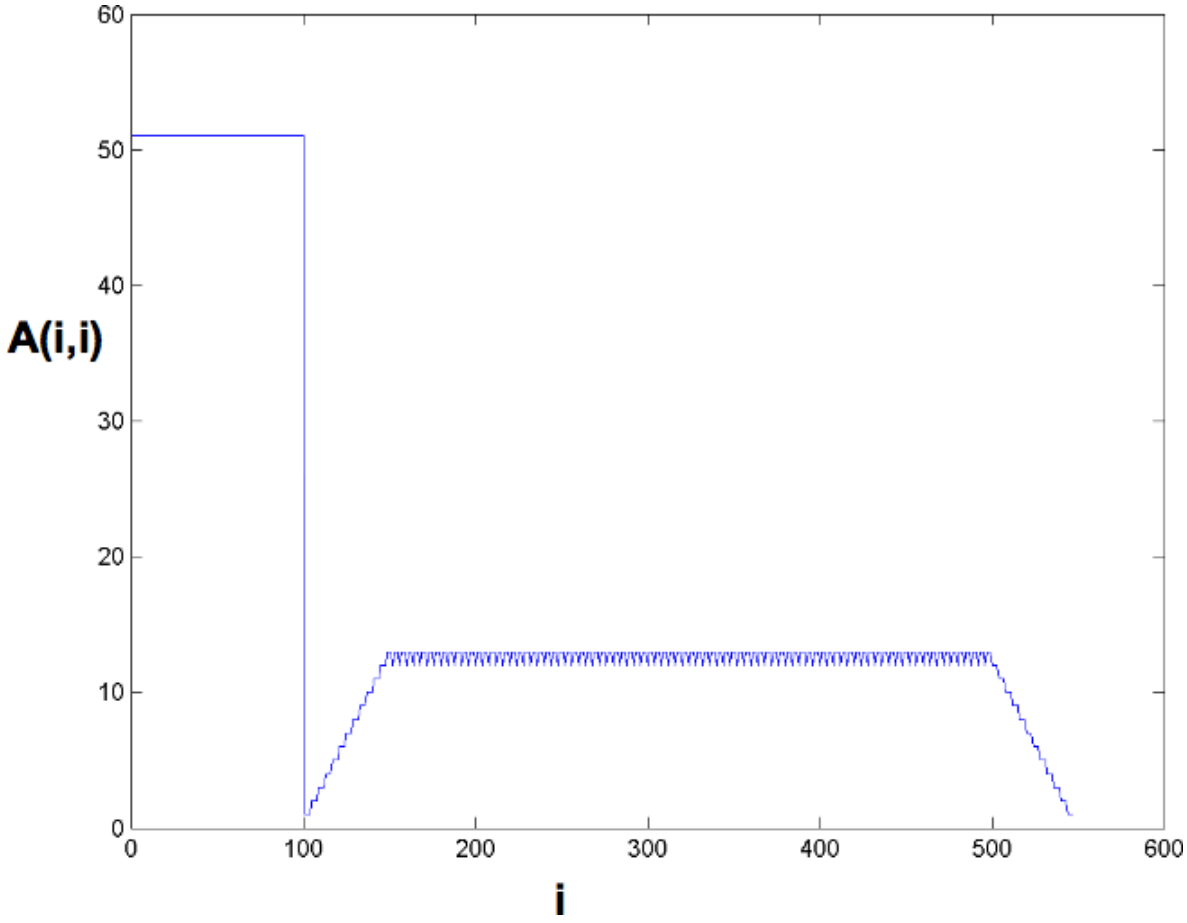

Figure 4.3: The main diagonal of the matrix $\mathbf{A}^T\mathbf{A}$. The first 100 unknowns are the shot unknowns. The first 100 values in the main diagonal are the fold for the shot gathers. The following values are the receiver fold, indicating for how many shots the receiver is live for.

equal to the number of shots for which that receiver is live. In Figure 4.3 the main diagonal of $\mathbf{A}^T\mathbf{A}$ is plotted. The receivers at either end of the survey have a lower fold than the receivers in the middle.

4.0.3 Four term solutions

Taner and Koehler (1981) recommend a four term surface consistent system be solved when correcting for surface consistent traveltime anomalies. Errors in velocity estimation and

normal moveout lead to offset consistent behaviour. The midpoint consistent term details the depth of the reflector across the survey in a midpoint stack.

Analogous to equation 4.1, each equation in the 4 term system takes the form of

$$t_{ijkl} = S_i + R_j + M_k + O_l. \tag{4.9}$$

Just as with the two term case, we assign new unknowns in the unknown vector $\mathbf{x}$, one for each offset and midpoint in the geometry of the survey.

$$\mathbf{As} = [\mathbf{A}_s|\mathbf{A}_r|\mathbf{A}_m|\mathbf{A}_o][\begin{smallmatrix}\mathbf{s}_s\\ \hline \mathbf{s}_r\\ \hline \mathbf{s}_m\\ \hline \mathbf{s}_o\end{smallmatrix}]. \tag{4.10}$$

The resulting matrix $\mathbf{A}$ is shown in Figure 4.4. The top left partition of the matrix, extending from indecies (1,1) to (547,547) is identical to the 2 term matrix for the same survey geometry. The midpoint and offset consistent terms each contribute another band of ones to the matrix. The main diagonal corresponding to the offset and midpoint bins equals the number of traces that contribute to the fold of the particular unknown.

The sample survey with 100 shots and 447 receivers has 843 midpoints, adding 843 midpoint consistent unknowns.

The offset term spawns the last 51 unknowns, and add the thick bands that comprise the bottom equations in the matrix, and the rightmost columns. It is also common to instead use the absolute value of the offset, reducing the number of offset consistent unknowns to 26 in this example.

By adding the midpoint and offset consistent terms the rank deficiency in the matrix changes from 1 in the two term case, to as many as about 10 % of the total number of unknowns in the 4 term case. The rank deficiency is influenced by the survey geometry, and

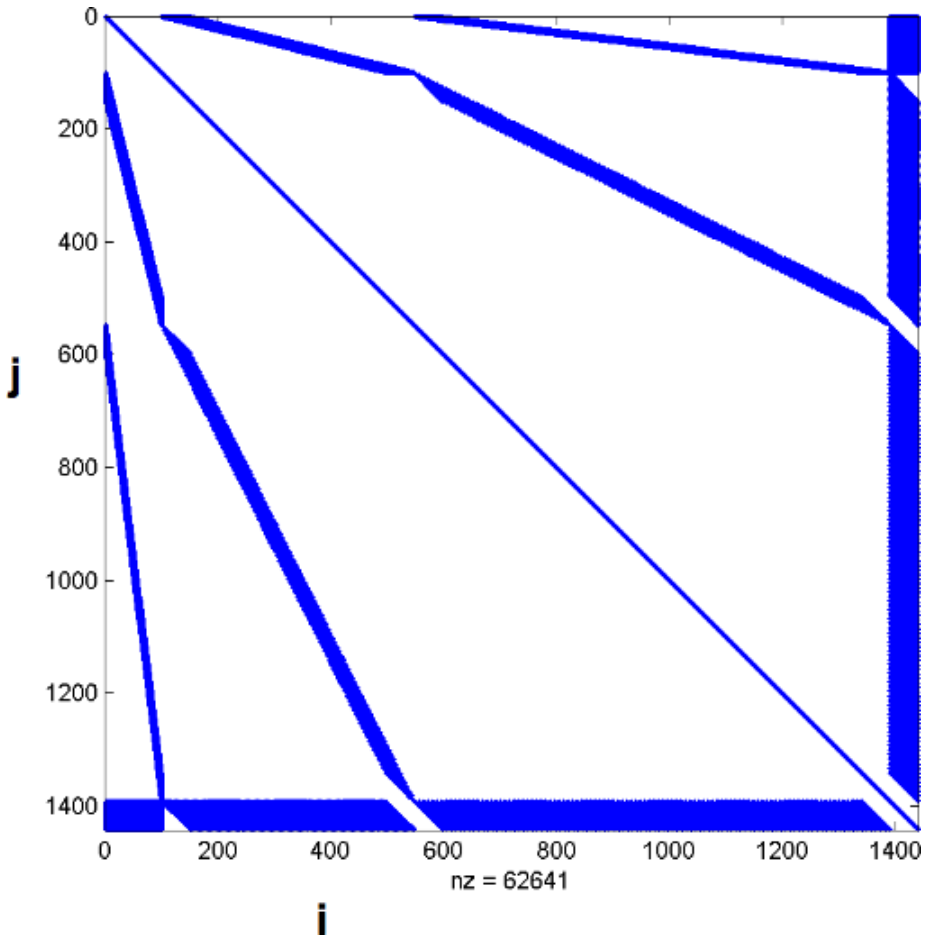

Figure 4.4: The non-zero entries in the four term matrix. The midpoint consistent terms adds the new diagonal bands from column 448 to 1390. The thick bands from index 1391 to 1441 are due to the offset term.

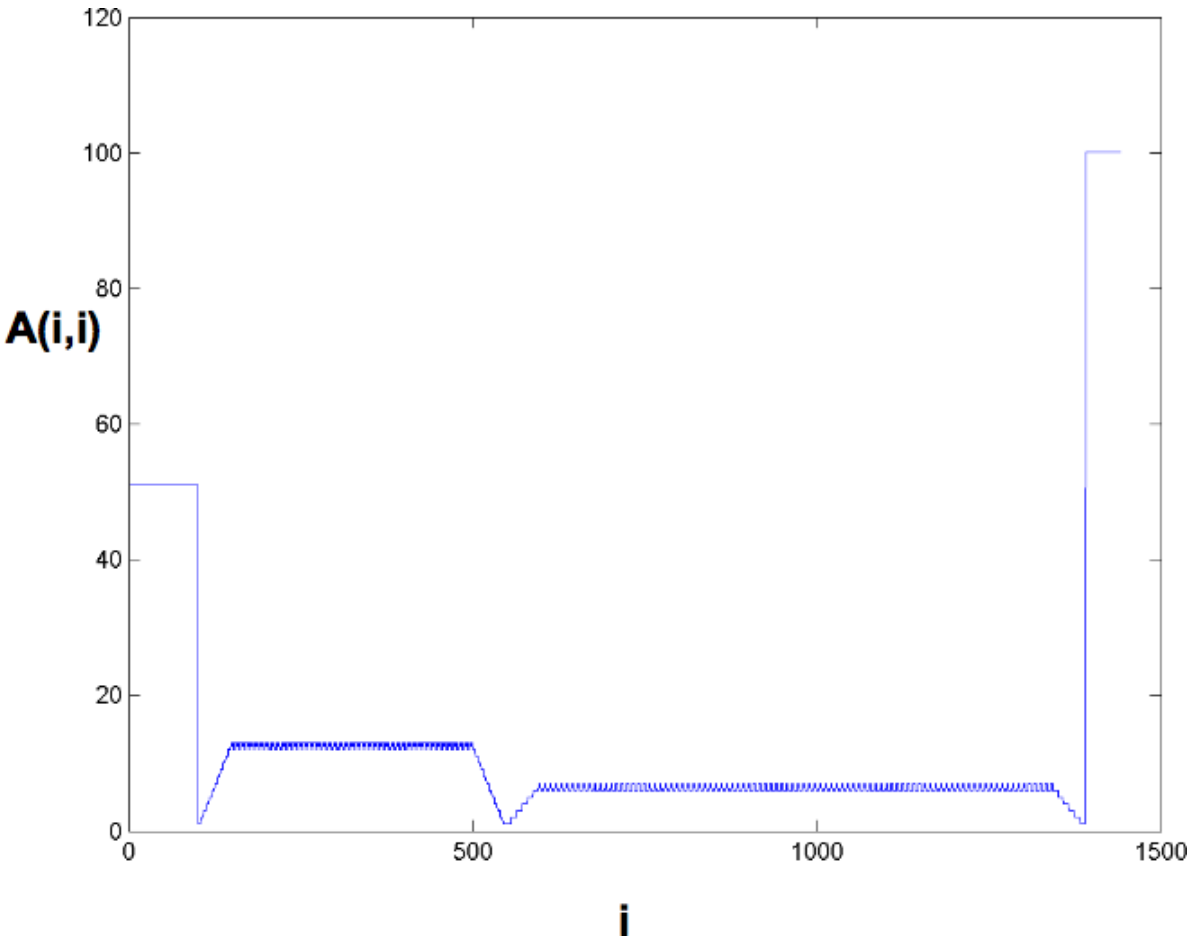

Figure 4.5: The main diagonal of the four term matrix is the value of the fold for that channel.

the way that ends of the survey are handled (the roll on). In our example problem, the rank deficiency is 27 out of 1441 unknowns. If we were to not use the offset consistent term, there would be 1390 unknowns and 14 singularities. If we were to not use the midpoint term there would be 598 unknowns with a rank deficiency of 6.

Adding singularities to the matrix is the same as adding degrees of freedom in the solution. In the two term case a single degree of freedom meant the solution was uncertain to within a constant, or very long wavelength errors. The higher order singularities result in an uncertainty that looks like a different higher order polynomial is superposed on each term of the solution. An analysis of this error is provided by Taner et al. (1974) and Taner and Koehler (1981), although the explanation provided differs slightly. The authors assume a rank deficiency of 3. This would be true if the offset and midpoint coordinates were totally independent of the source and receiver coordinates. This is not the case, the offset is the difference between the source and receiver coordinates, and the midpoint is the average. There are less independent equations in the system than is assumed by Taner and Koehler (1981).

Wiggins et al. (1976) recognized these instabilities, and suggested that we limit the number of Gauss-Seidel iterations we perform to avoid the long wavelength errors.

The singularities and instabilities in the 4 term case are handled the same way as in the two term case, by adding the stability factor in equation 4.8.

While the mute ensures that instabilities do not get out of control, there is a certain amount of error in the solution that we will not be able to resolve.

4.0.4 Amplitudes

Amplitude corrections are assumed to be a *product* of the four components (Taner and Koehler, 1981),

$$A_{ijkl} = S_i \times R_j \times M_k \times O_l. \tag{4.11}$$

To turn this into a linear system that we can solve, we take the logarithm of each side of equation 4.11,

$$\log(A_{ijkl}) = \log(S_i \times R_j \times M_k \times O_l), \tag{4.12}$$

$$\log(A_{ijkl}) = \log(S_i) + \log(R_j) + \log(M_k) + \log(O_l). \tag{4.13}$$

When we apply amplitude corrections, we design our operator using only the source and receiver components. The offset component is there because the surface noise is offset consistent, and we wish to project it into a separate channel. The reflection signature does not have an offset consistent component to it, so we purposefully leave the offset channel out of the operator design. If we use a two term solution, offset consistent noise will collect in the source and receiver terms, and lower the quality of our correction.

4.0.5 Deconvolution

Cary and Lorentz (1993) outline a method for using the surface consistent equations to derive deconvolution operators. To find deconvolution operators, we calculate the amplitude spectrum of each individual trace, and take the logarithm (equation 4.13). Each frequency

of the trace is used to calculate a separate source vector (t in equation 4.2). An iterative matrix method is used to find a solution ,s, at each frequency.

Regular trace by trace deconvolution uses the frequency content of each individual trace to design the inverse operator. For surface consistent deconvolution the reflection is assumed to have an amplitude spectrum that is the product of the source and receiver solution. For each trace in the seismic survey, we combine the the source signature with the receiver signature, and use that as the design trace.

For this study, Weiner-Levinson recursion is used to invert the design trace amplitude spectrum into the deconvolution operator. Details of this process can be found in Yilmaz and Doherty (1994), and is implemented using the CREWES matlab routine *deconw.m*. The recorded wavelet is assumed to be minimum phase. In production seismic processing, other wavelet shaping filters and phase calculations are applied to enhance the interpretability of the stack section. However, for the purposes of this paper, the amplitudes and phase was left as is after applying our surface consistent operators.

4.1 Surface consistent solutions

We previously demonstrated the Gauss-Seidel, conjugate gradient and multigrid methods, as applied to solving the Laplace's equation. The iterative estimate to the system of equations only resolve a part of the solution. There is a long wavelength error left, even after many iterations. A multigrid method is more able to correct the long wavelengths, giving us a more accurate solution.

In this section, we examine the relative ability of the iterative methods at resolving solutions to the surface consistent equations.

A simplified diagram of the model we are using is shown in Figure 4.6. The synthetic survey from the previous section with 100 shots, and 51 live receivers per record was used. Small perturbations in the elevation contribute to small static errors. The second half of the receivers are all subjected to a strong surface consistent anomaly. This can be seen looking at the red rays that emerge from the source. The signal from the receivers on the right hand side of the survey would be subject to a time delay.

An anomaly present in field data would be due to the seismic line crossing into an area with a sharp change in surficial geology. This could be a lake, a sand dune, or other surface low velocity feature.

Each source and receiver is assigned a value. The matrix $\mathbf{A}^T\mathbf{A}$ and the source term $\mathbf{A}^T\mathbf{t}$ are calculated using the survey geometry and the synthetic values calculated by our model displayed in Figure 4.6.

We solve equation 4.8 using the iterative methods discussed earlier, and compare the iterative solutions we find $\tilde{\mathbf{s}}$, to the original values computed directly from the known model. The true solution and the calculated estimates are displayed in Figures 4.8 and 4.7.

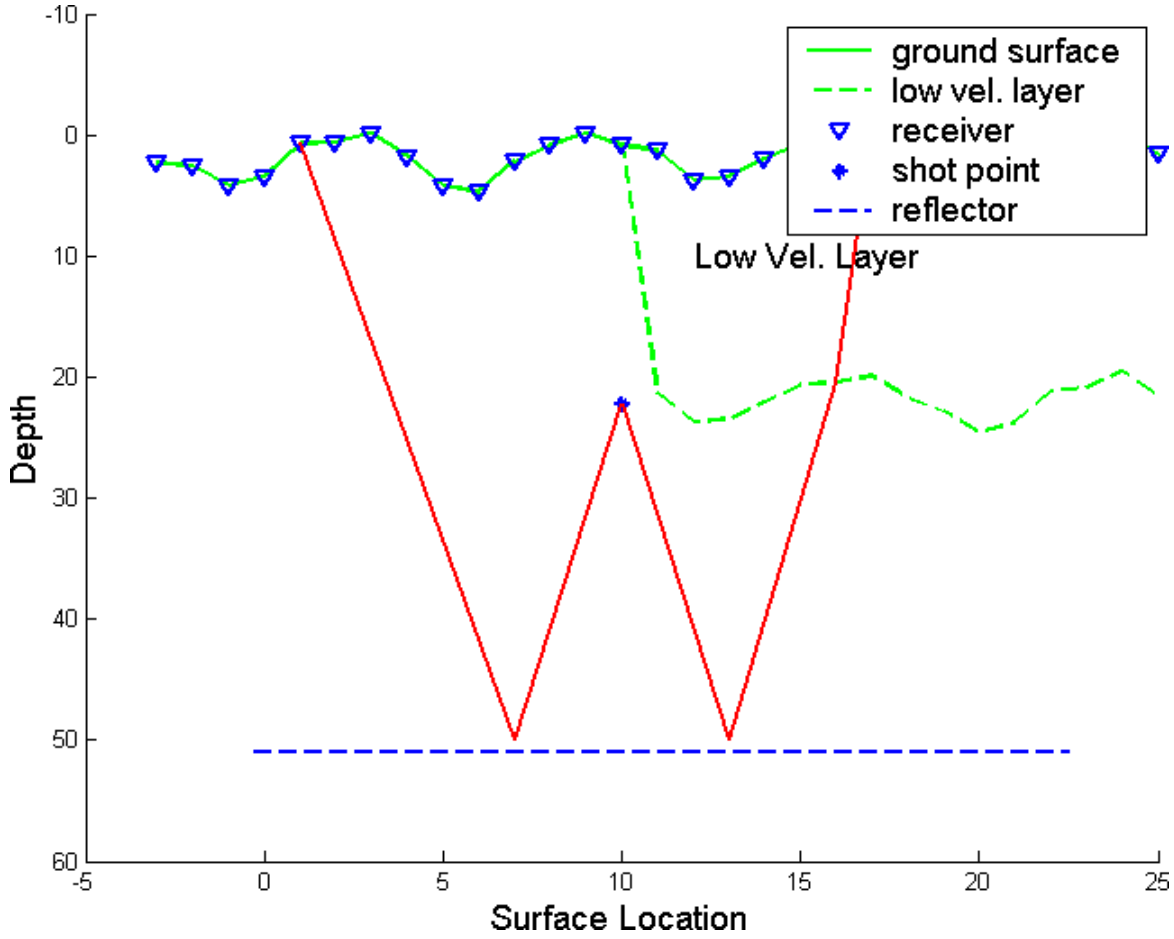

Figure 4.6: The synthetic surface consistent model we use to compare iterative procedures. A near surface low velocity layer causes a strong surface consistent anomaly in the receiver term.

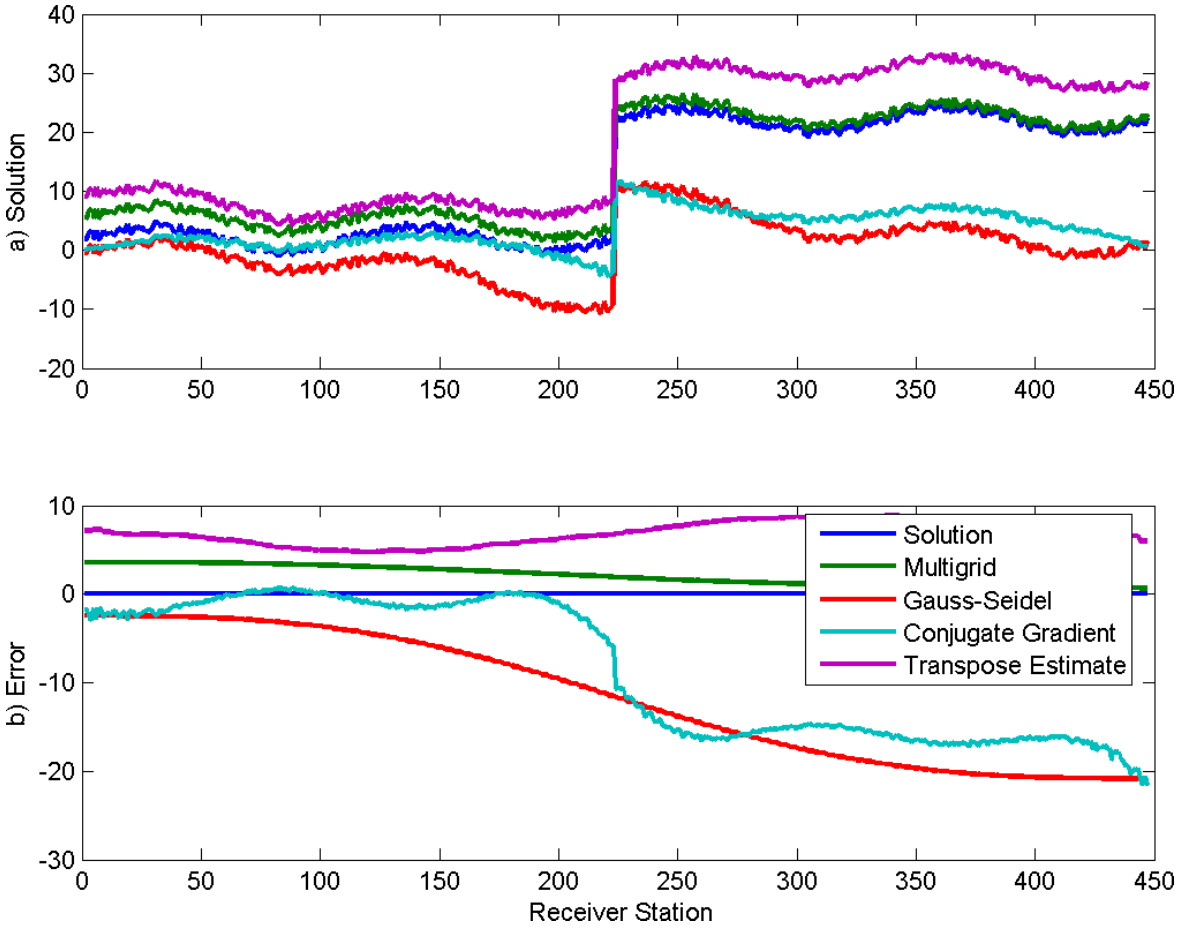

Figure 4.7: The solution and error in the receiver consistent term.

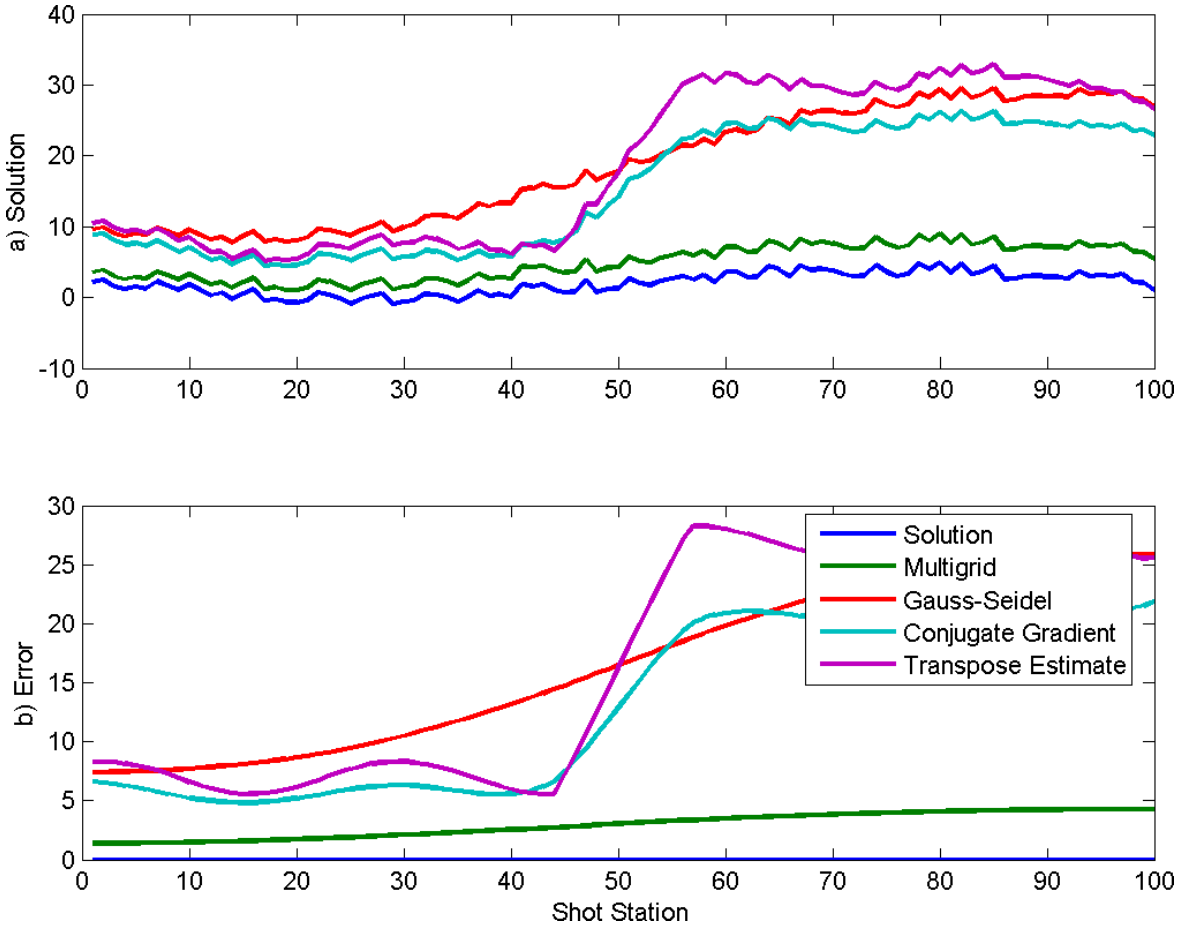

Figure 4.8: The solution and error in the source consistent term.

The transpose estimate of the receiver term (Figure 4.7) has relatively little error as compared with the Gauss-Seidel and other methods. Looking at the shot consistent error in Figure 4.8 we see that the transpose estimate has a much larger error than in the receiver consistent term, and larger error than the Gauss-Seidel or other methods. The error is concentrated in the shot consistent term.

The error in the transpose estimate is very smooth for both the shot and receiver consistent term. The reason the receiver term starts out relatively accurate is because there is no long wavelength changes in the shot consistent term.

The long wavelength error is concentrated in the receiver to start each iterative method. Subsequent iterations smooth the error out across the whole domain, into the shot consistent term. The error in the shot term slowly grows, as it is smoothed out of the receiver term. The shot and receiver errors seem to negatively reflect each other (a left to right mirror image).

The multigrid solution has a much lower error across the whole domain. The error has much less of the sigmoidal shape, but the errors appear to still negatively reflect each other.

We also solve the problem using the four term surface consistent equations. The midpoint and offset consistent terms were held constant in the model. This means any deviation from a constant value would be the error associated with the term.

The shot and receiver terms are very nearly identical to the two term solutions. The source and receiver consistent solutions can be seen in Figures 4.9 and 4.10. The midpoint and offset consistent terms are shown in Figure 4.11.

The multigrid midpoint consistent term has far more error in it than any of the other solution methods provide. The error is smooth, and is of a sinusoidal shape that spreads across the whole domain. The offset consistent terms calculated using each method all have

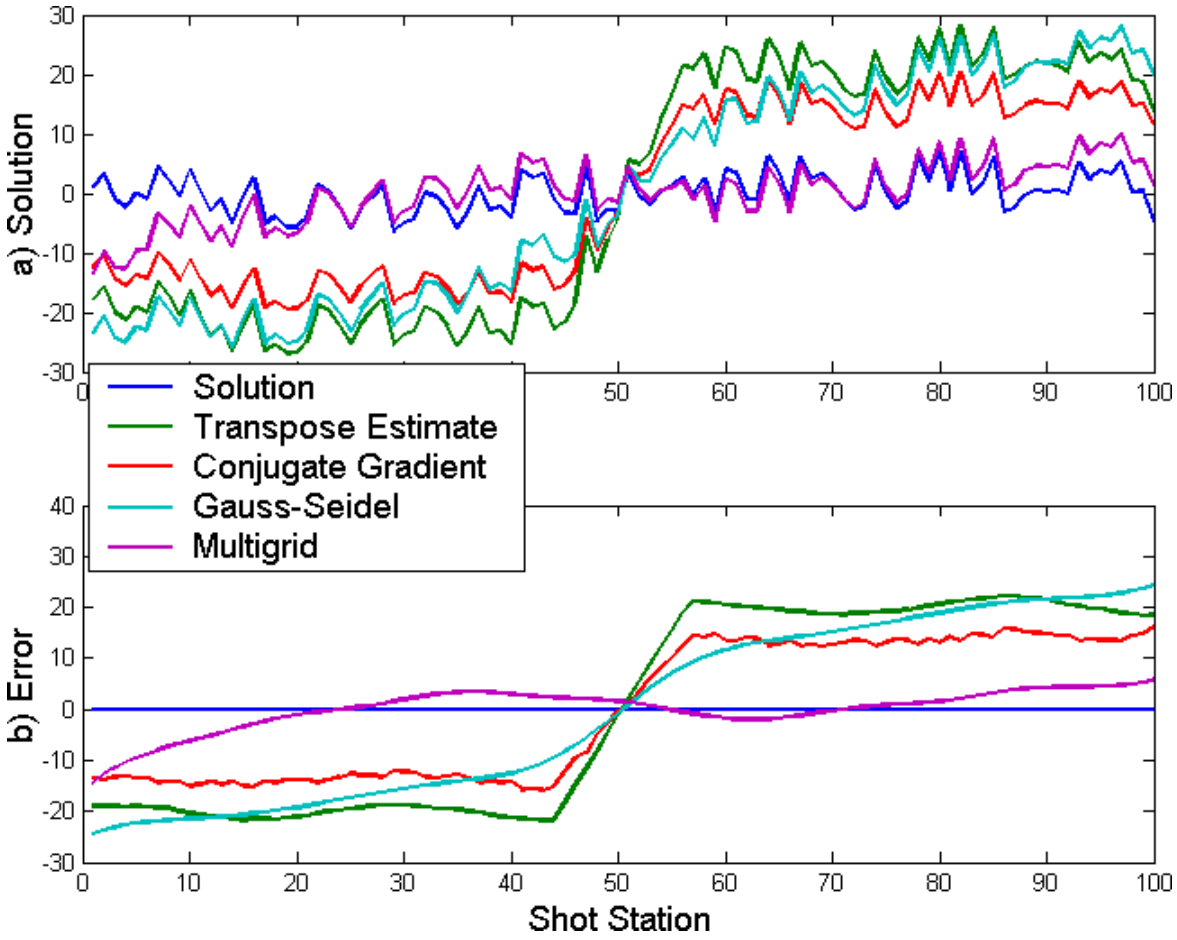

Figure 4.9: The solution and error in the source consistent term calculated using the four term surface consistent equations.

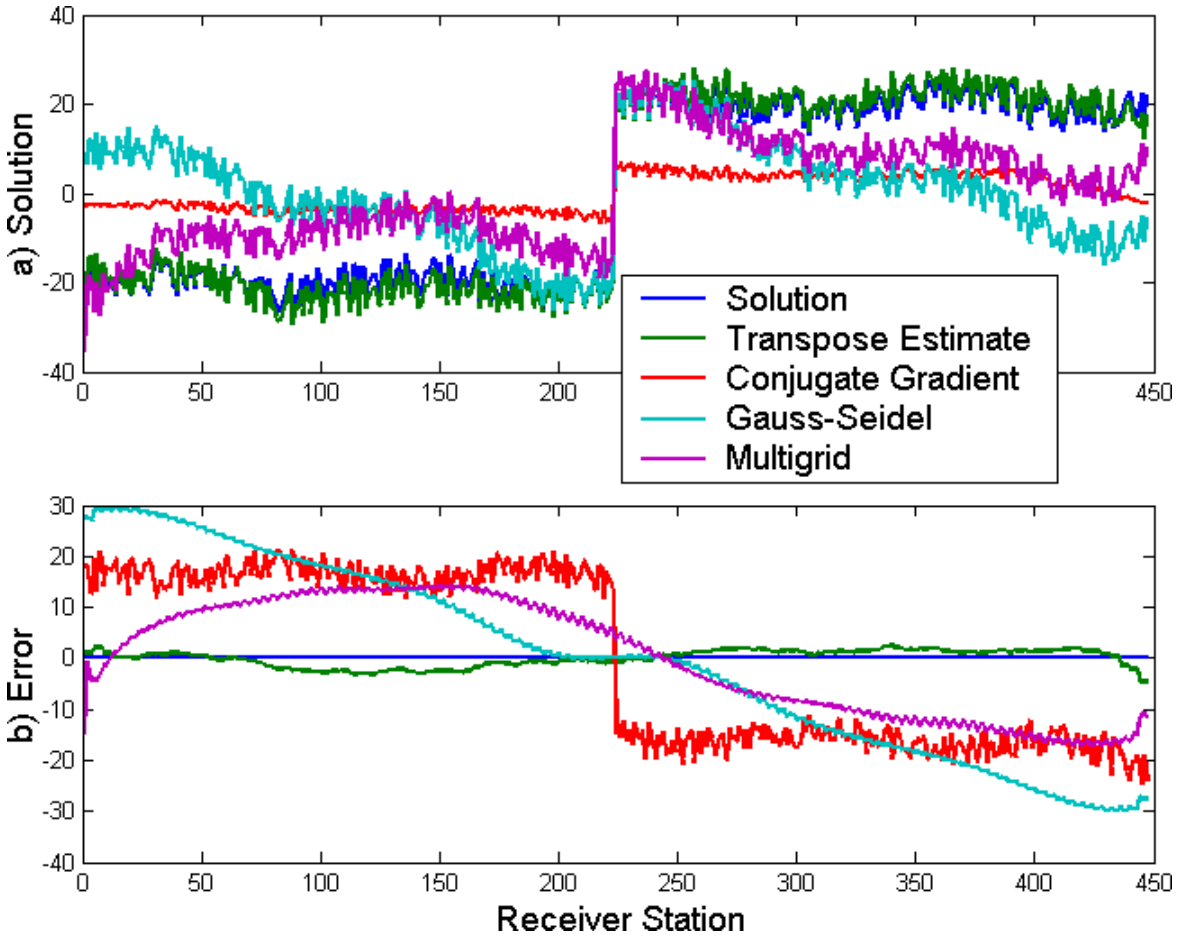

Figure 4.10: The solution and error in the receiver consistent term using the four term surface consistent equations.

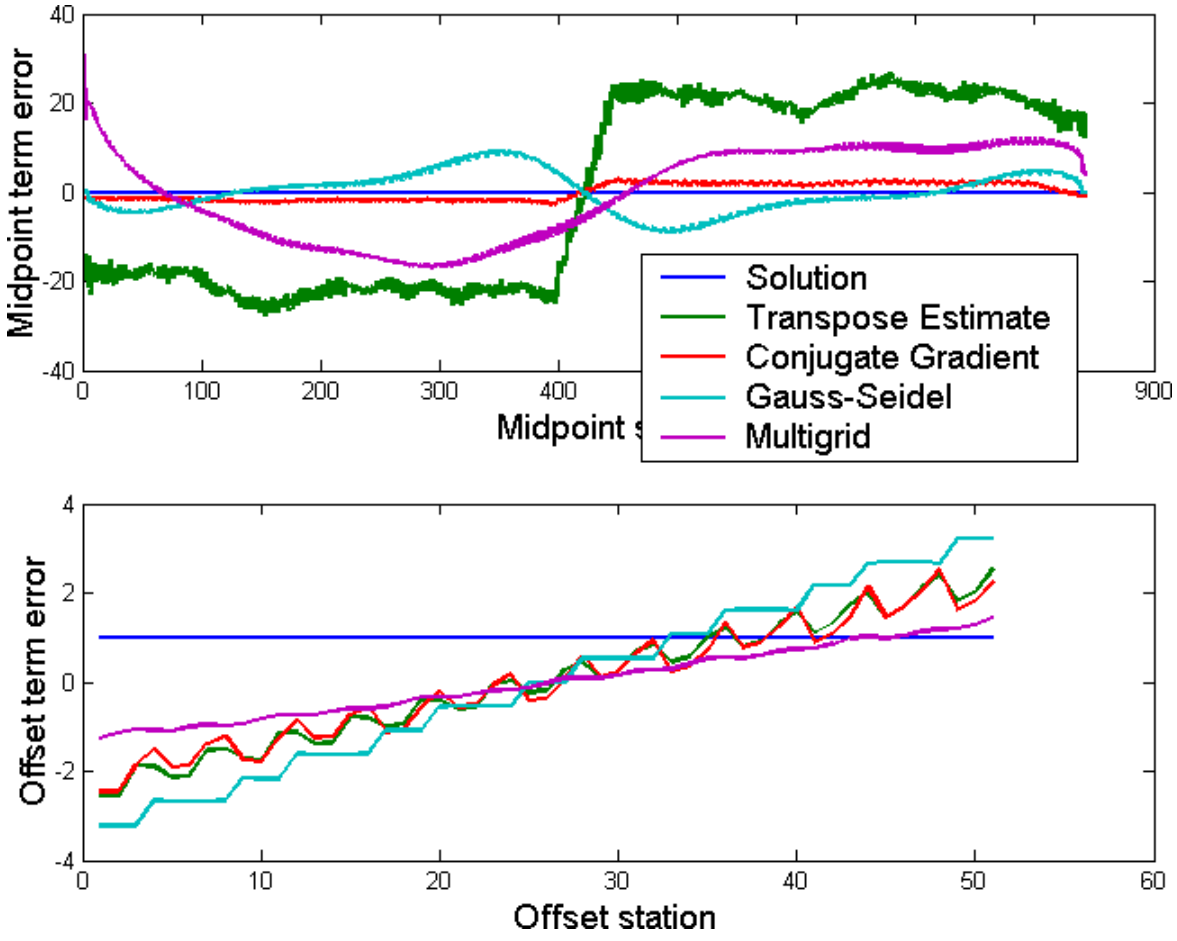

Figure 4.11: The midpoint and offset consistent error.

very similar errors.

Just as the error in the receiver consistent term was smoothed into the shot consistent term in the two term solution, the error in the four term solution is not necessarily reduced with each iteration, but spread across the 4 different terms. The multigrid method spreads the error across the 4 terms more evenly than the other methods. This conclusion is supported in the following section.

4.1.1 Spectral performance

Figure 4.12 plots both the source and receiver terms as a single vector $\mathbf{s}$, as opposed to plotting the source and receiver terms individually. This is done to highlight how the error migrates between the two terms.

The error after each iteration of the Gauss-Seidel methods is displayed in Figure 4.13. Each iteration smooths the error, the edges near the anomaly are progressively rounded off.

To examine the effect in the frequency domain, we find the Fourier amplitude spectrum of the Gauss-Seidel solution after each iteration. This is in Figure 4.14. The spectrum displayed here is low pass filtered before it is plotted, there are high amplitude rapid oscillations in the result that would otherwise obscure the main features of the figure.

The amplitude spectrum of the error after subsequent iterations does not change, all of the lines lie directly over top of each other. The smoothing out of the error visible in Figure 4.13 is not due to a reduction in the amplitude of the error, but a change in the phase of the Fourier components. After the first iteration of the Gauss-Seidel, further reductions in the magnitude of the error are not realized.

The blue line is the amplitude spectrum of the error for the all zero solution, before any corrections are made. The first iteration corrects the solution from the all zero estimate.

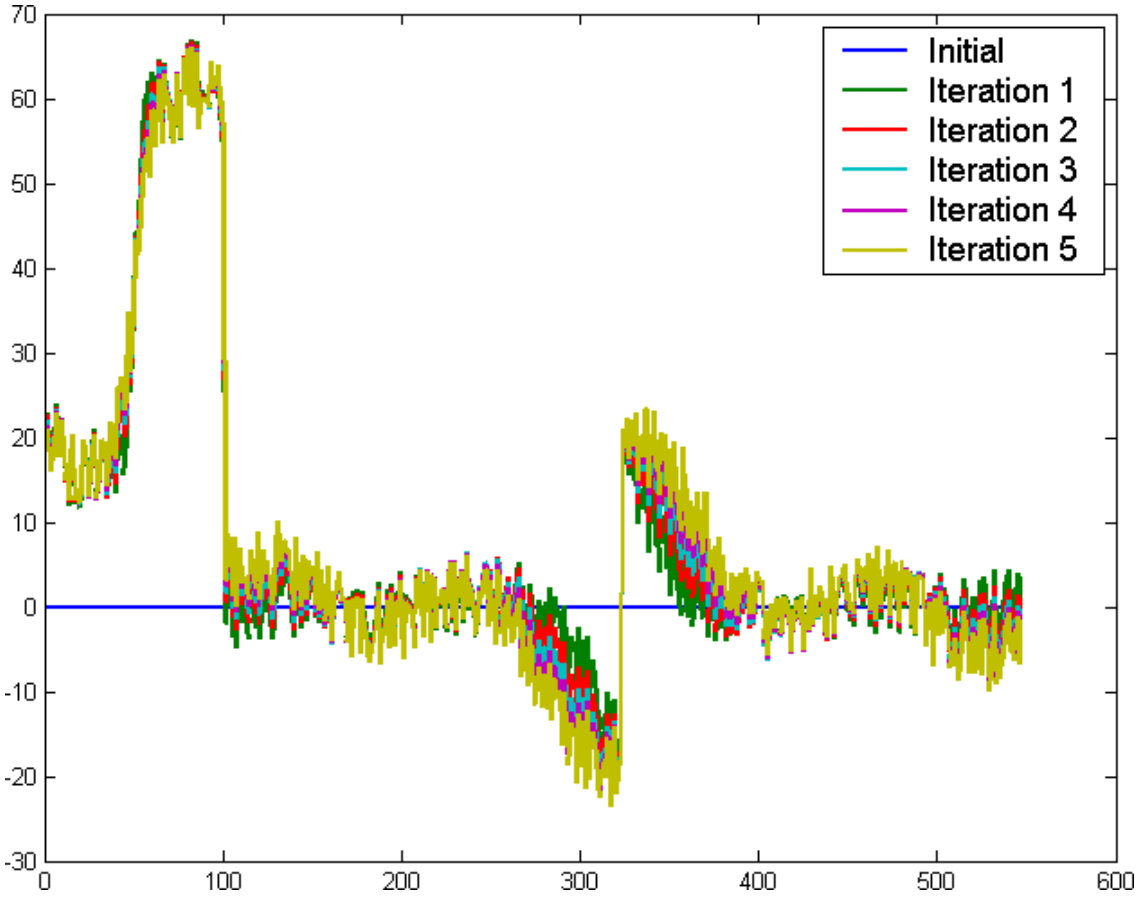

Figure 4.12: The solution as it evolves with each iteration of the Gauss-Seidel method, applied to the 4 term surface consistent equations

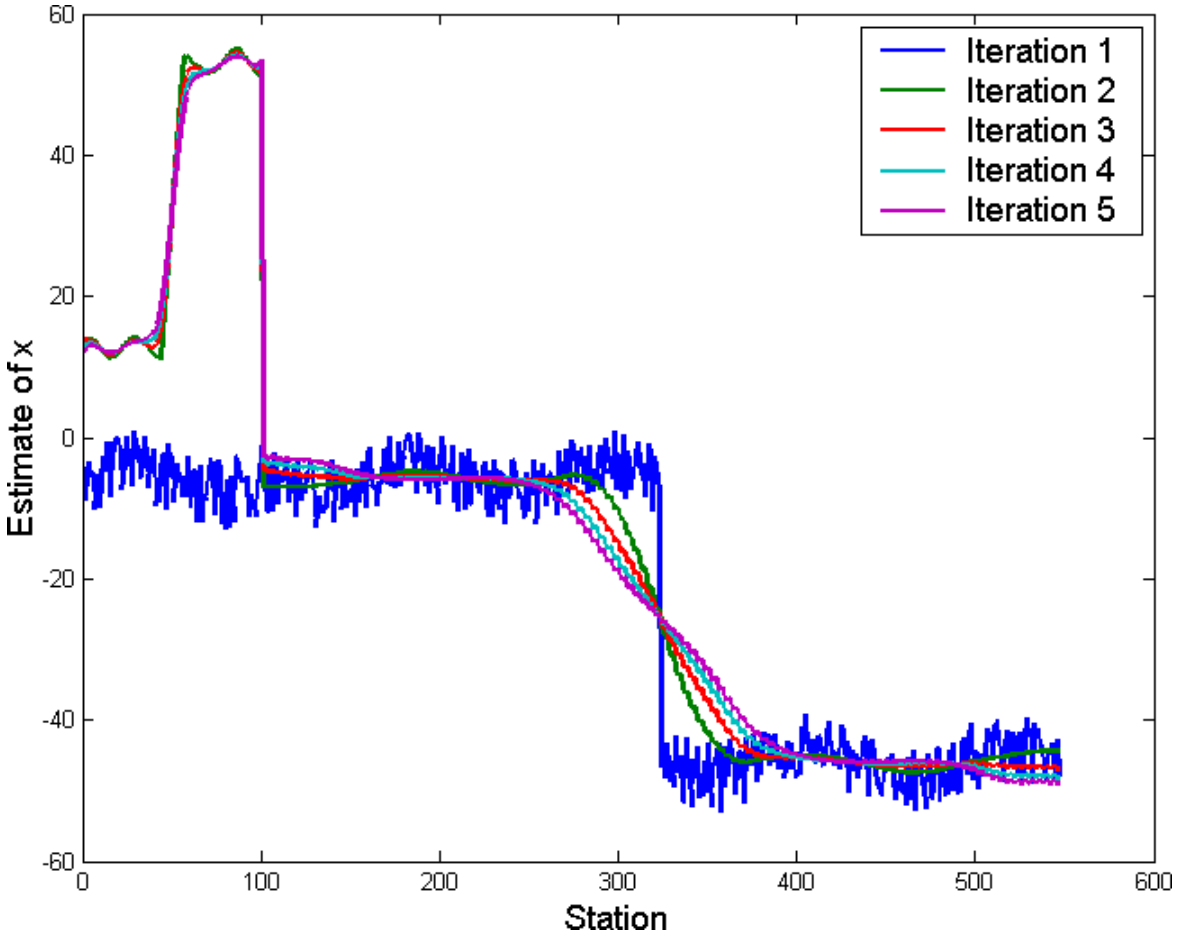

Figure 4.13: The error with each iteration of the Gauss-Seidel solution to the 4 term surface consistent equations. The first 100 stations are the shot unknowns, followed by the receiver unknowns.

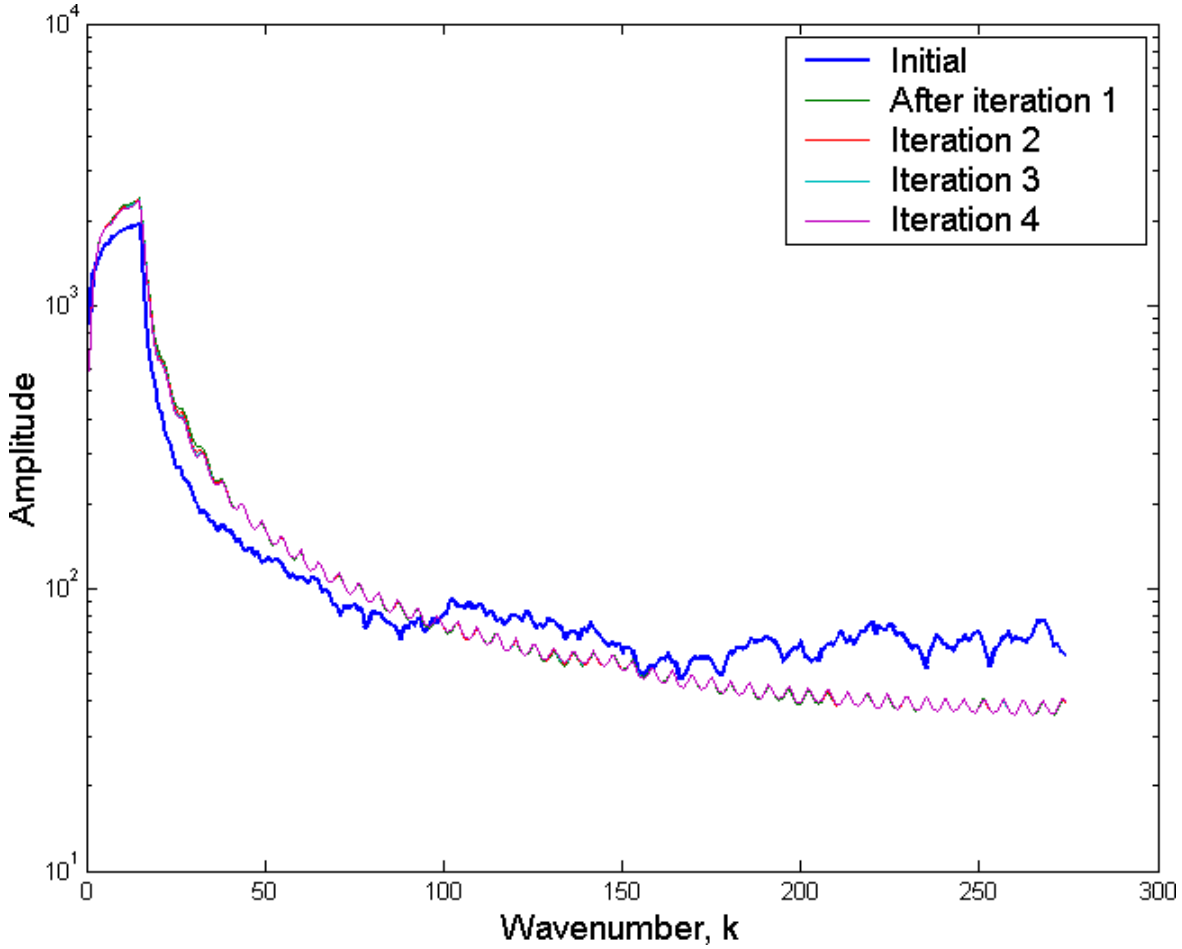

Figure 4.14: The amplitude spectrum of the error after subsequent iterations of the Gauss–Seidel operator.

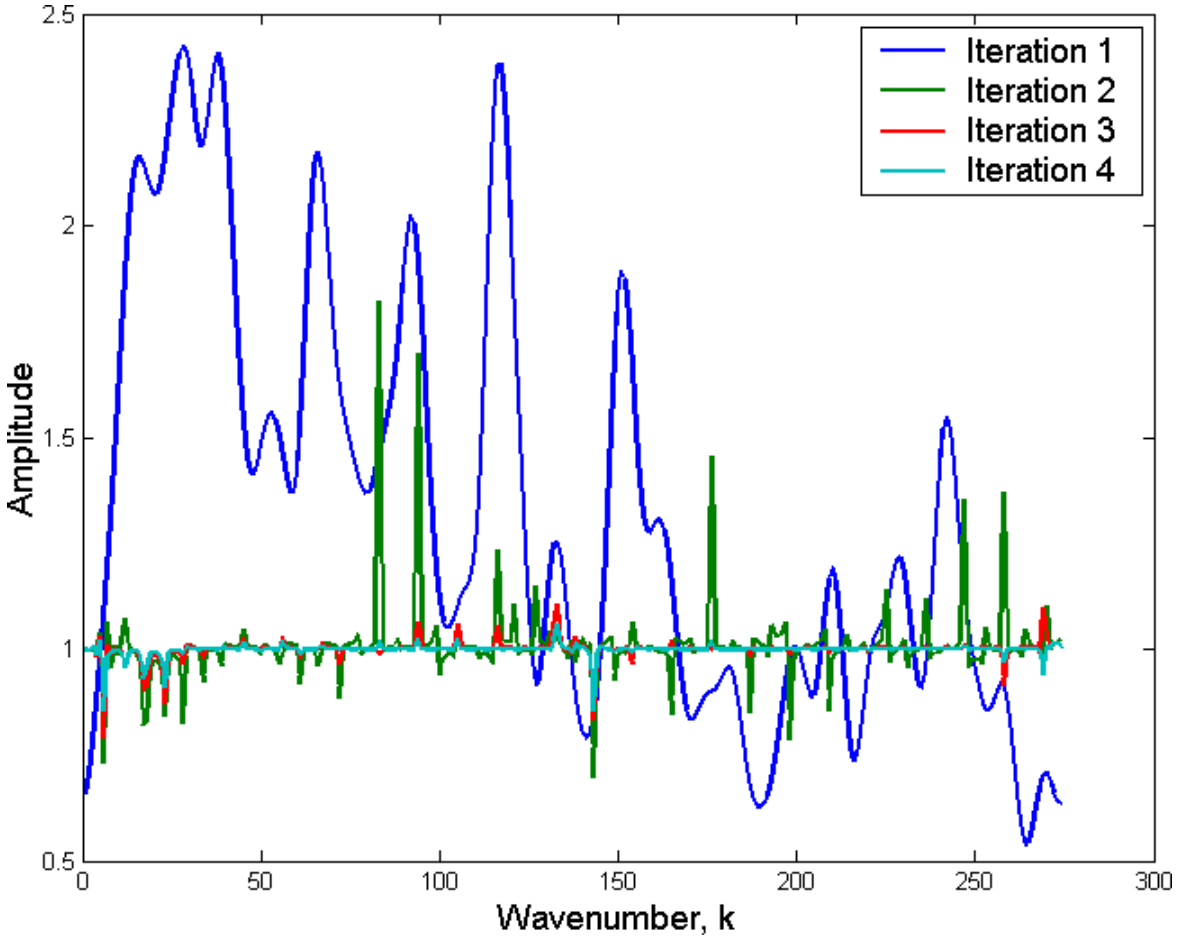

Figure 4.15: The change in the Fourier spectrum with each iteration of the Gauss-Seidel method.

The low frequency component of the error is amplified. Some intermediate frequencies are attenuated, as well as the high frequencies.

Figure 4.15 shows the change in spectrum with each pass of the Gauss-Seidel method. The first iteration has an erratic effect in the frequency domain. After the first iteration, the amplitude spectrum of the error does not change in a meaningful way.

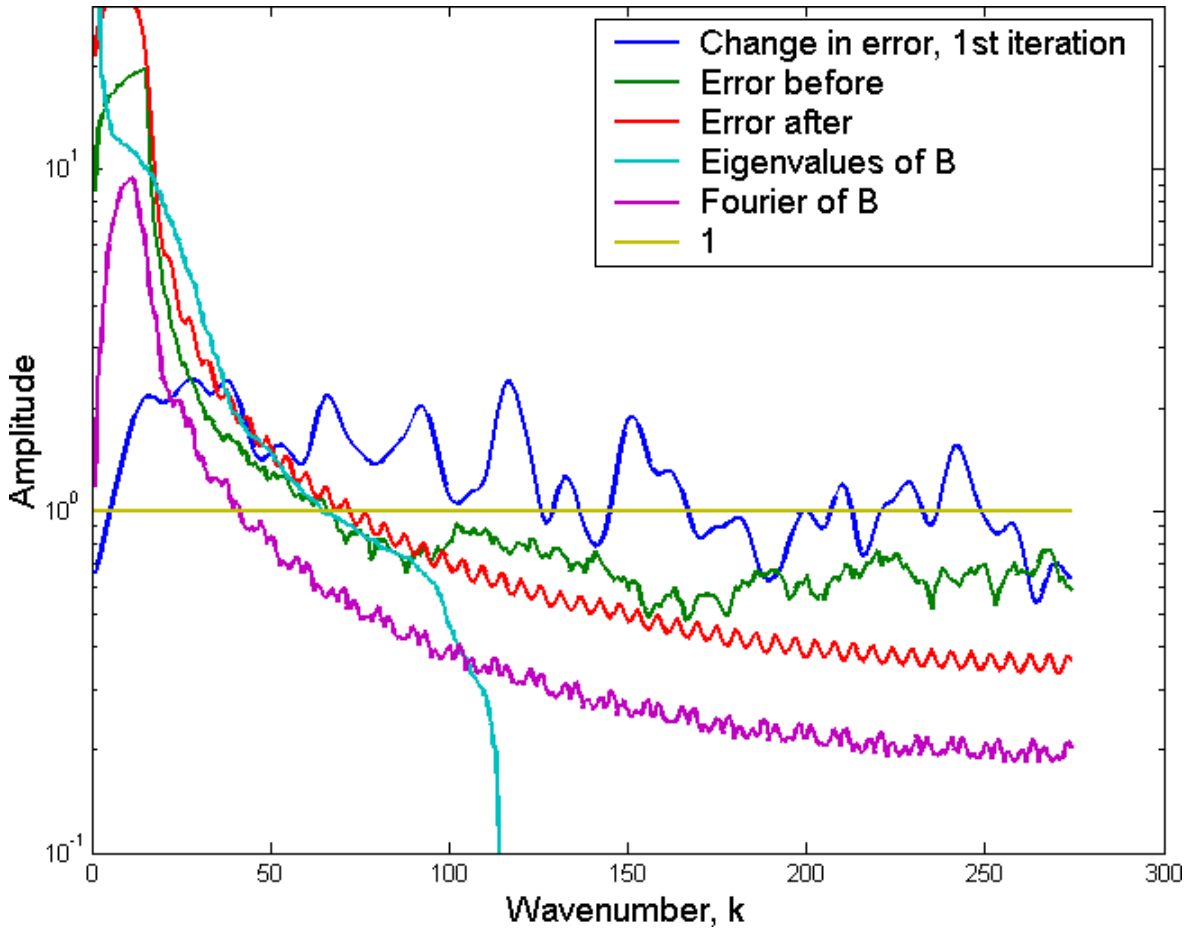

Figure 4.16: The theoretical change in amplitude spectrum calculated for the Gauss-Seidel method. The eigenvalue theoretical value is plotted against index, rather than wavenumber.

4.1.2 comparison with theoretical values

The theoretical performance of the Gauss-Seidel operator is displayed in Figure 4.16.

The eigenvalues calculated using equation 2.27 do not match the theoretical function calculated using the Fourier method. This is due to a fundamental difference between the surface consistent equations and our Laplaces equation example.

Shewchuk (2002) demonstrates that the eigenvalues of a 2-D geometry (like that of our sample problem) and its 2-D Fourier spectrum are equivalent. The surface consistent equations are not on a regular 2-D grid, so the calculating the eigenvalues of the matrix is not equivalent to finding the filter effect of the matrix.

In Figure 4.16, the eigenvalues of the Gauss Seidel operator are plotted in turquoise. The line starts above the scale of the plot at 10^3, quickly dropping down and leveling off at 10^1. It then continues falling until it is below the scale of the plot, where it drops right to 10^{-13} by index 150.

The most significant eigenvectors are being amplified extremely strongly with each iteration. The size of the less significant eigenvectors rolls off quickly. The components of the solution beyond index 120 are resolved very accurately by the first iteration.

The predicted change in the Fourier spectrum of the solution with each Gauss Seidel iteration is plotted in Figure 4.16 as a magenta line. It starts close to 10^0, jumps to 10^1 then falls rapidly. As the wavenumber increases it begins to fall less and less rapidly until it reaches a value just below $10^{-0.7}$ at the maximum.

The error spectrum before (all zero estimate) and after the first iteration is plotted in green and red in Figure 4.16. The actual effect of the first Gauss Seidel iteration is plotted in blue. It appears to have a downward trend with increasing wavenumber. The amplification

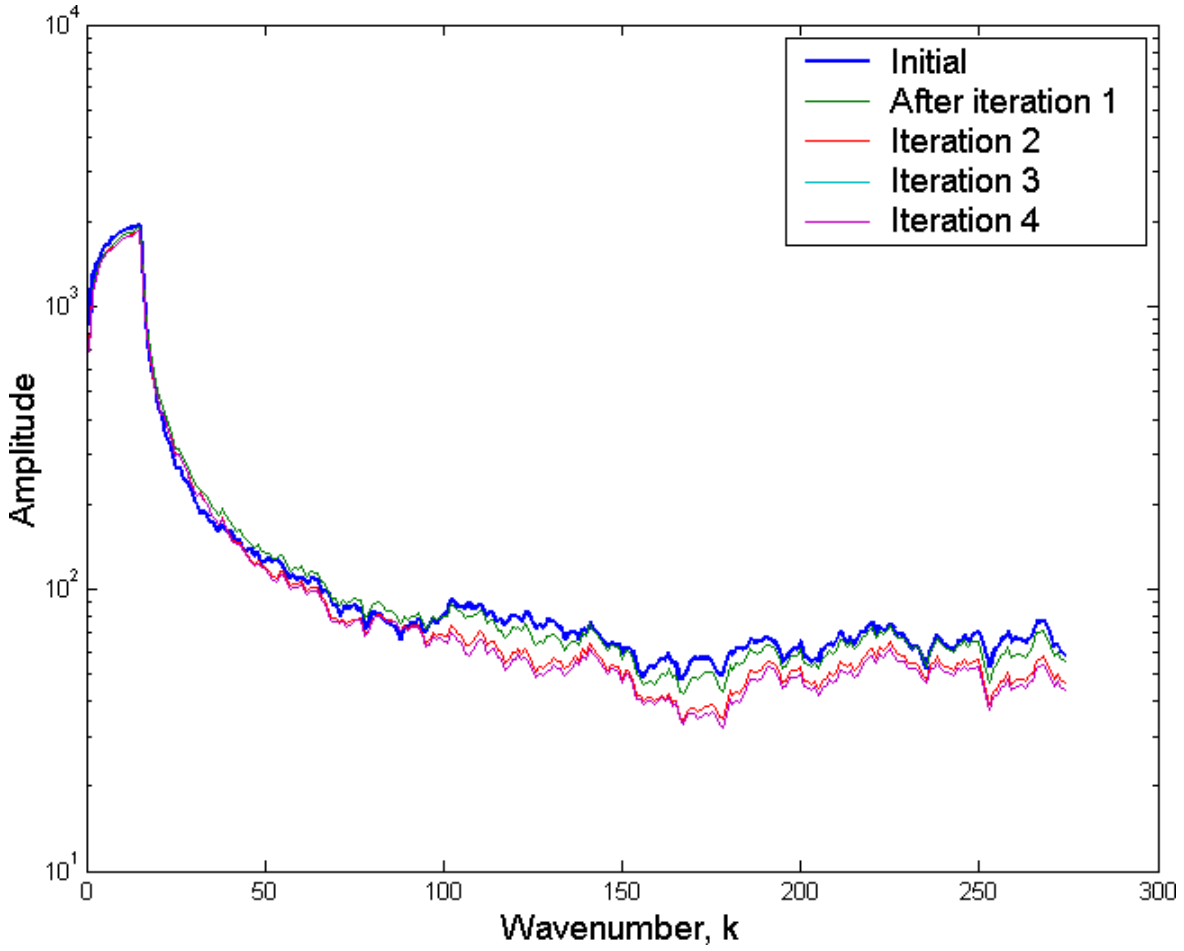

Figure 4.17: The amplitude spectrum of the error after subsequent iterations of the conjugate gradient operator.

of the low frequencies and the attenuation of the high frequencies is less than predicted.

The Fourier spectrum of the error after each iteration of the conjugate gradient operator is shown in Figure 4.17 . The effect of each individual iteration is shown in Figure 4.18. The magnitude of the error is slightly reduced with each iteration.

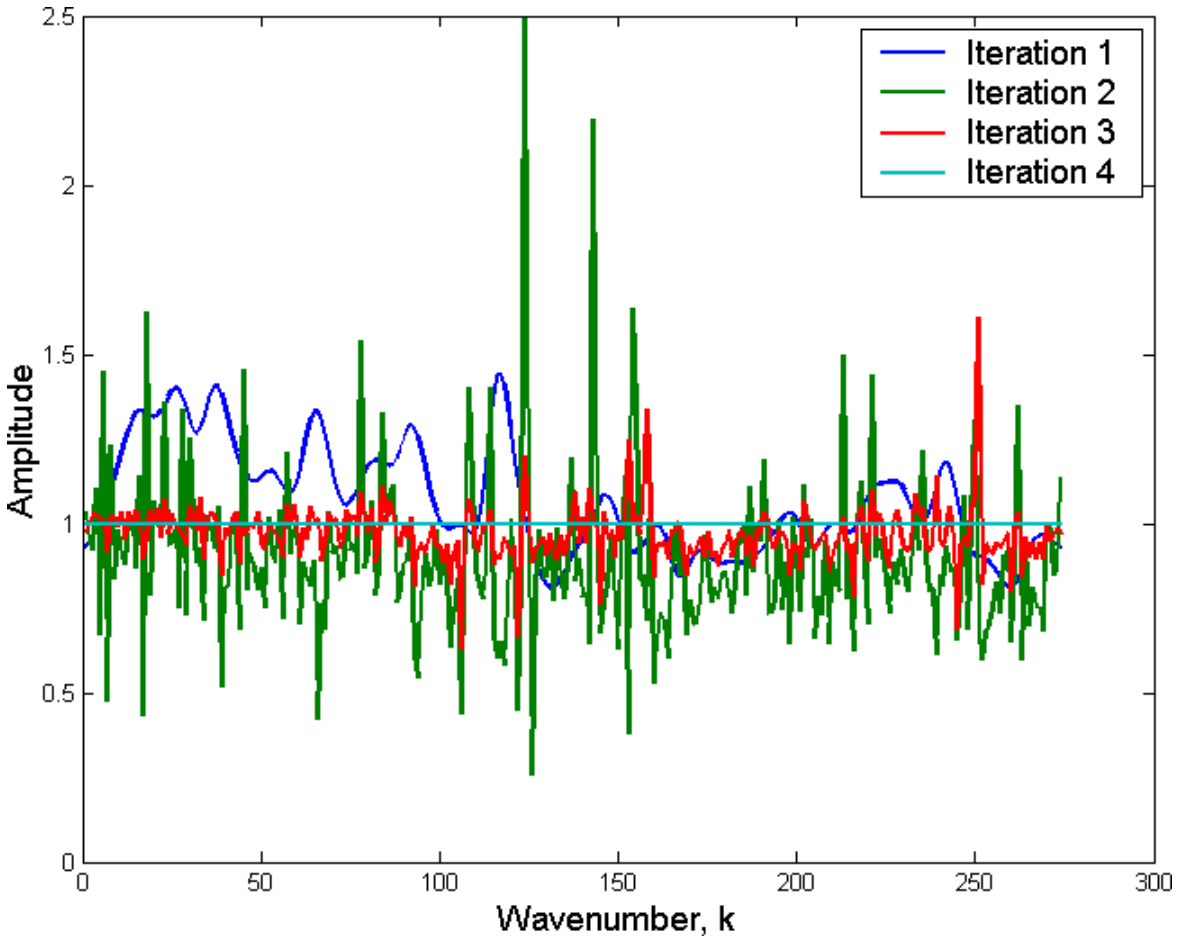

Figure 4.18: The change in the Fourier spectrum with each iteration of the conjugate gradient method.

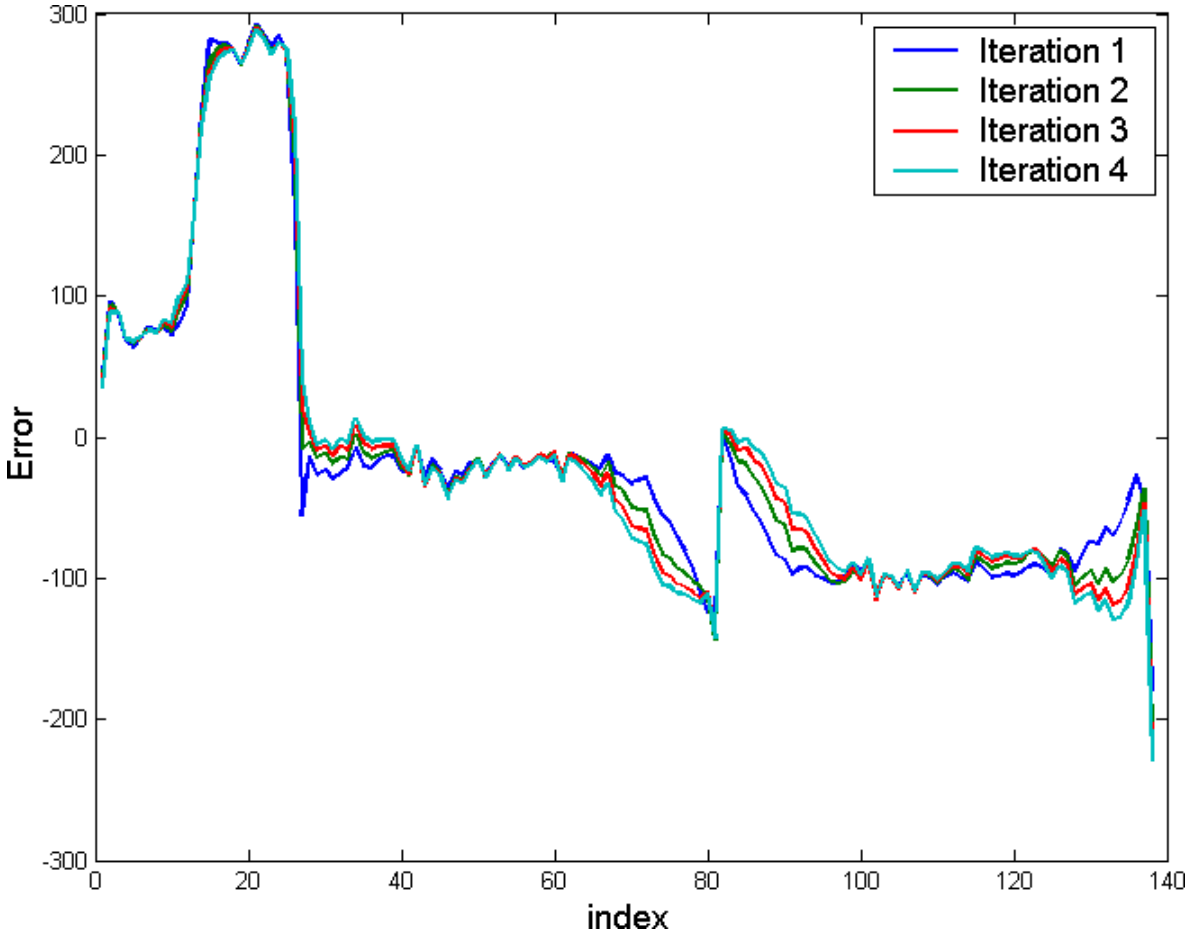

Figure 4.19: The first 4 iterations of the Gauss-Seidel solution to the restricted 4 term surface consistent equations.

4.1.3 The restricted equations

Here we apply the Gauss-Seidel method to a restricted set of equations, with the solutions presented in Figure 4.19. The solution can be seen to be evolving in a similar way to the full resolution Gauss Seidel.

The Fourier spectrum of the solution after each iteration on the reduced grid is in Figure 4.20. They are plotted next to the Fourier theoretical in magenta.

The restricted system behaves similarly to the full resolution system. The coarsening

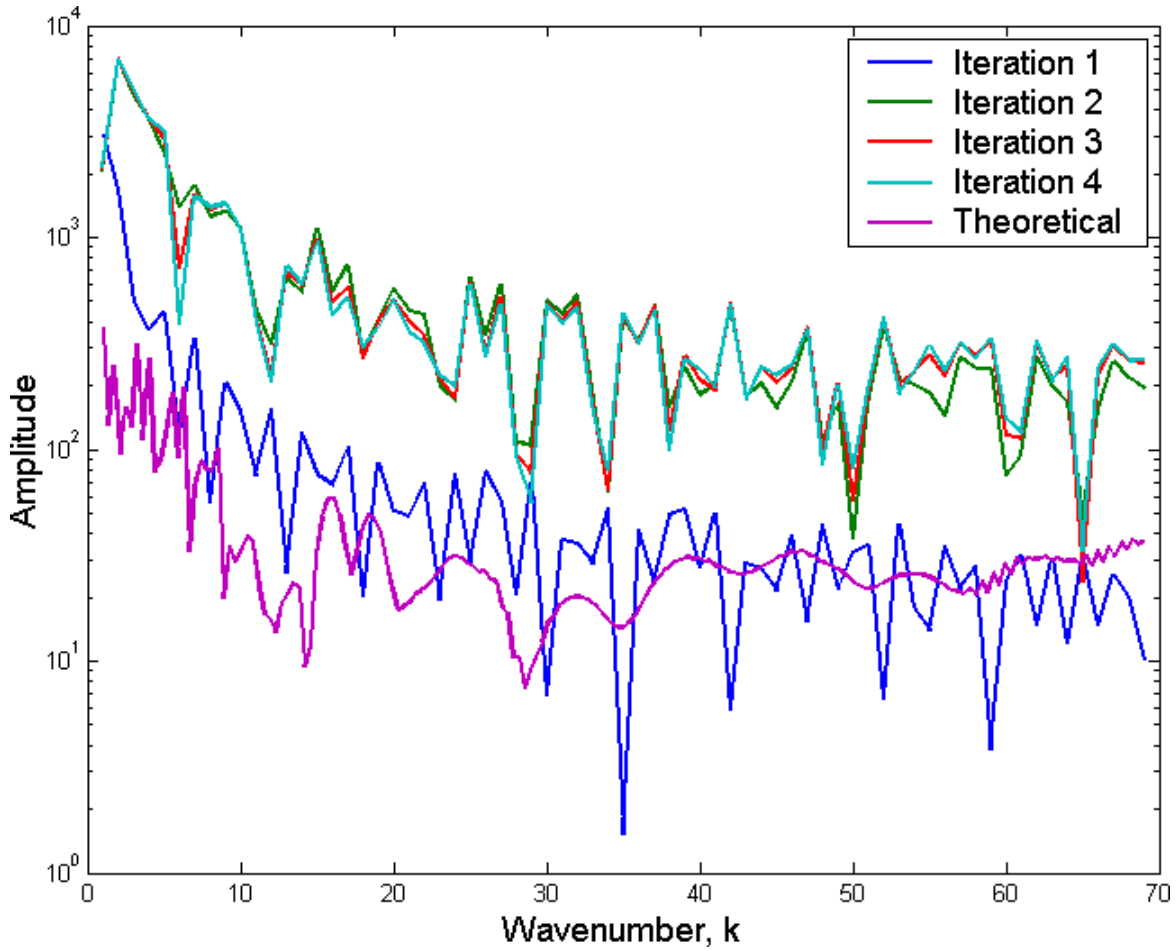

Figure 4.20: The amplitude spectrum of the error after subsequent iterations of the Gauss–Seidel operator on the restricted system. The Fourier theoretical values predict the effect of the operator in the frequency domain.

of the grid has increased the effectiveness of the smoother. The unstable initial estimate remains a problem. Gauss Seidel and conjugate gradient are only able to smooth errors away, not easily reduce their magnitude. To reduce the magnitude of the error we need to move the anomaly from the source term back to the receiver term where it belongs.

When making a multigrid correction that downsamples the problem to 5 unknowns, the Gauss Seidel operator is able to move the anomaly between channels, resulting in a much lower overall error. Figure 4.21 shows the multigrid solution after 20 iterations having an order of magnitude less error across most of the spectrum than any of the other methods.

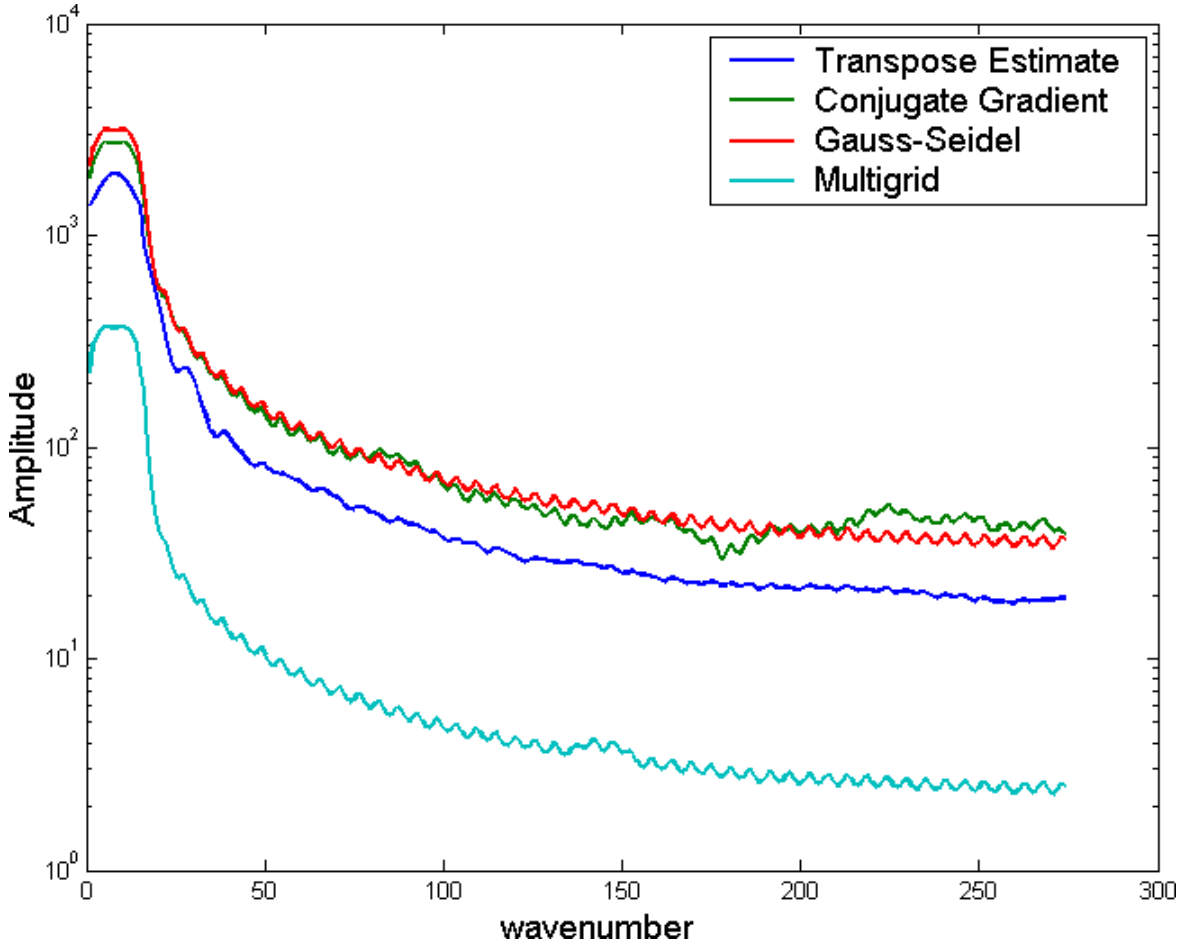

Figure 4.21: The Fourier transform of the error after 20 iterations.

4.1.4 Calculation time

The sum of the square of the residual ($\delta^T\delta$) is plotted versus calculation time for the Gauss-Seidel and multigrid methods in Figure 4.22. The residual is related to the error via equation 2.6. For singular matrices, the error can be growing while the residual is decreasing.

The line corresponding to the multigrid method is not shown for the parts of the calculation where the operator is working on a reduced grid. For this example the multigrid solution is not available until after approximately 15 Gauss-Seidel iterations. After the amount of time it takes to perform 20 iterations, the multigrid method has an order of magnitude less residual.

The conjugate gradient method does not seem to reduce the residual according to this measure after the first iteration. The method typically fails once it reaches a saddle point in the quadratic form (Shewchuk (2002)).

Typical default values for the number of Gauss-Seidel iterations in a commercial seismic data processing package range from 5-10. Using a multigrid method does therefore require about triple the amount of time that is typically spent on a surface consistent solution. When compared to the total computer time spent on the processing flow, the increase in calculation time is very small.

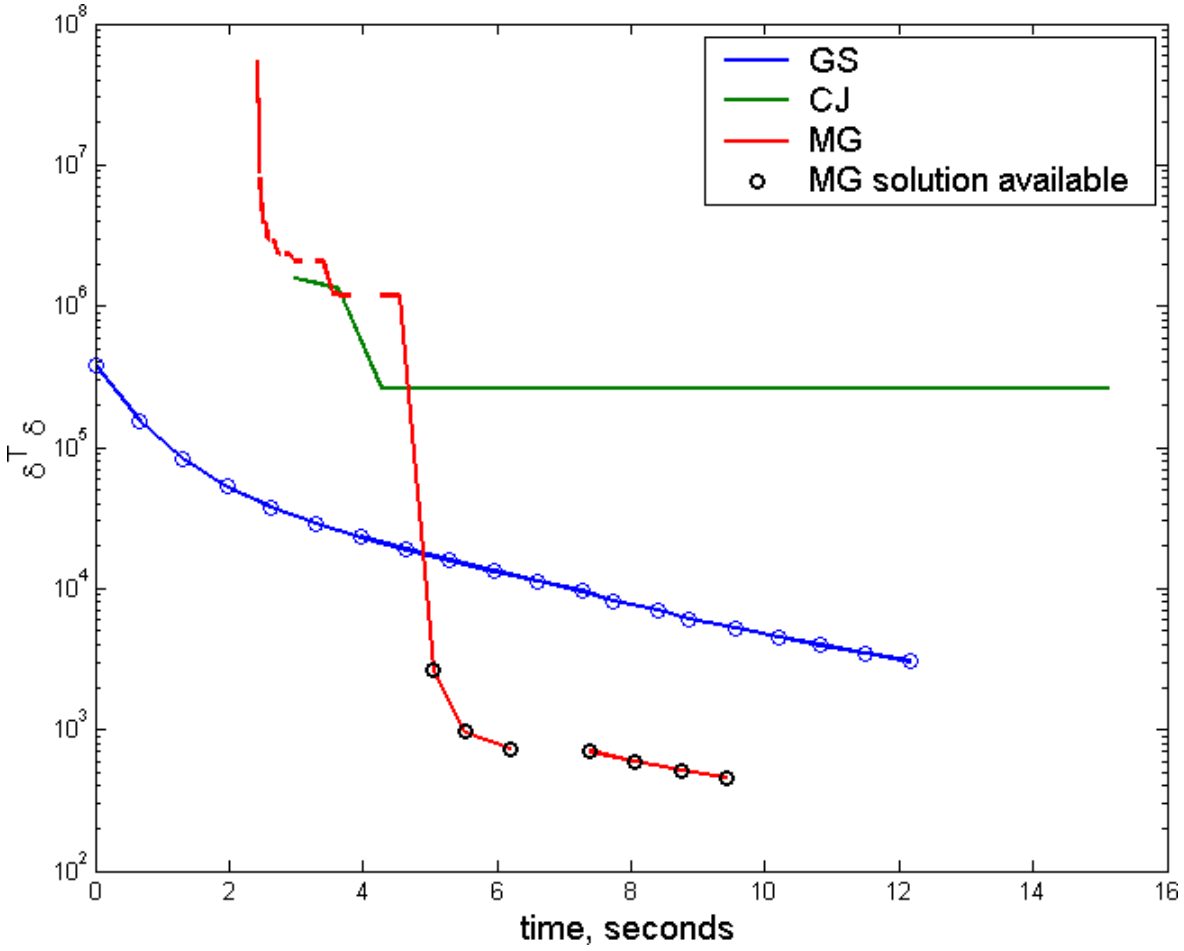

Figure 4.22: The sum of the residual squared plotted versus time.

4.2 Application to statics

In this section we demonstrate how the errors in our Gauss-Seidel and other methods show up in an example using synthetic seismic data.

We use the same model as the one shown in the last section. A strong surface consistent anomaly is present in the receiver term. The anomaly is a 40 millisecond static applied only to receivers.

This synthetic example assumes that we have picked the statics perfectly. A procedure such as an autocorrelation will likely make some erroneous picks on the data due to noise. These errors are considered to not exist in the example. The only error present is that due to the solution method. The true solution will produce a reflector with all of the wavelets lined up in a straight line.

The model is calculated by finding the static shift for each trace from the model. Each trace is shifted first by the value associated with its source, then by the value associated with its receiver. Each trace by trace value is stored in the vector $\mathbf{t}$. The matrix $\mathbf{A}$ is calculated from the survey geometry.

Once $\mathbf{A}^T\mathbf{A}$ and $\mathbf{A}^T\mathbf{t}$ are calculated using equation 4.8, we use a variety of different methods to estimate the solution $\mathbf{s}$. The different iterative methods each provide an estimate of the source and receiver consistent static from $\mathbf{A}^T\mathbf{t}$. Each trace is shifted again by its calculated source and receiver consistent static. The results are assembled into a midpoint stack section.

The stacked synthetic seismic sections calculated using a two term surface consistent inversion are presented in Figure 4.23. The stacked synthetic seismic sections calculated using a four term surface consistent inversion are presented in Figure 4.24.

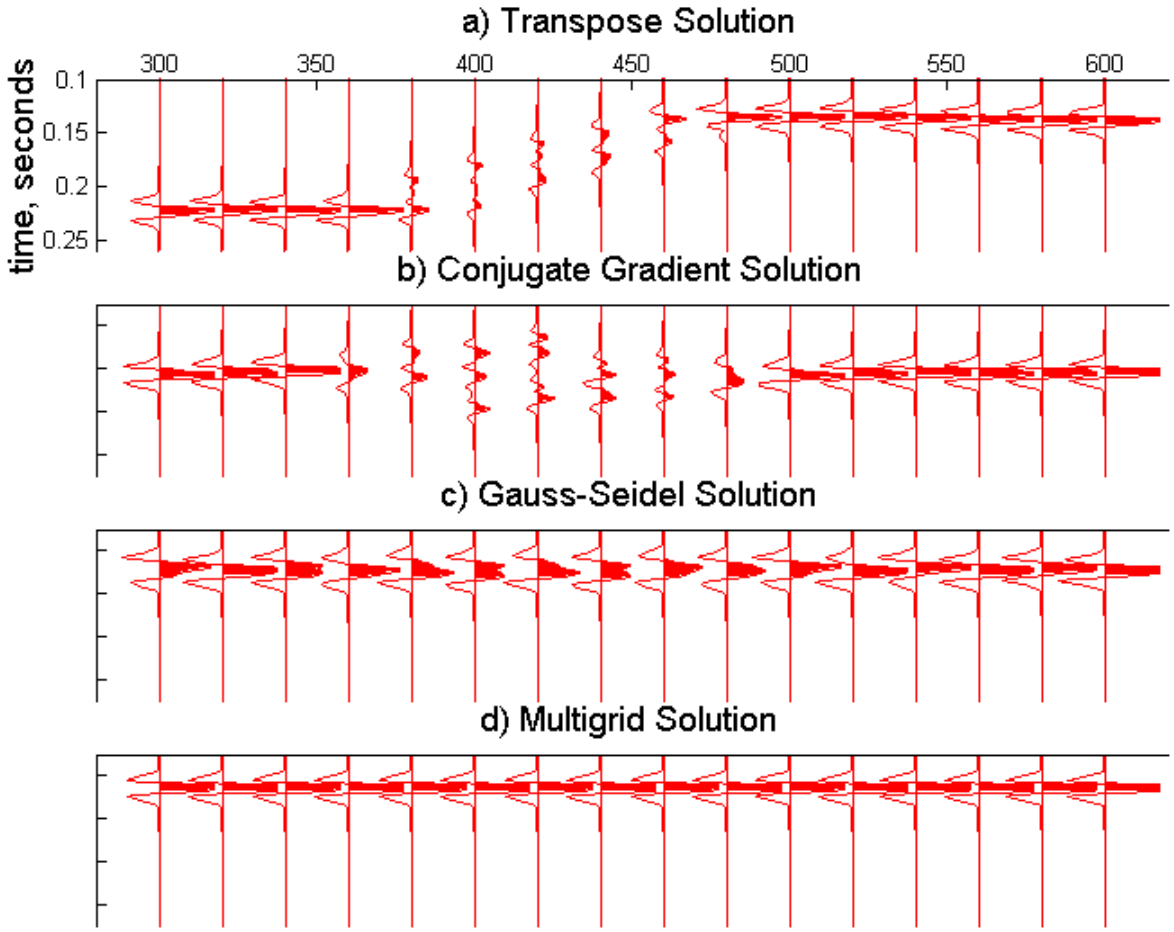

Figure 4.23: A synthetic stacked seismic section showing the results of using different iterative methods to solve a 2 term surface consistent static solution.

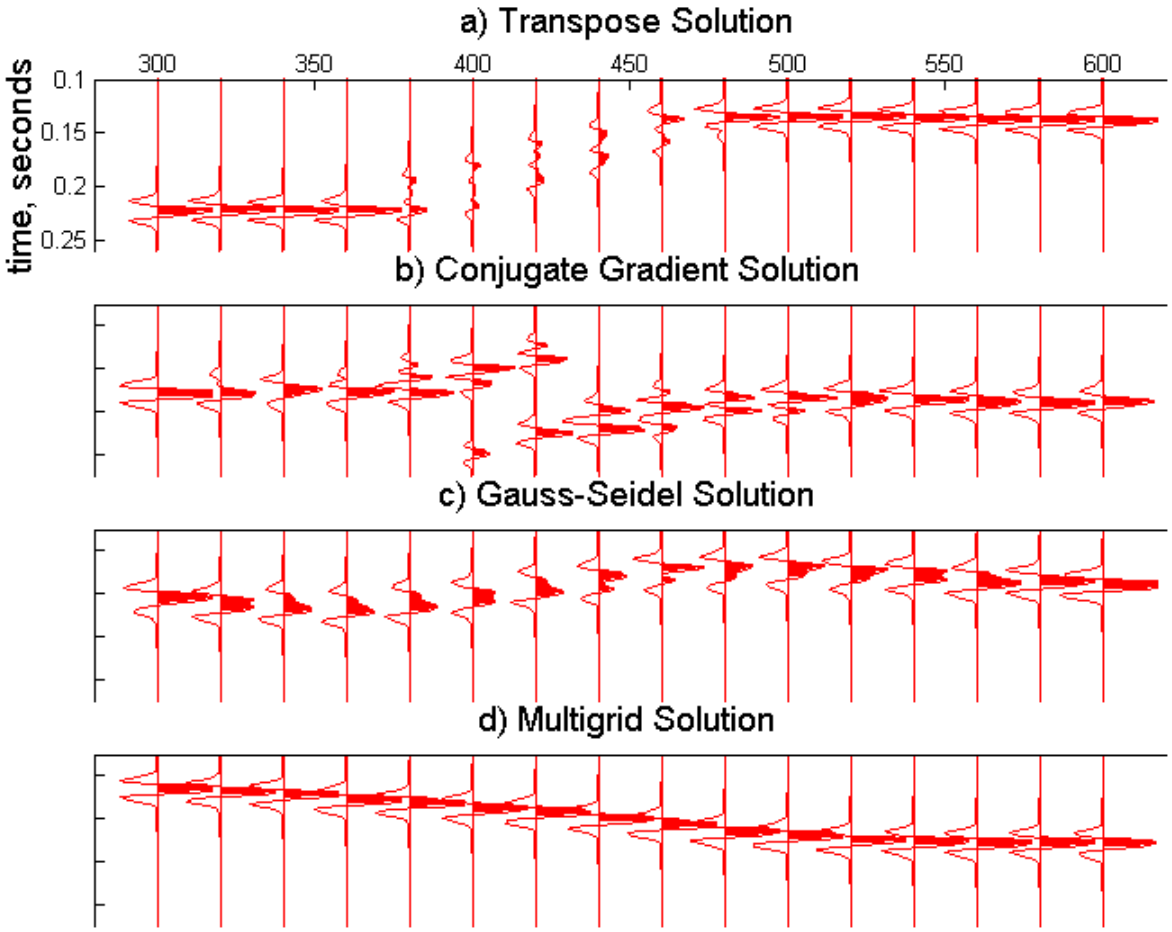

Figure 4.24: A synthetic stacked seismic section showing the results of using different iterative methods to solve a 4 term surface consistent static solution.

Figure 4.23 shows the effect of long wavelength error in the solutions on the stack section. Away from the anomaly, there is very little loss of quality in the stack. As we approach the anomaly, a false structure is introduced into the stack showing a sigmoidal shape. As well, the wavelets near the anomaly do not stack properly. The wavelet is *smeared* across the boundary of the anomaly.

The conjugate gradient method does remove some of the structural errors, however there is not good resolution of the reflector near the anomaly.

The stack section generated using the Gauss-Seidel solution is much better than the stack section resulting from the conjugate gradient method. Near the anomaly the reflector still appears slightly smeared, and there is a very small loss of resolution away from the reflector.

The multigrid solution provides the tightest stacked section of all of the methods. The long wavelength errors that produce the smearing are attenuated significantly.

When we look at the stacked seismic section created using the four term surface consistent solutions, the results are fairly similar. The smearing effect visible in the two term solution is still present. Unlike before, there is a small structural error in the Gauss-Seidel and multigrid sections. The shape of the false structural anomaly is the same shape as the error in the midpoint consistent term seen in Figure 4.11.

The long wavelength error in the solutions produces the smearing effect by the mechanism shown in Figure 4.25. Consider a positive and negative offset source receiver pair that share the same midpoint. The total error for a trace will be the sum of the error from the shot and the receiver that contribute to the trace. The plot in Figure 4.25 shows how the error in the positive and negative offsets combine to smear the reflector in the midpoint stacked section.

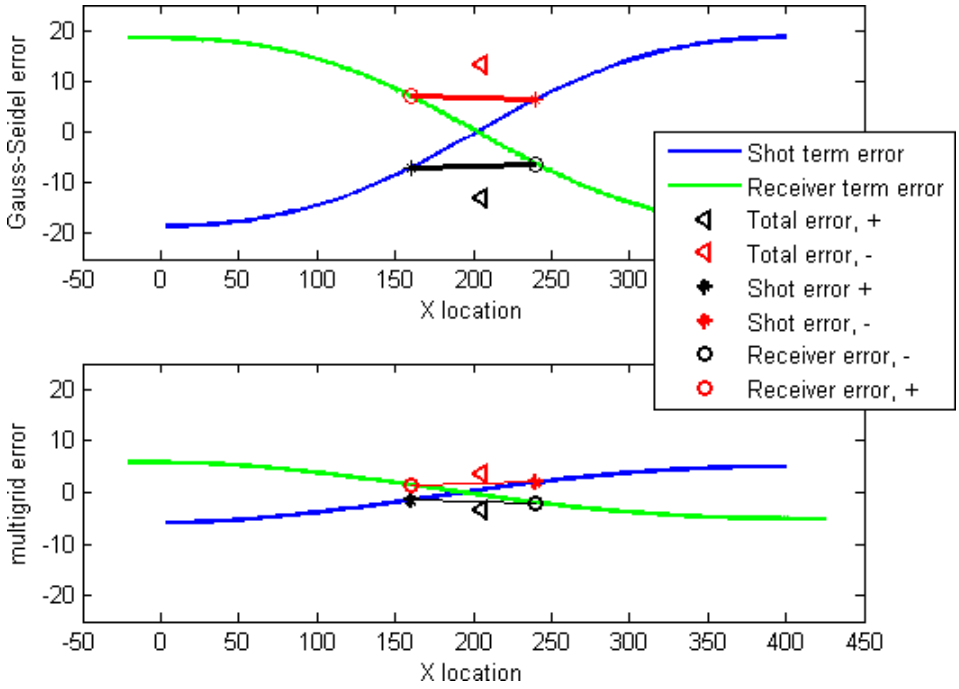

Figure 4.25: A diagram demonstrating how the long wavelength errors in the solution results in a smearing of the wavelet in the midpoint stack section.

4.3 Application to trace amplitudes

The error that causes the smearing present in the statics example manifests itself as an amplitude anomaly when the method is applied to correct trace amplitudes.

It is necessary to use the 4 term equations to solve for amplitude anomalies. Due to the presence of ground roll, there is a strong offset consistent component to the amplitudes, so a two term solution would include effects of ground roll when we are trying to correct amplitudes only considering the reflections.

Figure 4.26(a) shows the amplitude of all the traces from a midpoint far away from the surface consistent anomaly. Figure 4.26(b) shows the apparent amplitudes of all the traces with a midpoint close to the anomaly. These results were calculated using a Gauss-Seidel method.

The same results are shown for the conjugate gradient method in Figures 4.26(c) and Figure 4.26(d).

Figures 4.26(e) and 4.26(f) show the amplitude of the traces with midpoints close to and far away from the anomaly as calculated using the multigrid method.

In an ideal solution, every trace will lie directly over top of each other. A significant amount of difference between the traces in a single midpoint gather will mean that a false AVO anomaly would be picked in the section. The axis on the left hand side of the plots shows the amplitude of the trace. The amplitudes of the trace are equal to the error in the midpoint consistent term. When solving for the amplitudes it may be advisable to use the term to correct for amplitude variation from midpoint to midpoint.

The multigrid method again outperforms the conjugate gradient and Gauss-Seidel methods. Away from the anomaly the multigrid solution produces a consistent amplitude for all of

the traces that contribute to its midpoint. There is much more variation in the Gauss-Seidel amplitudes. Close to the anomaly, both solutions have a false AVO signature associated with it. The multigrid solution groups the traces slightly tighter than the Gauss-Seidel method.

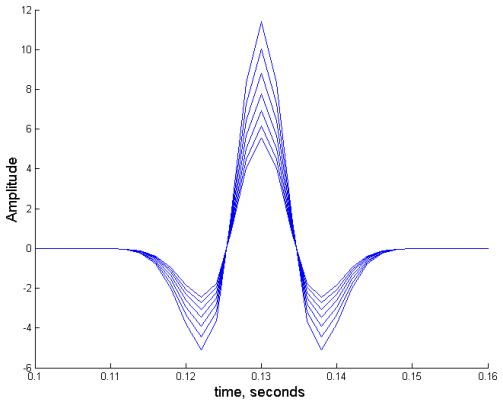

(a) The amplitude anomaly when using the Gauss-Seidel method, far from the anomaly.

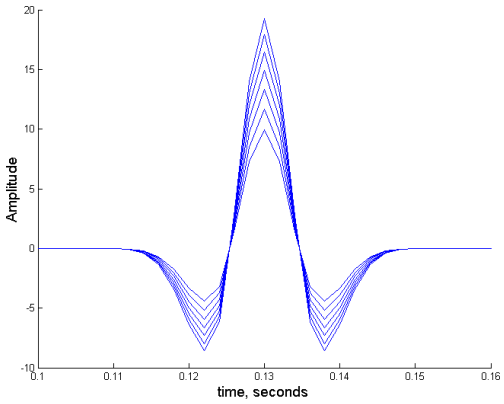

(b) The amplitude anomaly when using the Gauss-Seidel method, near the anomaly.

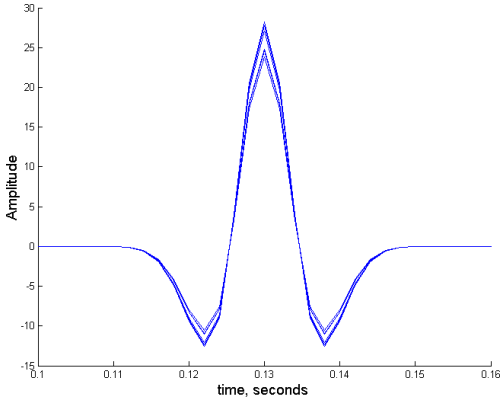

(c) The amplitude anomaly when using the conjugate gradient method, far from the anomaly.

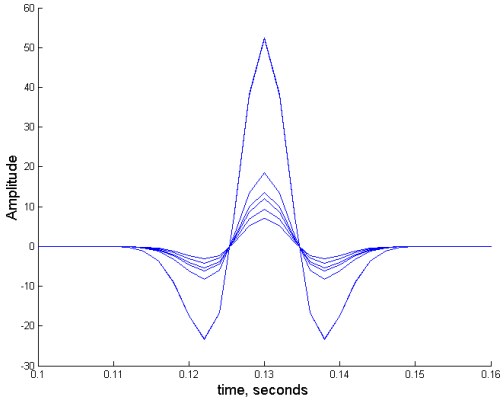

(d) The amplitude anomaly when using the conjugate gradient method, near the anomaly.

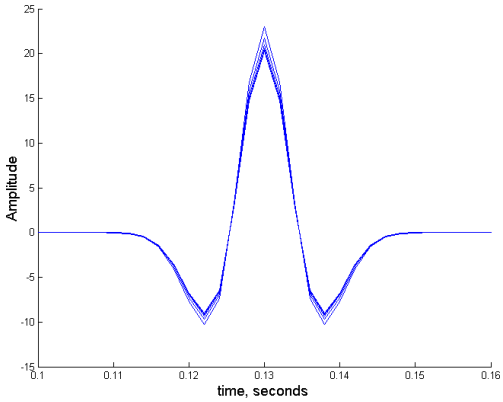

(e) The amplitude anomaly when using the multigrid method, far from the anomaly.

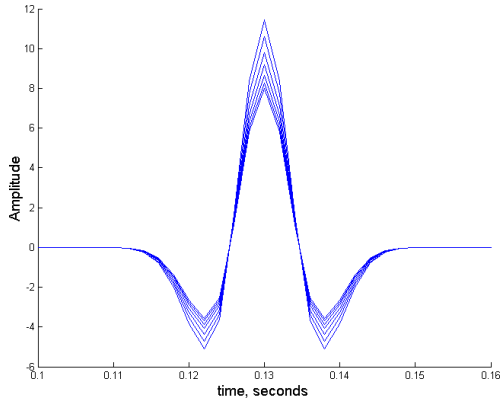

(f) The amplitude anomaly when using the multigrid method, near the anomaly.

Figure 4.26: The traces from two separate common midpoints are superposed in each frame. Subfigures (b), (d) and (f) have traces with midpoints very close to the surface consistent anomaly. A tight grouping of the traces corresponds to a smaller error in the amplitude estimate .

4.4 Application to deconvolution

To test the multigrid method in a surface consistent deconvolution, we need to construct a more sophisticated model. The amplitude spectrum of the source is calculated using the CREWES Matlab function *tntamp.m*. This function uses the formula

$$A_s(f) = \frac{1 - e^{-\frac{f^2}{f_{dom}^2}}}{1 + e^{-\frac{f^2}{f_{dom}^2}}}. \tag{4.14}$$

Each source is assigned a random dominant frequency, f_{dom}, and the amplitude spectrum is converted into a minimum phase wavelet.

A sample source wavelet and its amplitude spectrum can be seen in the left column of Figure 4.27.

Each unique receiver is assigned a value used to calculate a slightly modified Q filter. A straightforward filter can be expressed as

$$A_r(f) = e^{-\frac{f}{Q}}. \tag{4.15}$$

The Q filter calculated for a single receiver can be seen in the central column of Figure 4.27.

Each trace in the seismic data set is modelled by convolving a series that represents the relectivity profile by the shot wavelet, and filtered using the constant Q filter associated with the receiver.

The surface consistent model we use to test the algorithms is similar to the previous synthetic model, with a step function dominating the receiver term. All of the shots have a relatively consistant spectrum. The receivers in the second half of the survey suffer from a

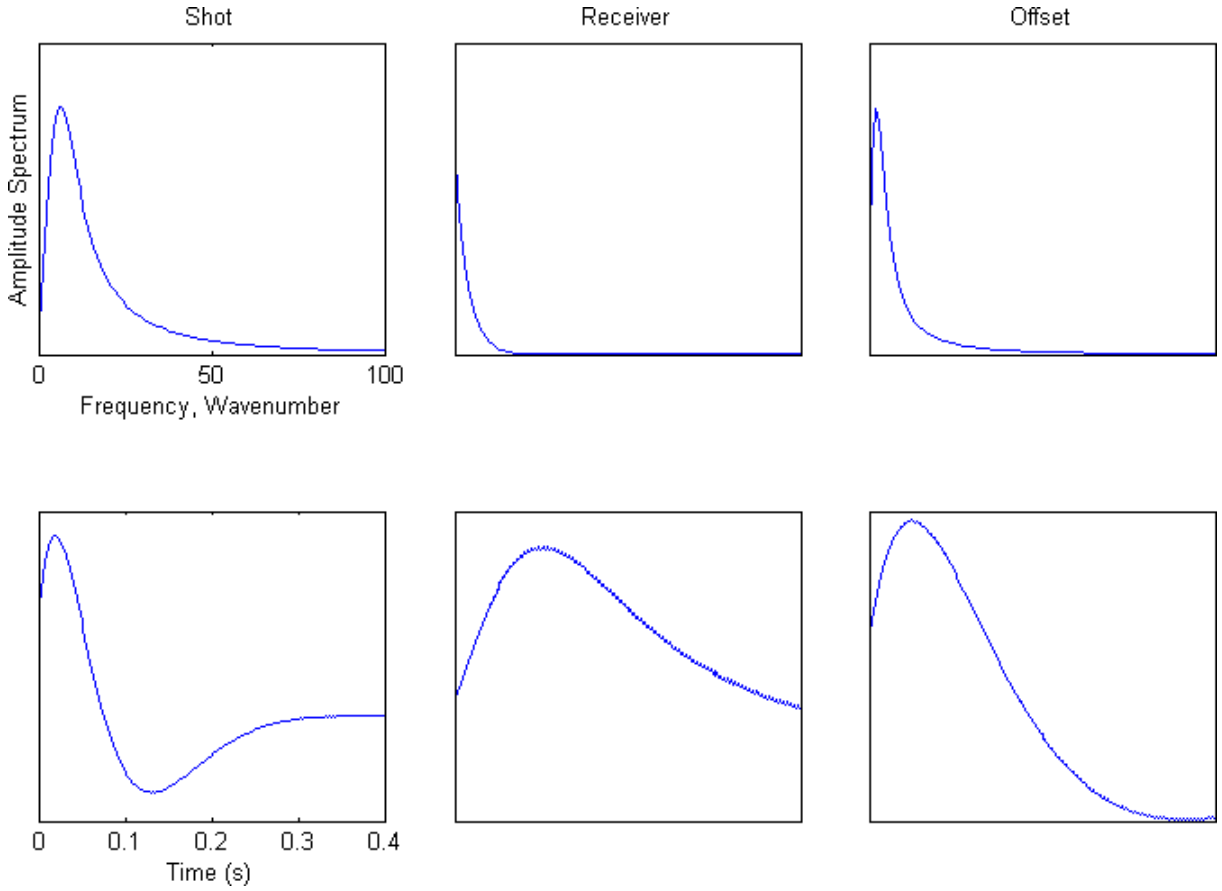

Figure 4.27: The amplitude spectrum and time series values for the source, receiver and offset components.

much stronger attenuation than the receivers in the first half. We assume that statics and normal moveout have been corrected, with no distortions.

The reflector of interest is at the 1s mark in the data. The reflectivity is a constant. A 20 hertz minimum phase ground roll is added to the trace above the reflector at 0.8s. The amplitude and time series for the ground roll is shown in the right hand column of Figure 4.27. How the ground roll and reflection are added together is shown in Figure 4.28. The amplitude of the ground roll decreases linearly with the source-receiver offset.

The purpose of the ground roll in the model is to interfere with the estimation of the

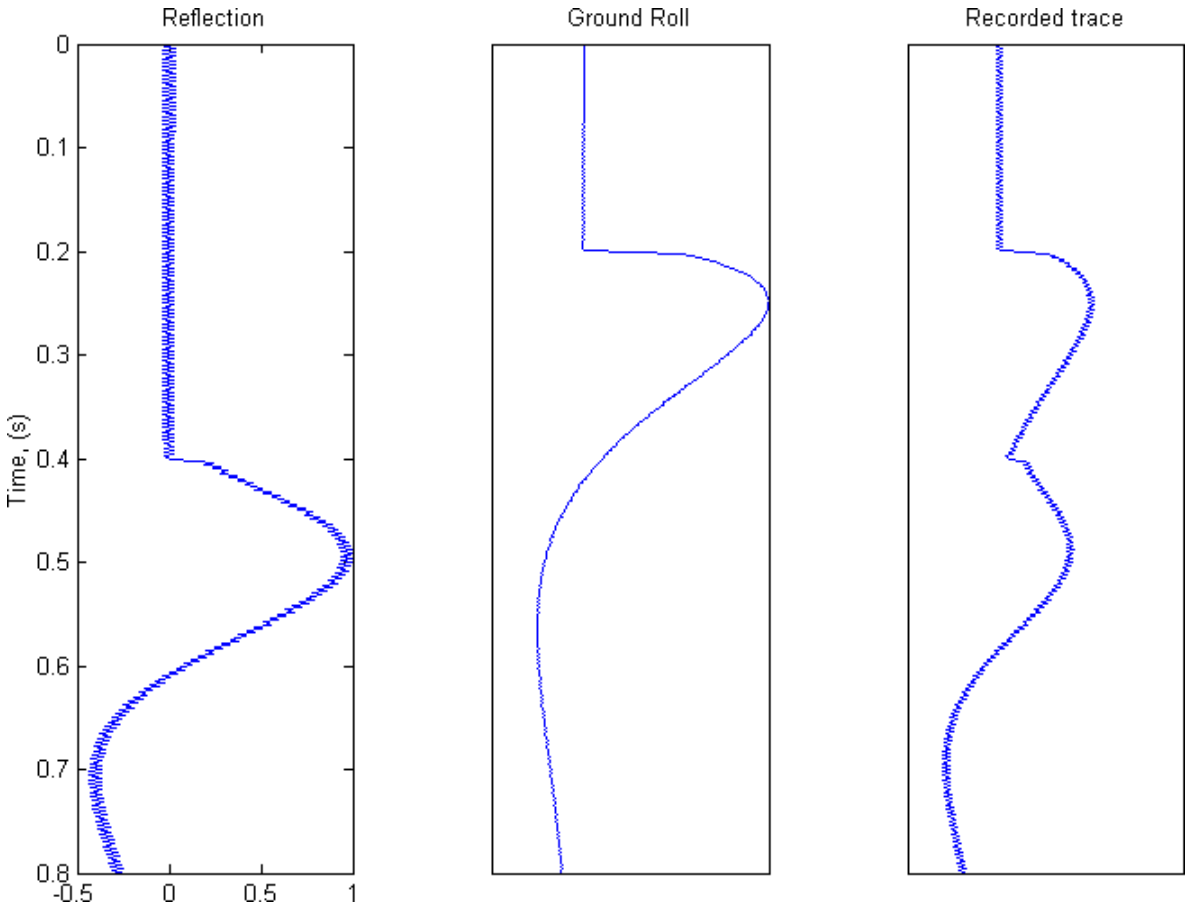

Figure 4.28: The amplitude spectrum of the reflection is calculated using the source and receiver signatures, with added random noise. The ground roll time series is added to the relection to get the recorded trace .

spectrum of the reflector. The trace by trace deconvolution algorithm will not be able to distinguish the ground roll from the reflector, and will distort the operator. The surface consistent equations allocate the ground roll to the offset consistent term. This term is not used to calculate the deconvolution operators. The shot and receiver operators are therefore more focussed on the reflected waves.

Random noise with an amplitude of 5 % the size of the reflector is applied to each trace.

The process for surface consistent deconvolution is as follows. Each trace in the survey is read in one by one. The amplitude spectrum of the trace is added to the bin corresponding to the source station. The spectrum is also added to the receiver, offset and midpoint bins. This is how we construct the vector $\mathbf{A^T t}$. After all of the traces are read, a surface consistent solution is found for each frequency in the spectrum. We proceed again through the data, but this time we construct a deconvolution operator by multiplying the source and receiver consistent terms. This deconvolution operator is an estimate of the frequency content of the reflector. This operator is used as the design trace to deconvolve the raw data.

The seismic survey is deconvolved using the CREWES Matlab routine *deconw.m*. The trace by trace deconvolution estimates the deconvolution operator by only considering the trace at hand. The surface consistent deconvolution operators are calculated by applying the surface consistent equations to each frequency.

The midpoint consistent term is sometimes used, or a bin that captures the average spectrum of all of the traces in the survey can be applied as well. After the application of surface consistent deconvolution a seismic processor may perform time variant spectral whitening, or some other post deconvolution wavelet processing.

Our investigation does not examine these variations in the application of the operators, only concentrating on the calculation of the operators. In this example there is no other

scaling or whitening of the data after the surface consistent deconvolution. Only the source consistent and receiver consistent operators are applied to the raw trace. The offset and midpoint consistent terms are discarded.

A shot record that straddles the surface consistent anomaly is shown in Figure 4.29. Also shown in this Figure is the results of trace by trace (not surface consistent) deconvolution, as well as the optimal surface consistent deconvolution using the operators we used to construct the model.

Figure 4.30 shows the deconvolved results of using Gauss Seidel, conjugate gradient and multigrid operators.

Figure 4.31 is the same shot record, but zoomed in on the reflector.

In Figure 4.31, the trace by trace deconvolution operator concentrates itself on the ground roll. The reflector is obscured in the near offsets.

The Gauss-Seidel and multigrid surface consistent deconvolutions are able to partially ignore the ground roll, and do a better job of deconvolving the traces in the near offsets. The quality difference between the two surface consistent deconvolutions is small, we cannot say the multigrid method outperforms the Gauss-Seidel method from this plot.

The operators used to model the traces are displayed in Figure 4.33. The y axis corresponds to the shot (receiver/midpoint/offset) station. The x axis is the frequency of the individual shots (receiver/midpoint/offset). In Figure 4.33(b), the anomaly in the receiver term can be seen in the middle of the plot where the spectra of the receivers changes sharply. The midpoint consistent operator is equal to one everywhere in the domain, signifying that there is no difference in the model from midpoint to midpoint (Figure 4.33(c)). The offset consistent term reflects the amplitude of the 20 hertz wavelet decreasing as we increase the absolute value of the offset (Figure 4.33(d)).

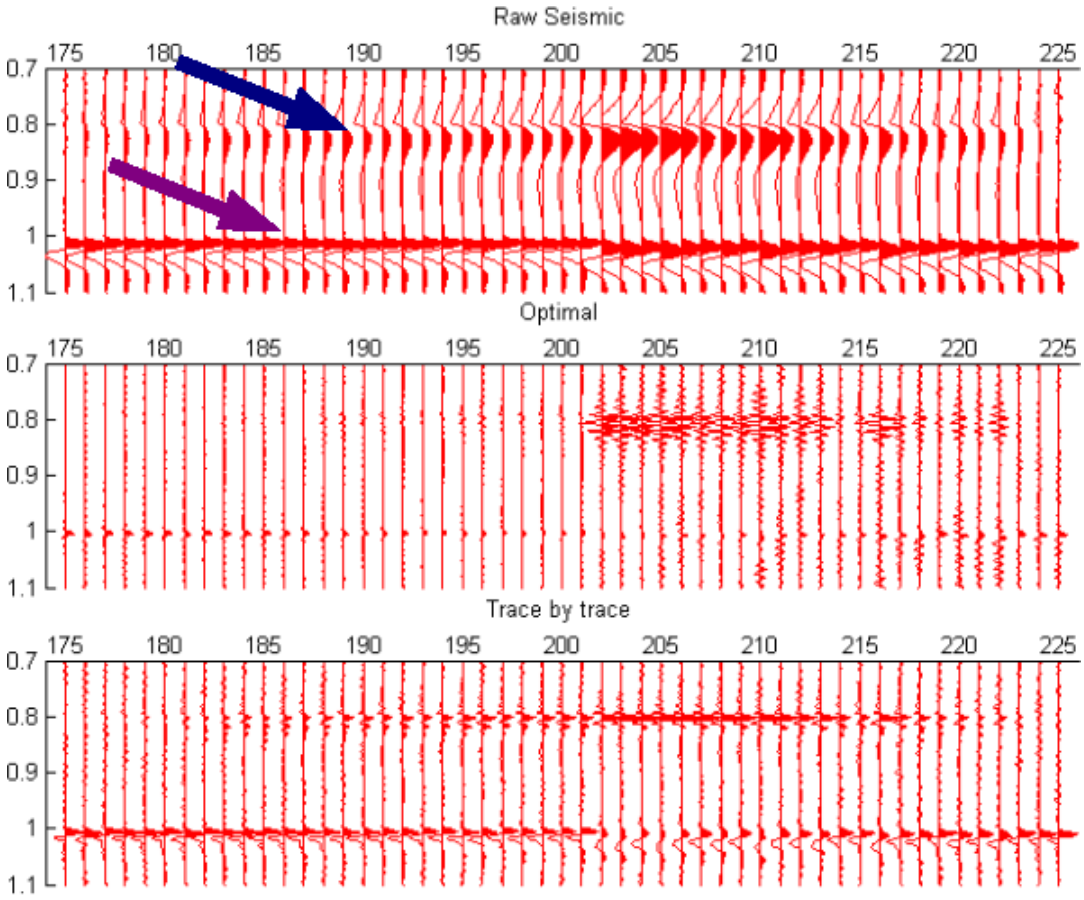

Figure 4.29: A shot gather straddling the surface consistent anomaly in the receiver term. The wavelet on top is the synthetic ground roll (blue arrow). The wavelet below is the reflector (magenta arrow).

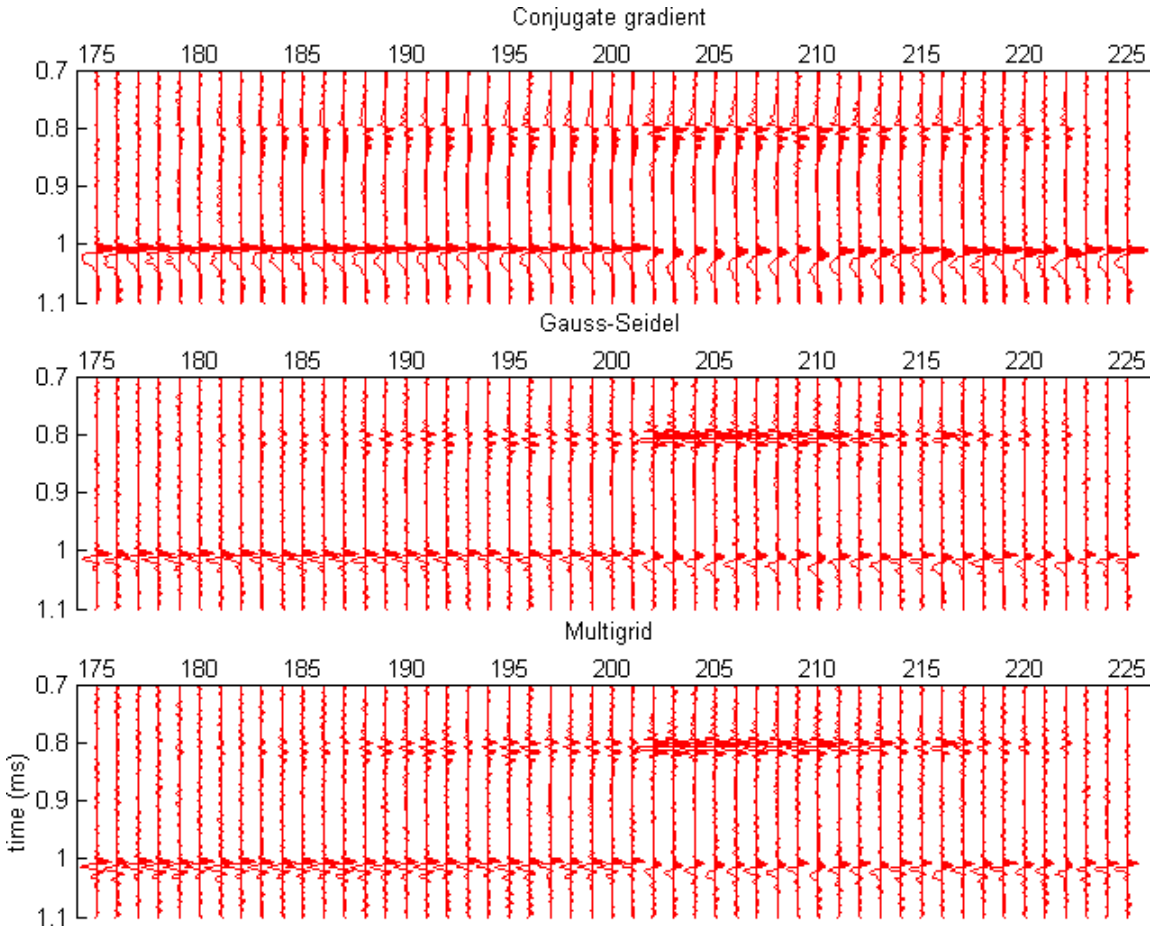

Figure 4.30: A shot gather straddling the surface consistent anomaly in the receiver term. The wavelet on top is the synthetic ground roll. The wavelet below is the reflector.

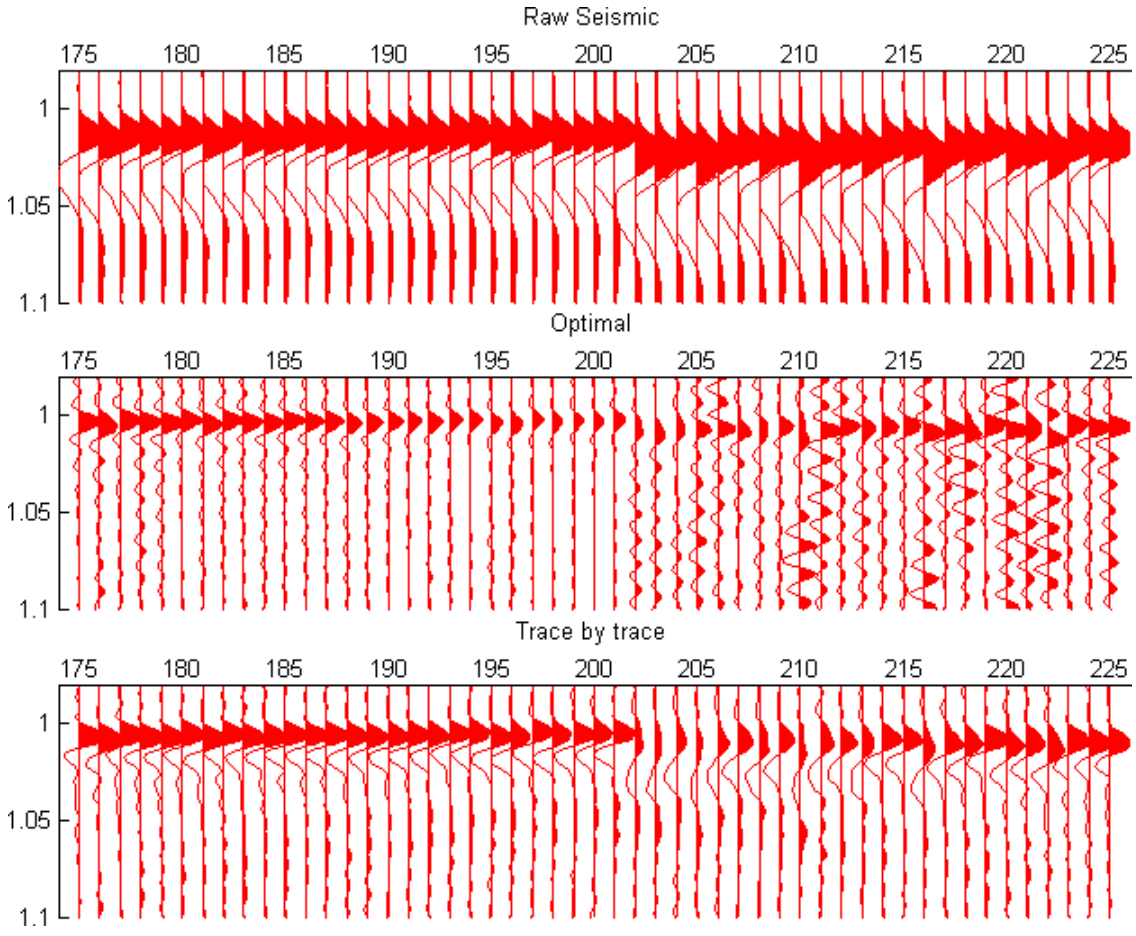

Figure 4.31: The shot gather from the synthetic example, zoomed in on the reflector.

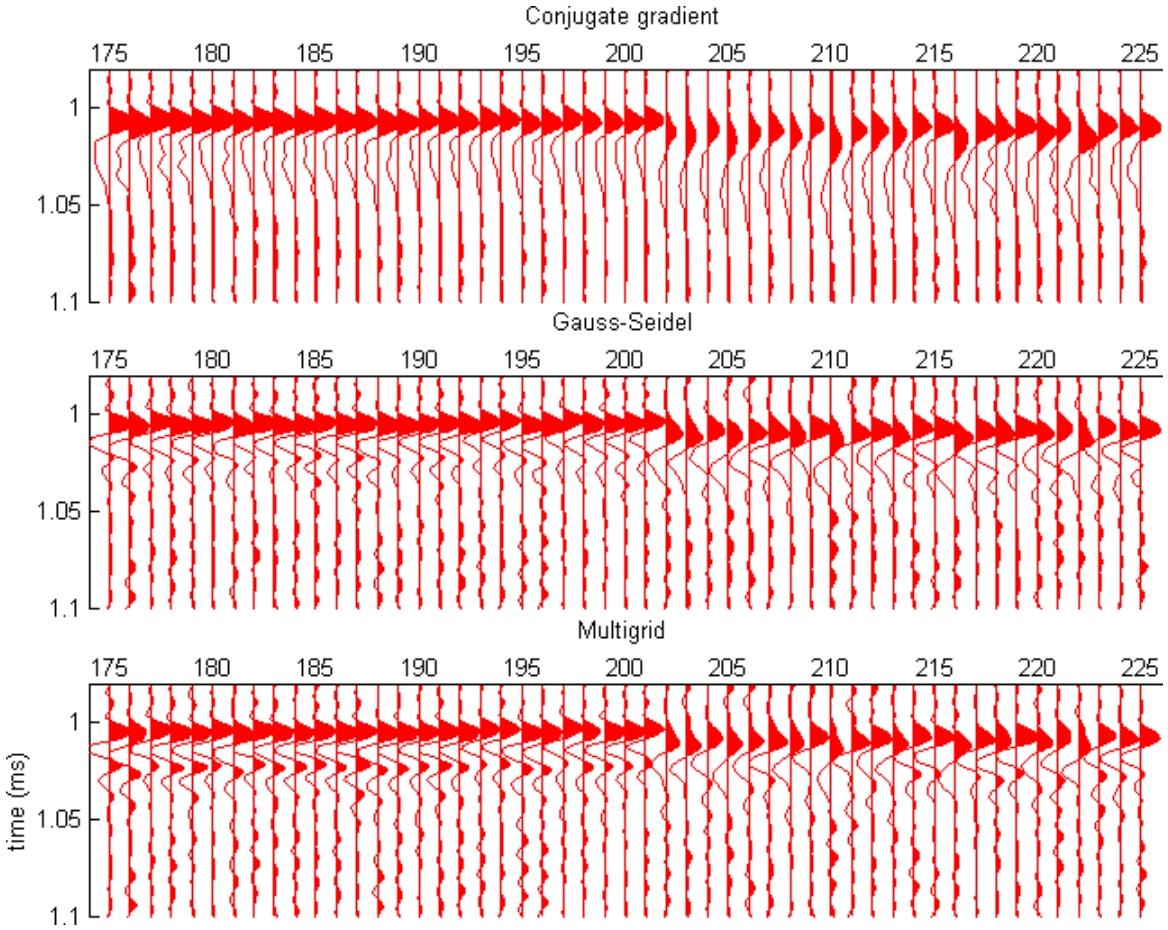

Figure 4.32: The deconvolution results from the synthetic example, zoomed in on the reflector.

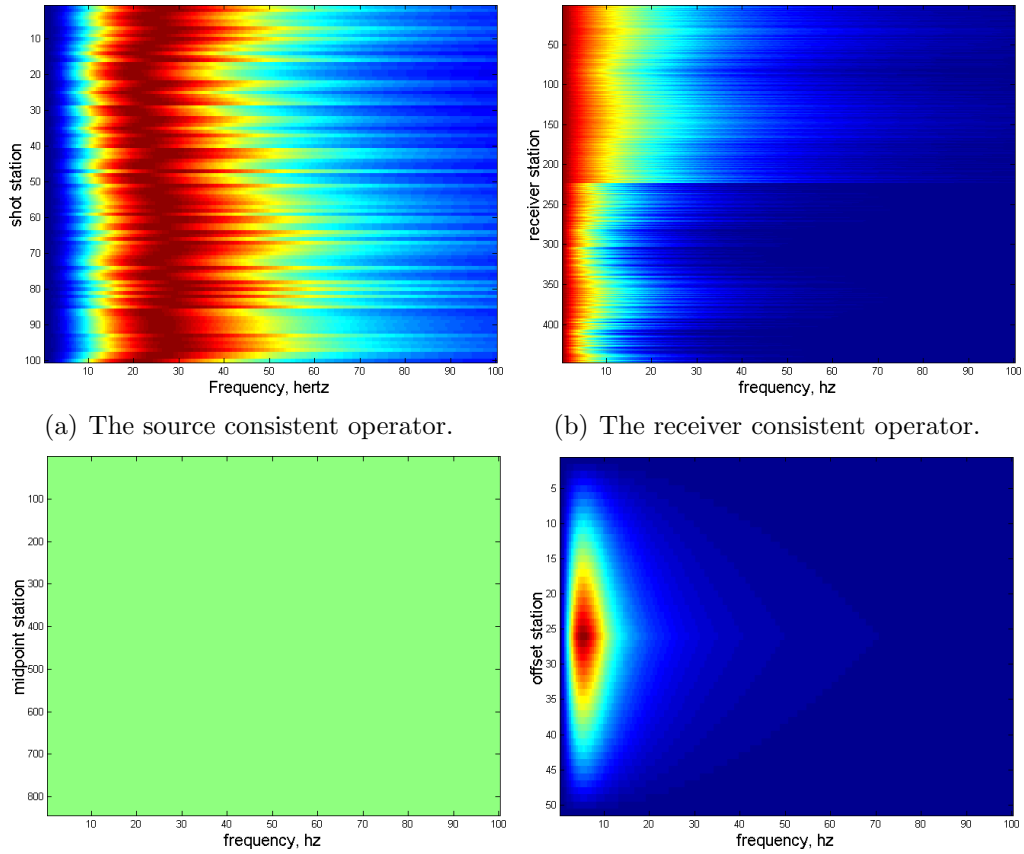

(a) The source consistent operator.

(b) The receiver consistent operator.

(c) The midpoint consistent operator.

(d) The offset consistent operator.

Figure 4.33: The operators used to forward model the synthetic seismic section. These operators are also used in the optimal deconvolution. All operator plots are normalized with the a maximum value of 1 (red), and a minimum 0 (blue)

The calculated Gauss-Seidel operators are shown in Figure 4.34. The calculated shot consistent term (Figure 4.34(a)) underestimates the change in spectrum from shot to shot. The spectrum of each shot is reasonable. The receiver and other terms are not well behaved. With the Gauss-Seidel solution, it appears that whichever term is addressed first by the solution method tends to be the smoothest and most reasonable result. The errors in this first term are magnified into the other terms, and the result is unphysical estimates of the receiver (in this case) and other terms. The large notches in the offset spectrum (Figure 4.34(d)) may be problematic. They are an artifact of the surface consistent anomaly in the receiver term.

These observations agree with the literature, where in Cary and Lorentz (1993) the authors recommend addressing the midpoint consistent term first in order to ensure that it is the smoothest. The results in the final stack section of changing the order of the variables addressed is minimal. If the smearing present in the statics and amplitude studies is present in this example, it does not appear to be a significant factor. One prediction for why this is, is that similar frequencies have similar errors. The relationship between individual frequencies for each trace is an important factor in deconvolution. Errors due to the smearing effect may be compensated for by having adjacent frequencies suffer the same smearing, negating the impact on the result.

The conjugate gradient operators are displayed in Figure 4.35. The source term (Figure 4.35(a)) has more relative high frequency data, while the receiver term is slightly less noisy in the high frequencies. The notching is not visible in the offset term. The midpoint term (Figure 4.35(a)) appears to absorbed a fair amount of the energy from the receiver term.

The appearance of the multigrid operators in Figure 4.36 is more realistic than the Gauss-Seidel operators. Some of the variation in the shot spectrum is captured (Figure 4.36(a)),

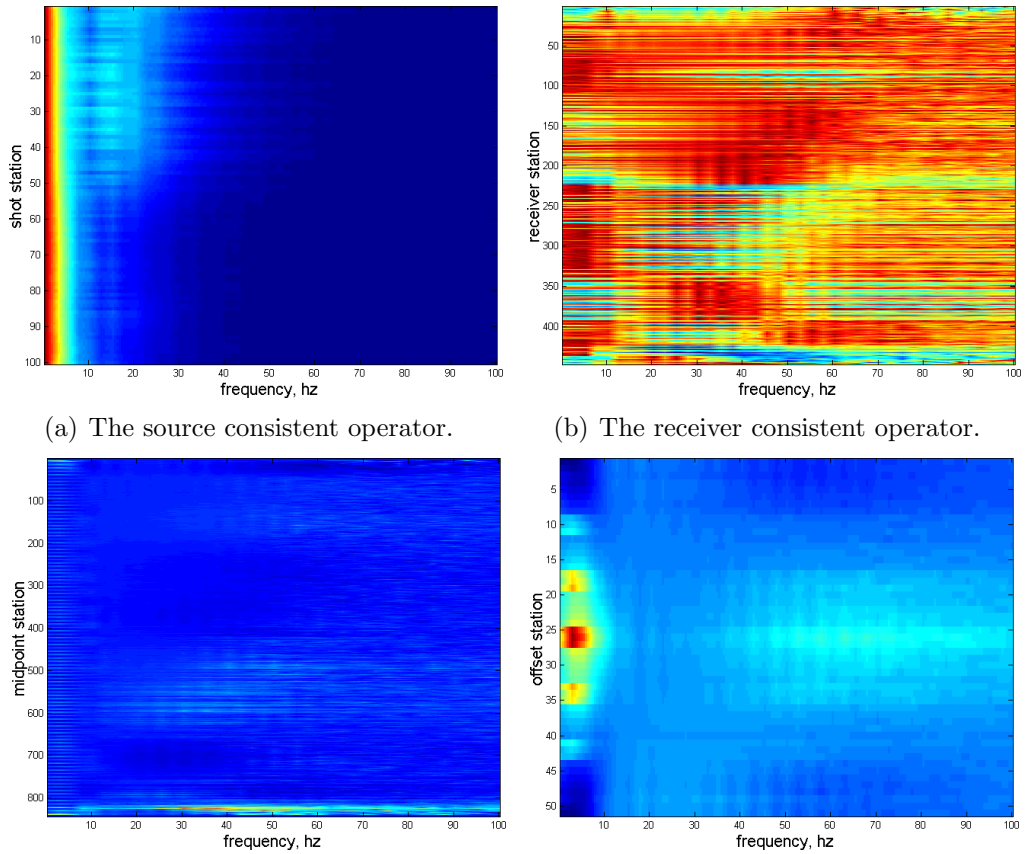

(a) The source consistent operator.

(b) The receiver consistent operator.

(c) The midpoint consistent operator.

(d) The offset consistent operator.

Figure 4.34: The deconvolution operators as calculated using the Gauss-Seidel method.

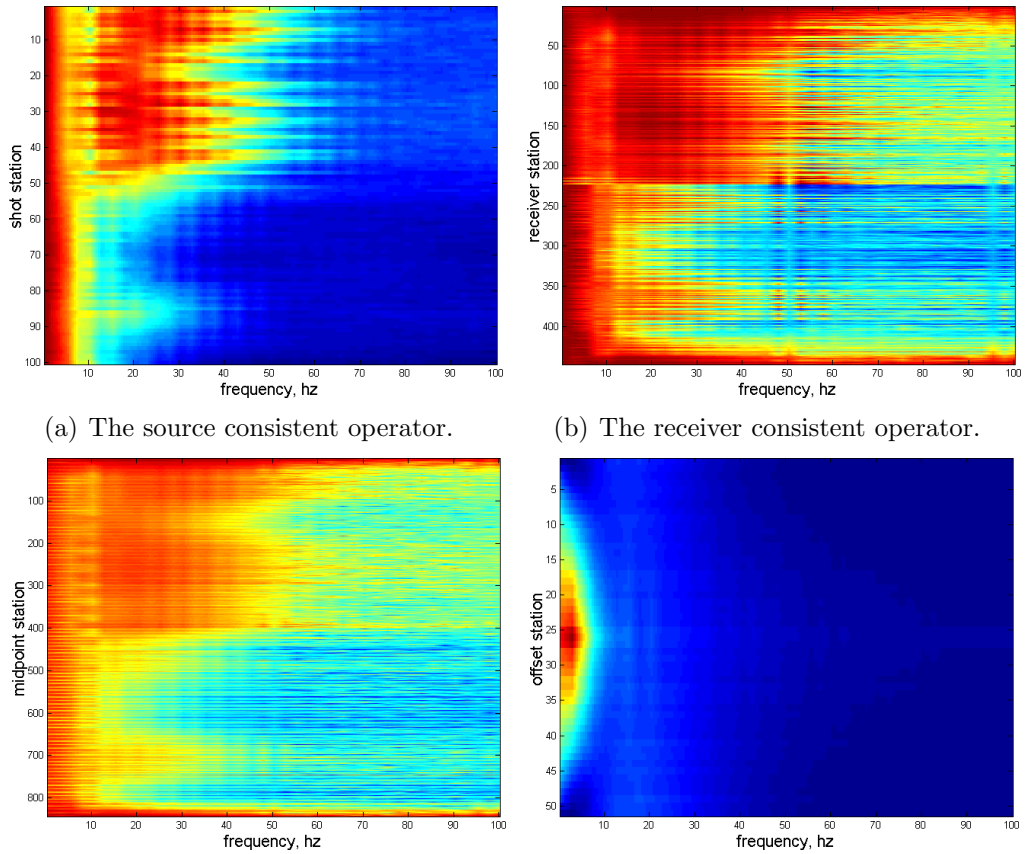

(a) The source consistent operator.

(b) The receiver consistent operator.

(c) The midpoint consistent operator.

(d) The offset consistent operator.

Figure 4.35: The deconvolution operators as calculated using the conjugate gradient method.

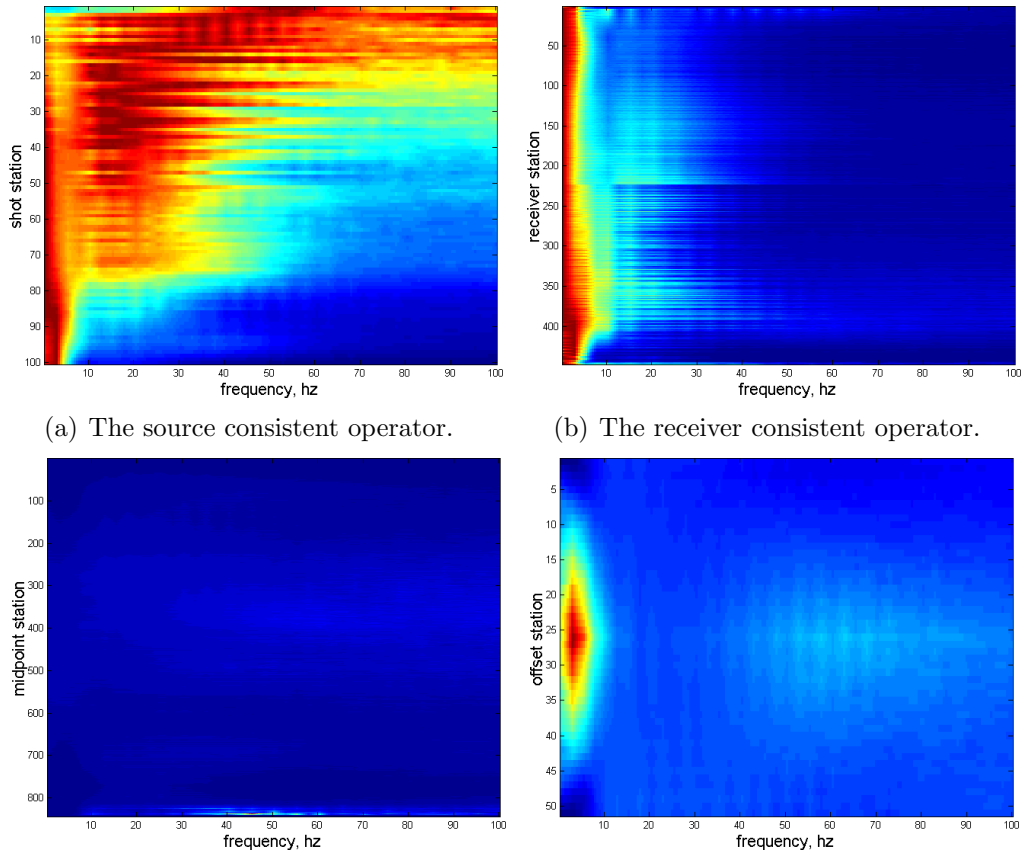

(a) The source consistent operator.

(b) The receiver consistent operator.

(c) The midpoint consistent operator.

(d) The offset consistent operator.

Figure 4.36: The deconvolution operators as calculated using the multigrid method.

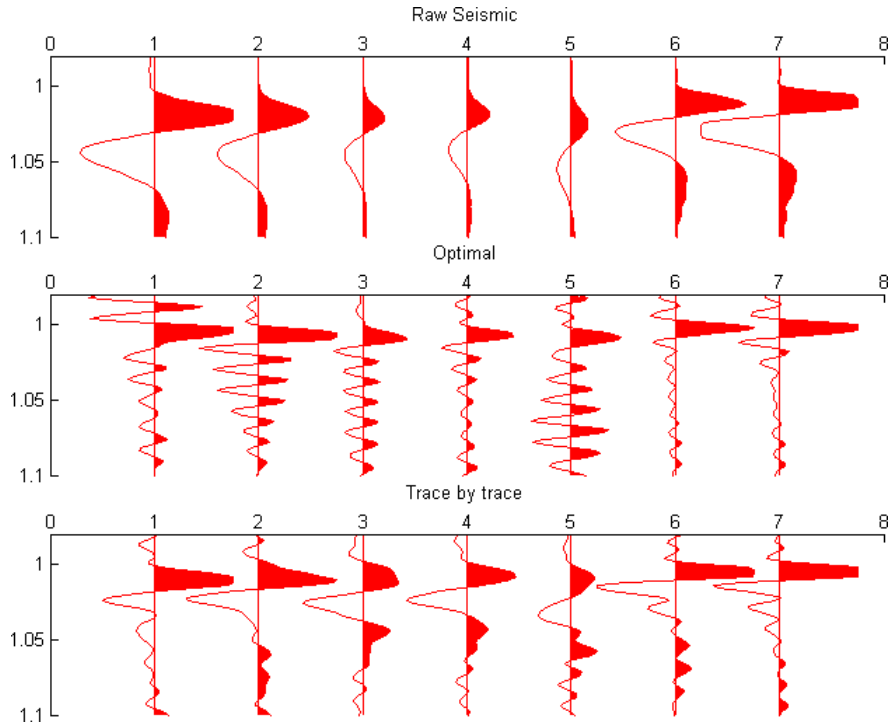

Figure 4.37: A midpoint gather of the raw and deconvoled data far away from the surface consistent anomaly. The offset increases to the right.

and the receiver consistent term has the sudden break in it that was included in the model (Figure 4.36(b)). The offset consistent term (Figure 4.36(d)) closely resembles the offset term in the model (Figure 4.33(d)), and the notches in the Gauss-Seidel offset term are not present.

Figures 4.37 through 4.40 show midpoint gathers far from and near the anomaly in the receiver term. The ground roll dominates the trace by trace deconvolution in the near offsets. The reflector is obscured by the ground roll. Again, both surface consistent deconvolutions provide superior solutions, however any difference between the two is difficult to discern in this view.

A better comparison between the Gauss-Seidel and multigrid solutions is provided in

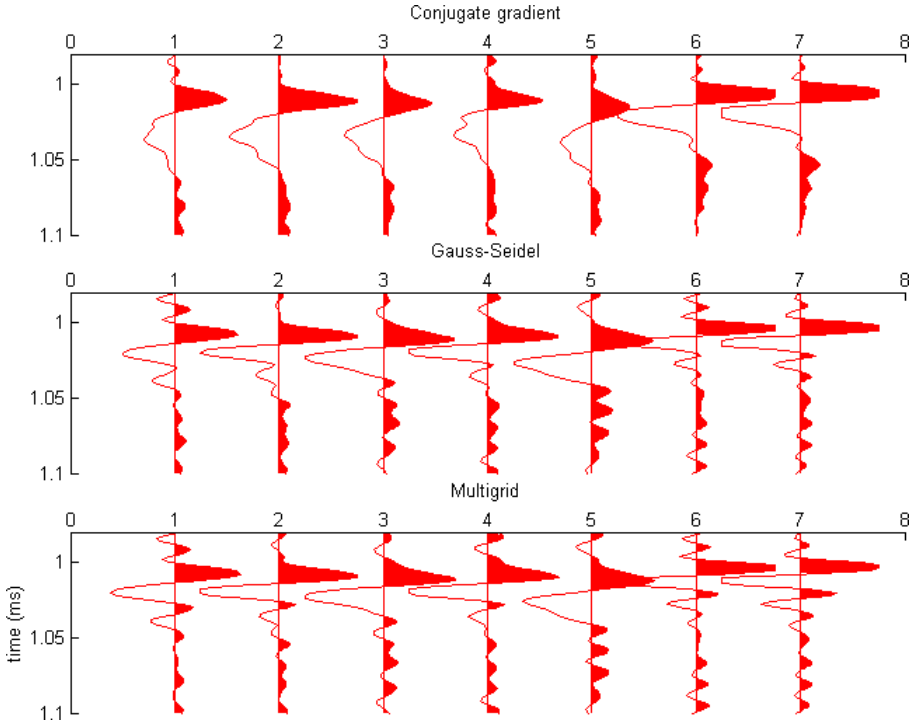

Figure 4.38: A midpoint gather of the surface consistent deconvoled data far away from the surface consistent anomaly. The offset increases to the right.

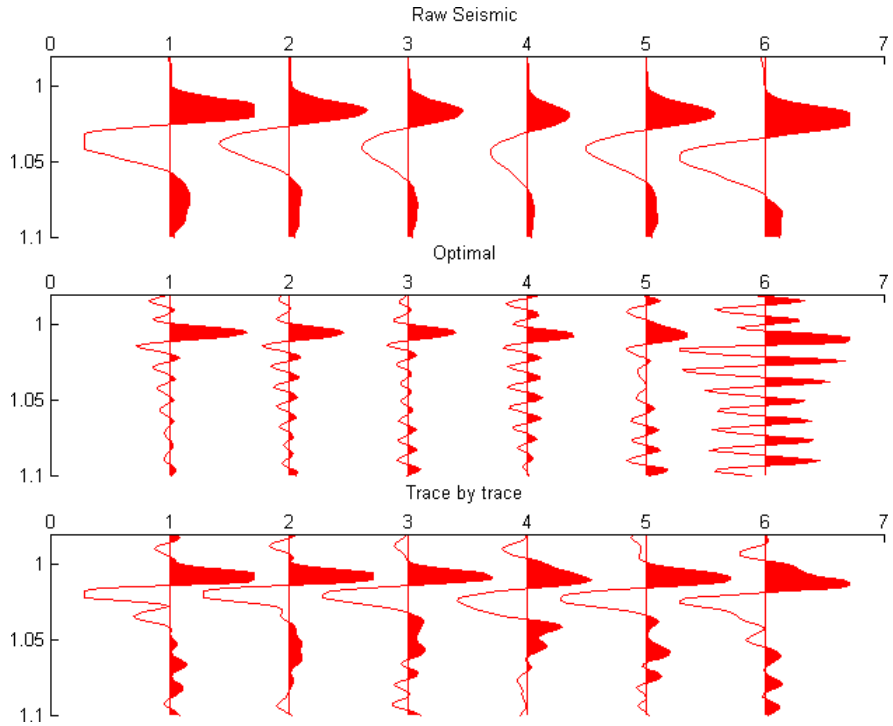

Figure 4.39: A midpoint gather with raw and deconvolved data near the surface consistent anomaly.

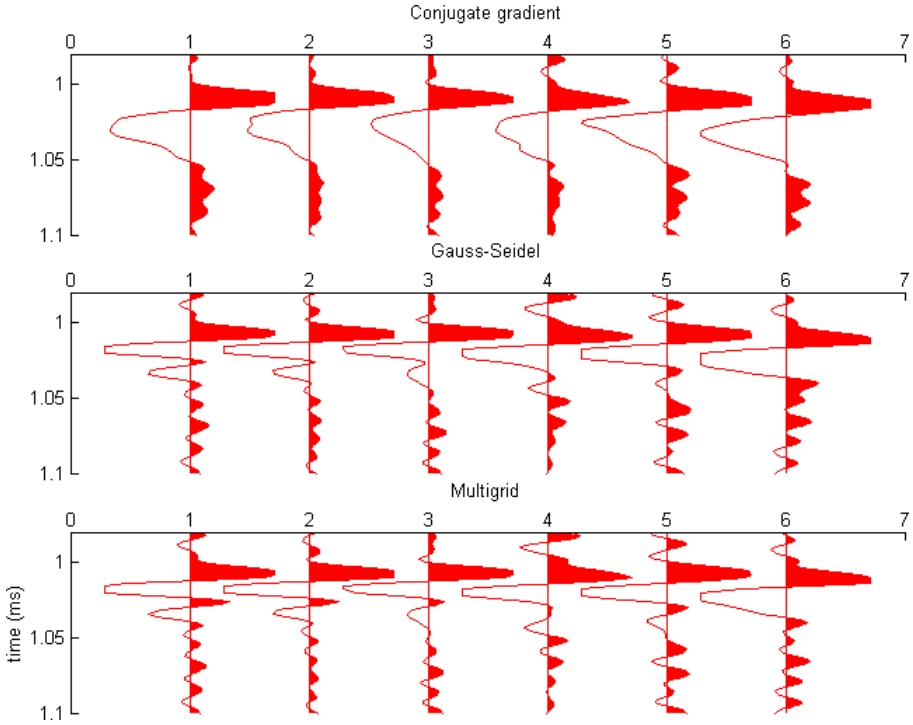

Figure 4.40: A midpoint gather of (surface consistent) deconvolved data near the surface consistent anomaly.

Figures 4.41(a) and 4.41(b). In both figures, and throughout the whole section, the multigrid operators output a wavelet more close to a Dirac delta function than either of the other methods. The Gauss-Seidel operators provide some improvement over the trace by trace deconvolution. The trace labeled *optimum* is the trace that was deconvolved using the surface consistent operator that were used to construct the trace. It is the absolute best deconvolution we can produce using the constraints of the model, including random noise and resolution limits.

The amplitude spectra of the reflector in the midpoint stacked traces are displayed in Figures 4.42(a) and 4.42(b). Consistent with the previous observation, the multigrid spectra is very slightly more broad than the other methods. The high frequencies are boosted more effectively than the other deconvolution methods.

The amplitude spectrum of the optimally deconvolved trace appears to over-whiten the spectrum of the trace. This tendency is because of the additive random noise included in the model. The signal and noise are both amplified by the deconvolution. This is a sign that we should tighten up the high frequency of our band pass filter.

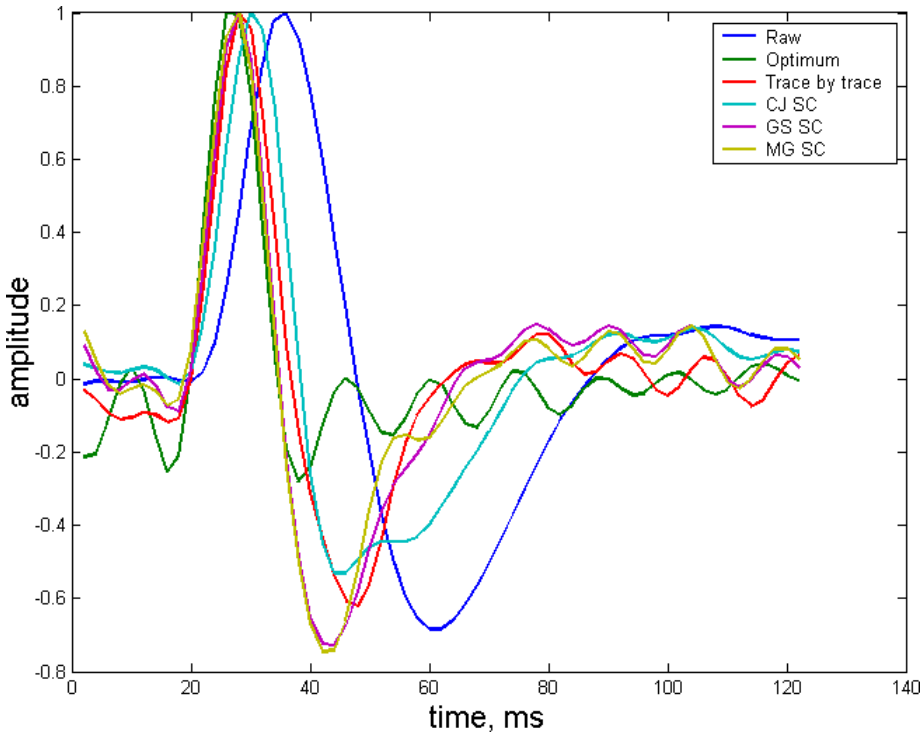

(a) A stacked midpoint trace, zoomed in on the reflector. This is from the midpoint far from the anomaly in the receiver term.

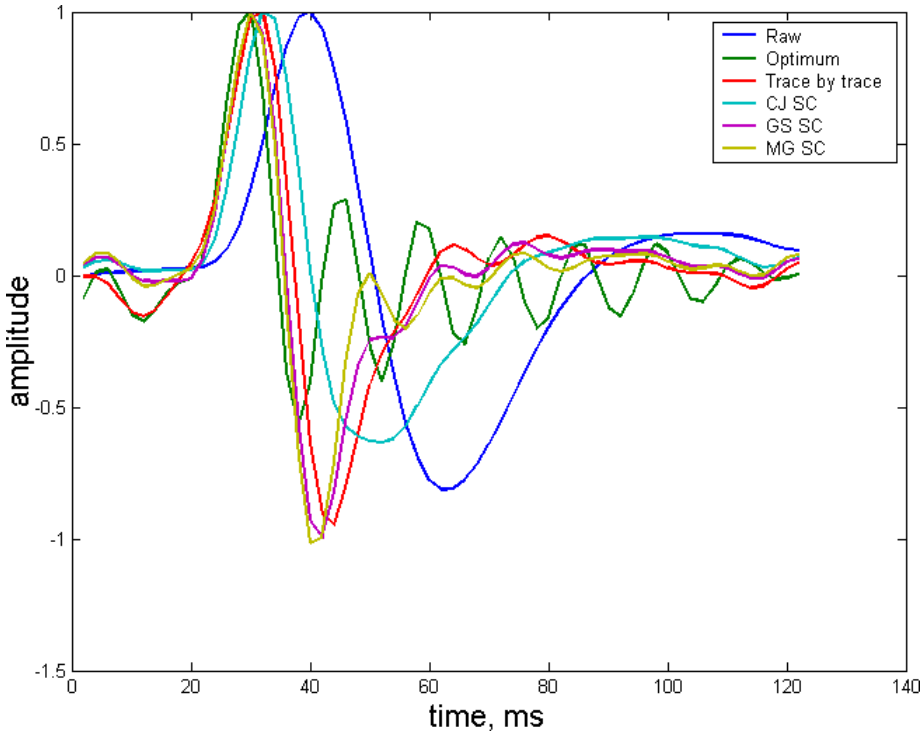

(b) A stacked midpoint trace, zoomed in on the reflector. This is from the midpoint near the anomaly.

Figure 4.41:

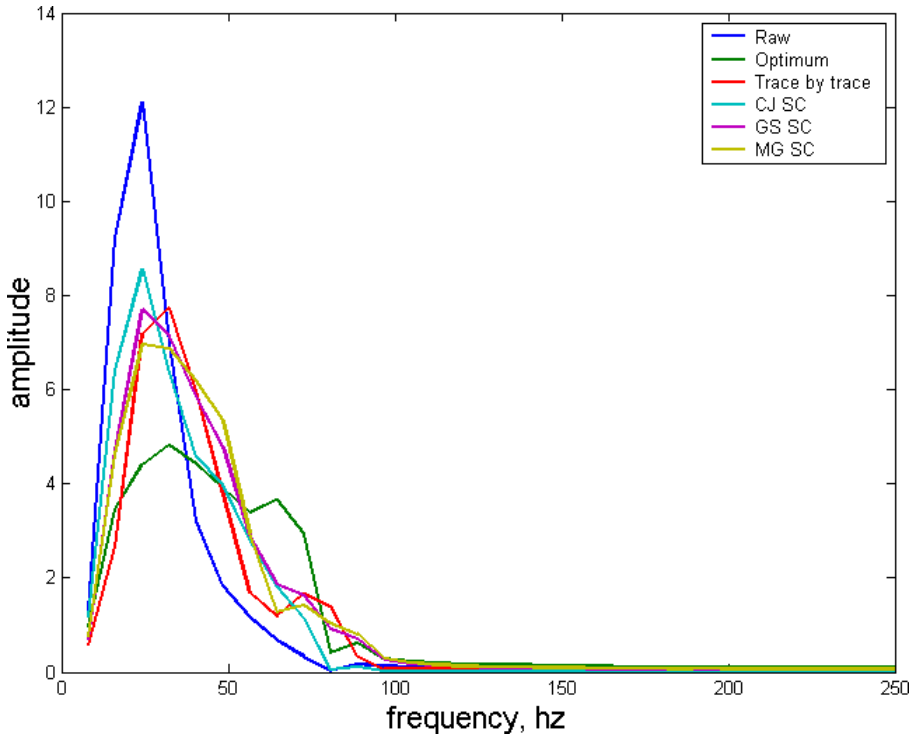

(a) The amplitude spectrum of the midpoint stacked trace far from the surface consistent anomaly. Only the spectrum of the reflector is included.

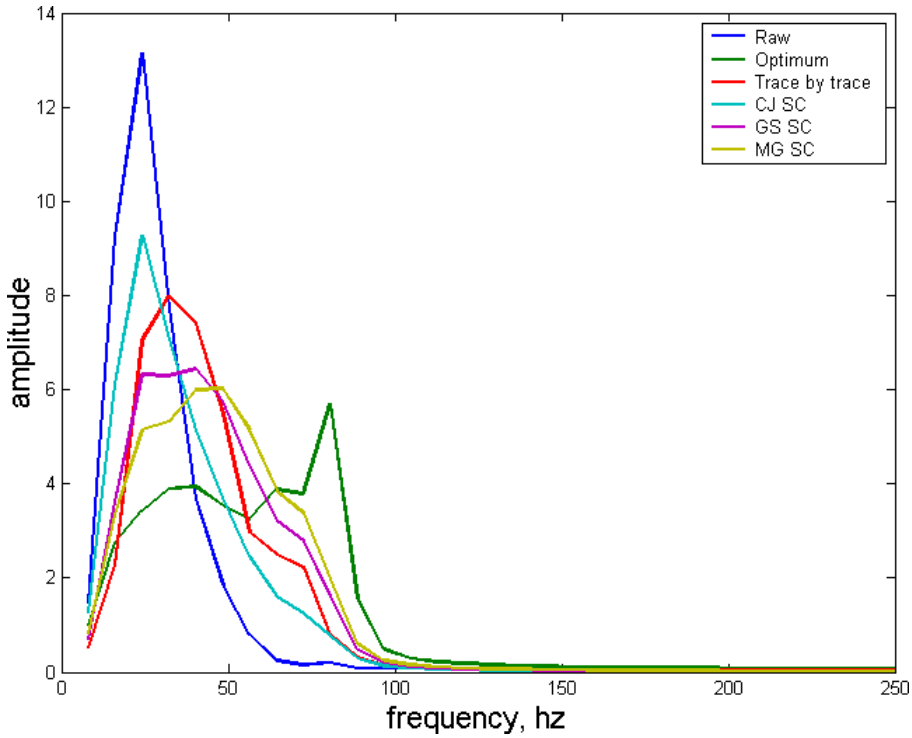

(b) The amplitude spectrum of the reflector in the midpoint stacked trace near the surface consistent anomaly.

Figure 4.42:

Chapter 5

Deconvolution of Blackfoot seismic data set

In the previous section we compared the results of a surface consistent deconvolution using Gauss-Seidel and multigrid estimates to produce deconvolution operators. In this section a similar analysis is performed on a field seismic data set.

The seismic data set chosen as an example is the CREWES Blackfoot data set. The data was collected in 1997. The survey measured 3 components of displacement, a vertical, radial, and in-line horizontal component. Only the vertical channels are considered in this study.

The survey consists of 151 receivers laid out in a line with a separation of 5 meters. 159 Dynamite sources were used. For each shot all of the receivers along the line were live, yielding 24009 traces. The shots move across the survey line from one end of the to the other. This geometry leads to a four term surface consistent system of equations consisting of 909 equations and unknowns.

Each trace has a sample rate of 0.001 ms, and trace length of 2.5 seconds. The entire trace was used for the analysis, however only the first second of the data is shown.

The surface consistent deconvolution operators calculated for the Blackfoot data set are displayed in Figures 5.1 , 5.1 and 5.3.

Similar to the results of the synthetic example, the multigrid operators (Figure 5.3) have a much less noisy expression than those calculated using Gauss-Seidel.

The Gauss-Seidel shot operator (Figure 5.1(a)) is quite smooth and does not appear significantly different than the synthetic shot operator from the previous section (Figure 4.33(a)).

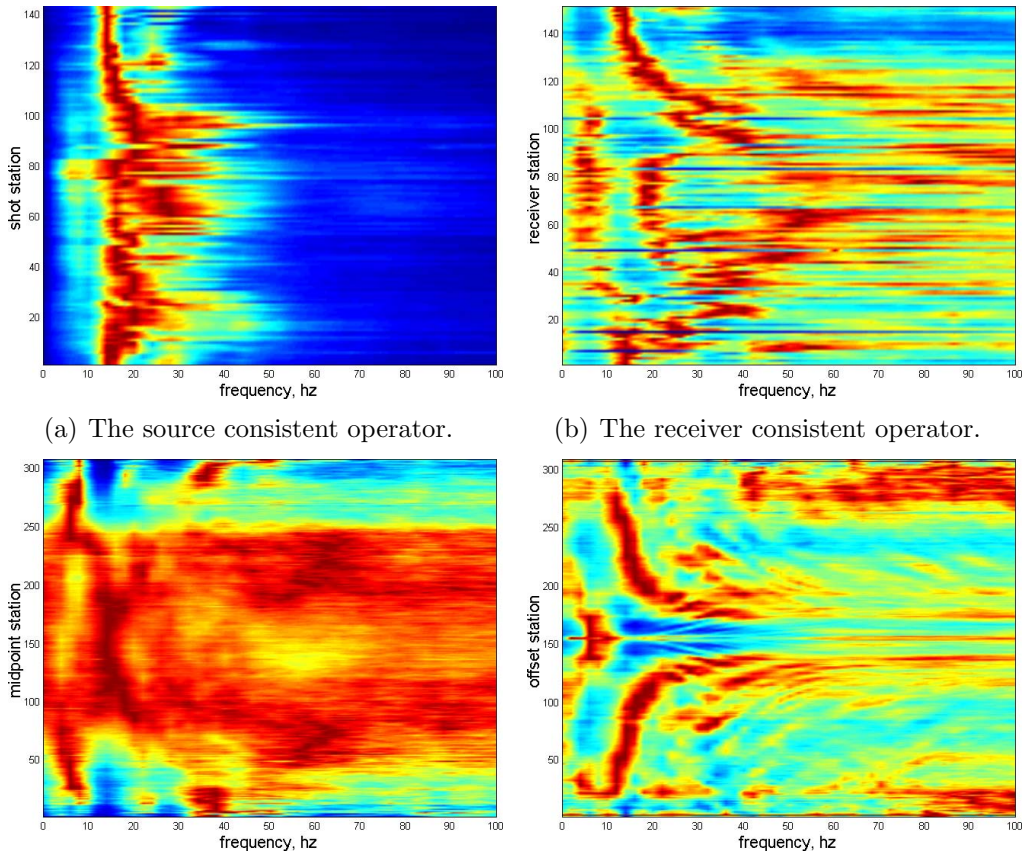

(a) The source consistent operator.

(b) The receiver consistent operator.

(c) The midpoint consistent operator.

(d) The offset consistent operator.

Figure 5.1: The surface consistent deconvolution operators as calculated by the Gauss-Seidel method. All operator plots are normalized with the a maximum value of 1 (red), and a minimum 0 (blue)

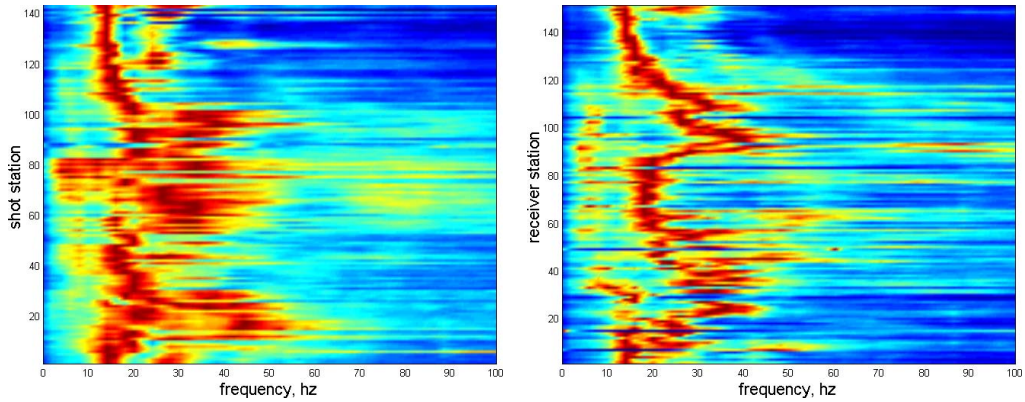

(a) The source consistent operator.

(b) The receiver consistent operator.

(c) The midpoint consistent operator.

(d) The offset consistent operator.

Figure 5.2: The surface consistent deconvolution operators as calculated by the conjugate gradient method.

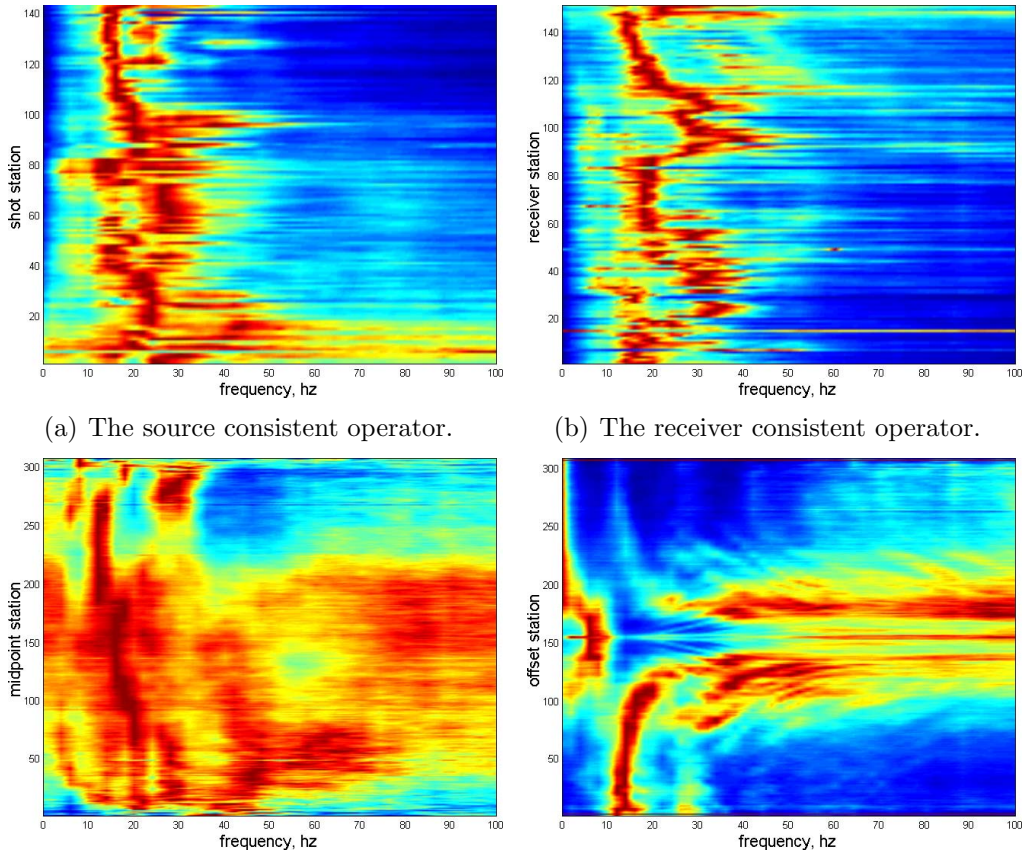

(a) The source consistent operator.

(b) The receiver consistent operator.

(c) The midpoint consistent operator.

(d) The offset consistent operator.

Figure 5.3: The surface consistent deconvolution operators as calculated by the multigrid method.

This was the first unknown addressed by the Gauss-Seidel algorithm.

The receiver term in the Gauss-Seidel solution (Figure 5.1(b)) shows a significant amount of noise and variation in the high frequencies. In the low and medium frequencies the data is concentrated into 3 distinct bands. The low frequency concentration in the Gauss-Seidel receiver term is thought to be due to ground roll being miss-allocated from the offset term. The source of the highest frequency band ($\approx$ 50 hertz, wavenumber 125 and towards the center of the survey) is not known, but is assumed to have a negative impact on the data, as it doesn't properly fit into our model. The central band of energy is though to be the area associated with the receiver absorption spectrum.

The offset consistent channel (Figure 5.1(d)) has a regional high at the short offsets (center of plot) that corresponds to ground roll in the section. The center frequency of this feature lies at roughly wavenumber 20, or 8 hertz. As well there are vaguely hyperbolic concentrations of energy, starting at the long offsets (top and bottom edges of plot) and wavenumber 25 (10 hertz). These energy bands increase in frequency as they move towards the shorter offsets (center of plot), and asymptote to the zero offset at the highest frequencies. The nature of these bands of energy are not understood, Cary and Lorentz (1993) notes that some excess bands of energy in the offset term may be related to travel-time move-out. Another possibility may be that they are related to the refracted first arrivals. Further investigation is needed, as this feature was not successfully modelled in this study.

The midpoint consistent term (Figure 5.1(c)) in the solution is generally fairly smooth, with more energy appearing towards the center of the survey. The lower frequencies have some local maxima that stretch across a large number of the midpoint stations. These bands lie in roughly the same frequencies as some of the bands in the other terms. It is thought that they may simply be energy leaking into the midpoint term from the other channels.

The conjugate gradient method provides qualitatively very similar to the Gauss-Seidel operators. In Figure 5.2, the shot gather appears to have more high frequencies, while the receiver term is less noisy. The offset and midpoint consistent solutions contain similar features to the Gauss-Seidel solutions.

The multigrid shot operator (Figure 5.3(a)) appears less smooth than the corresponding Gauss-Seidel operator. There is a small concentration of noise present in the high frequencies for the first 20 shot stations.

The receiver consistent multigrid operator (Figure5.3(b)) is relatively free of the high frequency noise that plagues the Gauss-Seidel receiver operators (Figure 5.1(b)). The energy in the multigrid receiver operator is also no longer in multiple bands. The lowest frequency band, thought to represent ground roll leaking into the Gauss-Seidel solution is not present in the multigrid solution, as well as the higher frequency error whose origin is unknown.

The multigrid offset consistent term (Figure 5.3(d)) is qualitatively very similar to the solution produced by the Gauss-Seidel method. The longer offsets appear to have less noise, and the entire domain appears more smooth.

The midpoint consistent multigrid channel (Figure 5.3(c)) is again qualitatively very similar to the corresponding Gauss-Seidel channel.

A raw shot record (shot station 50) is displayed in Figure 5.4. Only the first second of recorded data is shown. The reflector of intrest is at about 0.9s. The blue box outlines the area where we will be zooming in on that is relatively free from ground roll contamination. The green box outlines where we will be looking for reflectors obscured by the ground roll.

The data, deconvolved using a trace by trace estimate of the operator is shown in Figure 5.5.

Figures 5.6, 5.7 and 5.8 show the seismic data in shot record 50 deconvolved using the

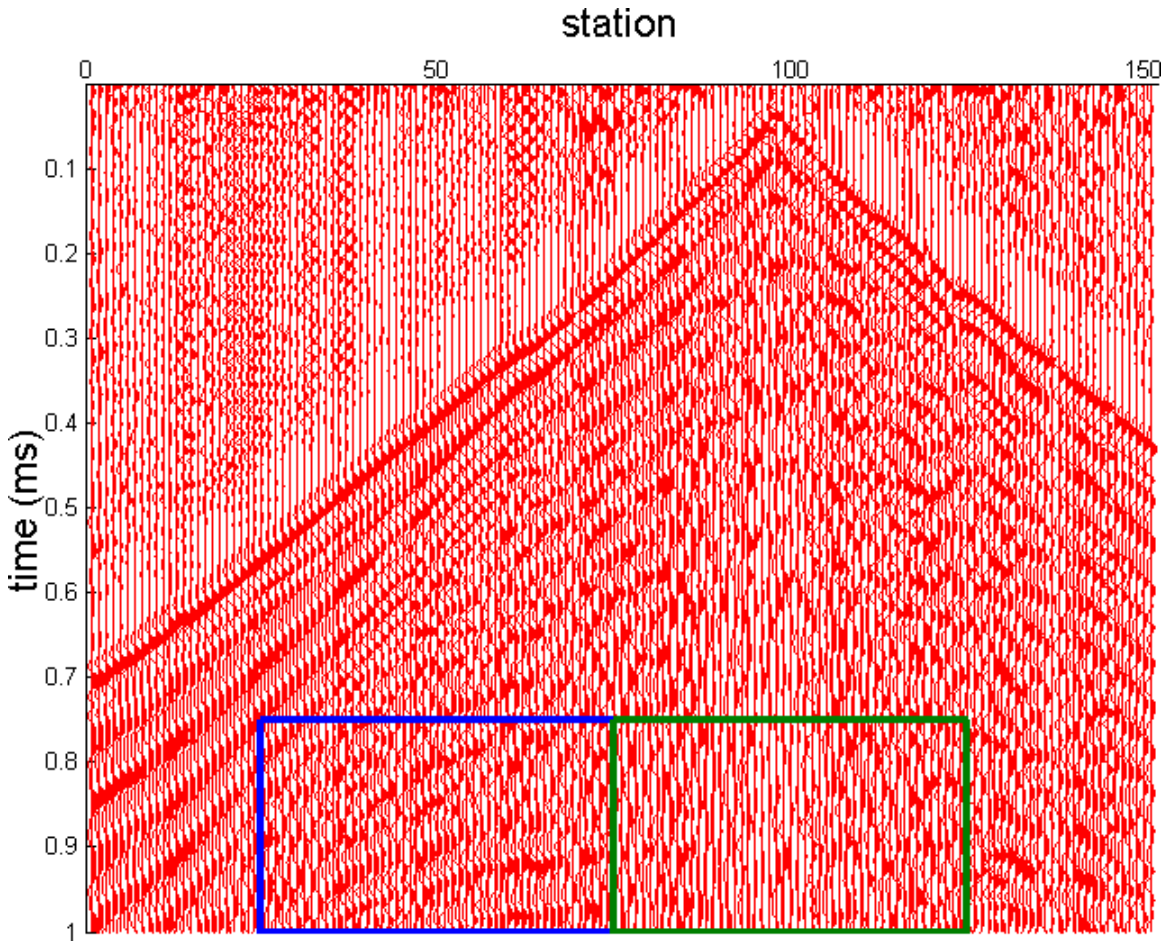

Figure 5.4: A raw shot record from shot station 50 of the Blackfoot data set.

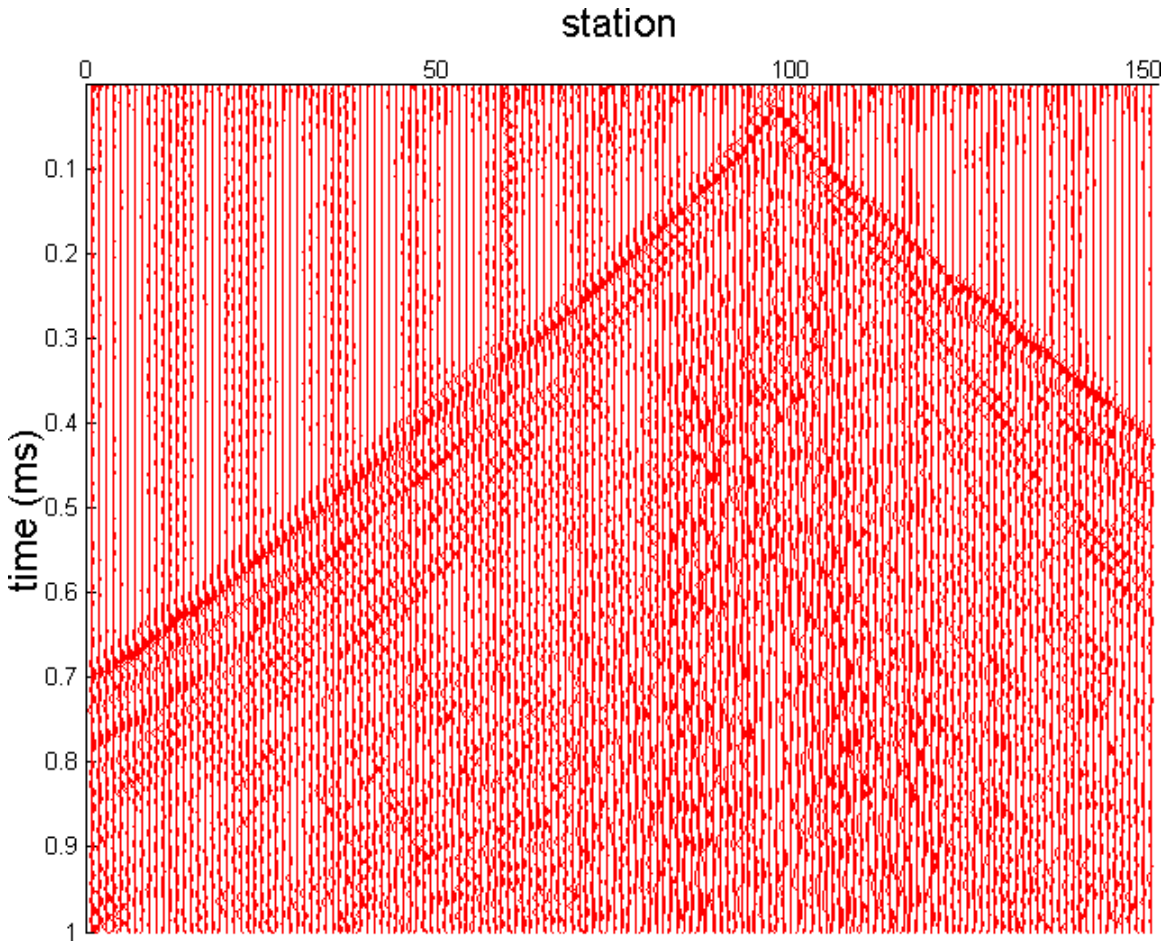

Figure 5.5: The same shot record from Figure 5.4, deconvolved using trace by trace operators.

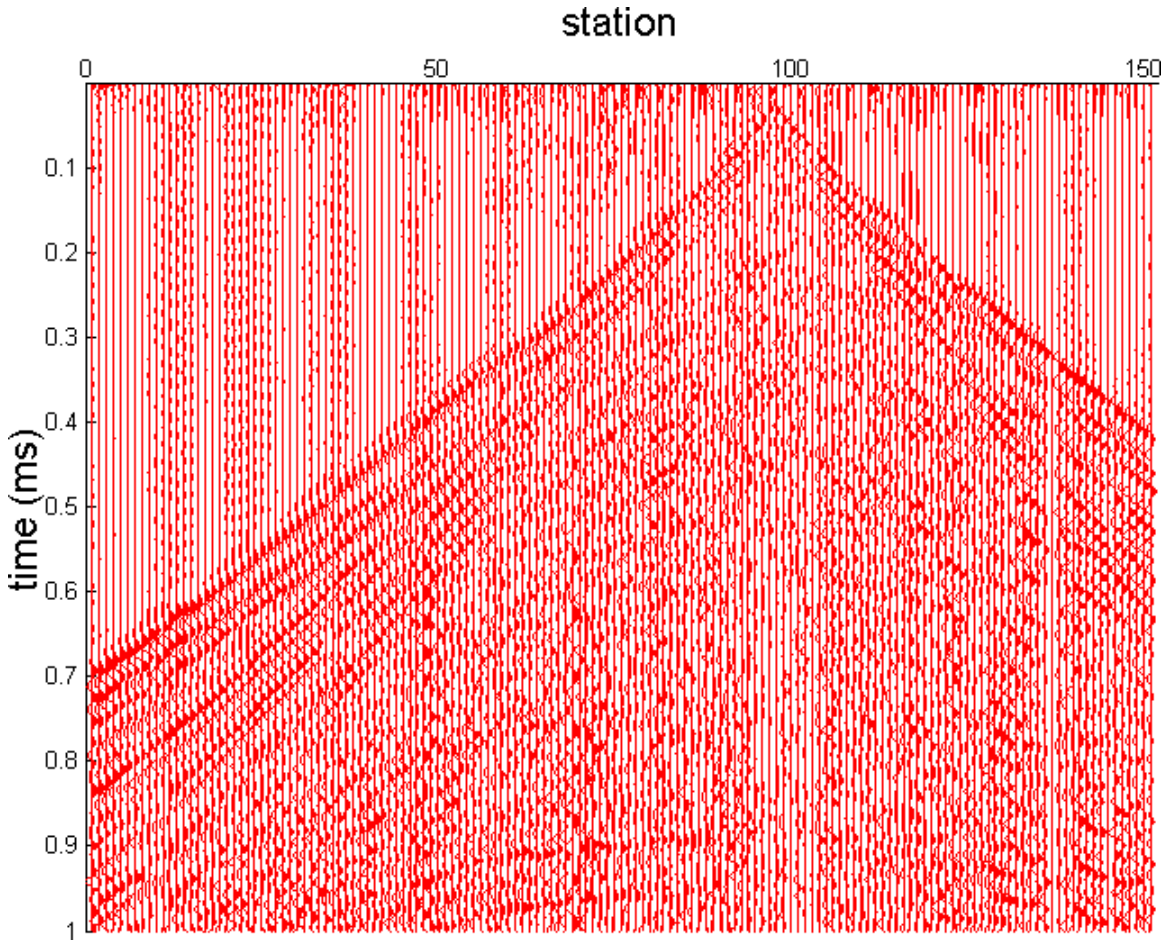

Figure 5.6: The same shot record from Figure 5.4, deconvolved using Gauss-Seidel surface consistent operators.

operators in Figures 5.1, 5.2 and 5.3.

To examine more closely the effect of our deconvolution operators, we zoom in on two distinct sections of the shot record. In Figures 5.9 through 5.13 we look at a section of data in shot record 50 that has very little interference between the ground roll and the reflectors. The section is between receivers 25 and 75, and in between times of 750 and 1000 milliseconds. Figures 5.15 through 5.19 contains data at the same time, but between receivers 75 and 125, where the reflectors are significantly obscured by ground roll and other

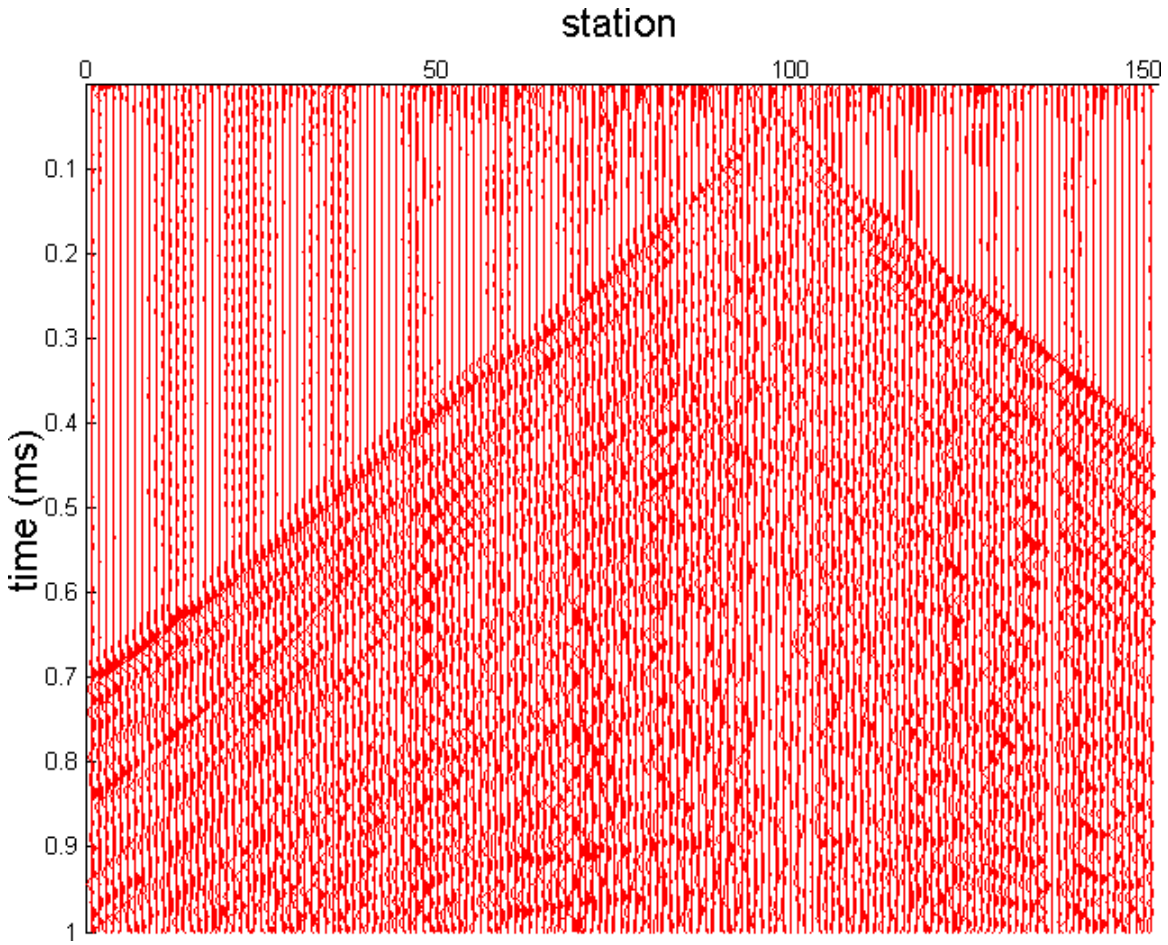

Figure 5.7: The same shot record from Figure 5.4, deconvolved using conjugate gradient surface consistent operators.

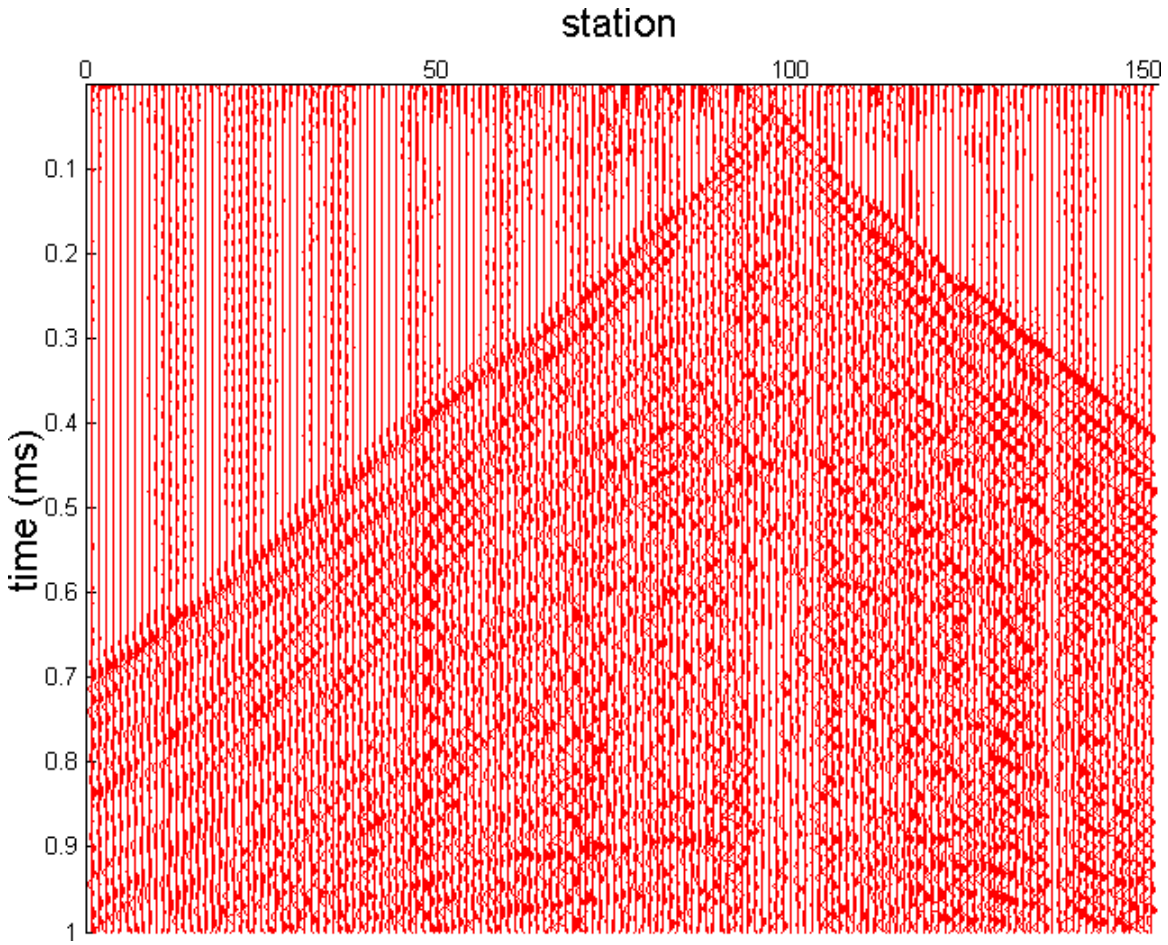

Figure 5.8: The shot record from Figure 5.4, deconvolved using multigrid surface consistent operators.

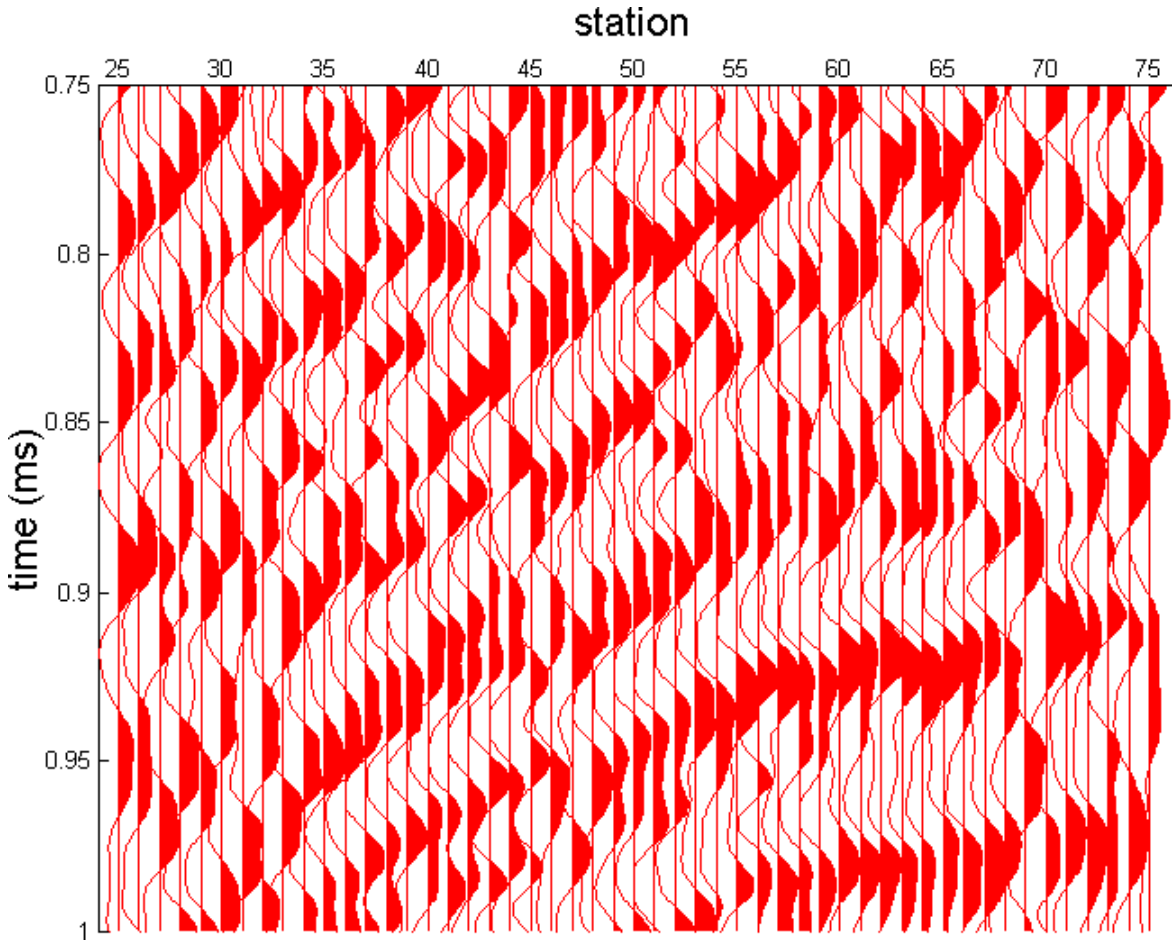

Figure 5.9: The raw data from shot record 50, zoomed in on the reflection.

surface noise.

There is very little difference in the character of the unobscured reflections deconvolved using the Gauss-Seidel and multigrid solutions in Figures 5.11 and 5.13. Both appear to be a big improvement over the results using trace by trace operators, and slightly higher frequency than the conjugate gradient data. The reflections through the shot record are are more coherent, and show more continuity.

Figure 5.14 shows the average Fourier amplitude spectrum of all of the data in the window with no ground roll. Only the components of the spectrum below 100 hertz are shown.

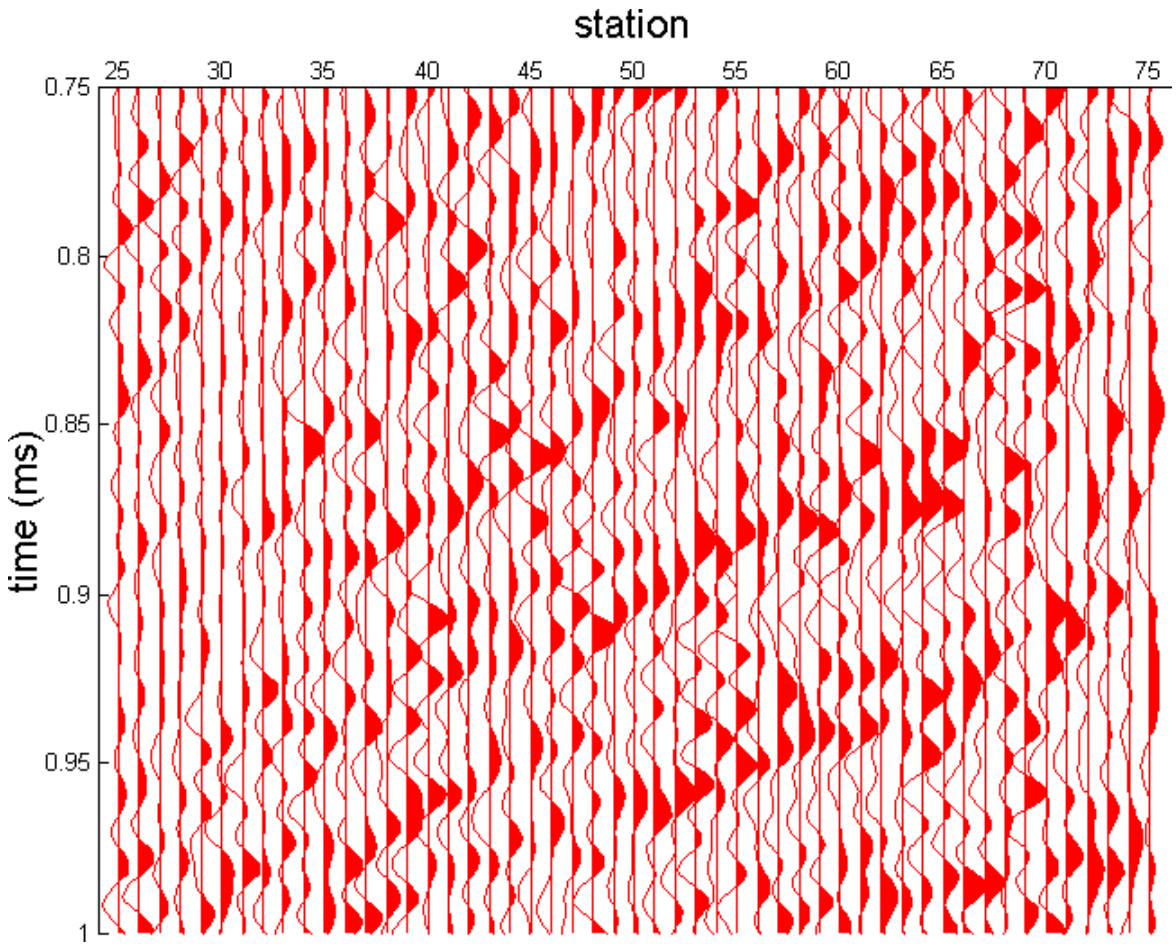

Figure 5.10: The trace by trace deconvolved data from shot record 50, zoomed in on the reflection.

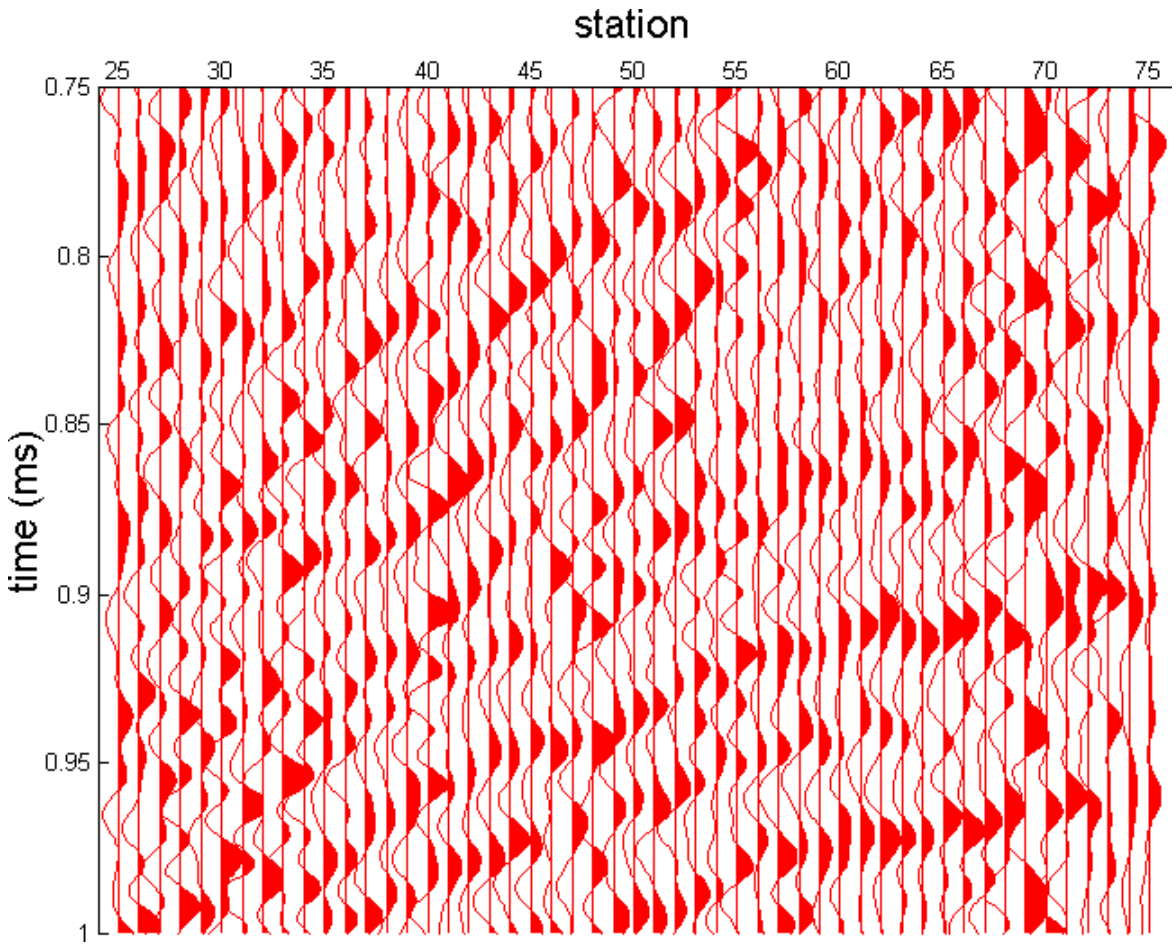

Figure 5.11: The from shot record 50, deconvolved using Gauss Seidel operators and zoomed in on the reflection.

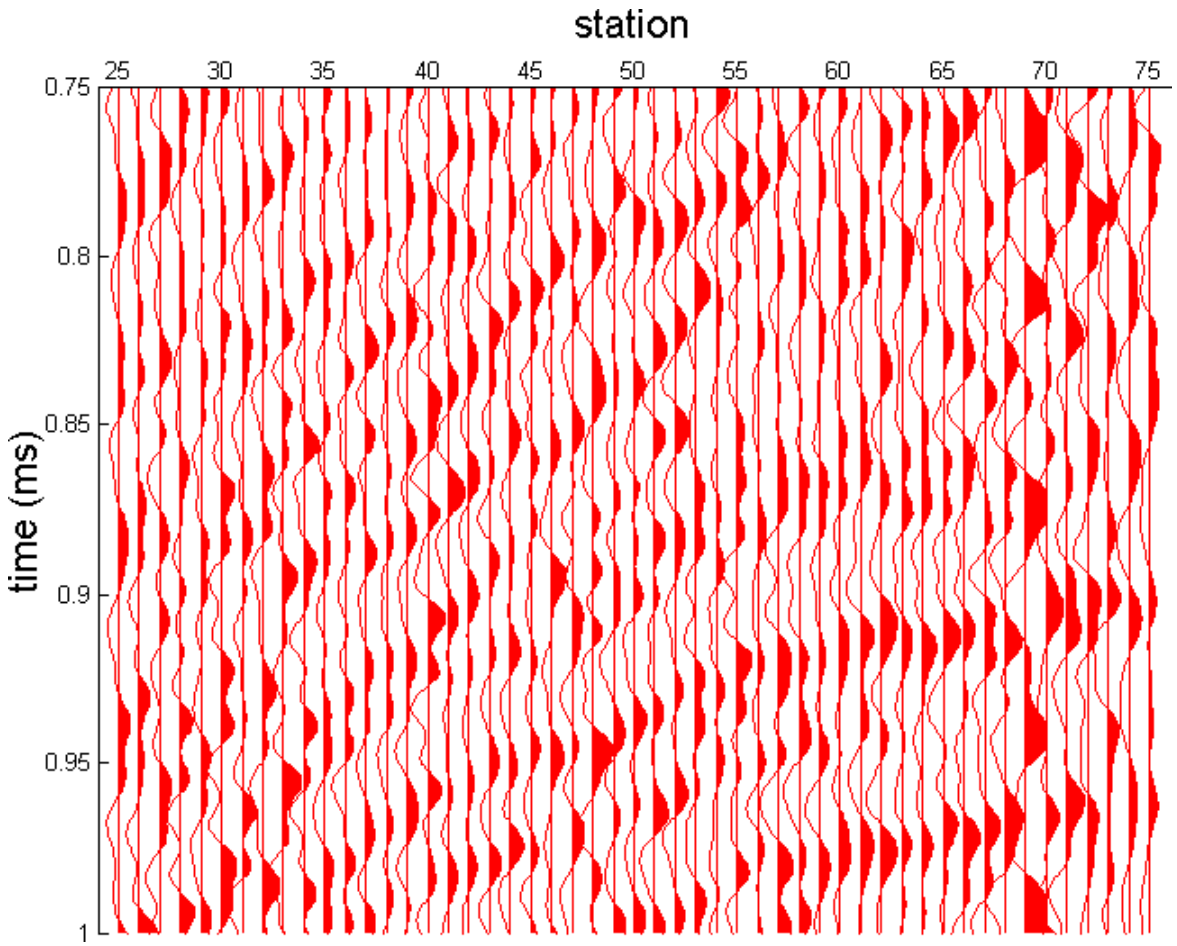

Figure 5.12: The from shot record 50, deconvolved using conjugate gradient operators and zoomed in on the reflection.

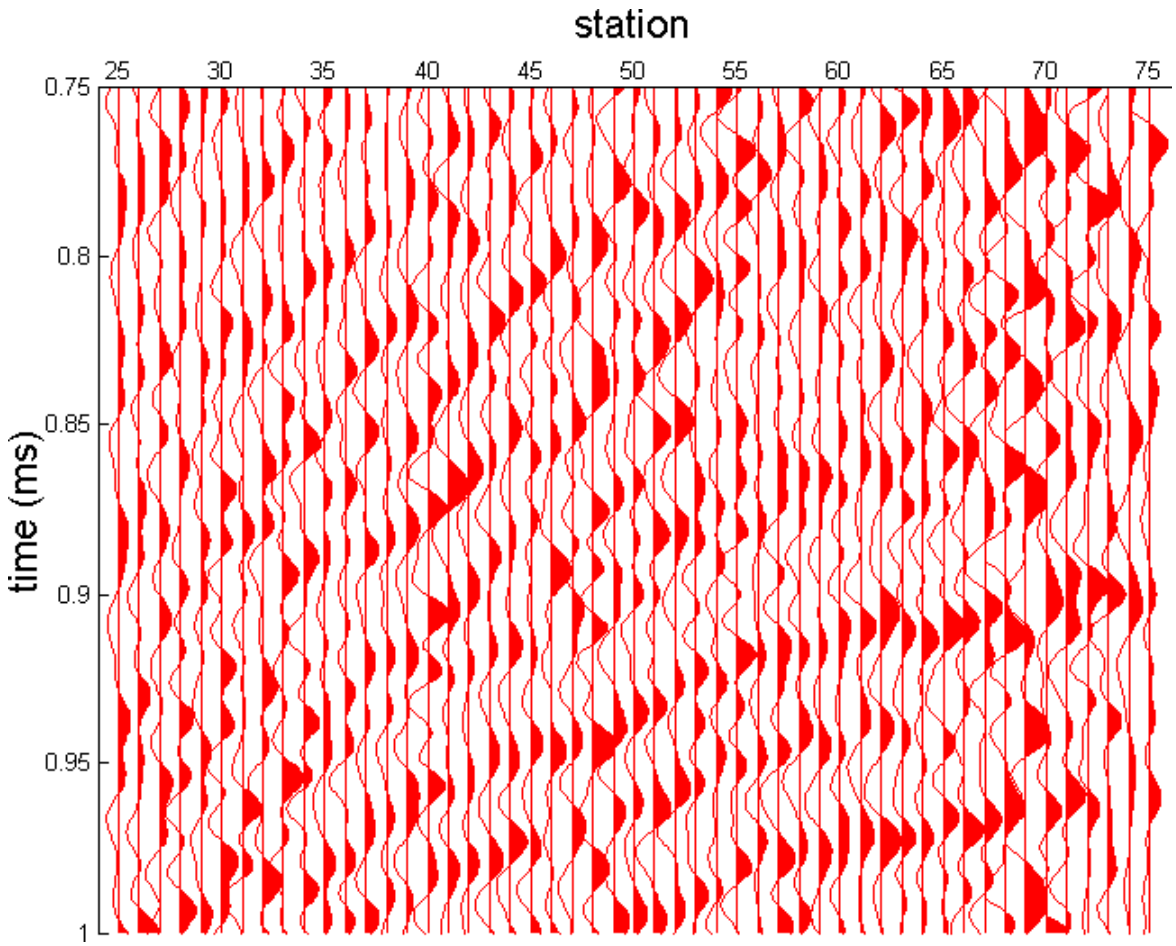

Figure 5.13: The data from shot record 50, deconvolved using multigrid operators and zoomed in on the reflection.

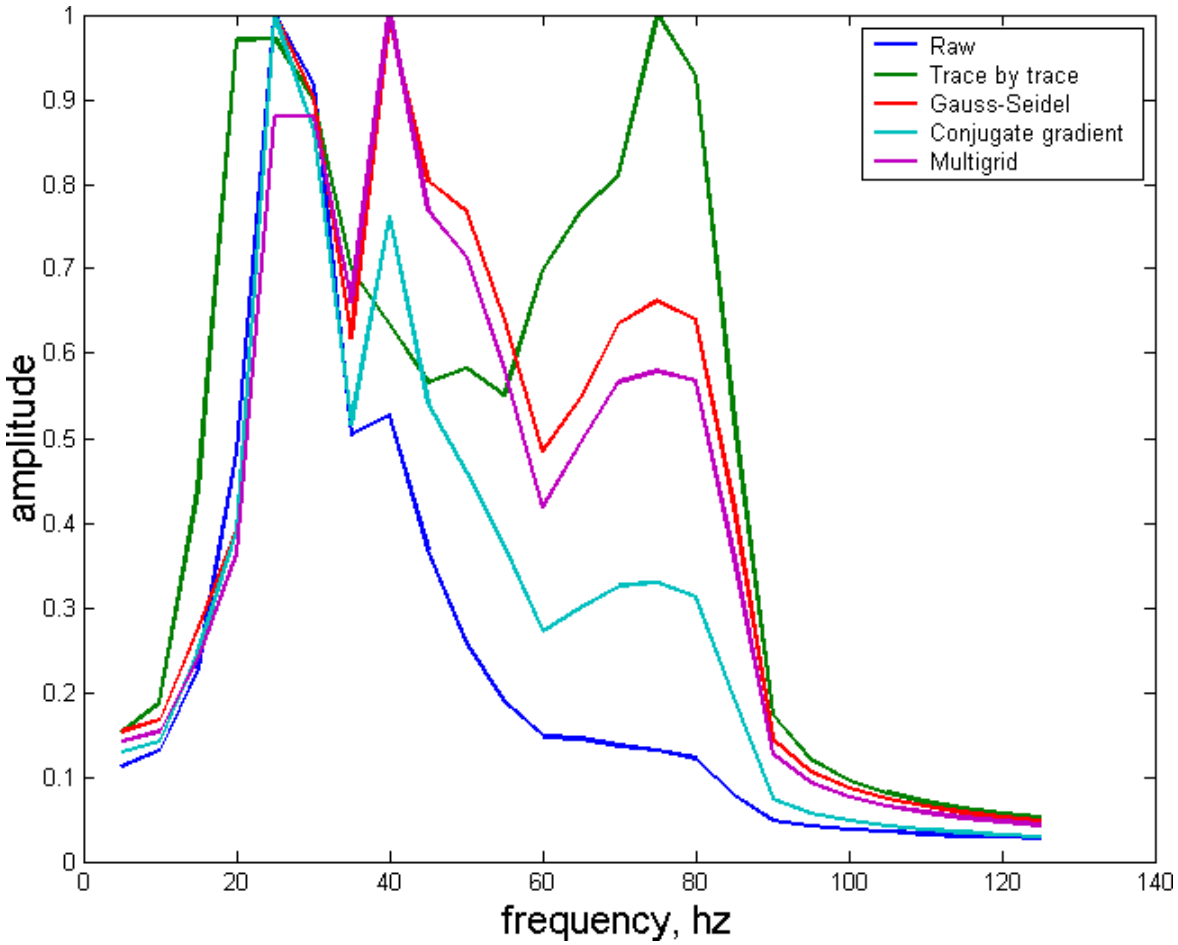

Figure 5.14: The average Fourier amplitude spectrum of the windowed data from Figure 5.9. This was the section of data where the reflections were fairly clean, and free from surface noise.

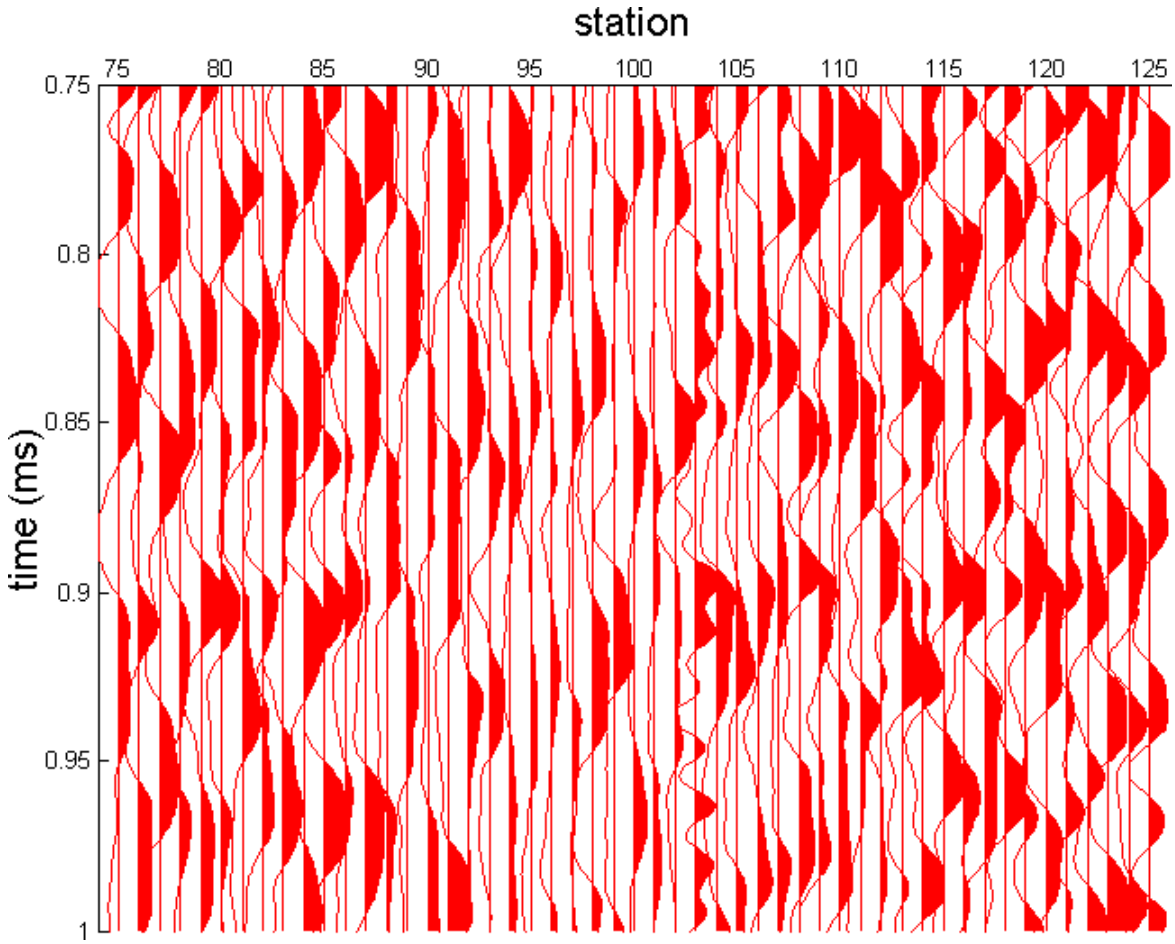

Figure 5.15: The raw data from shot record 50. There is significant ground roll interference in this part of the section.

Near wavenumber 10 ($\approx$ 40 hertz) the multigrid and Gauss-Seidel methods both boost the frequency higher than the trace by trace deconvolution. The two methods themselves are very similar, as the data in the time domain is itself nearly identical.

Around wavenumber 15, there is a large jump in the trace by trace deconvolution output spectrum, and a slightly smaller jump in the surface consistent output spectrums. This anomaly occurs at 60 hertz, and is likely due to the presence of 60 cycle power transmission noise.

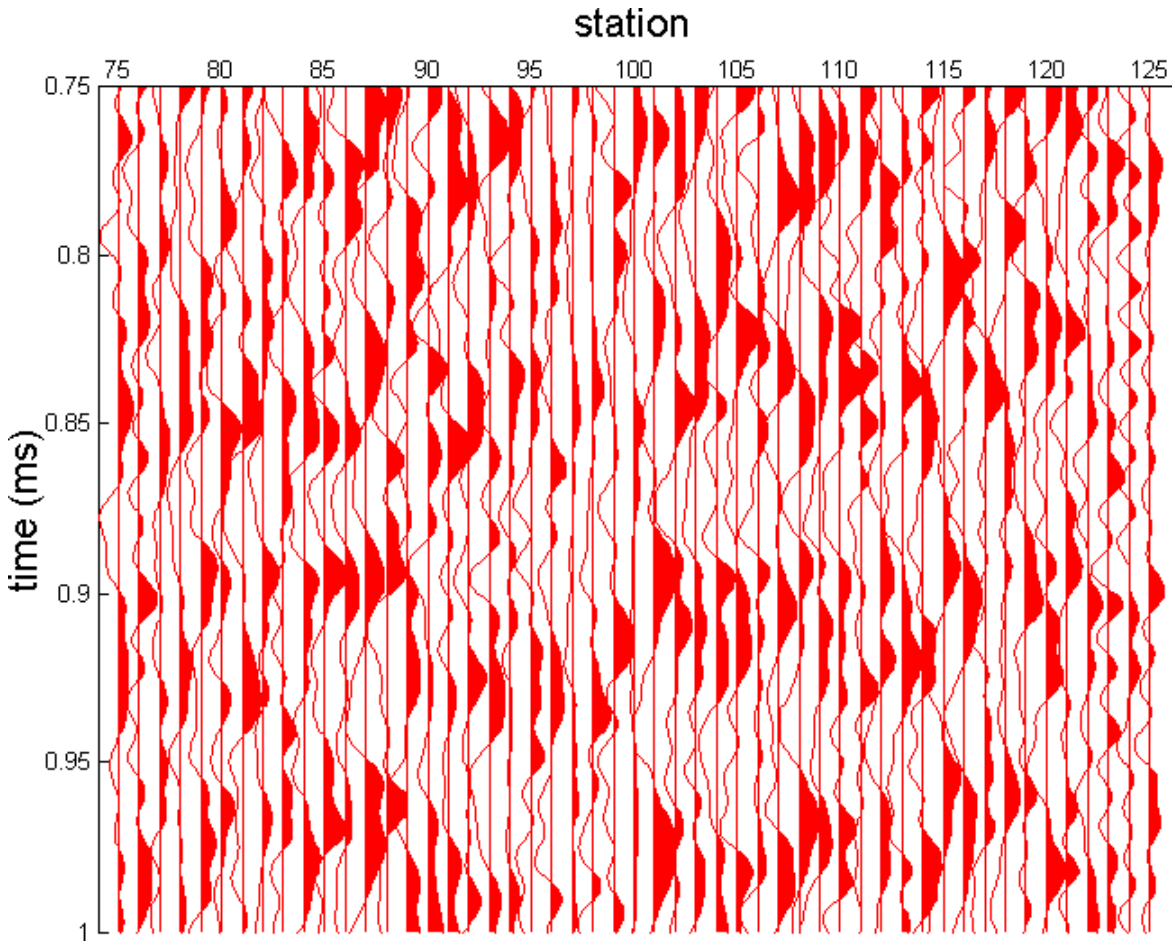

Figure 5.16: Data from shot record 50, trace by trace deconvolved. There is significant ground roll interference in this part of the section.

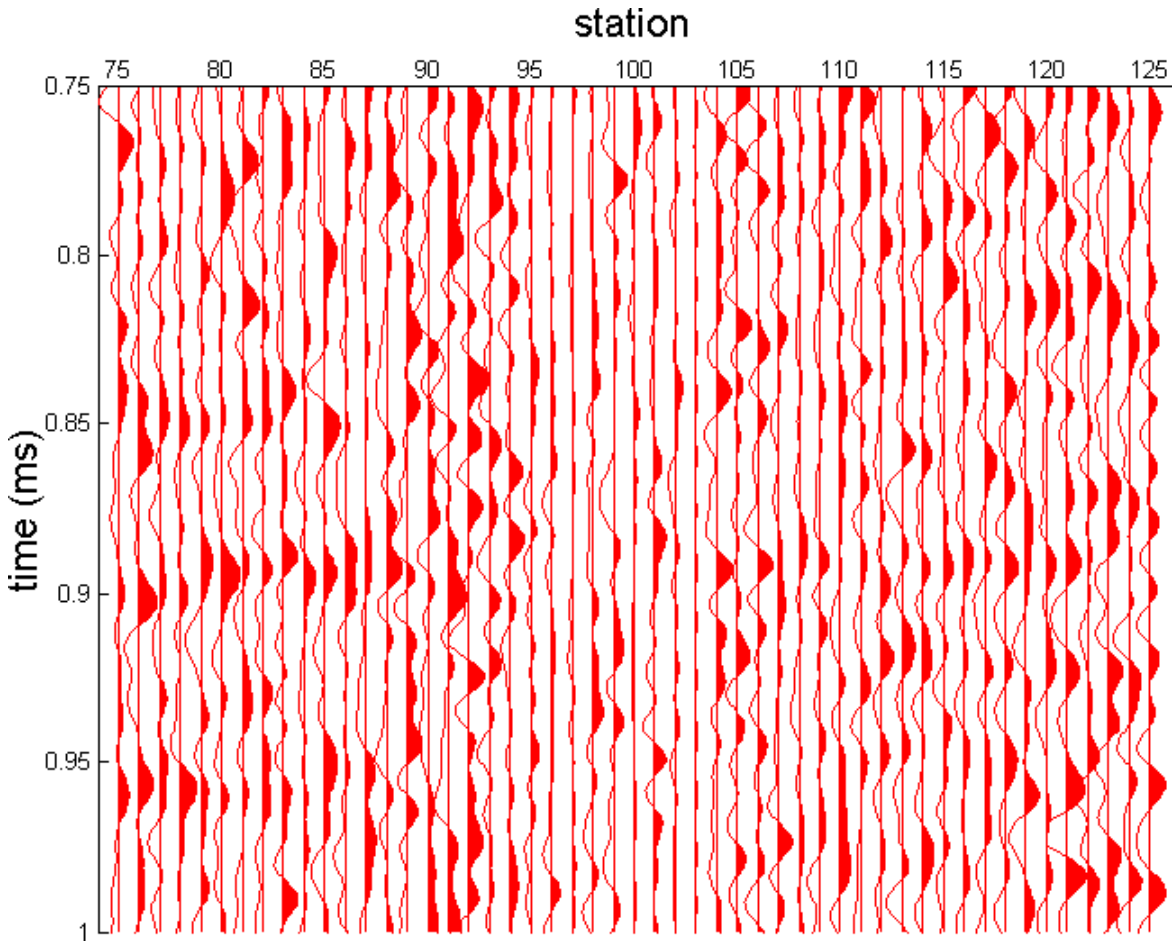

Figure 5.17: Data from shot record 50, deconvolved using Gauss-Seidel surface consistent operators. There is significant ground roll interference in this part of the section.

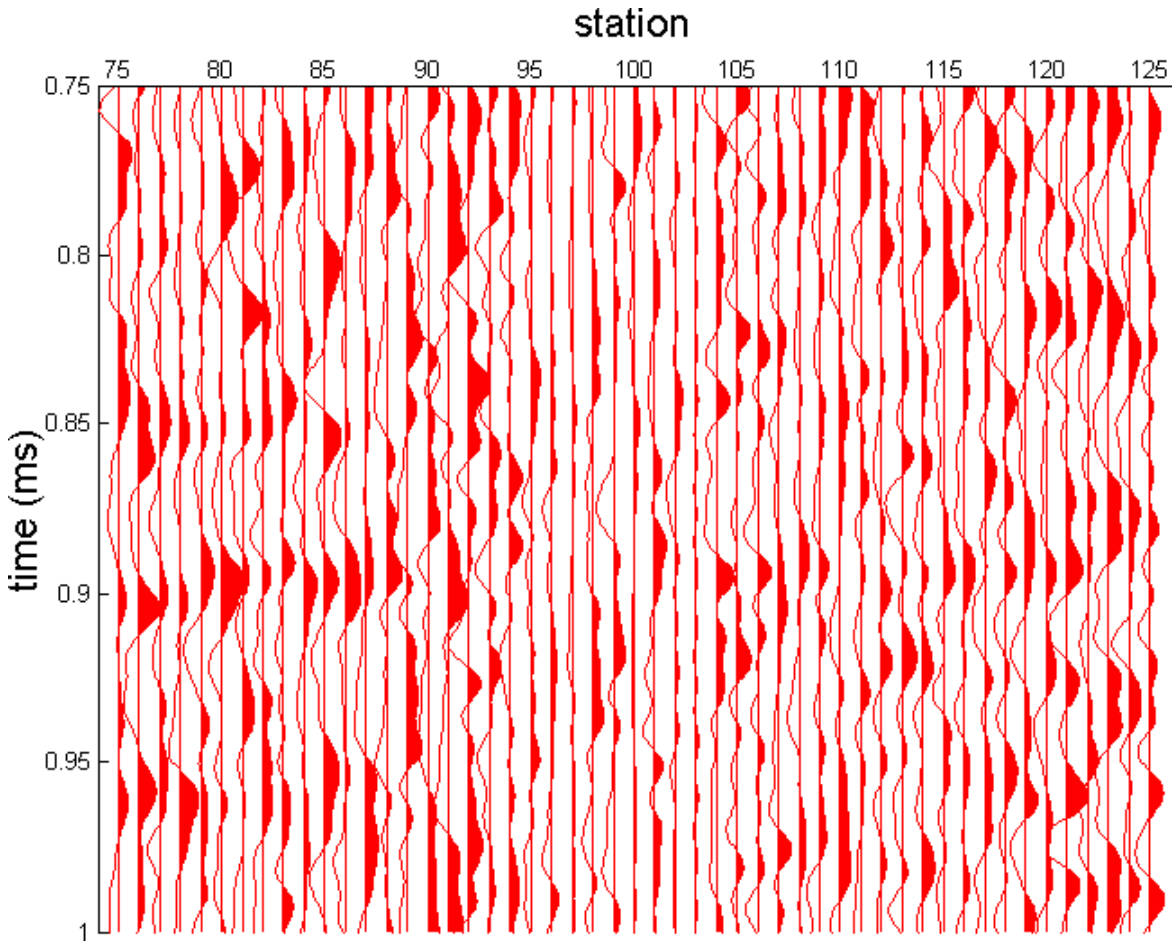

Figure 5.18: The raw data from shot record 50, deconvolved using conjugate gradient surface consistent operators. There is significant ground roll interference in this part of the section.

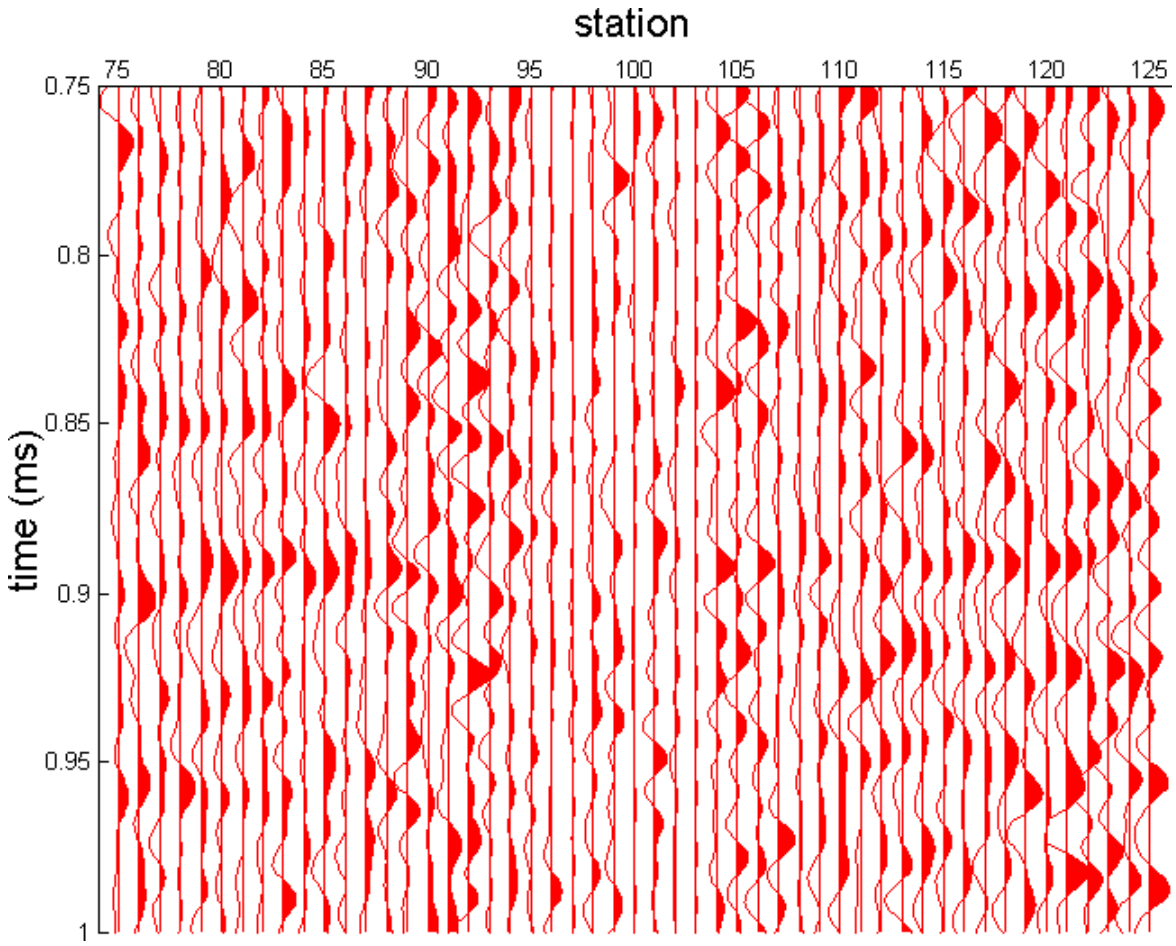

Figure 5.19: The raw data from shot record 50, deconvolved using multigrid surface consistent operators. There is significant ground roll interference in this part of the section.

The section of data that is obscured by ground roll shows a distinct difference between the results provided by the conjugate gradient, Gauss-Seidel and multigrid methods. The Gauss Seidel solution has more frequency content than the section calculated with a conjugate gradient solution. The reflectors in the multigrid deconvolved data appear to be both more coherent and continuous than the other methods. The horizontal reflector that appears at 0.9 seconds in the surface consistent deconvolutions is barely visible in the trace by trace deconvolution. It is more apparent in the Gauss-Seidel deconvolution, however is lost in the surface noise from receiver station 85 to receiver station 105. In the multigrid deconvoluted section, the data is visible across nearly the whole record, with the exception of a few traces directly below the shot (receiver station 98).

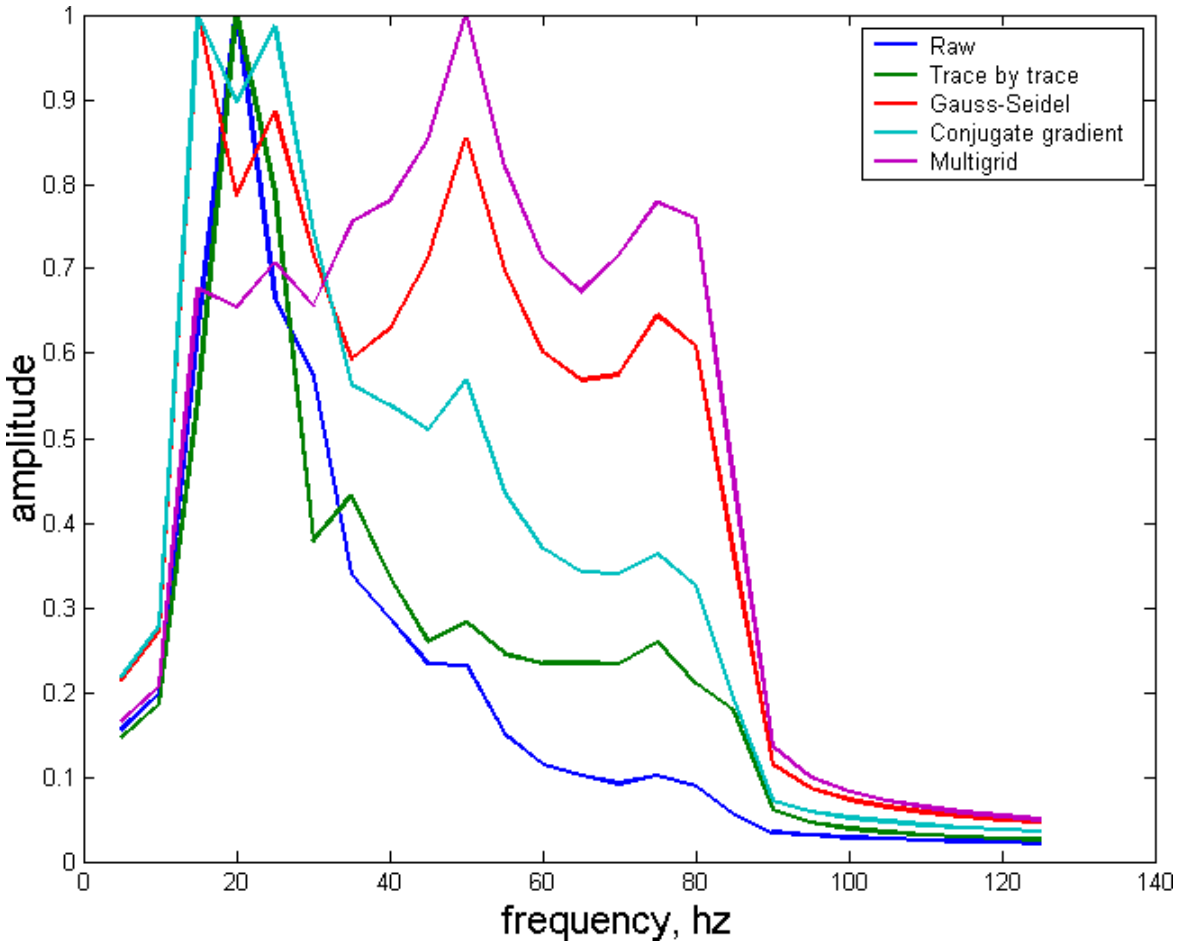

Figure 5.20: The average Fourier amplitude spectrum of the data from the deconvolved seismic data, in the section where there was significant interference to the reflectors from surface noise.

5.1 Other Gathers

Seismic data is collected as groups of receivers measuring the response of a single source. The data is naturally sorted into shot records when we collect it. Four term surface consistent deconvolution projects the data into source, receiver, midpoint, and offset components. It is important to evaluate the solution methods in each of these dimensions.

Reflected seismic energy will be coherent in all four coordinate dimensions, whereas noise is unlikely to be so. A genuine improvement in signal quality should be visible when we sort the data into gathers containing only the traces from a particular receiver, or traces that have a midpoint or offset between a specified range.

The following section contains a variety of different gathers of the same Blackfoot data, starting with Figure 5.21.

Figure 5.21 compares the amplitude spectrum of all the reflectors in a common receiver gather, before and after each of our decovolution techniques.

In Figures 5.22 through 5.26 we look at all of the traces recorded by the receiver at station 75, near the center of the survey. We have zoomed in on the reflections between 750 and 1000 ms. The traces are plotted against the source station number. The center section of data is obscured by ground roll, much like in the source gathers. The seismic reflections are hyperbolic in the receiver gather. The data deconvolved using multigrid operators appears to have the most high frequency content, and has more coherent reflections in the section obscured by surface noise than the other gathers.

Figure 5.27 compares the amplitude spectrum of all of the traces that have a source-receiver midpoint between 350 and 360m from receiver station 1, near the center of the survey. Figures 5.28 through 5.32 show the raw and deconvolved midpoint gathers from the

same location. The multigrid processed gathers again have what appears to be a stronger signal showing through the noisy middle part of the gather. These observations are consistent with those made when examining the shot records.

Figure 5.33 shows shot record 50. The navy blue box surrounds the traces in this gather with a source receiver offset of between 200 and 210 meters. There is not a lot of ground roll interference in this part of the survey. Figures 5.36 through 5.40 contain common offset stacks of traces in the survey with this offset. Every fifth trace is displayed. The horizontal axis is the distance of the source-receiver midpoint from receiver station 1.

Normal moveout is a function of offset, so the reflections that appear hyperbolic in the other gathers are imaged flat across the offset section. Figures 5.41 through 5.45 depict traces with offsets of between 20 and 30 meters, corresponding to the green highlight in Figure 5.33. Traces whose receivers are this close to the source station experience significant ground roll interference obscuring the seismic reflections.

Figures 5.34 and 5.35 compare the amplitude spectrum of all the traces in the offset gathers.

The difference between the deconvolution results in the far offsets (Figures 5.36 through 5.40) is not very large. The multigrid section appears to have the best image quality, in that the reflections have a more consistent amplitude, and some minor features in the data that are not visible in the conjugate gradient and Gauss-Seidel derived sections, are visible in the multigrid result.

The strength of the multigrid solution is most apparent in the near-offset gathers. This concentrates the data with the most severe ground roll problems into a single plot. There is almost no coherent energy in the conjugate gradient (Figure 5.43) and Gauss-Seidel derived gathers (Figure 5.44). The data deconvolved using multigrid surface consistent operators

has imaged several of the reflections obscured by ground roll.

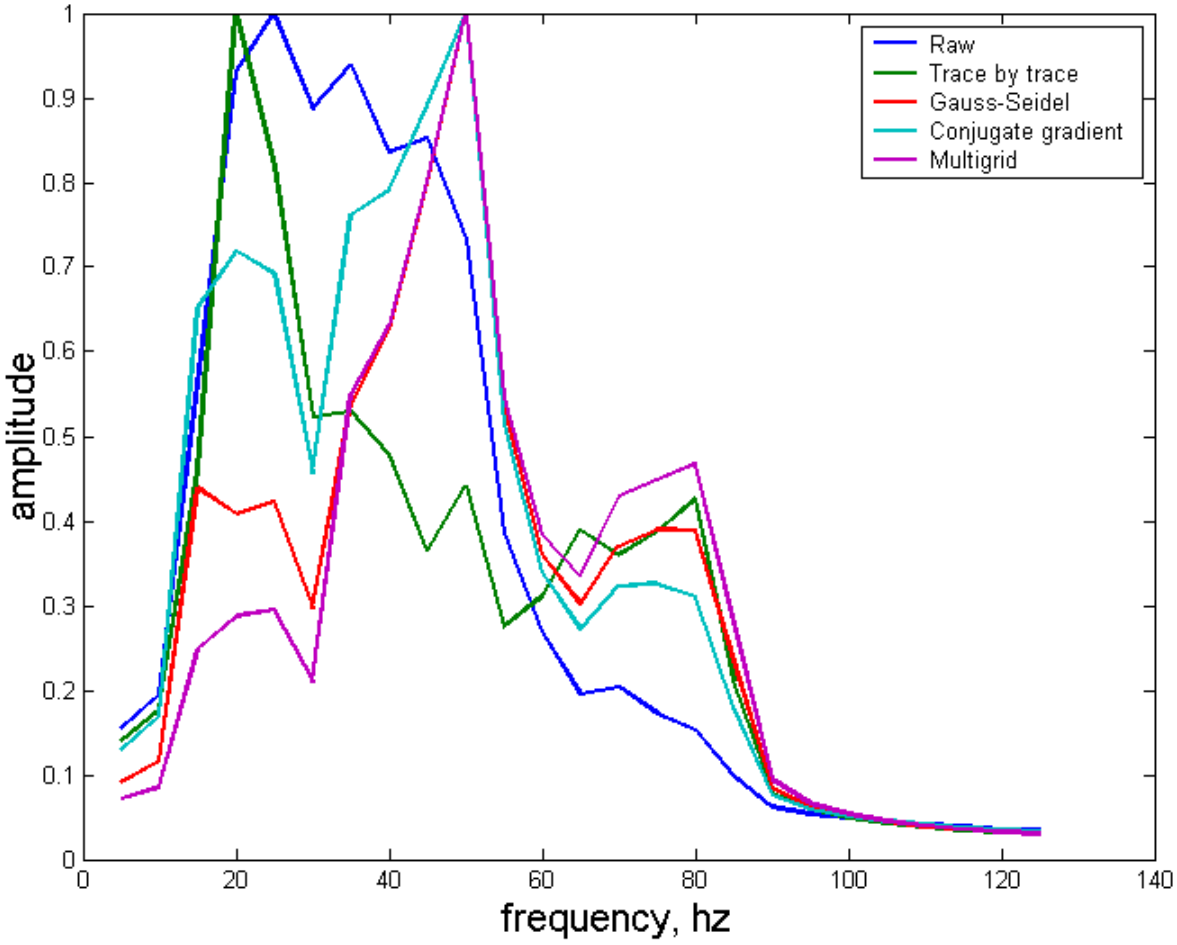

Figure 5.21: The amplitude spectrum of all traces recorded at receiver station 75, between 0.75 and 1 second.

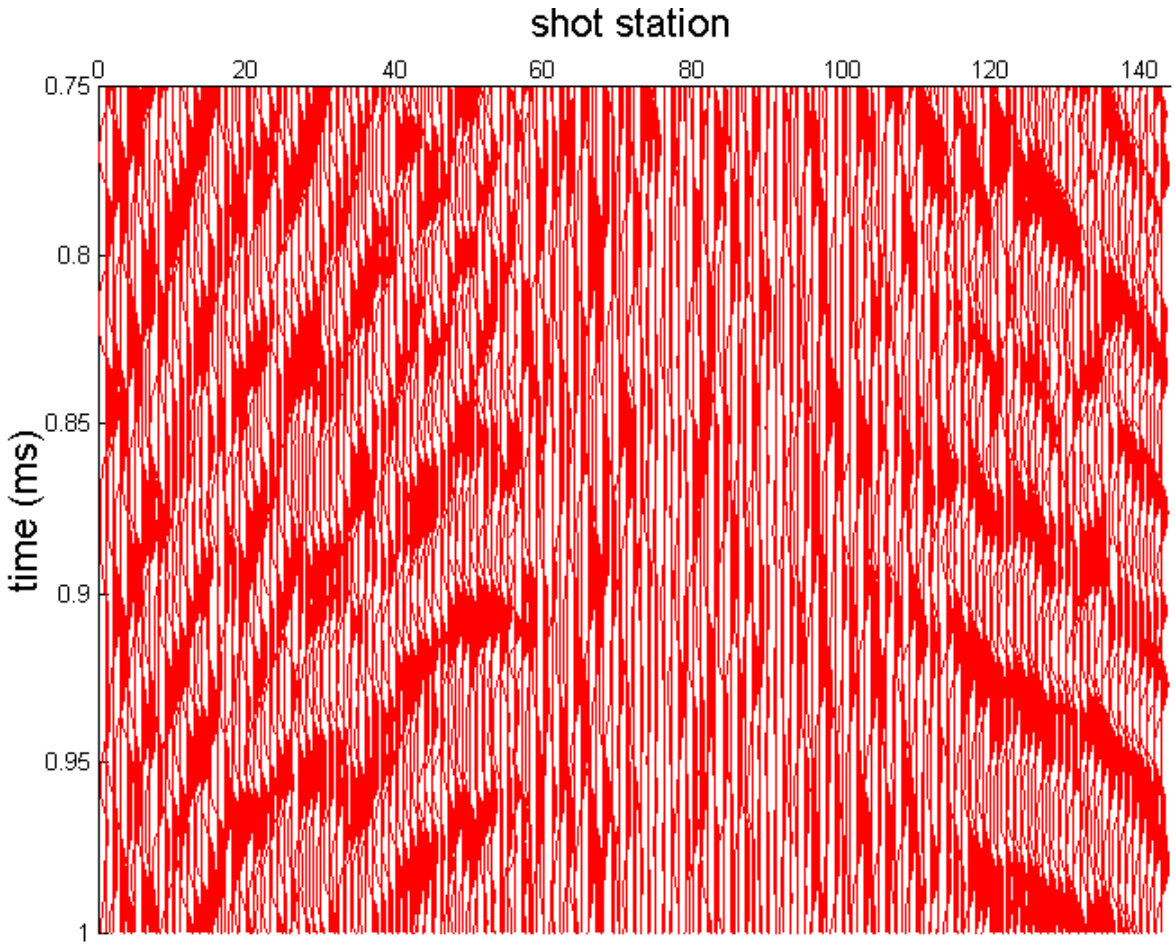

Figure 5.22: This raw receiver gather is from receiver station 75, and is zoomed in on $0.75 - 1.0s$.

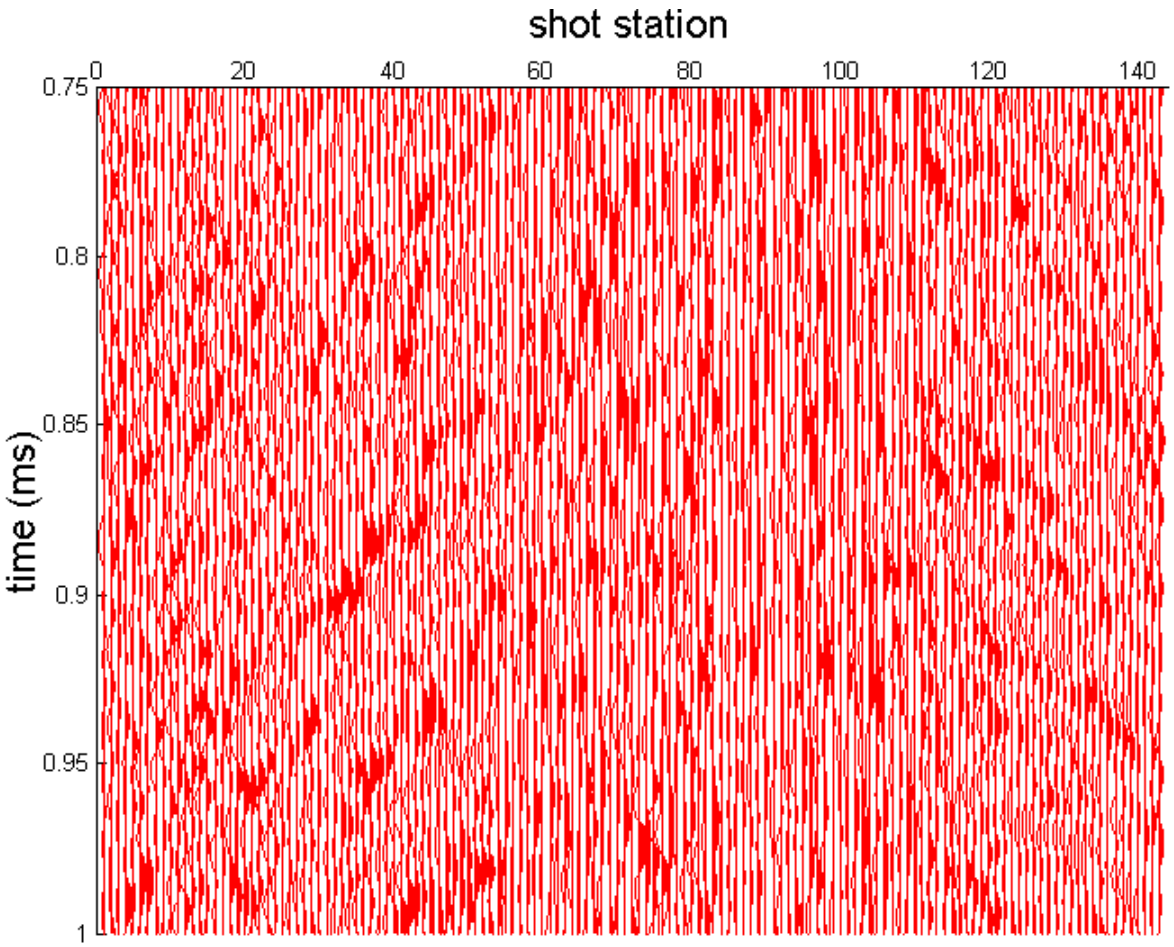

Figure 5.23: This receiver gather was deconvolved using operators calculated trace by trace.

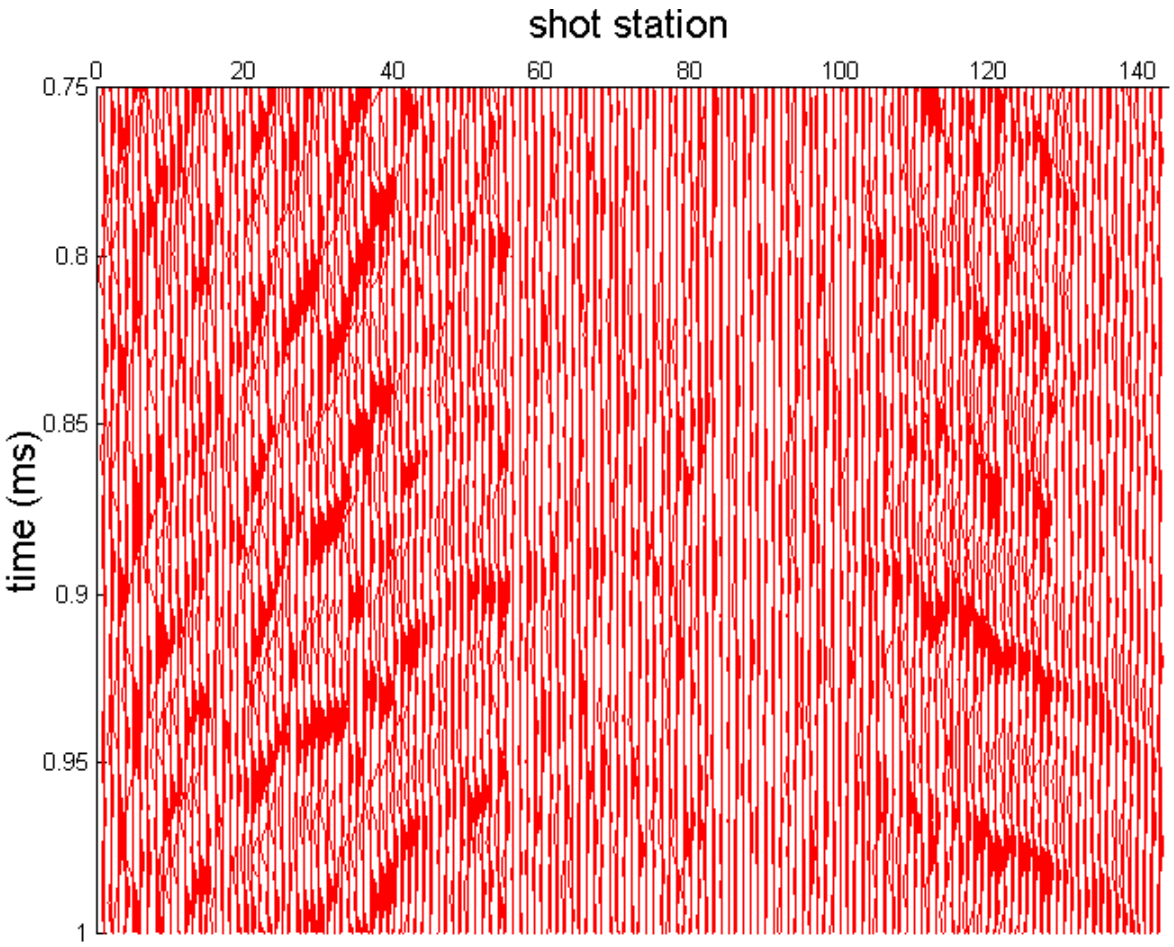

Figure 5.24: This receiver gather was deconvolved using surface consistent operators calculated using the conjugate gradient method.

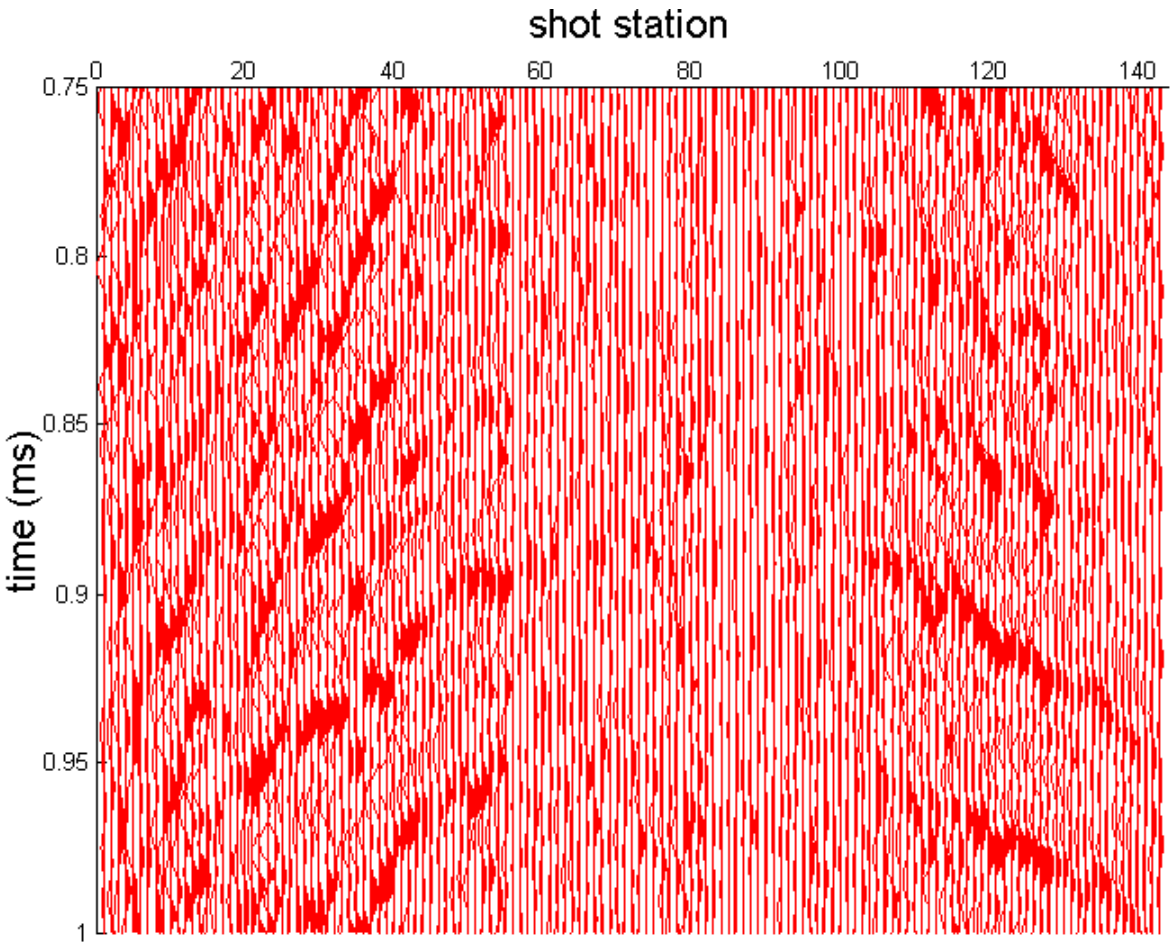

Figure 5.25: This receiver gather was deconvolved using surface consistent operators calculated using the Gauss-Seidel method.

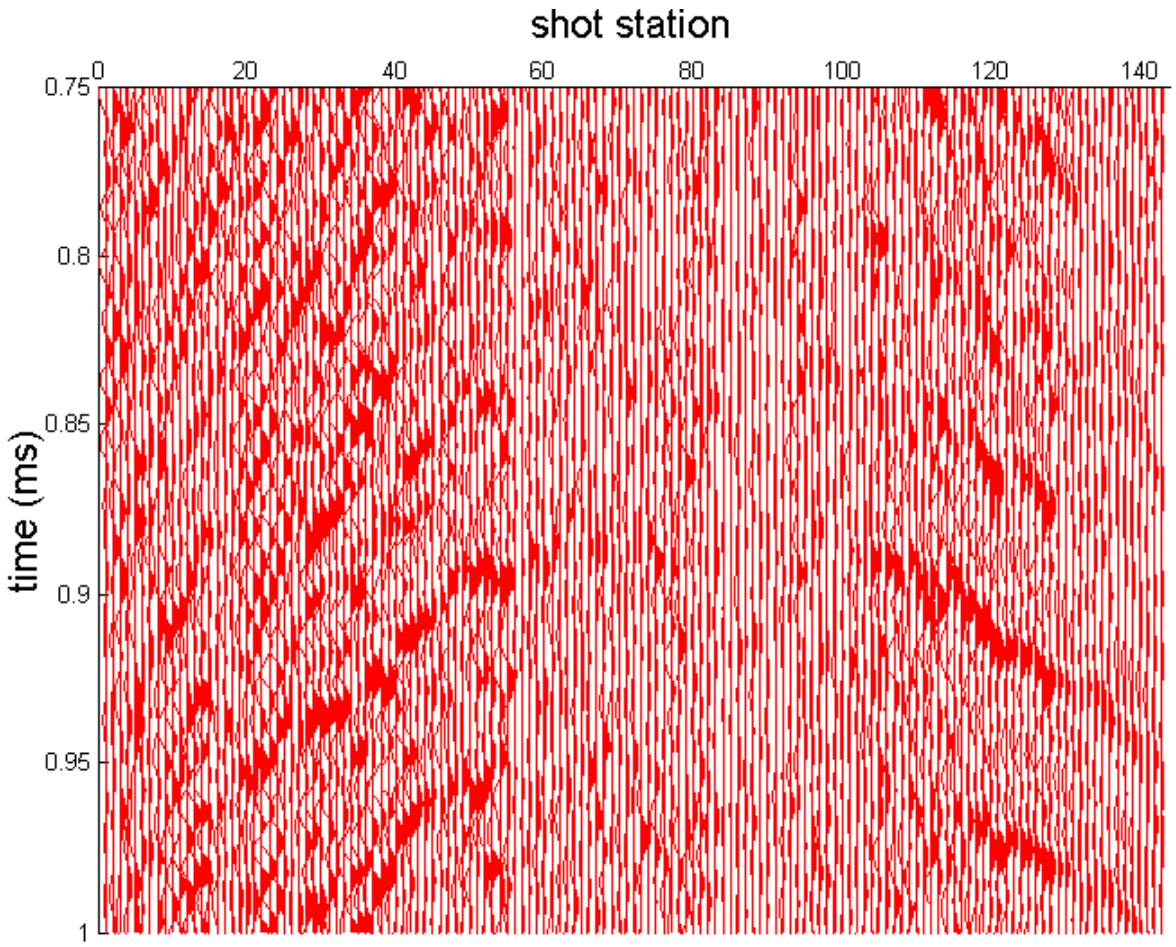

Figure 5.26: This receiver gather was deconvolved using surface consistent operators calculated using the multigrid method.

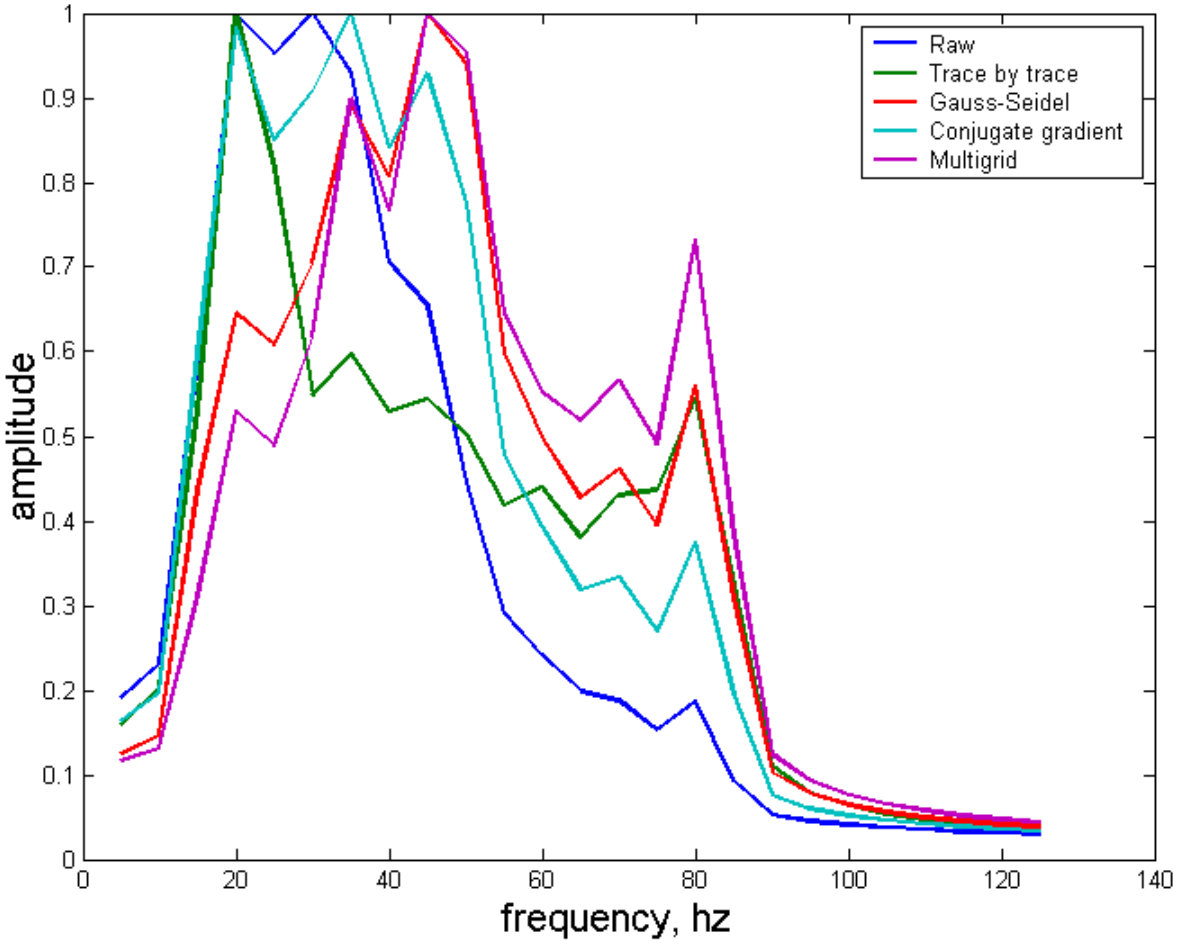

Figure 5.27: The amplitude spectrum of all traces with a midpoint between 350 and 360 meters from the first receiver station.

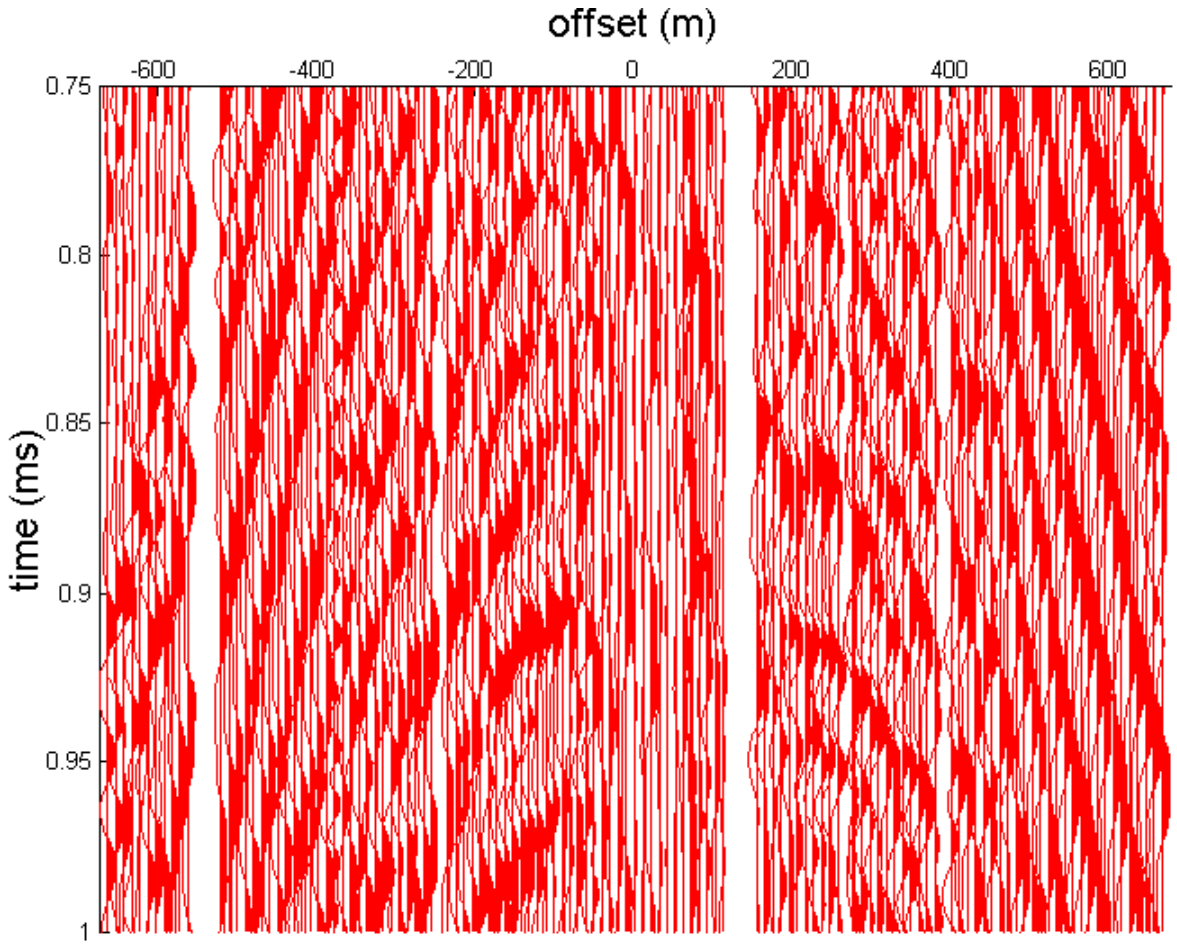

Figure 5.28: This raw gather has all of the traces with a midpoint coordinate between 350 and 360 meters.

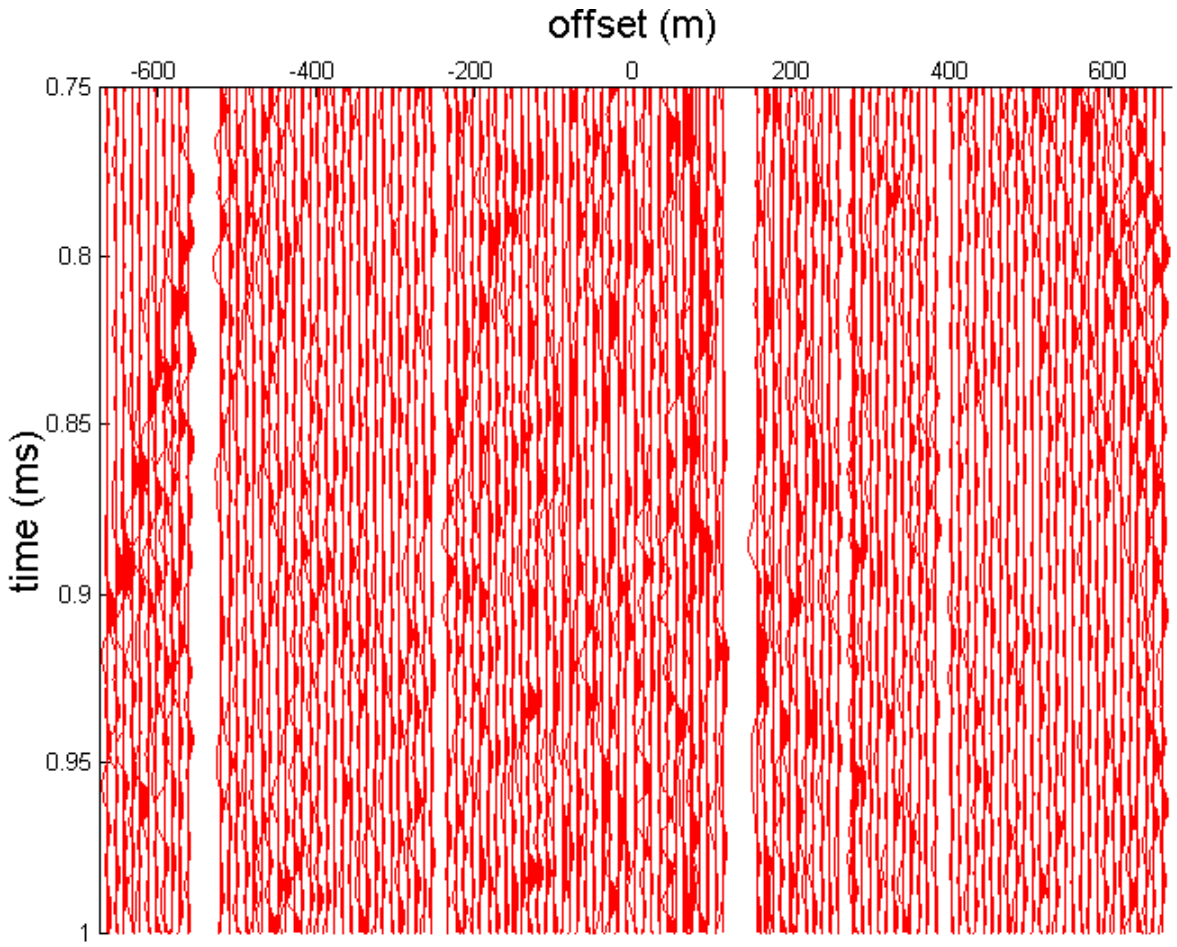

Figure 5.29: This is the same midpoint gather, deconvolved using operators calculated trace by trace

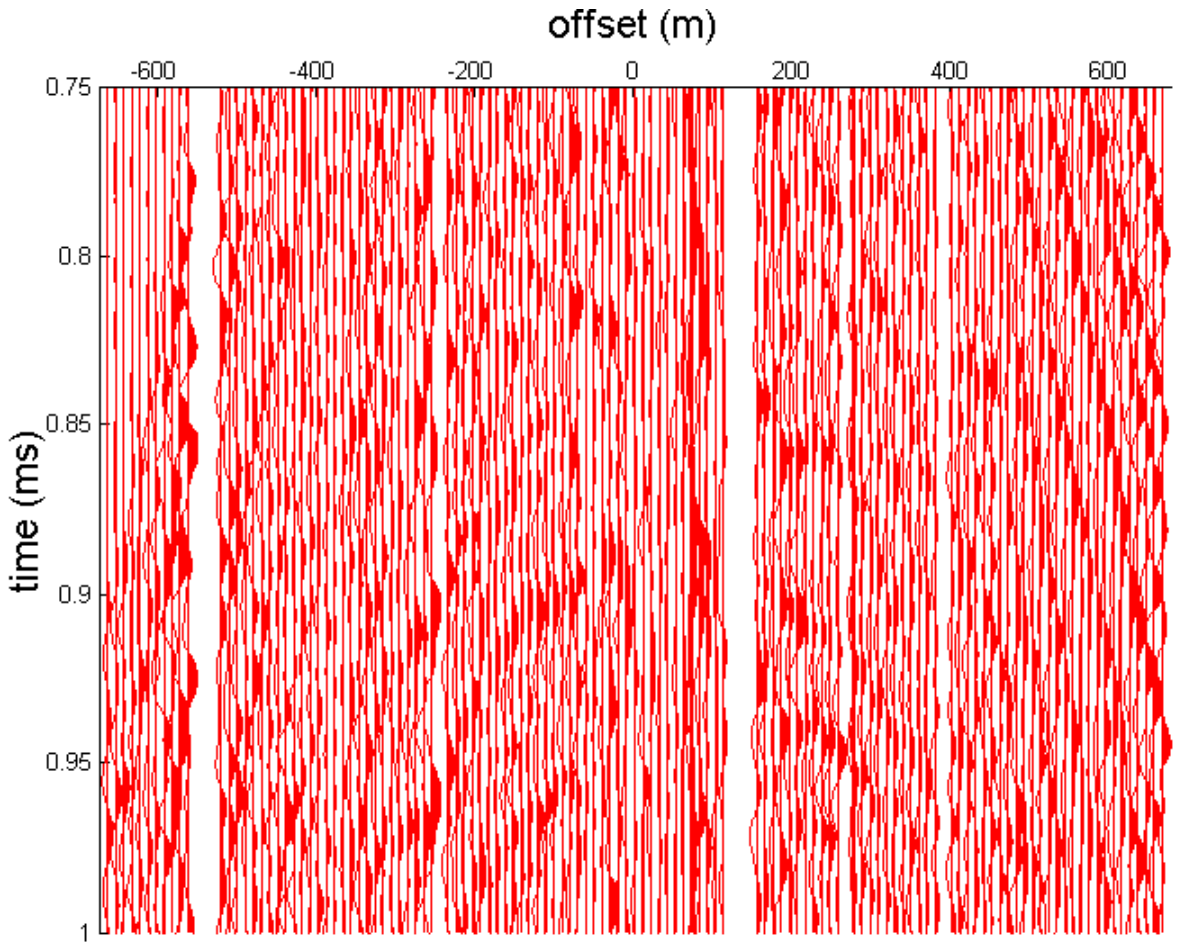

Figure 5.30: This midpoint gather was deconvolved using surface consistent operators calculated using the conjugate gradient method.

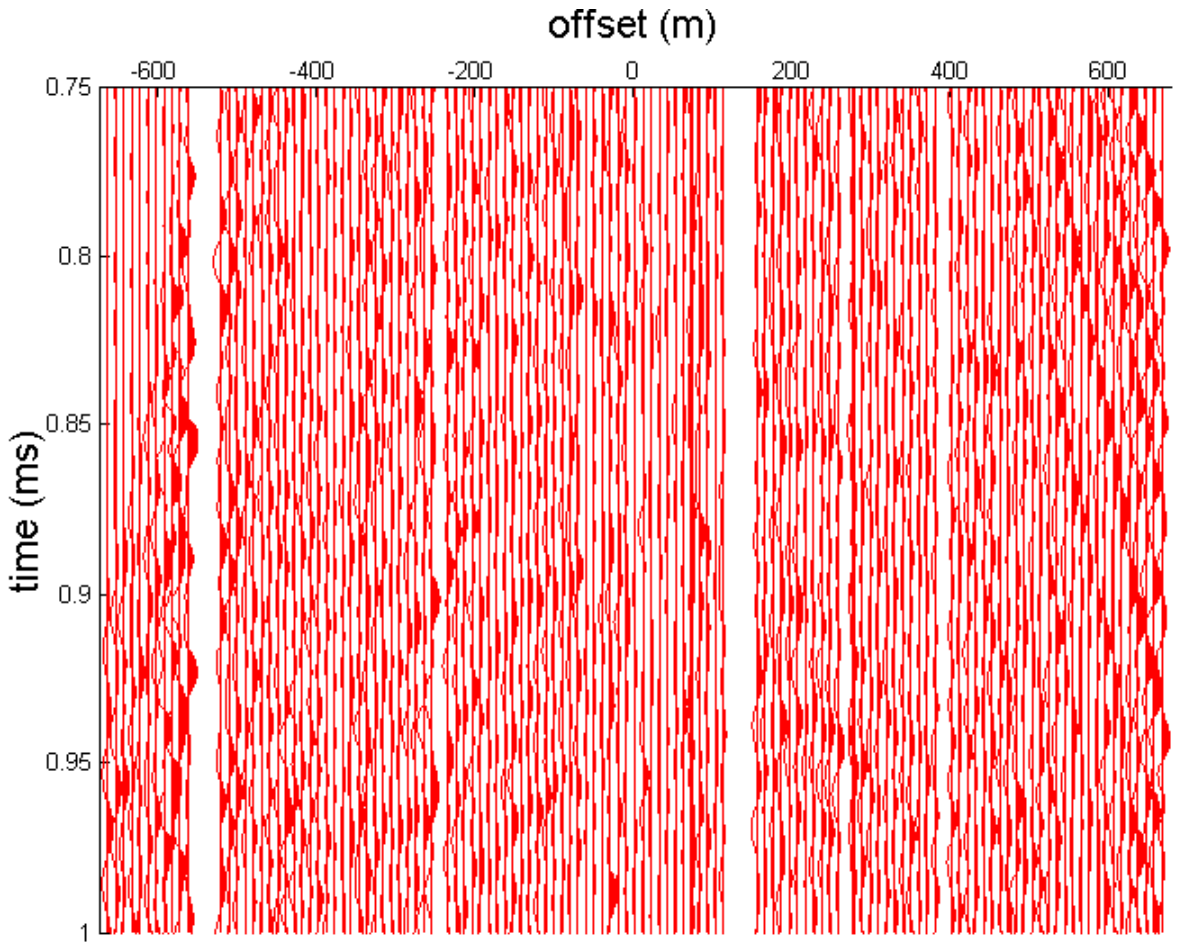

Figure 5.31: This midpoint gather was deconvolved using surface consistent operators calculated using the Gauss-Seidel method.

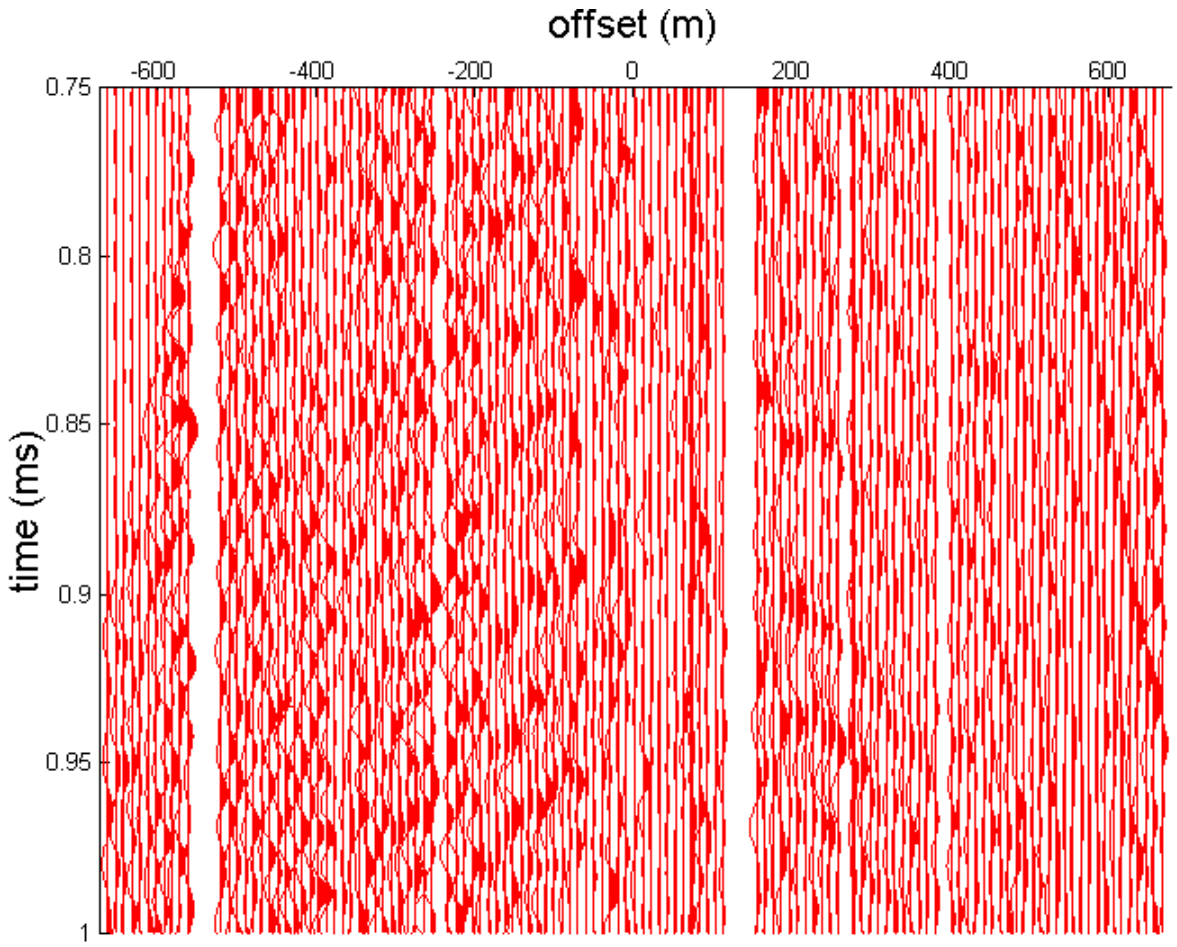

Figure 5.32: This receiver gather was deconvolved using surface consistent operators calculated using the multigrid method.

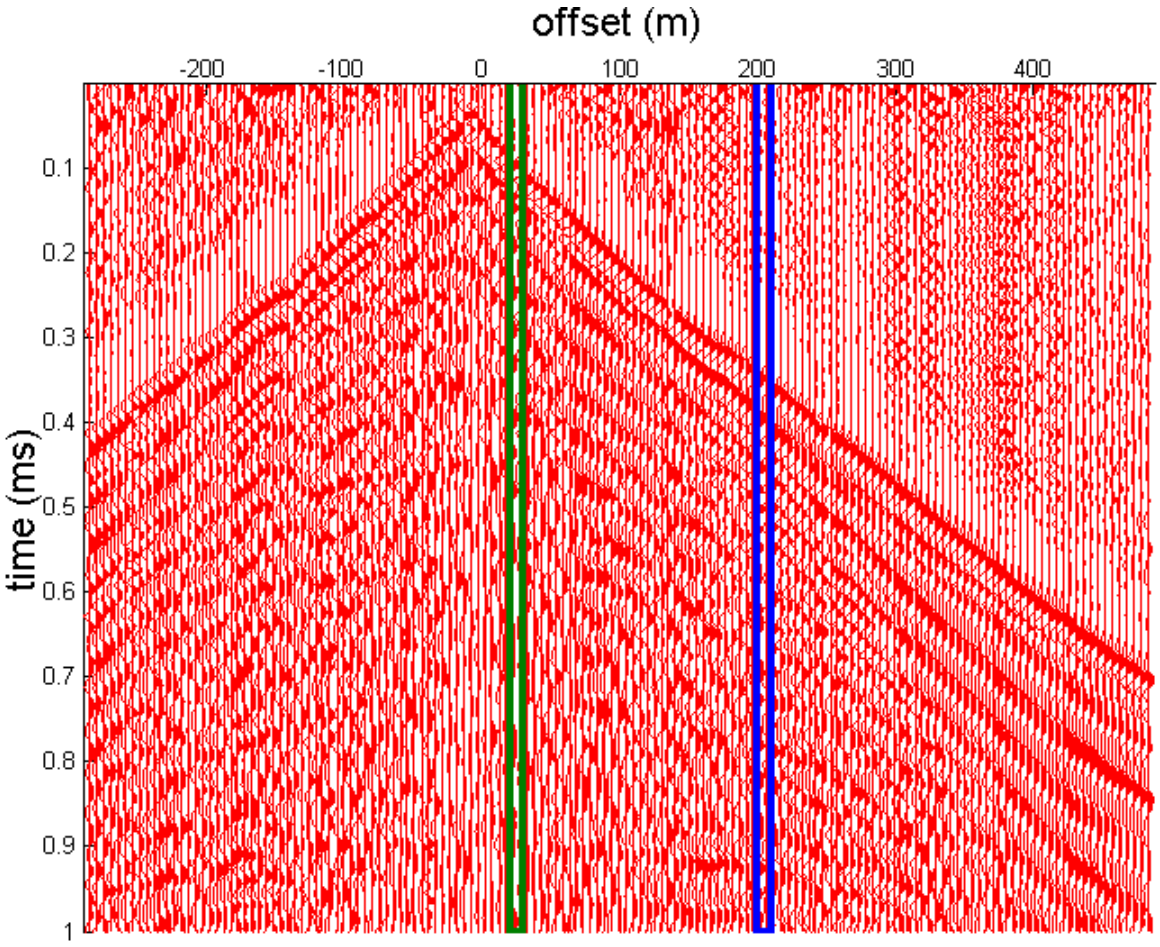

Figure 5.33: This is shot record 50, with a navy blue square around the trace that belong to the far-offset stack, and a green highlight of the trace from this record in the near-offset stack.

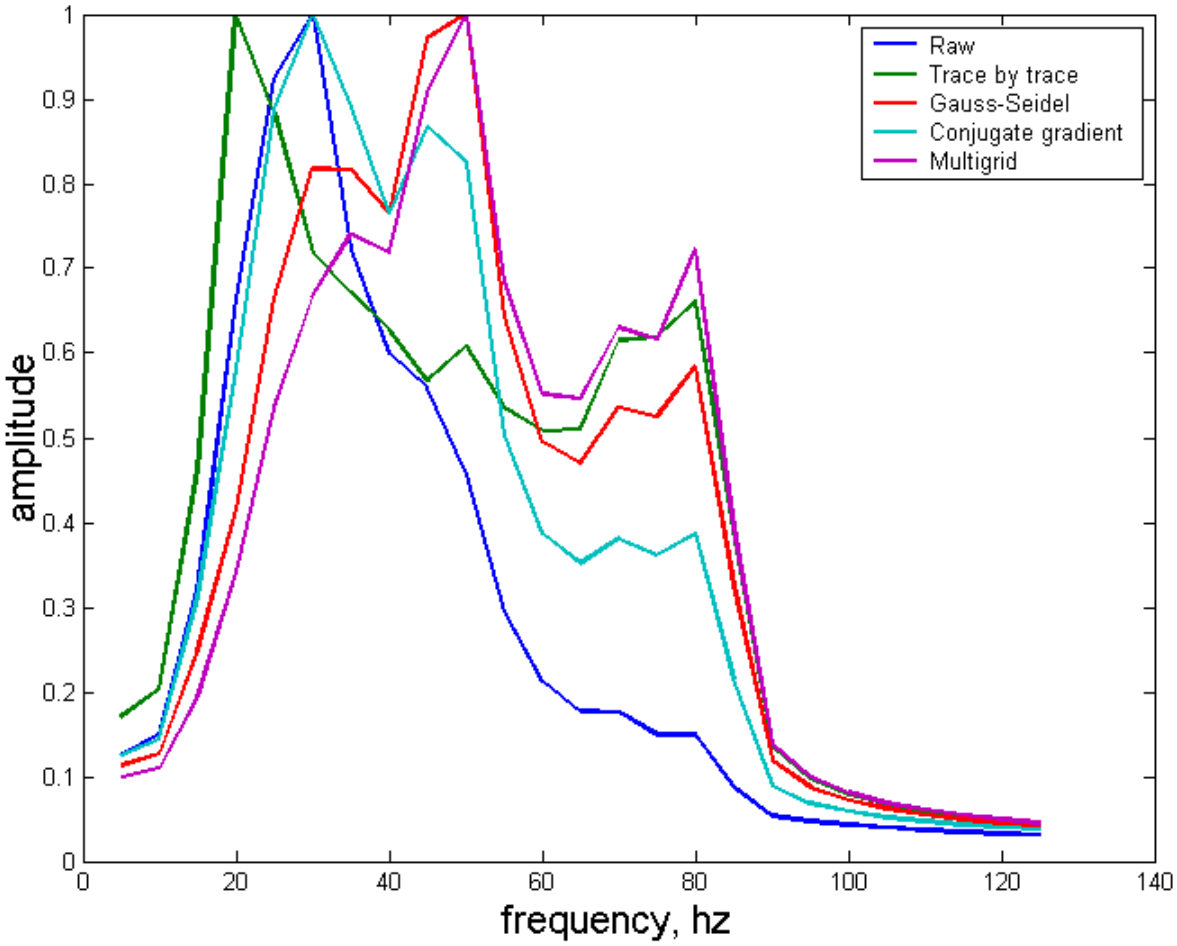

Figure 5.34: The amplitude spectrum of all traces with offsets between 200 and 210 meters.

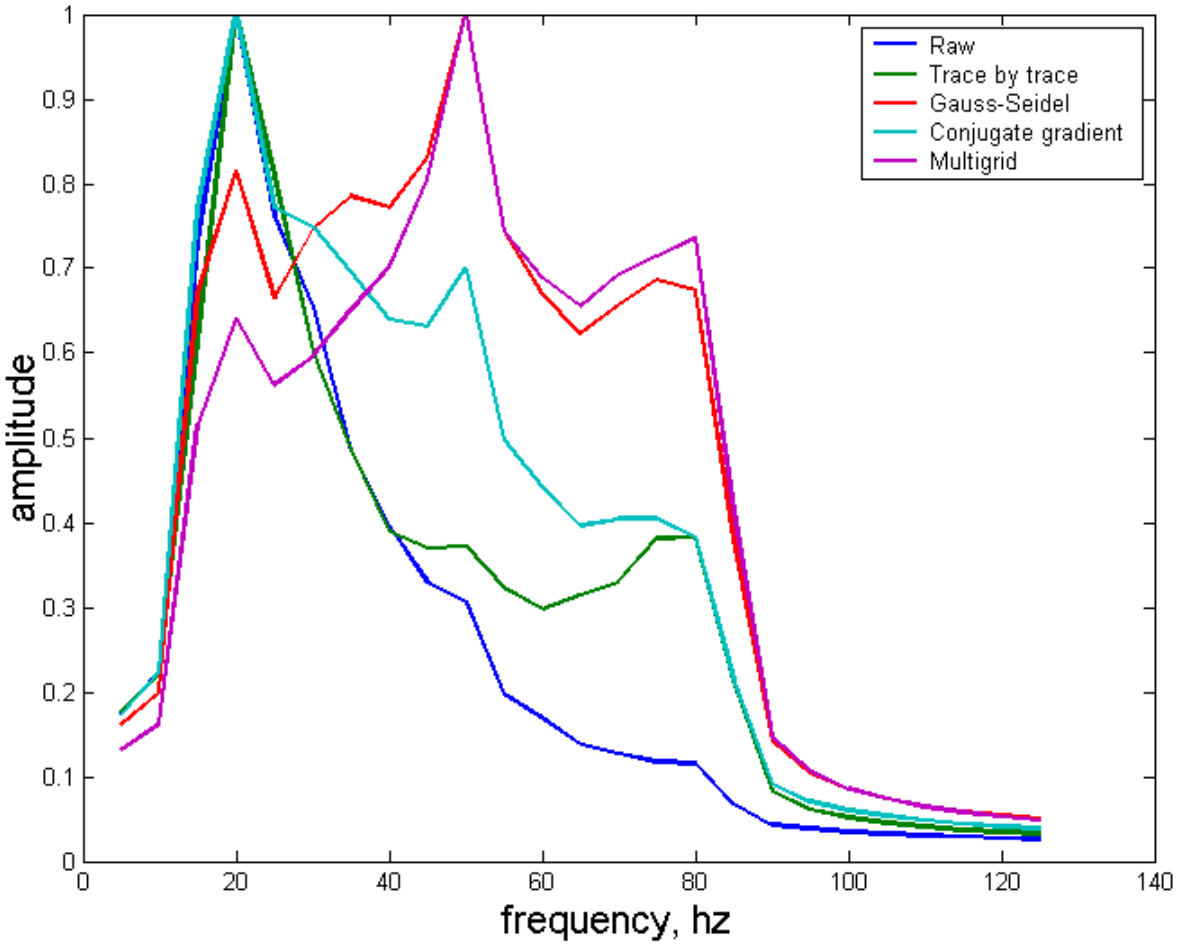

Figure 5.35: The amplitude spectrum of all traces with offsets between 20 and 30 meters.

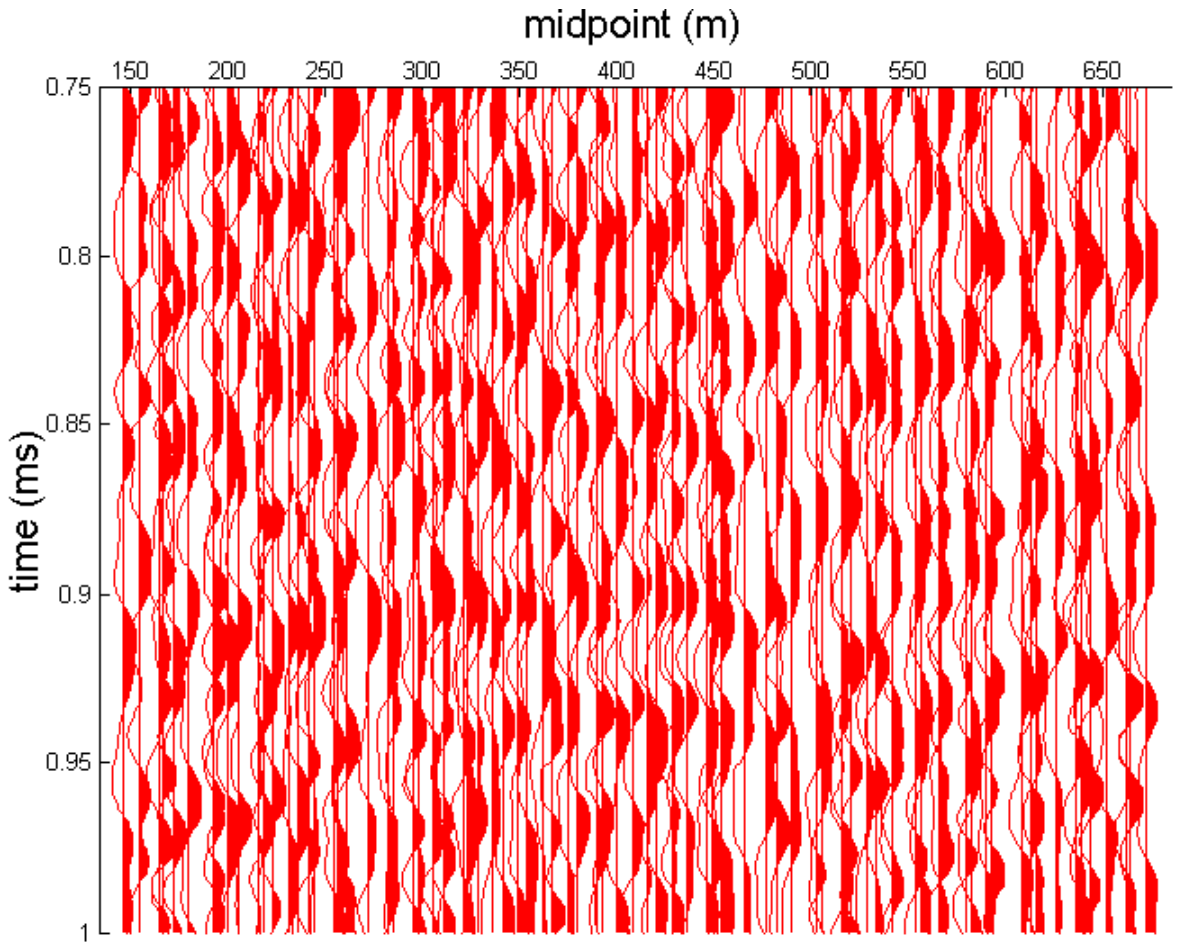

Figure 5.36: This Raw gather contains traces with source to receiver offsets between 200 and 210 meters. Every 5th trace is displayed.

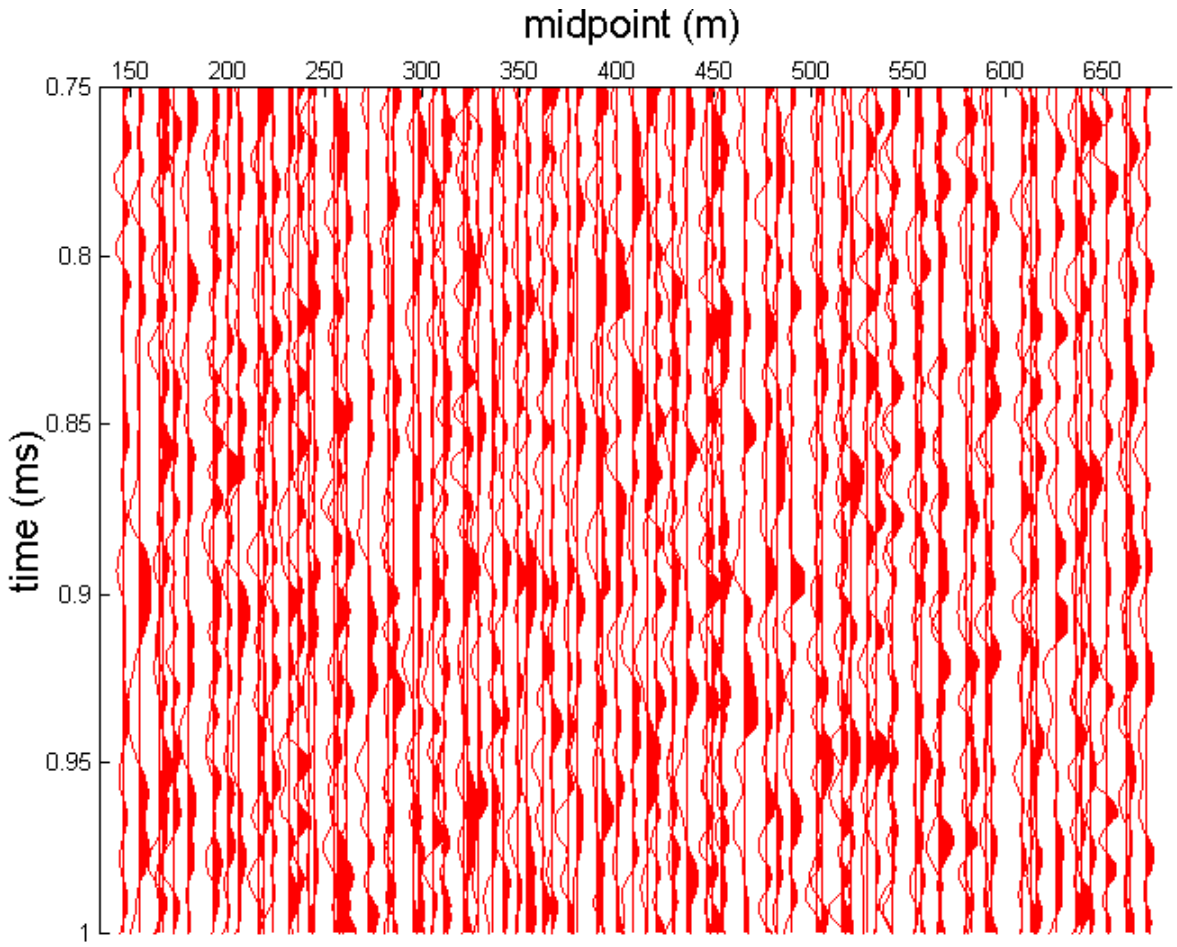

Figure 5.37: This offset gather contains traces with source to receiver offsets between 200 and 210 meters, and is deconvolved using operators calculated trace by trace.

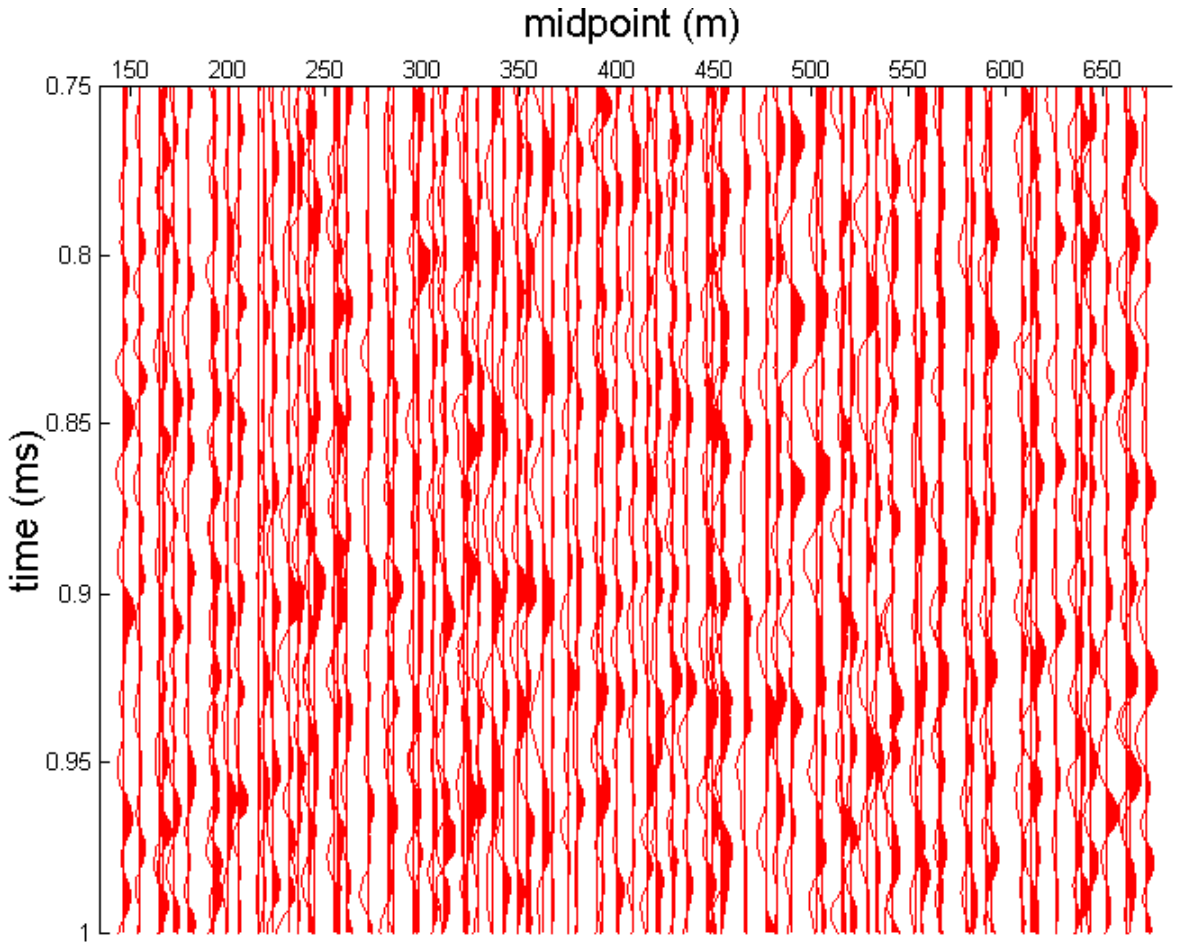

Figure 5.38: This offset gather contains traces with source to receiver offsets between 200 and 210 meters, and is deconvolved using surface consistent operators calculated using the conjugate gradient method.

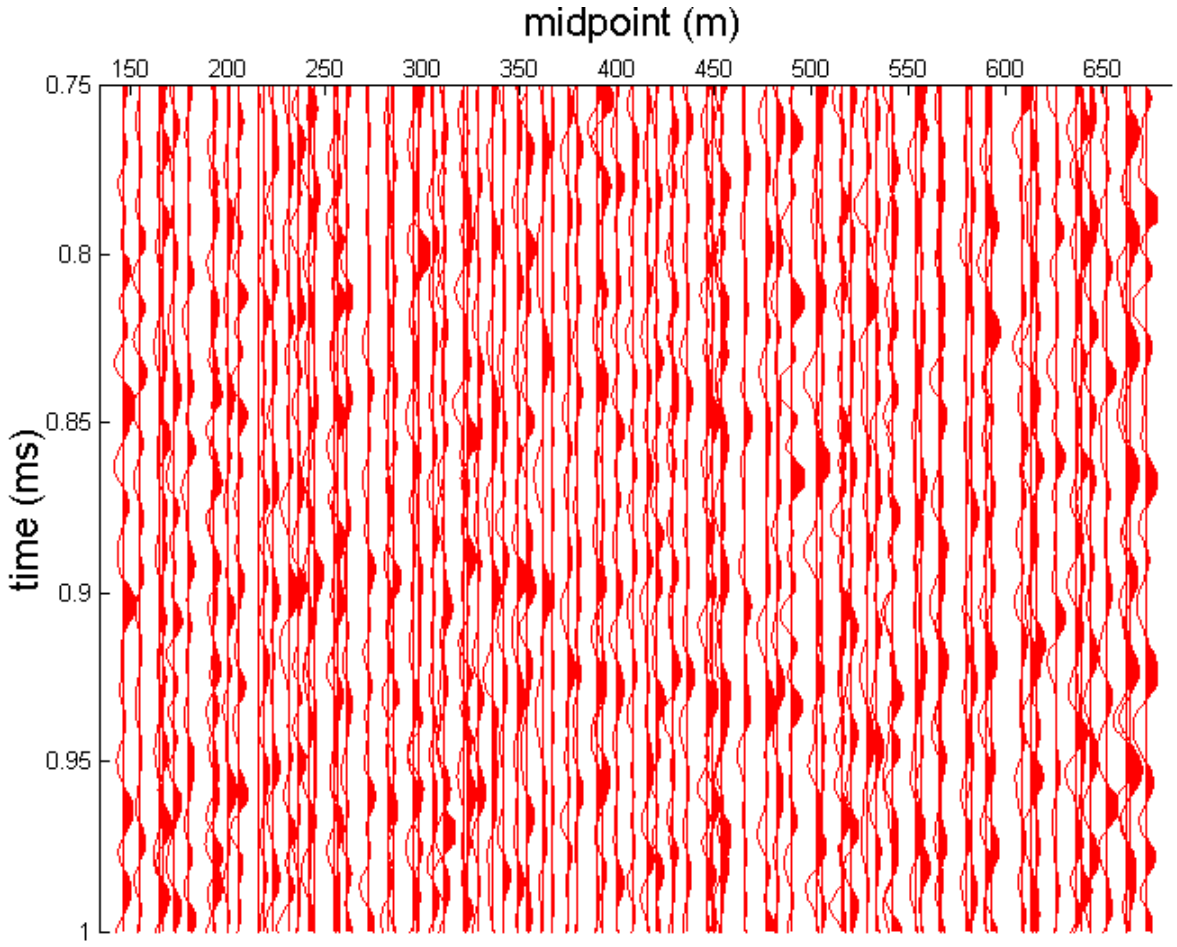

Figure 5.39: This offset gather contains traces with source to receiver offsets between 200 and 210 meters, and is deconvolved using surface consistent operators calculated using the Gauss-Seidel method.

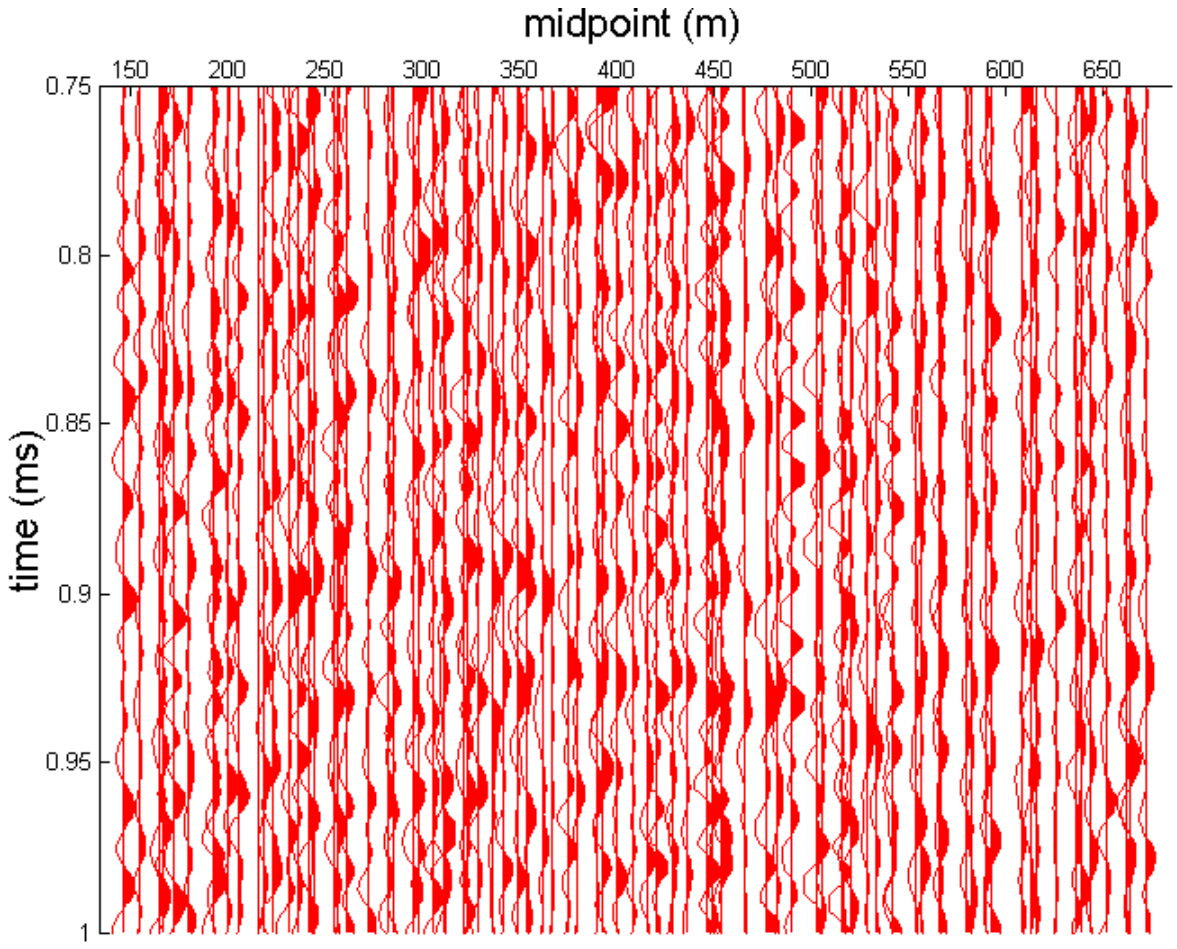

Figure 5.40: This offset gather contains traces with source to receiver offsets between 200 and 210 meters, and is deconvolved using surface consistent operators calculated using the multigrid method.

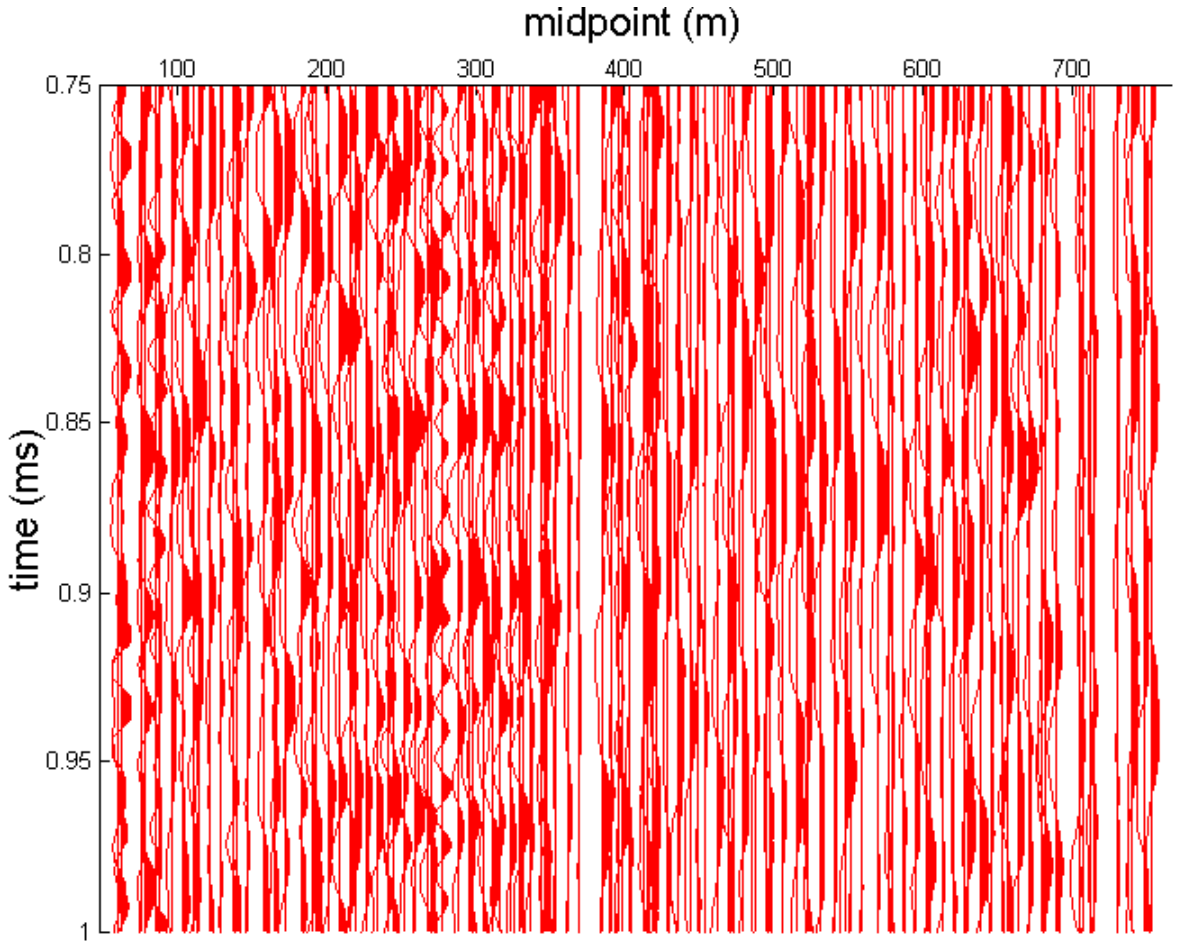

Figure 5.41: This Raw gather contains traces with source to receiver offsets between 20 and 30 meters. Every 5th trace is displayed. There is significant ground roll interference in this section.

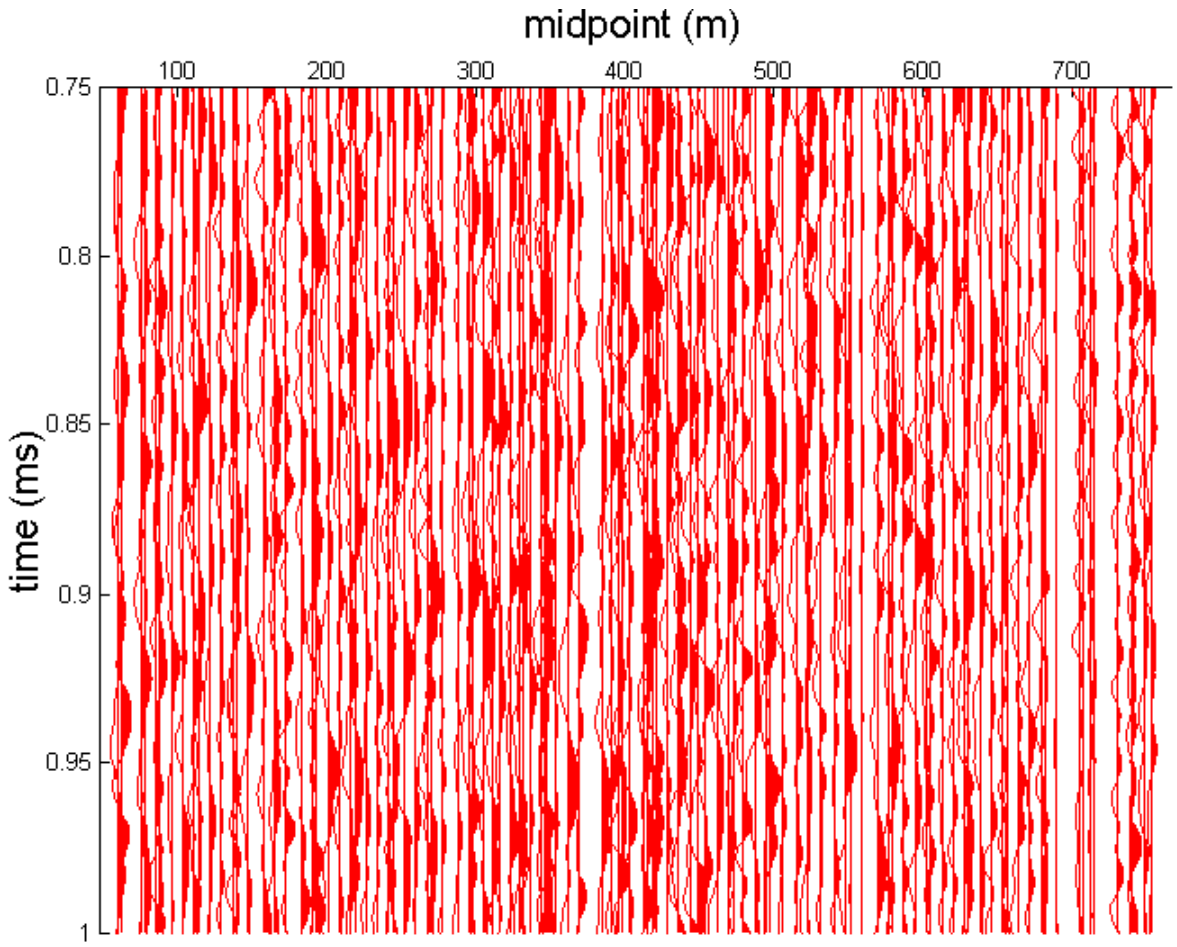

Figure 5.42: This offset gather contains traces with source to receiver offsets between 20 and 30 meters, and is deconvolved using operators calculated trace by trace.

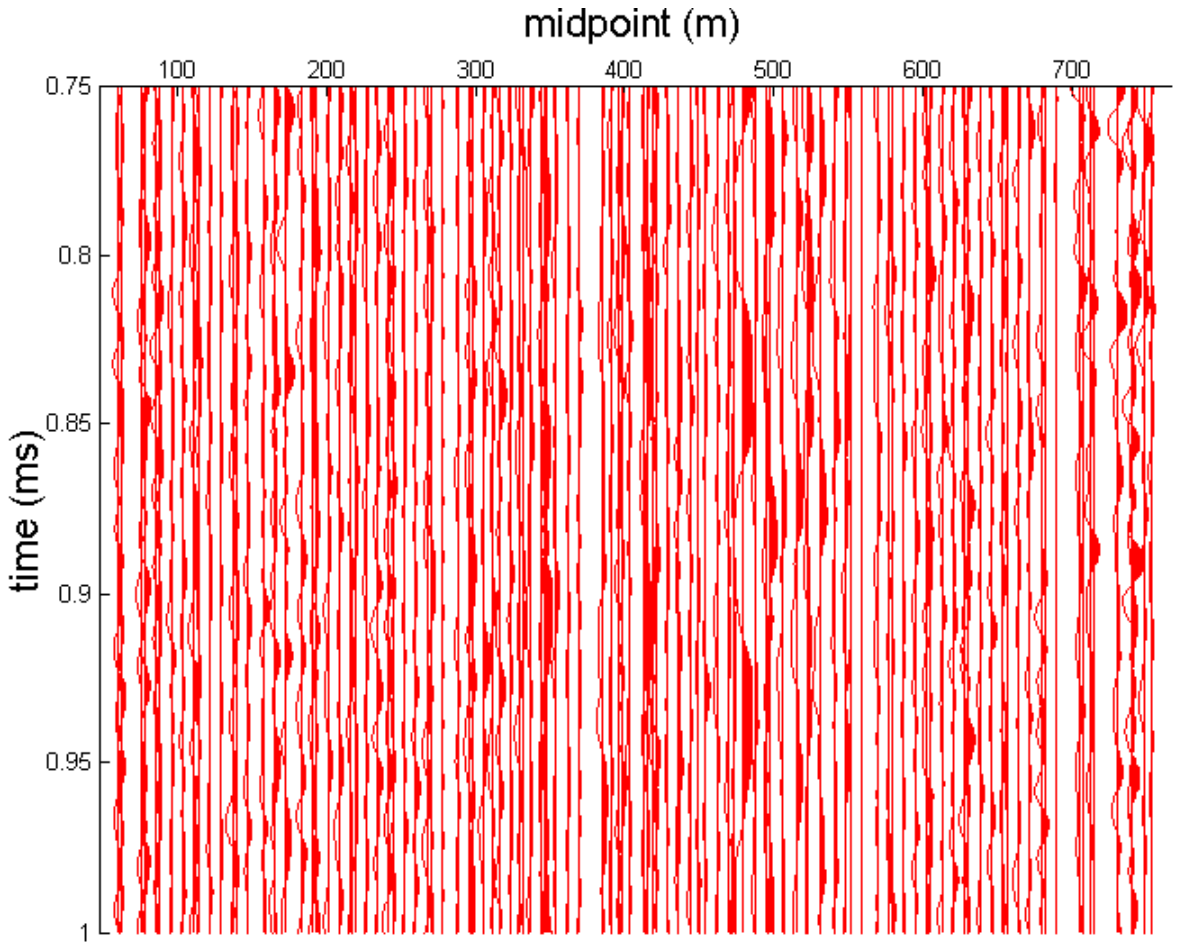

Figure 5.43: This offset gather contains traces with source to receiver offsets between 20 and 30 meters, and is deconvolved using surface consistent operators calculated using the conjugate gradient method.

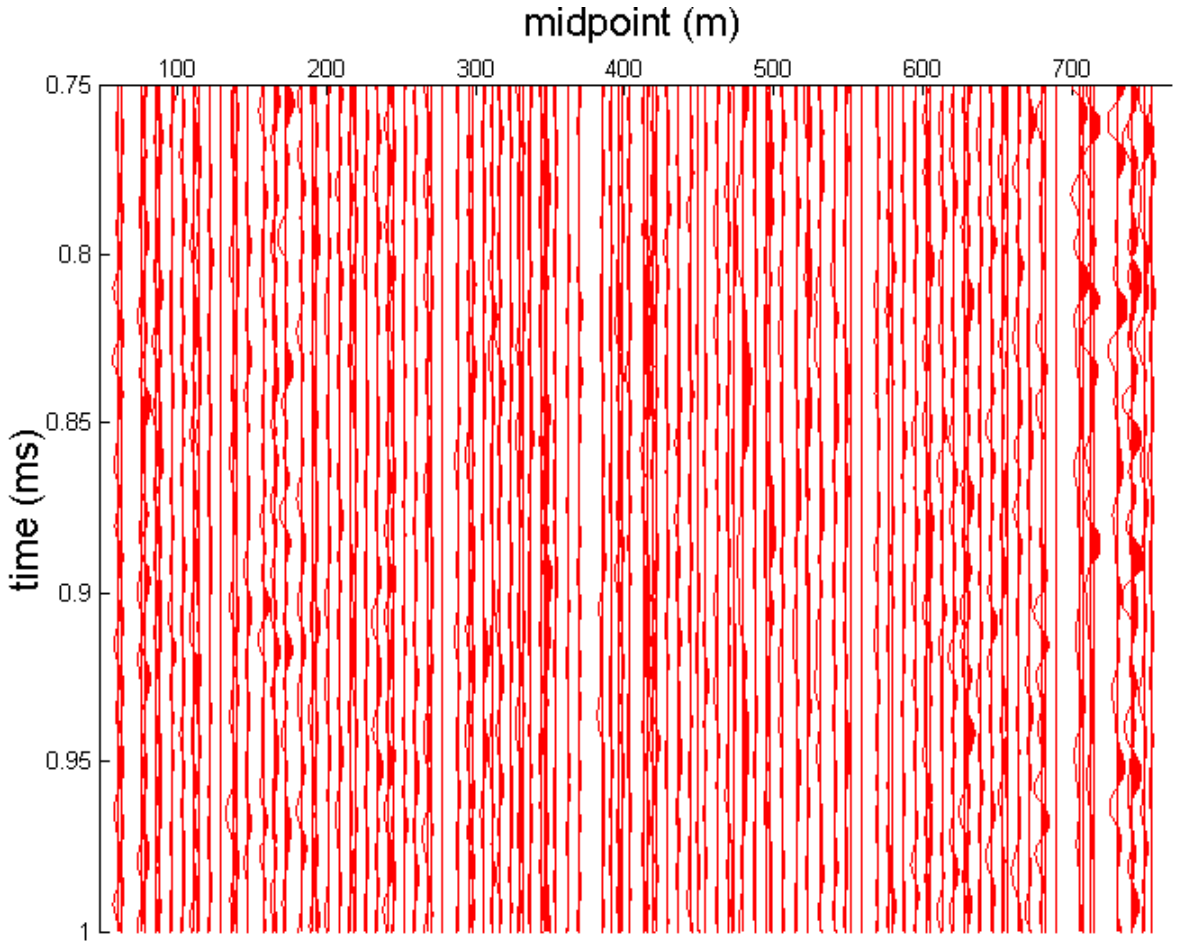

Figure 5.44: This offset gather contains traces with source to receiver offsets between 20 and 30 meters, and is deconvolved using surface consistent operators calculated using the Gauss-Seidel method.

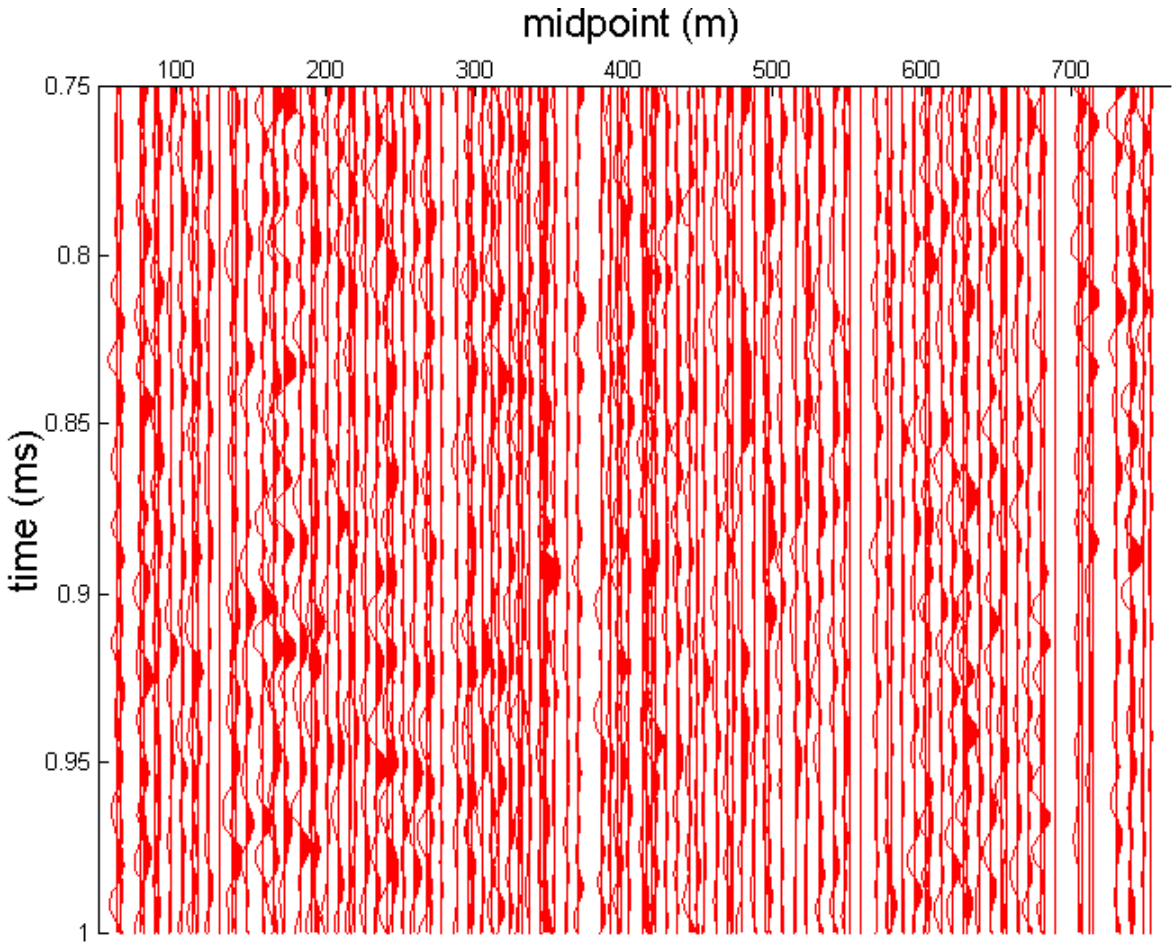

Figure 5.45: This offset gather contains traces with source to receiver offsets between 20 and 30 meters, and is deconvolved using surface consistent operators calculated using the multigrid method.

Chapter 6

Conclusions

The multigrid method has been shown to provide superior solutions to the surface consistent equations. In the presence of a large surface consistent anomaly, long wavelength errors that remain after Gauss-Seidel and other corrections negatively impact the quality of the processed seismic section.

Our synthetic examples have shown that long wavelength errors in a static solution produce a smearing of the wavelet in a midpoint stacked section. At the worst this could certainly cause a decrease in resolution, and it certainly increases our reliance on trim statics. Applying a multigrid method to solve statics problems improves the resolution of reflectors in the presence of a large surface consistent anomaly.

The more accurate multigrid solutions also improve our ability to solve for amplitudes. The long wavelength errors in source and receiver consistent amplitude studies were shown to cause an artificial AVO anomaly in our synthetic example.

Multigrid surface consistent deconvolution calculates more accurate deconvolution operators than Gauss-Seidel can provide. Synthetic results show the multigrid solutions do more accurately relegate ground roll to the offset term. This translates into more effective noise suppression in parts of the shot records dominated by ground roll. This benefit is realized even without the presence of a large surface consistent anomaly.

The synthetic model presented appears to do a good job of capturing the difficulties in solving the surface consistent equations. When we apply our methodology to the Blackfoot field data, Ground roll and surface noise were best projected into the offset consistent channel

by multigrid. Gauss-Seidel and conjugate gradient methods ended up with a less effective deconvolution operator due to this noise staying in the source and receiver channels. Parts of the data where ground roll was not significant showed a marginal improvement in resolution with multigrid. The reflections appeared slightly tighter, and some minor features in the data were recovered. These improvements were visible in all of the gathers. In the areas beset by ground roll, the multigrid method was able to recover reflections that were completely obscured in the Gauss-Seidel and conjugate gradient sections.

The benefits of using multigrid come at a small cost of computer time. Calculating a multigrid solution takes approximately the same amount of time as 20 Gauss-Seidel operations. Commercial processing packages default settings range from 5-10 iterations of Gauss-Seidel corrections. While using this method may triple the amount of time currently spent solving the equations, this comprises a very small fraction of the computer time dedicated to seismic processing.

Substitution a multigrid method in place of a Gauss-Seidel method into a processing flow is straight forward, and the change is totally transparent to a processing geophysicist using the system. The cost in terms of time and effort in implementing a multigrid solver into a surface consistent application is low, but there is a definite benefit in terms of quality of the seismic section.

6.1 Future Work

Many questions remain regarding the surface consistent equations, statics and deconvolution. This paper focusses on how multigrid provides us with superior numerical solutions, and the effect of the improvements on reflection seismic data. Some questions we had were left

unanswered:

Is the presence of the midpoint consistent term justified?

Could we instead use an equivalent offset term, as defined by Bancroft et al. (1998) ?

Can we add a time variant term?

How do we evaluate the surface consistent assumption?

Survey geometry has a strong influence on the number of singularities in the solution, would it be worth it to consider this during survey design?

Another possible source of future work is looking at applying multigrid to other processes in geophysics and seismic processing. Some work is already being done, in Yousefzadeh and Bancroft (2009), the authors look at applying a multigrid method to a Kirchoff inversion. Lo and Inderwiesen (1994) applies Gauss-Seidel corrections for traveltime tomography, in their generalized ART algorithm. Multigrid inversion may be of help there as well. Using multigrid for PP and PS joint inversion, or to improve semblance analysis plots may be feasible. Anywhere that Gauss-Seidel or another iterative method is in use is a great candidate to test a multigrid approach.

Bibliography

Bancroft, J. C., Geiger, H. G., and Margrave, G. F., 1998, The equivalent offset method of prestack time migration: Geophysics, **63**, 2041–2053.

Bancroft, J. C., and Millar, J., 2003, Applications of multigrid processing featuring deconvolution: Presented at the 17th Ann. Mtg., ASEG.

Bancroft, J. C., Richards, A., and Ursenbach, C., 2000, Statics, the abusive power of trimming: CREWES Research Report.

Bunks, C., Saleck, F., Zalesky, S., and Chavent, G., 1995, Multiscale seismic waveform inversion: Geophysics, **60**, No. 5, 1457–1473.

Cary, P. W., and Lorentz, G. A., 1993, Four-component surface-consistent deconvolution: Geophysics, **58**, No. 3, 383–392.

Hunter, P., and Pullen, A., 1997-2003, The Finite Element/Boudary Element Notes: Department of Engineering, University of Aukland.

Lo, T.-W., and Inderwiesen, P. L., 1994, Fundamentals of Seismic Tomography: SEG Geophysical Monograph Series, No 6.

Noble, B., and Daniel, J. W., 1988, Applied Linear Algebra: Prentice Hall, 3rd edn.

Press, W. H., Teukolsky, S. A., Vetterling, W. T., and Flannery, B. P., 1992, Numerical Recipes in C: Cambridge University Press, 2nd edn.

Riley, K. F., Hobson, M. P., and Bence, S. J., 2002, Mathematical Methods for Physics and Engineering: Cambridge University Press, 2nd edn.

Sacchi, M. D., 2006, Intro to Inverse Problems in Exploration Seismology: PIMS Inversion and Imaging workshop.

Shewchuk, J. R., 2002, An Introduction to the Conjugate Gradient Method Without the Agonizing Pain: http://www.cs.cmu.edu/ quake-papers/painless-conjugate-gradient.pdf.

Taner, M. T., and Koehler, F., 1981, Surface consistent equations: Geophysics, **46**, No. 1, 17–22.

Taner, M. T., Koehler, F., and Alhilali, K. A., 1974, Estimation and correction of near surface time anomolies: Geophysics, **39**, No. 4, 441–463.

Trottenberg, U., Oosterlee, C., and Schűller, A., 2001, Multigrid: Academic Press.

Wang, H., and Zhou, H., 1992, Multi-grid inversion and noise suppression of isc traveltimes around west pacific subduction zones: American Geophysical Union, spring meeting.

Wesseling, P., 1992, An Introduction to Multigrid Methods: John Wiley & Sons.

Wiggins, R. A., Larner, K. L., and Wisecup, R. D., 1976, Residual statics analysis as a general inverse problem: Geophysics, **41**, No. 5, 10.

Yilmaz, O., and Doherty, S. M., 1994, Seismic Data Analysis: Processing Inversion and Interpretation of Seismic Data: Addison-Wesley.

Yousefzadeh, A., and Bancroft, J. C., 2009, Feasibility of solving least squares prestack kirchhoff migration using multigrid methods: CREWES Research Report.